Material Characterization and Modeling for Piezoelectric Actuation and Power Generation under High Electromechanical Driving Levels

by

Ching-Yu Lin

Submitted to the Department of Aeronautics and Astronautics
in partial fulfillment of the requirements for the degree of

Doctor of Philosophy in Aeronautics and Astronautics

at the

MASSACHUSETTS INSTITUTE OF TECHNOLOGY

June 2002

Author .....
Department of Aeronautics and Astronautics
May 3, 2002

Certified by .....
Nesbitt W. Hagood
Principal Research Scientist
Department of Aeronautics and Astronautics
Thesis Supervisor

Certified by .....
S. Mark Spearing
Associate Professor
Department of Aeronautics and Astronautics
Thesis Supervisor

Certified by .....
Yet-Ming Chiang
Professor
Department of Material Science and Engineering
Thesis Supervisor

Accepted by .....
Wallace E. Vander Velde
Professor
Department of Aeronautics and Astronautics
Chair, Committee on Graduate Students

Material Characterization and Modeling for Piezoelectric Actuation and Power Generation under High Electromechanical Driving Levels

by

Ching-Yu Lin

Submitted to the Department of Aeronautics and Astronautics
on May 3, 2002, in partial fulfillment of the
requirements for the degree of
Doctor of Philosophy in Aeronautics and Astronautics

Abstract

High electromechanical loads parallel to piezoelectric polarization might result in depolarization of the material, depending on the material property itself and the external excitations such as electrical field, electrical driving frequency, stress and stress duration. In this work, material properties under these effects were first characterized experimentally. The experiments included monitoring general piezoelectric responses of PZT-5H and PZT-5A subjected to large electric excitations (butterfly curves) under various static compressions and measuring generalized piezoelectric constants under short and open circuit conditions for actuation of PZT-5A and power generation of PZT-5H, single crystals PZN-PT, and single crystals PMN-PT.

To model these observed material behaviors, one- and three-dimensional rate dependent nonlinear constitutive models based on thermodynamic potentials for PZT-5H and PZT-5A piezoelectric materials were then developed. An internal variable, net remnant polarization D^*, was used to simulate the hysteric behaviors of piezoelectric materials. An evolution law of D^* was derived to specify the rate dependent responses of the materials. The parameters of the material models were determined by minimizing the error between the data and the models. The material models were capable of describing the responses subjected to large electric excitations under static compression, but incapable of predicting accurate piezoelectric constants under dynamic compression. This flaw was believed due to the absence of stress rate dependency in the models. It was also found that the PZT-5A model performed worse than the PZT-5H model because of its highly hysteretic strain-polarization relation. This hysteresis could be explained by the slow switching rate of 90-degree domain movement.

Finally, to simulate devices under non-uniform field or with irregular geometries using these material models, differential algebraic equations for mixed finite element analysis of 3-D nonlinear rate dependent piezoelectric materials were formulated and solved numerically by DASPK solver. Using 4-node tetrahedral elements, this formulation was demonstrated by examples with uniform and skewed electric excitations. The combination of the nonlinear mixed FEM model and the material model provided a useful tool for modeling the response of active devices with complicated geometries and irregular boundary conditions.

Thesis Supervisor: Nesbitt W. Hagood
Title: Principal Research Scientist
Department of Aeronautics and Astronautics

Thesis Supervisor: S. Mark Spearing
Title: Associate Professor
Department of Aeronautics and Astronautics

Thesis Supervisor: Yet-Ming Chiang
Title: Professor
Department of Material Science and Engineering

Acknowledgments

First, I would like to thank my advisor, Professor Nesbitt Hagood, for his encouraging advice. The additional assistance from Professors Yet-Ming Chiang, Mark Spearing, John Dugundji and Marthinus van Schoor is also acknowledged. Other assitance from people in AMSL, Dave Robertson, Mauro Atalla, Mai Nguyen, Mary Jones, Kamyar Ghandi, Aaron Bent, Chris Dunn, Timothy Glenn, Benon Janos, Dave Roberts, Lodewyk Steyn, Onnik Yaglioglu, Malinda Lutz, Yong Shi, and Michael Fripp, is thanked, too.

I would also like to thank my family for their support. My parents educated me well so that I could come to MIT. My brother and sister set good examples for me. My beloved wife Chun-Ling (Lindsey), who helps me focus on this doctoral thesis, is mostly appreciated.

Funding for this research was provided by U.S. Army Research Office (ARO) under contract DAAH04-95-1-0104 monitored by Dr. Gary Anderson and by DARPA under contract of Active Fiber Composite Consortium (AFCC, 49620-97-0527) monitored by Dr. William Coblenz and Dr. Spencer Wu. Support also came from Office of Naval Research (ONR) under contract N00014-01-1-0857 monitored by Dr. Smith Wallace and from DARPA under contract DAAG55-98-1-036 monitored by Dr. Robert Nowak and Dr. Richard Paur.

Contents

List of Figures

List of Tables

Nomenclature

α	Parameter of Weibull function.
β	Ferroelectric domain switching function in Soukhojak's model.
ΔD_c	Critical value to determine the initialization of the repolarization.
ΔE	Energy barrier.
η	Diode property.
$\dot{\hat{\mathbf{D}}}^*$	Derivative of $\hat{\mathbf{D}}^*$ with respect to time t.
$\hat{\mathbf{D}}$	Electric displacement degree of freedom in finite element analysis.
$\hat{\mathbf{D}}^*$	Fictitious electric displacement degree of freedom in finite element analysis.
$\hat{\mathbf{U}}_\mathbf{a}$	Unknown displacement degree of freedom in finite element analysis.
$\hat{\mathbf{U}}_\mathbf{b}$	Prescribed displacement degree of freedom in finite element analysis.
$\hat{\mathbf{U}}$	Displacement degree of freedom in finite element analysis.
$\hat{\mathbf{V}}_\mathbf{a}$	Unknown voltage degree of freedom in finite element analysis.
$\hat{\mathbf{V}}_\mathbf{b}$	Prescribed voltage degree of freedom in finite element analysis.
$\hat{\mathbf{V}}$	Voltage degree of freedom in finite element analysis.
$\mathbf{a}$, a_i	Reference vector of tensor invariants.
$\mathbf{D}^*$, D_i^*	Fictitious internal variable for hysteretic electric displacement in matrix and tensor forms.

$\mathbf{D}$, D_i	Electric displacement in matrix and tensor forms.
$\mathbf{E}$, E_i	Electric field in matrix and tensor forms.
$\mathbf{S}$, S_{ij}	Strain in matrix and tensor forms.
$\mathbf{T}$, T_{ij}	Stress in matrix and tensor forms.
$\mathcal{P}$	Power.
Ω	Energy Density.
σ	Entropy.
τ	Time constant.
τ_d	Dielectric time constant in Soukhojak's model.
τ_{sw}	Time constant of domain switching in Soukhojak's model.
θ	Temperature.
A	Helmholtz free energy.
D, D_3	Electric displacement in 3 direction. To be rigorous, the transformation between the polarization(P) and electric displacement(D) is $D = P + \epsilon_0 E$. The difference is negligible, since ϵ_0 is comparatively small.
D^*, D_3^*	Fictitious electric displacement.
d_{ij}	Piezoelectric constant.
E, E_3	Electric field in 3 direction.
E_0	Normalization field in Soukhojak's model.
E_c	Coercive field.
f	Frequency in Hz.
G	Gibbs free energy.
G_1	Elastic Gibbs energy.

G_2	Electric Gibbs energy.
g_{ij}	Piezoelectric constant.
H	Enthalpy.
H_1	Elastic enthalpy.
H_2	Electric enthalpy.
I_0	Diode property.
k	Boltzmann constant
k_{ij}	Coupling coefficient.
n	Net fraction of dipoles pointing up, as defined in Soukhojak's model.
P, P_3	Polarization in 3 direction.
P_d	Dielectric polarization in Soukhojak's model.
P_F	Ferroelectric polarization in Soukhojak's model.
P_r	Remnant polarization.
P_s	Spontaneous polarization.
P_{sat}	Saturation of polarization in Soukhojak's model.
S, S_{33}, S_3	Strain in 3 direction.
s_{ij}^D	Elastic constant at open circuit condition.
s_{ij}^E	Elastic constant at short circuit condition.
T, T_{33}, T_3	Stress in 3 direction.
U	Internal energy.
V_{DC}	Battery voltage.
w_E	Weights of least squares regression for electric field.
w_S	Weights of least squares regression for strain.

Chapter 1

Introduction

1.1 Piezoelectricity

1.1.1 What is a piezoelectric material?

Piezoelectric materials are those certain crystalline materials which have the ability to develop an electric charge proportional to an applied mechanical stress. It was first discovered by J. and P. Curie in 1880. Soon it was realized that materials showing this phenomenon must also have the converse behavior, a geometric strain (deformation) proportional to an applied voltage[47]. Since then, piezoelectric materials have become the common electromechanical transducers which can transfer energy between electrical and mechanical forms. Compared to electro-magnetic transducers, a piezoelectric has the advantages of its high stiffness and broad bandwidth.

Various types of ceramics with different material composition have been discovered and improved since 1940s. The early commercial piezoelectric barium titanate products were phonograph pickup devices marketed by Sonotone Corporation. Composition modification was found desirable to improve the temperature stability and to gain moderate improvement in voltage output. An advance of great practical importance was the discovery of very strong and stable piezoelectric effects in lead zirconate titanate (PZT) solid solutions. Lead zirconate titanate with various additives has since become the dominant piezoelectric ceramic. The most common piezoelectric material used today includes the PZT family commercialized by Morgan Matroc. Recently, single crystal piezoelectric materials such as lead

zinc niobate-lead titanate (PZN-PT) and lead magnesium niobate-lead titanate (PMN-PT) have gained the attention of engineers who need high coupling coefficients, i.e. efficient power transformation.

1.1.2 How does it work?

To describe the essential features of the ferroelectric phenomenon, Jona and Shirane[48] used a hypothetical ferroelectric crystal. The model is simplified such that only a two dimensional crystal is considered having the chemical formula AB and a fictitious structure illustrated in Figure 1-1(a).

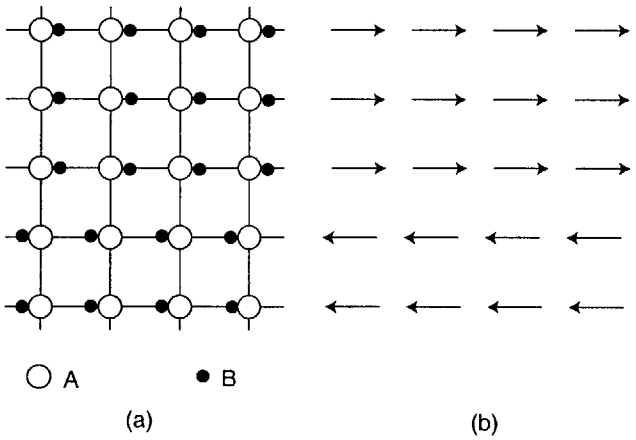

Figure 1-1: Schematic structure of a fictitious ferroelectric crystal.

The A ions, assumed to carry a negative charge, are located on the lattice points of a simple square net. Beside the A ions on the horizontal lines are the positively charged B ions. The equilibrium positions of the B ions are such that they always bond closer to one of the two adjacent A ions than to the other. This is a possible situation if the potential between two adjacent A ions is one of the types sketched in Figure 1-2(a). For a B ion on the line between two A ions, two equilibrium points correspond to the same minimum value of the energy. The B ions can shift from one equilibrium to the other. To do so, they must be supplied with sufficient energy to overcome the energy barrier ΔE.

At a given temperature T, all A ions are closer to their B partners on the right. Each pair AB can be seen as an electric dipole and the structure can then be schematically represented

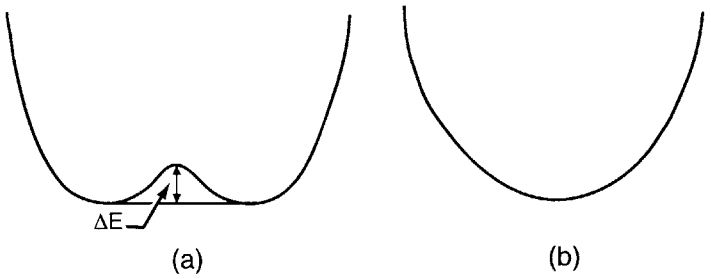

Figure 1-2: Schematic potential wells.

by an array of dipoles aiming all in the same direction, as illustrated in the three upper rows of Figure 1-1(b). This kind of crystal is considered spontaneously polarized. Alignment of the electric dipoles may extend only over a region of the crystal, while in another region the direction of the spontaneous polarization may be reversed, as shown in the lower part of Figure 1-1(b). Such regions of uniform polarization are called domains.

Suppose now that an electric d.c. field in the horizontal direction of Figure 1-1 is applied. The dipoles which are already oriented in the direction of the field will remain so aligned, but those which are oriented in the direction opposite to the field will show a tendency to reverse their orientation. If the applied field is sufficiently large, the B ions of this model will be able to overcome the barrier ΔE, and in so doing will cause the corresponding dipoles to flip over into the direction of the field. This phenomenon of polarization reversal takes place by way of a nucleation process and domain-wall motion. If this AB crystal is initially composed of an equal number of positive and negative domains, the overall polarization of the crystal is zero. If a small electric field in the positive direction is applied, the material will follow a linear P-E relation as shown by the OA portion in the plot of P vs. E in Figure 1-3.

Nonlinearity and Hysteresis

If the electric field strength is increased, the linearity will no longer hold. A number of the negative domains will switch over in the positive direction and the polarization will increase rapidly (portion AB), until the material reaches a state in which all the domains are aligned in the positive direction: this is a state of saturation (portion BC) and the crystal consists

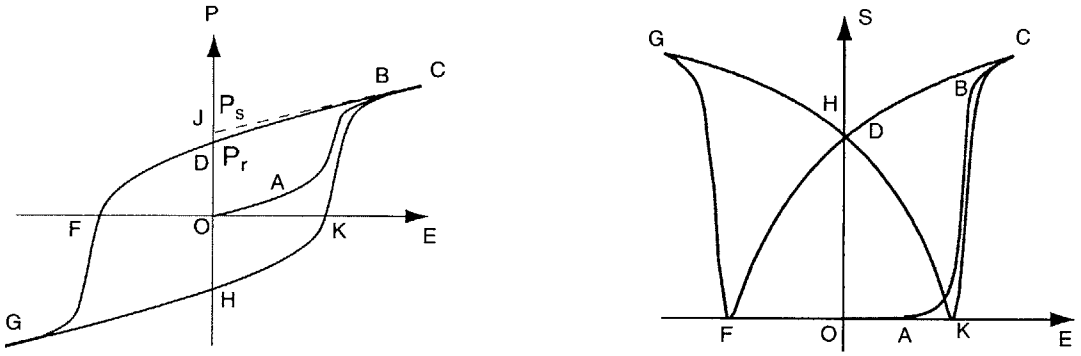

Figure 1-3: Schematic P-E and S-E loops.

now of a single domain. If the field strength is decreased, the polarization will generally not return to zero but rather follow the path CD of Figure 1-3. When the field is reduced to zero, some of the domains will remain aligned in the positive direction and the crystal will exhibit a remnant polarization P_r (OD).

It is possible to reduce polarization by applying an electric field in the opposite direction. The value of this field is called the coercive field E_c. Further increase of the field in the negative direction will cause complete alignment of the dipoles in this direction (FG) and the cycle can be completed by reversing the field direction once again (GHC). The relation between P and E is thus represented by a hysteresis loop (CDGHC), which is the most important characteristic of a ferroelectric crystal. The essential feature of a ferroelectric is thus not the fact that it has a spontaneously polarized domain, but rather the fact that this spontaneously polarized domain can be reversed by means of applying an electric field.

The strain of the material induced by the applied field is also illustrated in Figure 1-3. The strain response is approximately linear to the magnitude of the material polarization as illustrated in Figure 1-4. This shows that the material deformation is due to the growth of dipole and domain movement. Although the dipole may either orient to the left or right in Figure 1-1(b), the deformation only depends on the projected magnitude of the dipole. This explains how electric field induces the deformation of the materials.

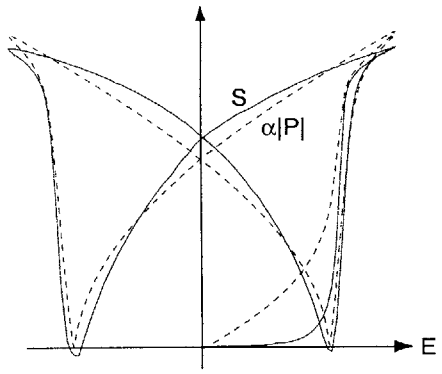

Figure 1-4: S-E (solid line) and $\alpha|P|$-E (dashed line) loops, where α is a scale factor.

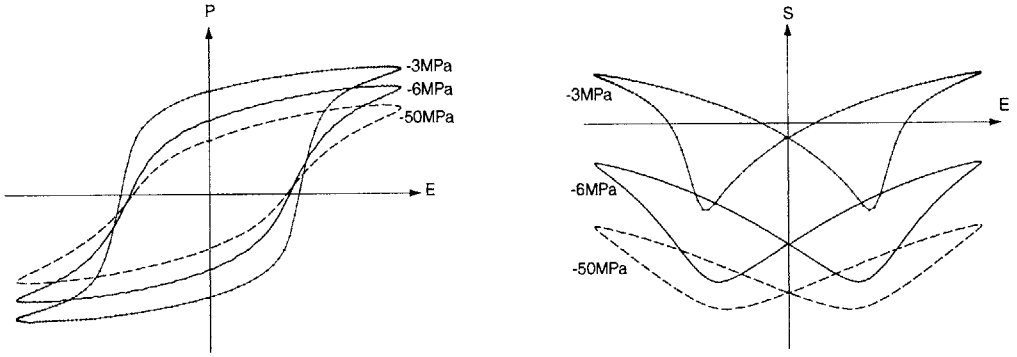

Figure 1-5: Schematic P-E and S-E loops under compression.

Stress Dependency

If a compresssive stress parallel to the polarization is applied to the material, obviously more energy needs to be overcome for ion B to change the equilibrium position. If the same electric field is applied, as in Figure 1-5, the polarization of material under compression may not increase to the same value as the stress-free material. For the same reason, the deformation of the material is suppressed by the compression. The material can also be subjected to tensile stress. The effect of tension is converse for the compression; however, it is not practical to apply tension on piezoelectric ceramics because of their fragility.

Linearization

In general, piezoelectric response (outputs) such as electric displacement[1] and mechanical strain can be described as functions of applied electric field and stress (inputs), for example:

$$\begin{aligned} \mathbf{D} &= \mathbf{D}(\mathbf{E}, \mathbf{T}) \\ \mathbf{S} &= \mathbf{S}(\mathbf{E}, \mathbf{T}) \end{aligned} \tag{1.1}$$

As can be seen in Figure 1-5, these two functions involve a high order of nonlinearity. The nonlinearity, hysteresis, and stress dependency make it difficult to model and design a piezoelectric device for advanced application. In the next section, a discussion of these issues will be presented. Before that, it is useful to linearize the material response using material constants. For example, assuming that the piezoelectric material is polarized in the 3 direction, the response in Eq. 1.1 can be linearized as:

$$\begin{Bmatrix} D_1 \\ D_2 \\ D_3 \\ S_{11} \\ S_{22} \\ S_{33} \\ 2S_{23} \\ 2S_{13} \\ 2S_{12} \end{Bmatrix} = \begin{bmatrix} \epsilon_{11}^T & 0 & 0 & 0 & 0 & 0 & 0 & d_{15} & 0 \\ 0 & \epsilon_{22}^T & 0 & 0 & 0 & 0 & d_{15} & 0 & 0 \\ 0 & 0 & \epsilon_{33}^T & d_{31} & d_{31} & d_{33} & 0 & 0 & 0 \\ 0 & 0 & d_{31} & s_{11}^E & s_{12}^E & s_{13}^E & 0 & 0 & 0 \\ 0 & 0 & d_{31} & s_{12}^E & s_{11}^E & s_{13}^E & 0 & 0 & 0 \\ 0 & 0 & d_{33} & s_{13}^E & s_{13}^E & s_{33}^E & 0 & 0 & 0 \\ 0 & d_{15} & 0 & 0 & 0 & 0 & s_{44}^E & 0 & 0 \\ d_{15} & 0 & 0 & 0 & 0 & 0 & 0 & s_{44}^E & 0 \\ 0 & 0 & 0 & 0 & 0 & 0 & 0 & 0 & s_{66}^E \end{bmatrix} \begin{Bmatrix} E_1 \\ E_2 \\ E_3 \\ T_{11} \\ T_{22} \\ T_{33} \\ T_{23} \\ T_{13} \\ T_{12} \end{Bmatrix} \tag{1.2}$$

This form is useful to calculate the linear response of materials under the short circuit condition. For materials under the open circuit condition, it is convenient to use another

[1] To be rigorous, the transformation between the polarization (P) and electric displacement (D) is $D = P + \epsilon_0 E$. The difference is negligible, since ϵ_0 is comparatively small.

form:

$$\begin{Bmatrix} E_1 \\ E_2 \\ E_3 \\ S_{11} \\ S_{22} \\ S_{33} \\ 2S_{23} \\ 2S_{13} \\ 2S_{12} \end{Bmatrix} = \begin{bmatrix} \beta_{11}^T & 0 & 0 & 0 & 0 & 0 & 0 & -g_{15} & 0 \\ 0 & \beta_{22}^T & 0 & 0 & 0 & 0 & -g_{15} & 0 & 0 \\ 0 & 0 & \beta_{33}^T & -g_{31} & -g_{31} & -g_{33} & 0 & 0 & 0 \\ 0 & 0 & g_{31} & s_{11}^D & s_{12}^D & s_{13}^D & 0 & 0 & 0 \\ 0 & 0 & g_{31} & s_{12}^D & s_{11}^D & s_{13}^D & 0 & 0 & 0 \\ 0 & 0 & g_{33} & s_{13}^D & s_{13}^D & s_{33}^D & 0 & 0 & 0 \\ 0 & g_{15} & 0 & 0 & 0 & 0 & s_{44}^D & 0 & 0 \\ g_{15} & 0 & 0 & 0 & 0 & 0 & 0 & s_{44}^D & 0 \\ 0 & 0 & 0 & 0 & 0 & 0 & 0 & 0 & s_{66}^D \end{bmatrix} \begin{Bmatrix} D_1 \\ D_2 \\ D_3 \\ T_{11} \\ T_{22} \\ T_{33} \\ T_{23} \\ T_{13} \\ T_{12} \end{Bmatrix} \tag{1.3}$$

1.2 Application

As mentioned earlier, the first piezoelectric device was a phonograph pickup marketed by Sonotone Corporation. Since then, underwater sonar has been the major application. After the concept of smart structures proposed by Crawley and Deluis[50], piezoelectric materials are primarily used as sensors and actuators. Other applications include electrical transformers and electrical power harvesters. In this section, several common sensors, actuators and energy harvesters are introduced.

1.2.1 Actuator

An early application of piezoelectric materials was an underwater sound transducer used by the navy for submarine detection. This application needs broad bandwidth but only small deformation. However, to achieve successful smart structures, such as space structures and aircraft wings, engineers have made an effort to maximize the strain of the piezoelectric materials with minimum driving voltage.

To achieve this goal, one method is to drive the piezoceramics with large amplitude electric field. However, due to their natural characteristics, the piezoceramics behave nonlinearly at high electric fields, as shown in Figure 1-3. It is essential to have a good model to predict these behaviors in order to design the devices and take advantage of this large deformation. Another way to achieve large deformation is to configure the device as a stack, as illustrated in Figure 1-6(a). Using this technique, one can reduce the driving voltage but

increase the actuation stroke. However, the arrangement of connecting leads may not be easy. An alternative configuration in Figure 1-6(b) used by Morgan Matroc[2] improves this problem. However, the drawbacks of this design include a costly manufacturing process and stress concentration at the ends of electrodes. This nonuniform stress may degenerate the performance of the material. As shown in Figure 1-7, the same problem also exists in a piezoelectric wafer with Interdigitated Electrodes (IDE), proposed by Hagood *et al.*[49] To realize this stress concentration, sophisticated nonlinear models and finite element tools are essential.

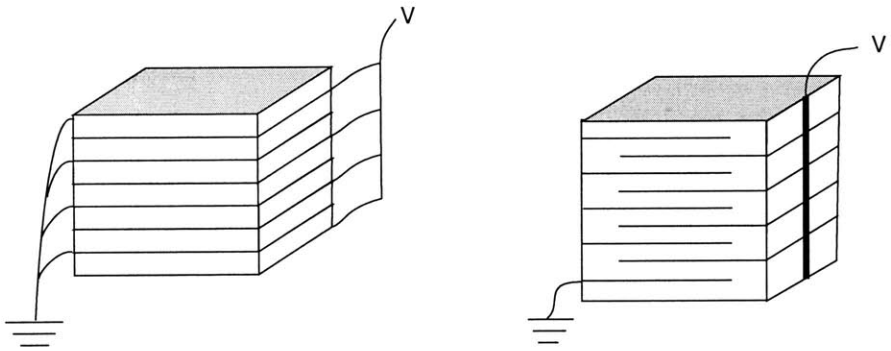

Figure 1-6: Piezo stacks

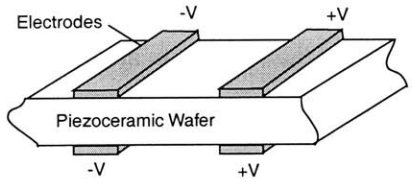

Figure 1-7: Piezoelectric wafer with Interdigitated Electrodes (IDE).

Another problem of common piezo-actuators is their fragility. It is also difficult to reshape the materials. A novel actuator, Active Fiber Composites(AFCs), was invented by MIT researchers to solve this problem[27]. The application of AFCs includes integral actuation of helicopter blades[51], as shown in Figure 1-9. As shown in Figure 1-8, piezoelectric

[2]Morgan Matroc, Inc. Bedford, Ohio 44146

materials made in fiber forms are sandwiched by two layers of interdigitated electrodes. Between the layers is epoxy material cured to protect the piezoelectric fibers and to increase the overall strength of the composites. The voltage is applied such that major electric fields go through the fiber direction. This results in direct actuation of the piezoelectric in 33-mode, which means the deformation is along the applied field.

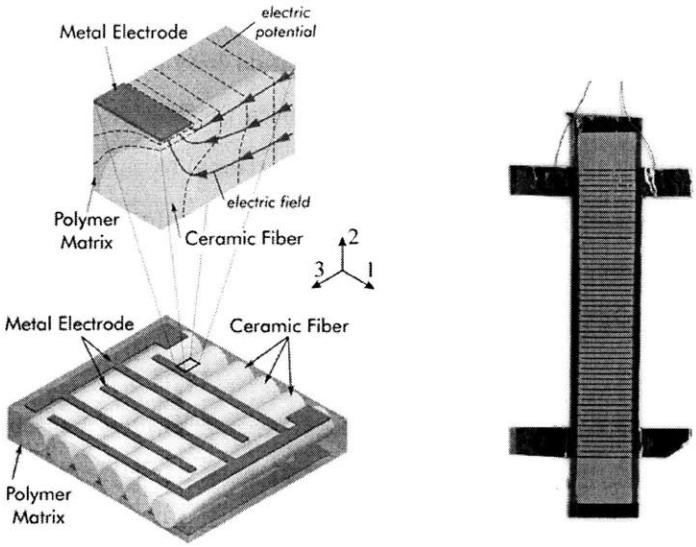

Figure 1-8: Active Fiber Composites

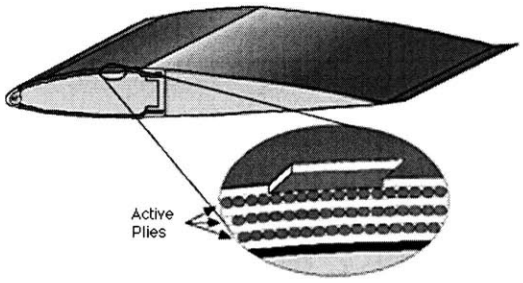

Figure 1-9: Active Fiber Composites for integral actuation of helicopter blades

Some applications may need the materials to deform in large strain instead of high force output. For instance, precision optical devices may need large actuating deformation but low force, while some applications need material to generate large actuating forces.

To achieve large actuating force, hard materials such as PZT-5A or PZT-8[3] are usually desired, despite their small deformations. In contrast, to achieve large actuating strain, soft materials such as PZT-5H[4] or single crystal material PZN-PT, in spite of their small forces, are usually selected.

1.2.2 Sensor

Typical sensors made of piezoelectric materials include load cells, accelerometers, and microphones. Figures 1-10 and 1-11 are the schematics to show how they work. The load cells utilize the fact that the induced charge is proportional to the applied force. The same concept was used for accelerometers since the force applied on the piezoelectric materials is proportional to the product of mass and acceleration, according to Newton's law.

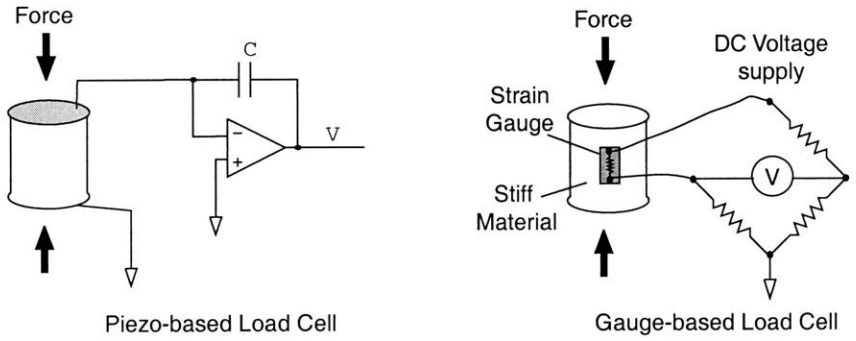

Figure 1-10: Piezo-based load cell vs. strain-based load cell

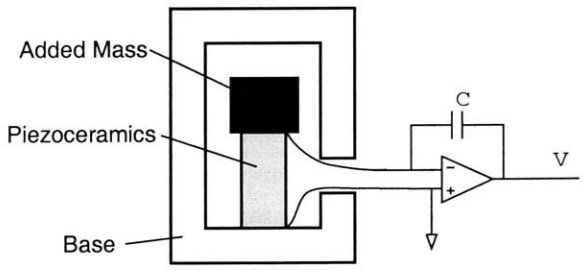

Figure 1-11: Schematics of accelerameter

[3]Trademark of Morgan Matroc
[4]Trademark of Morgan Matroc

Using piezoelectric materials as sensors can benefit from their broad bandwidth and high frequency response. Compared to strain-based load cells which rely on resistive strain gages to obtain force, piezo-based load cells can measure response that ranges from several Hz to kHz or MHz, while strain-based load cells can only measure response from DC to several 100Hz. One of the drawbacks of piezo-based sensor, however, is its poor performance at very low frequency, say 1/10 Hz. This is due to the capacitive impedance of the piezoelectric material.

In addition to bandwidth, a good sensor also needs precise calibration and is prefered to operate linearly. For application with large range response, in order to operate linearly, the stiffness is usually increased by reducing thickness and expanding cross section. However, some applications in micro-electromechanical systems (MEMS) may not allow this design approach. In this case, a precisely calibrated and accurate nonlinear piezoelectric material model is essential to make a sensor function properly.

1.2.3 High Voltage Source and Energy Harvester

By analogy to load cell operation, if the charge generated by squeezing piezoelectric materials can be collected and stored, this harvested electric energy can be used to do work. Practical levels of compression, say up to 20 MPa, will generate open circuit fields in the range of 5-15 kV/cm. Devices using this feature can provide the spark for gasoline motor ignition[47].

Other applications, such as the micro hydraulic energy harvester, are under development by a group of MIT researchers[52]. The electric power transformed from mechanical energy can be harvested through circuitry. For instance, as demonstrated in Figure 2-33, the current can be rectified by diode bridges to recharge a battery. The greater and faster the compressive action is, the more energy per second (i.e. power) is collected in the battery. The reason to make the device in micro scale is to increase the natural frequency so that the piezoceramics can be driven much faster.

One of the major obstacles in developing this micro hydraulic energy harvesting technique is the compressive depolarization of the piezoelectric material. As can be imagined, the high compression can depolarize the poled piezoceramics and therefore degenerate the expected performance. Due to the nonlinearity of piezoelectric material, it is also diffi-

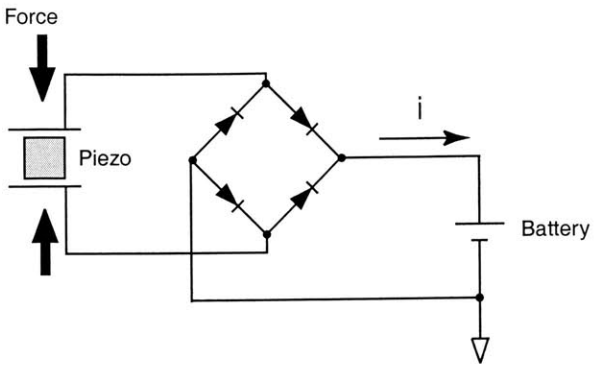

Figure 1-12: Diode bridge circuitry

cult to predict the behavior of this compressive depolarization without accurate material characterization or a material model.

1.3 Thesis Motivation and Objectives

Motivation

As mentioned earlier, nonlinearity and hysteresis make it difficult to analyze and design a piezoelectric device for smart structure application, such as actuating and sensing components as well as energy harvesters. As a result, this thesis is initially motivated to characterize the hysteretic behavior and to develop an analytical model and the tools to predict this behavior.

In addition to hysteresis, compressive depolarization is also a major concern in terms of performance. Most actuators, sensors, and even energy harvesters operate at high compression. This compression, which usually is parallel to the poling direction, will depolarize the material and degenerate the performance. One of the goals is to characterize this phenomenon and embed it in the material model.

The preliminary experiments, as illustrated schematically in Figure 1-13, showed that the response is dependent upon not only the applied fields (electric and mechanical) but also the driving frequency. It is also the objective to observe this behavior and include it into the material model.

It is also of interest to investigate the difference between hard and soft materials such

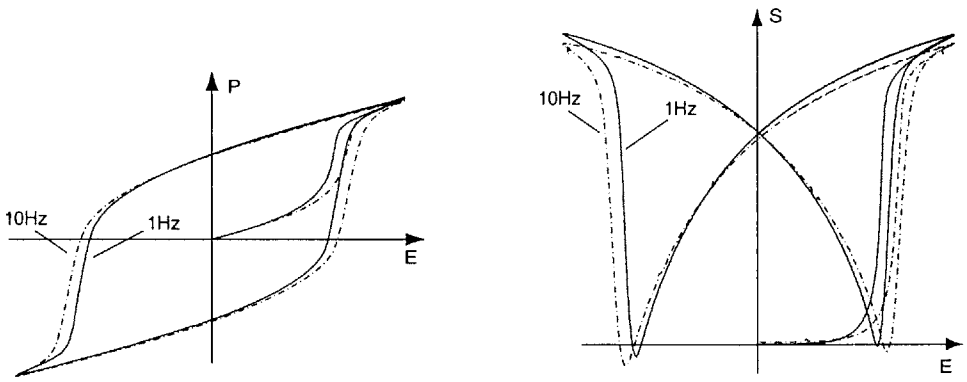

Figure 1-13: Preliminary data implies rate dependent piezoelectricity

as PZT-5A/5H versus single crystal PZN-PT and PMN-PT. For most actuation applications, PZT-5A is the most common selection because of its moderate piezoelectric constant, stiffness, and cost. For power generation, PZT-5H, PZN-PT, and PMN-PT are the best candidates. These materials have different characteristics subjected to applied compression. It is also the goal to establish a library of these material properties.

One of the obstacles to make AFCs function properly is to predict the actual electric field along the fibers. This prediction can help determine the poling voltage and design the gap between the electrodes. However, to do so, a three dimensional analysis tool such as the finite element method is desired because of the complicated boundary conditions of AFCs,.

Objectives

Motivated by the discussion above, this thesis is aimed at characterizing the material under different loading conditions. As shown in Figure 1-14, the test matrix consists of three axes of dependencies: electric field, compression, and driving frequency. The phenomena of interest include

1. nonlinearity and hysteresis
2. electric field dependency
3. compressive stress dependency
4. rate dependency

5. difference between hard and soft material

6. three dimensional material properties for finite element analysis

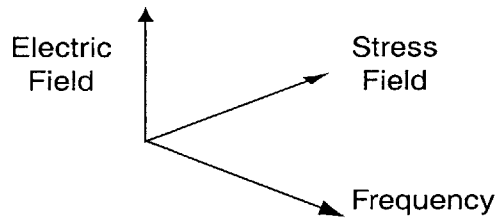

Figure 1-14: Three major axes of dependencies: electric field, compression, and driving frequency

It is also the goal to build a reliable model to simulate these behaviors. The approach is to establish a physical framework within which empirical descriptions of the behavior of some of the variables are embedded. The development of the model has three stages, as listed in Table 1.1. The description of these stages follows the guideline set forth by Ashby[70]. Each stage has its targeted task and corresponding precision. To improve the accuracy of the model, it is necessary to proceed to the next developing stage to increase the complexity of the model.

Table 1.1: Task and targeted precision of the model

Stage	Precision	Task	Required Mechanisms
1st	Factor 10	To gain understanding and insight	1-D, electric rate, static stress
2nd	Factor 2	FEM, stress analysis	3-D tensor invariants
3rd	Factor 1.1	data condensation, design guide	(stress-rate, S-D hysteresis)

The first stage is to understand the electric rate and static stress dependent effects. For such purpose, accuracy of factor 10 is the precision target. At this stage, an evolution law of internal state variables D^* was proposed; only electric rate dependence was included; a parametric study was performed; only 1-D model was considered.

The second stage is to make the model more useful and to capture these major effects into equations and code for the use of the finite element method. To do this, 3-D tensor invariants were included in addition to Level 1. The finite element analysis is often used to predict the stress of active devices. For such purpose, the factor of 2 accuracy is targeted at this stage.

The third stage is to condense the data into material constants so that a material library or a design guide for material selection can be built. For this purpose, a 1.1 precision factor is desired in order to differentiate the characteristics of various materials and compositions. If this can be done, one can perform the butterfly curve test and find the parameters of the model for each material. The piezoelectric constants for power generation and actuation applications can then be extracted from this model. No additional tests are required to obtain these constants.

The model should also be based on consistent thermodynamic potentials so that the model can be implemented into fully three dimensional finite element analysis. Without the consistent thermodynamic potentials, the electric energy and mechanical energy may not be interchangeable. Namely, it will fail to couple the electromechanical degrees of freedom in the finite element formulation. In addition to developing a material model, a finite element analysis tool is to be built in this thesis in order to simulate the response of devices with irregular loading conditions.

1.4 Thesis Outline

Chapter 2 will first document the approach and the result of material characterization. Two types of material characterization, minor and major loops, were conducted. The minor loop test with moderate amplitudes of field applied is primarily for specific applications, such as actuation and power generation. In contrast, the major loop test with large amplitudes of field applied (butterfly curves) is intended to find the general material parameters for model development.

Although a number of material models have been proposed since decades ago, none of them are capable of fulfilling the needs of the desired model. Fortunately, some of them provide good insights and physical explanation of the material behaviors. Chapter 3 will start with the review of these existing models, followed by the development of a rate dependent material model. To simplify the derivation and to emphasize the essence of the material model, a 1-D model will be first introduced. A parametric study will be performed to show the effects of material parameters. After understanding the 1-D material model, a 3-D model using tensor invariants will then be developed. In this chapter, the parameters

of both the 1-D and 3-D material models for PZT-5A and PZT-5H will be also optimized by minimizing the error between the model and the data acquired in Chapter 2. Chapter 4 will validate the material models with the minor loop data for energy harvesting and actuation applications.

To analyze piezoelectric devices with complicated geometry or non-uniform loading, a differential algebraic formulation of mixed finite element analysis will be developed in Chapter 5. Solution techniques to this differential algebraic equation system will be discussed in detail. Several cases will be studied to demonstrate this finite element approach. In Chapter 6, the test results will be summarized, and the developed model will be evaluated. Future work will be recommended, and the contributions of this thesis will be detailed.

Chapter 2

Material Characterization

Before building the material model, it is important to first observe the detailed material behaviors under different driving conditions. Three categories of experiments were conducted to investigate the material behaviors regarding actuation application, energy harvesting application, and material model development. In addition to electric field dependency, stress dependency and rate dependency are also of interest in these tests.

There are numerous types of piezoelectric materials. It is impossible to test all of them. However, the testing task can be minimized by selecting important materials for special applications. Table 2.1 shows the linear material constants of common materials. This table will help to decide the material selection. For actuation application, PZT-5A was examined in this work because it has moderate piezoelectric constants and stiffness. It is therefore suitable for actuation application. In addition, it was selected as fibers in AFCs[27]. To understand and correlate the behavior of AFCs, it is essential to test the PZT-5A bulk material. For energy harvesting application, PZT-5H was tested because of its availability and low cost. It is also because PZT-5H has higher d_{33} than PZT-5A. PZN-PT and PMN-

Table 2.1: Selection of piezoelectric materials for testing

	d_{33} (pC/N)	s_{33}^E (pm^2/N)	$k_{33} = (d_{33}g_{33}/s_{33}^E)^{1/2}$
PZT-5H [53]	593	20.7	0.752
PZT-5A[53]	374	18.8	0.705
PZN-PT[54]	2000	111	0.93
PMN-PT[55]	2000	133	0.92

PT single crystal materials were also tested because of their extremely high d_{33} constants. For model development, the goal is to establish a material library for engineers. PZT-5A and PZT-5H were targeted because they are the most commonly used piezoelectric material. Due to the limited availability of PZN-PT and PMN-PT single crystal materials, they were not intensively tested for model development.

In this chapter, the electrical and mechanical experiment setups will be first introduced. It will be followed by the approach and results of three types of material characterizations.

2.1 Experimental Setup

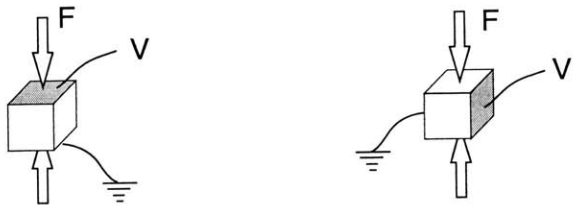

Figure 2-1: Axial test configurations: (a) longitudinal test and (b) transverse test.

Two types of tests under load can be performed: longitudinal and transverse tests, as illustrated in Figure 2-1. In the longitudinal test, the mechanical load is parallel to the electric field, while in the transverse test, the mechanical load is perpendicular to the electric field. This section will discuss how the specimen is prepared and how the electromechanical loadings are applied.

2.1.1 Mechanical Loading and Measurement

Specimen Preparation

To investigate the stress dependency, it is desired to measure the response only under uniform fields. In order to guarantee a uniform stress field on the specimen, the aspect ratios of the specimen should be increased. Ghandi[35] determined that at least a 3-to-1 ratio is required to eliminate the clamping effect and to provide the uniform field in the center of the specimen.

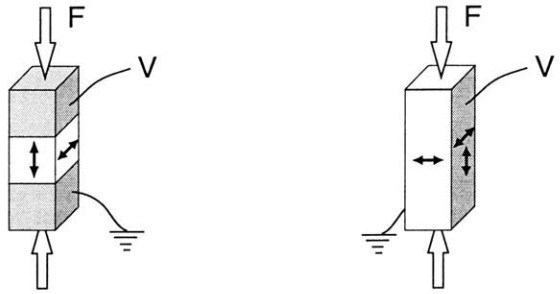

Figure 2-2: Axial test configurations: (a) longitudinal test and (b) transverse test.

In order to increase the aspect ratio of the longitudinal test specimen, the specimen shown in Figure 2-2(a) was sandwiched by two end pieces of the same unpoled material. These end pieces were coated with nickel electrodes on six faces by the vendor. By fully plating the end pieces, the electric fields in the end pieces and the net charges on their surfaces were constrained to zero, and the voltages were applied via two end pieces using alligator clips. The strains on the longitudinal specimen along its longitudinal and transverse directions were measured by attaching opposing strain gage pairs[1] to the four side faces of the specimen. The solid arrows shown in Figure 2-2(a) indicate the measured strain directions. These gage pairs were also used to ensure no bending moment on the specimen.

The aspect ratio of specimens in the transverse test was also increased to 3 to 1. However, instead of three stacks, one slender piece as shown in Figure 2-2(b) was used because of the way electric field was applied. The strain gauges were attached in pairs such that the bending moment could be monitored.

After the gauges were attached, the specimen was finally coated with polyurethane and submerged in silicone oil to avoid dielectric breakdown during the test. To avoid electrical damage to the computer system, a customized isolated strain gauge conditioning electronic device[35] was used to isolate the high voltage drive level from the strain gauge signal level.

The specimen size was determined by several factors: (1) the saturation field E_s of the material, (2) the maximum load capability of the testing machine, (3) the strain gauge size, (4) the electric power amplifier, and (5) the maximum isolation voltage of the strain gauge conditioner. Different tests use different sizes of specimens. The specific sizes of specimens

[1]EA-06-031EC-350 and EA-06-031DE-350 from Measurements Group Inc.

will be described in detail later when the different test sets are discussed.

Bending Reliever

As shown in Figure 2-3, a test fixture incorporating a spherical joint was customized to help align the testing specimen. This fixture not only interfaced the loading between the specimen and testing machine, but also relieved the bending moment on the specimen due to any misalignment.

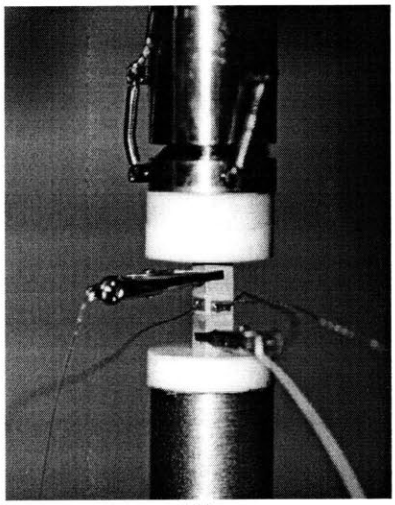

(A)

Figure 2-3: Experimental setup: Test fixture consisted of a spherical joint and alumina disks.

Low Frequency Test

Low frequency up to 100Hz and high mechanical load up to 10kN was performed using an Instron hydraulic testing machine shown in Figure 2-4. The load was monitored using either an Instron load cell (Model 2518-603) or a piezo-based Kistler load cell (Model 9342) connected in series. The Instron load cell was required for load feedback control, while the piezo-based load cell was optional for high frequency load monitoring.

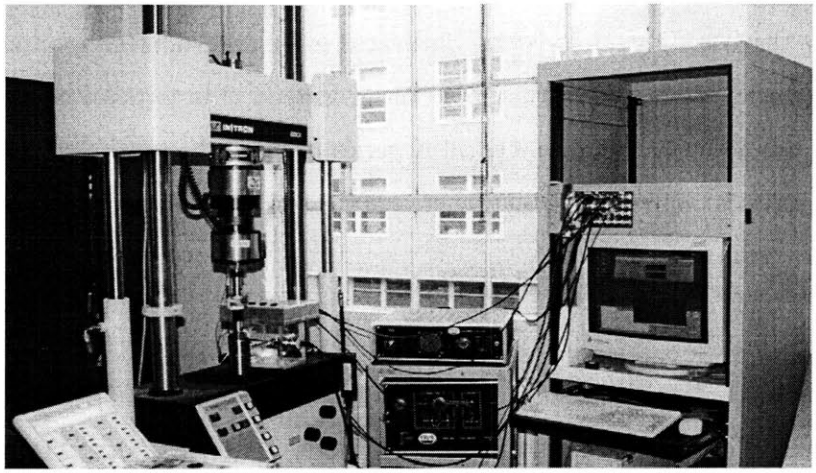

Figure 2-4: Instron Test Machine

High Frequency Test

High frequency up to 1kHz and low mechanical load up to 400N was performed on a piezo-based component tester developed at MIT[39], as shown in Figure 2-5. The tester used three actuators[2] in parallel to move against the specimen fixed on the blocking plate and therefore generated mechanical compression. In addition, a membrane was used to support the specimen in order to prevent the buckling of a slender specimen. The details of the original design can be found in Lutz's work[39].

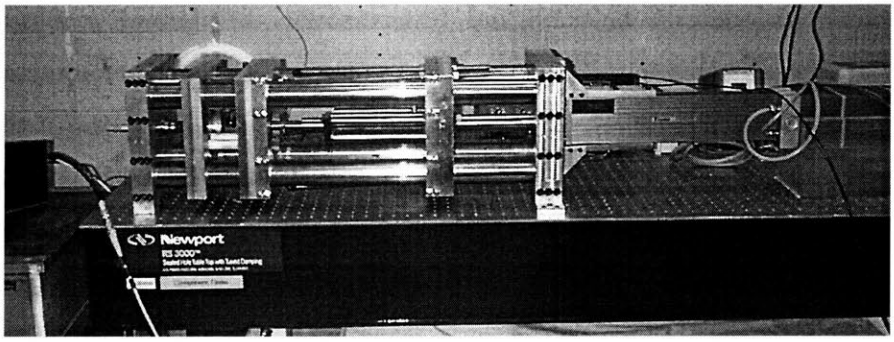

Figure 2-5: Component Testing Machine

Several modifications were made in order to maximize the load output of this tester.

[2]Kinetic Ceramics, Inc.

The original design using three actuators in parallel works well if the specimen has higher stiffness than the actuators. However, as illustrated in Figure 2-6, if the specimen is less stiff than the actuator, placing the actuators in series instead of in parallel may be beneficial. As a result, two actuators were connected in series to drive the specimen. The number of actuators in series is limited by the space between the two blocking plates. It is also essential

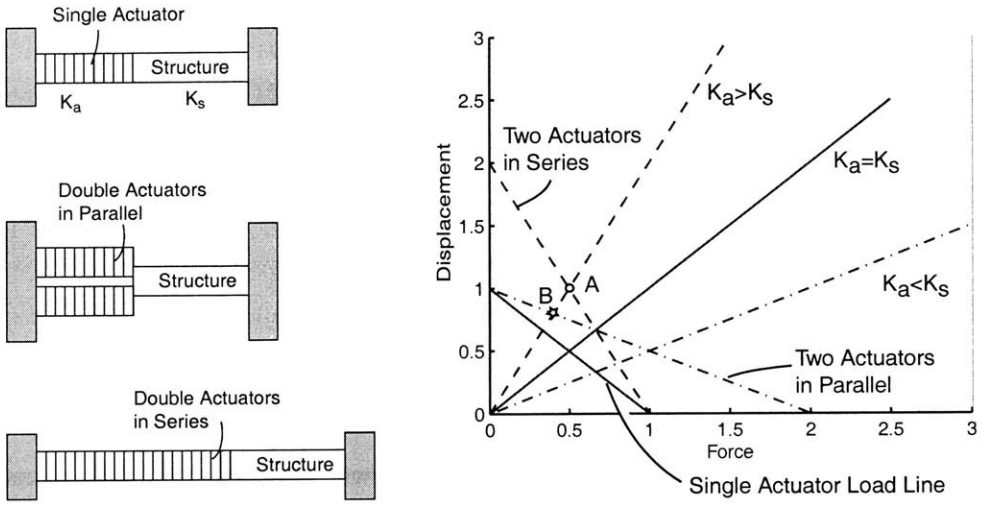

Figure 2-6: Component Testing Machine

to find the weakest link of the structure in series. This structure includes all components such as the load cell and connectors but not the actuators. If one of the components is very soft, the whole structure will be compliant. Unfortunately, the piezoelectric load cell used by the original design was found very compliant compared to the other components. To solve this problem, a piezo-based load washer by Kistler (Model 9212) was used together with a strain gauge-based load cell by Entran (Model ELH-TC790-3000) to monitor the load. The piezo-based load washer can provide high frequency load reading, while the strain gauge-based load cell is primarily used to measured DC load offset.

Another major contributor resulting in incorrect force measurement is the supporting membrane because it carries load against the actuators. To remedy this problem, the membrane was replaced by a linear bearing. The final problem of this tester is that its performance is limited by the budget and the current limit of the power amplifier that drives the piezoelectric actuators. The current limit of the amplifier is 3A, the maximum

voltage is 800V, and the actuator capacitor is 1.5μC. From the relation

$$|\frac{V}{I}| = |\frac{1}{2\pi fC}| \tag{2.1}$$

the maximum frequency of the tester at maximum voltage is about 400Hz.

In summary, the exact maximum load generated by this component tester depends on the stiffness of the specimen and the interlinked devices such as the load cells. The stiffer the specimen or the interlinked structure is, the more blocking force can be generated by the driving piezoelectric actuators. The maximum driving frequency is restricted by the current limit of the power amplifier that is used to drive piezoelectric stacks.

2.1.2 Electrical Loading and Measurement

Electrical Driving Instruments

Electric field was generated using a 20kV power amplifier, Model 20/20B by Trek Inc. A 10kV and a 4kV power amplifiers were also available. These amplifiers were used for different purposes. The 20kV and 10kV amplifiers were primarily used for poling process and large electric field characterization. For thicker specimen, 20kV could provide more electric field, however, less current. 4kV was preferred to drive minor loop with smaller electric field because its current monitor had higher signal to noise ratio.

Measurement of Electrical Properties at Open Circuit

In order to characterize the electrical properties of the piezoelectric at constant electric displacement, i.e. open circuit, a high potential voltmeter with high impedance was developed. An equivalent circuit of a piezoelectric material shown in Figure 2-7 can be helpful in designing a high potential voltmeter.

The high potential voltmeter shown in Figure 2-8 consists of a feedback resistor R_f, a high impedance resistor R, and an inverting operational amplifier. Using this configuration, one can measure the open circuit voltage with frequency higher than

$$f_{low} = \frac{1}{2\pi RC}$$

where C is the capacitance of the piezoelectric test specimen, and the gain of measurement

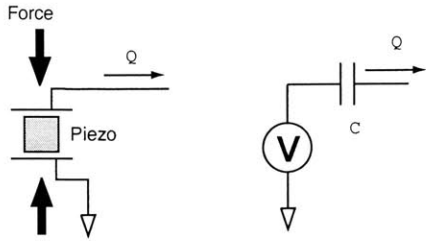

Figure 2-7: Simple equivalent circuit of piezoelectric material

is

$$\frac{V_{piezo.}}{V_{out}} = -\frac{R}{R_f}$$

By measuring the open circuit voltage while subject to compression, one can calculate the g_{33} constant.

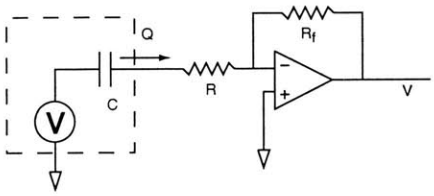

Figure 2-8: High potential voltmeter

The frequency dependence characterized in this thesis work ranges from 1Hz to 1kHz. The capacitance of the specimen ranges from 100pF to 200pF. As a result, the resistor R must be at least 10GΩ in order to satisfy the lower bound of frequency range. Unfortunately, the impedance of the resistor is not just ideally pure resistance but also contains capacitance and inductance. The virtual capacitance and inductance of the high impedance resistor, as illustrated in Figure 2-9, result in frequency dependency of the voltage meter. In order to avoid unstable dynamics at high frequency, a capacitor C_f was added in parallel with the feedback resistor R_f. With $R = 10G\Omega$, $R_f = 10M\Omega$, $L = 3.6MH$, $C_f = 15pF$, and $C = 0.07pF$, the simulated transfer function of V to V_p

$$\frac{V_{out}}{V_p} = -\frac{R_f}{R}\frac{LCs^2 + sRC + 1}{(1 + sR_fC_f)(R + sL)} \tag{2.2}$$

is compared to the measured one, as shown in Figure 2-15. The pole-zero mapping of

this dynamic system is also shown in Figure 2-10. To make a precise open circuit voltage meter, an additional filter circuit must be designed to compensate this dynamic effect. An active filter [40] using three operation amplifiers shown in Figure 2-11 has been successfully implemented to ensure ±1% error within 125 Hz, as demonstrated in Figure 2-16. For frequencies higher than 125Hz, it is necessary to develop a new technique. One possible compensation can be made by using high voltage power amplifier feedback to compensate the dynamics of the resistors, as shown in Figure 2-12. However, it is easier to use another resistor with a smaller value for high frequency, since a resistor with a smaller value has less capacitive and inductive effects. Instead of the 10GΩ resistor, a 100MΩ resistor for R was used to obtain a voltage meter with bandwidth from 100Hz to 4kHz and gain error within ±2%.

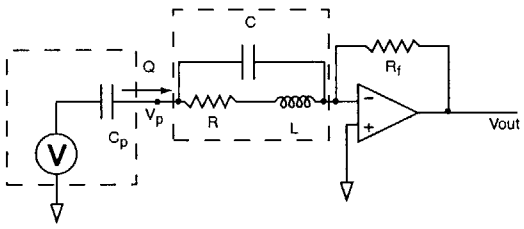

Figure 2-9: High potential voltmeter, considering dynamics of the resistor

In summary, two open circuit voltage meters were developed for this thesis work. One is for test frequencies less than 100Hz, and the other is for frequencies higher than 100Hz up to 4kHz. Figures 2-13 and 2-17 summarize their final configurations and transfer functions. These two meters were calibrated using the Trek amplifier at different voltage levels ranging from ±200V to ±2000V. The transfer functions demonstrate that these voltage meters operate linearly in the specified bandwidth.

A final note on using the open circuit voltmeters is that a precaution must be taken to minimize the cable capacitance. This is due to the limited charge source of the piezoelectric material. If the piezoelectric output port somehow forms a capacitive path to the ground, as illustrated in Figure 2-14, part of the limited charge source will be drained to the ground. This leakage charge will result in measurement error of the open circuit voltage. As a result, the length of wire between the piezoelectric output and volt meter input must be designed

as short as possible to minimize the error due to wire capacitance.

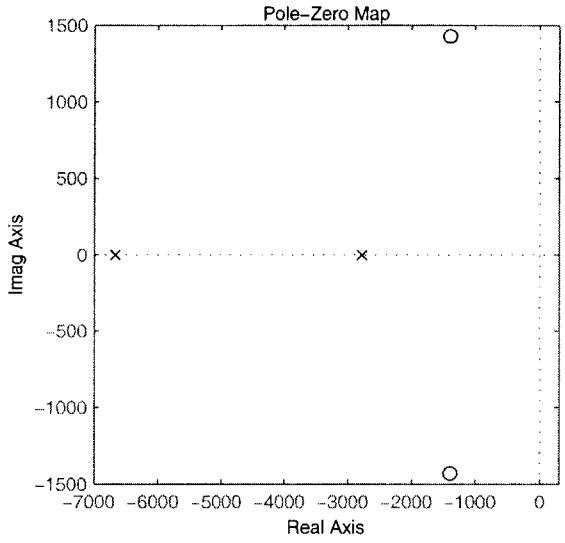

Figure 2-10: Pole-zero mapping of high potential voltmeter, considering dynamics of the resistor

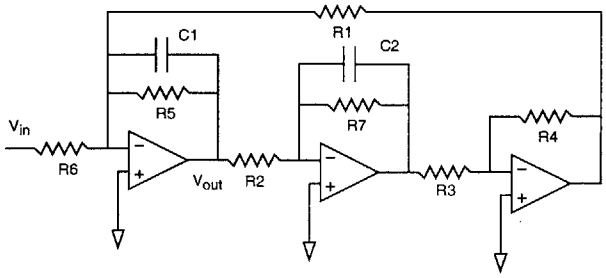

Figure 2-11: Schematics of active filter

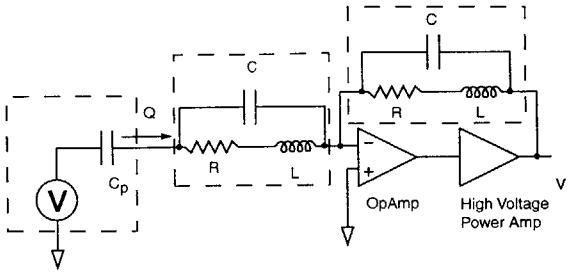

Figure 2-12: High potential voltmeter using high voltage power amplifier feedback to compensate the dynamics of the resistor

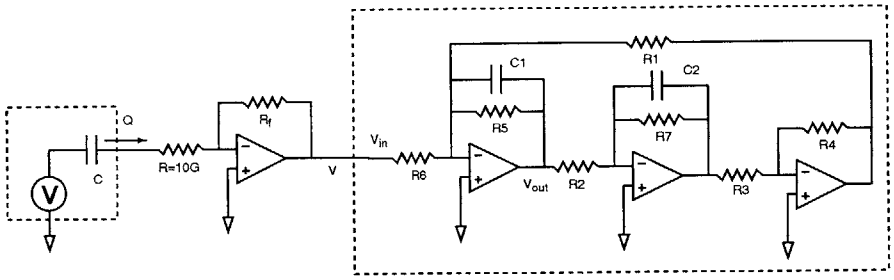

(a)

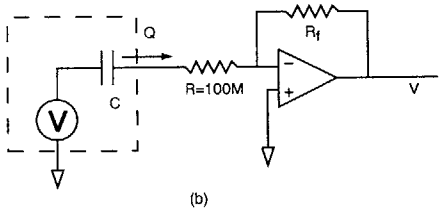

(b)

Figure 2-13: The final configuration of open circuit voltage meter used in this thesis work: (a) 10GΩ with filtered output, (b) 100MΩ

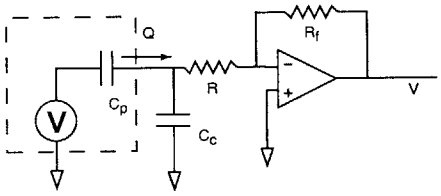

Figure 2-14: High potential voltmeter, considering capacitance of cable

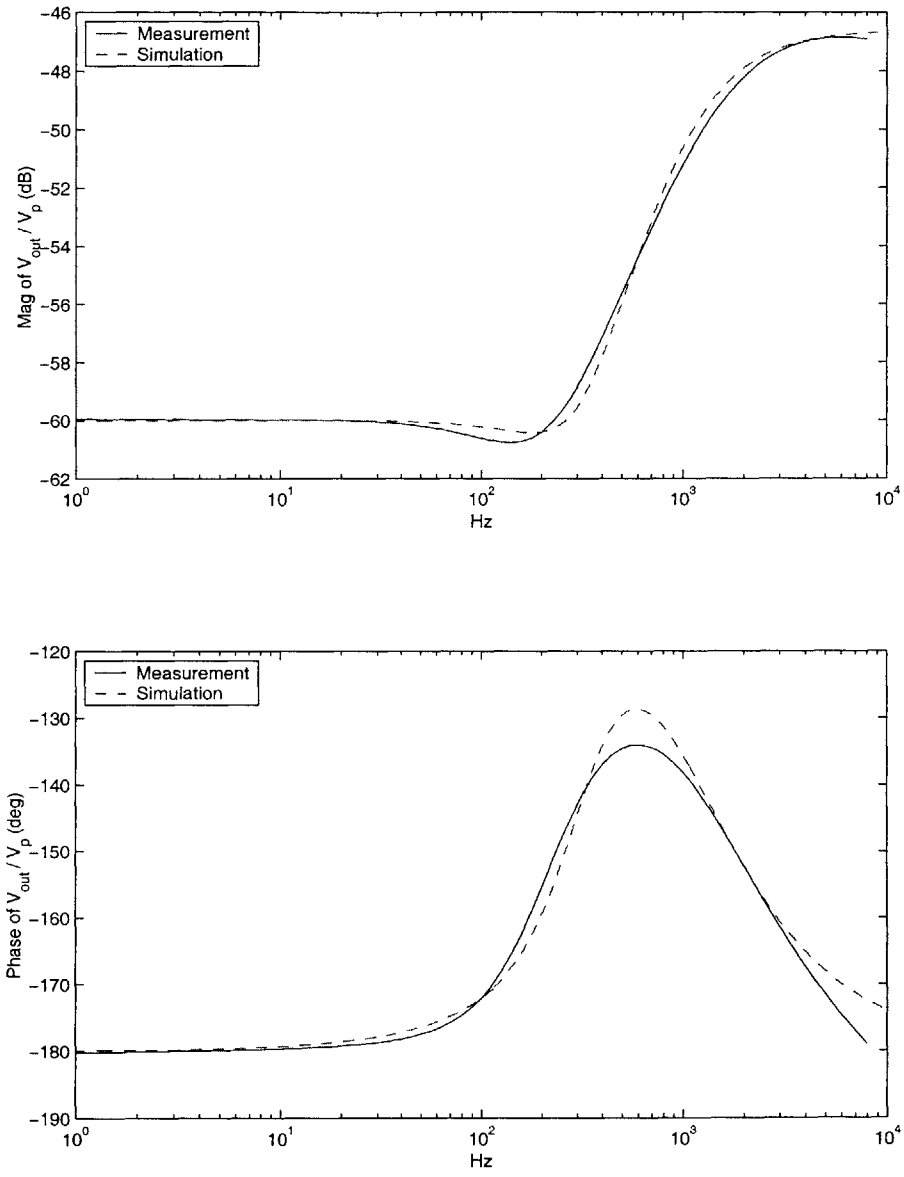

Figure 2-15: Transfer function of high potential voltmeter, considering dynamics of the resistor

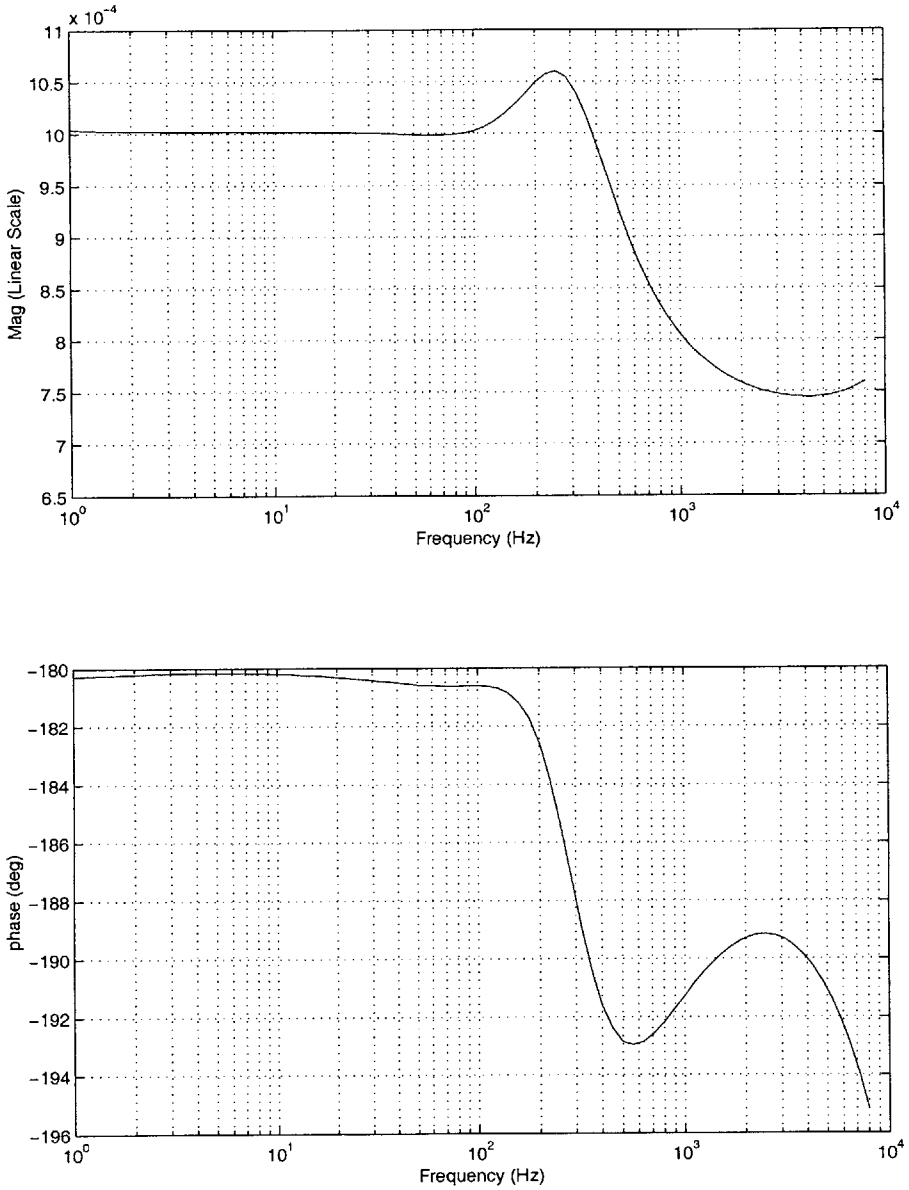

Figure 2-16: Transfer function of compensated high potential voltmeter using active filter

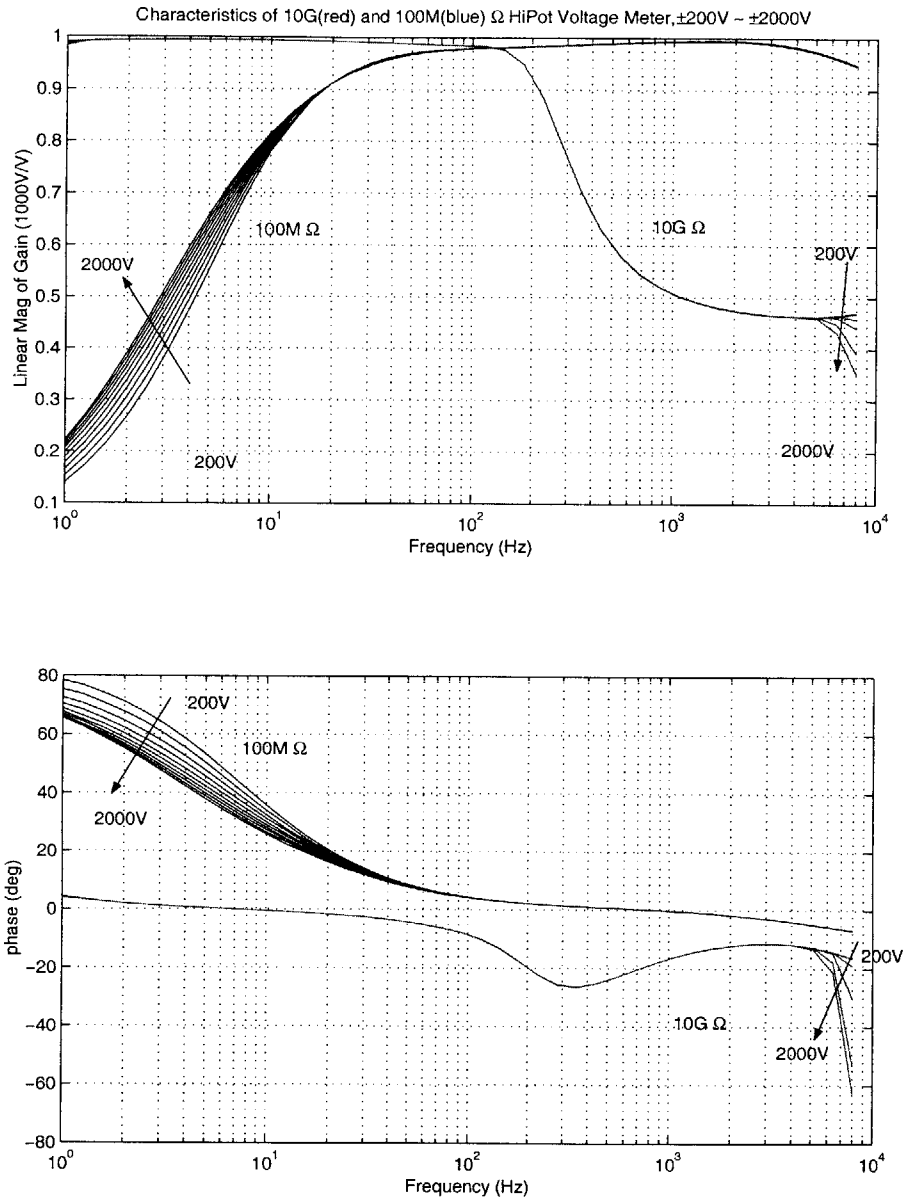

Figure 2-17: Transfer function of high potential voltmeter: one with 10GΩ resistor operates from 1 to 100Hz, one with 100MΩ resister operates from 100Hz to 4kHz.

Measurement of Electrical Properties at Short Circuit

In order to measure short circuit properties, one must use a charge/current amplifier which consists of an inverting operational amplifier and a feedback capacitor or resistor as shown in Figures 2-18 and 2-19. With the feedback capacitor or resistor, the operational amplifier amplifies charge or current, respectively. The gain for the charge amplifier [42] is

$$Q(j\omega) = -\frac{V(j\omega)}{j\omega C}$$

and for the current amplifier [43] is

$$I(j\omega) = -\frac{V(j\omega)}{R}.$$

Operational amplifier OPA111[3] was selected because of its high impedance.

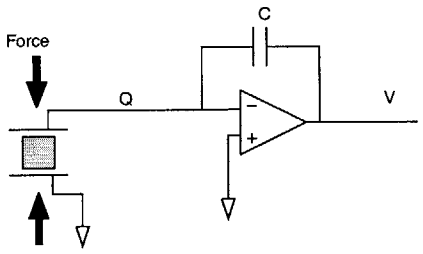

Figure 2-18: Charge amplifier.

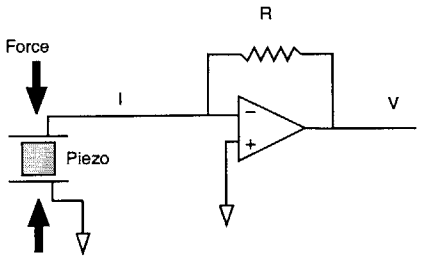

Figure 2-19: Current amplifier.

[3]Burr-Brown Corporation, Tucson, AZ 85706

2.2 Characterization for Actuation Application

This work is motivated by the depolarization of PZT-5A piezoelectric fibers in AFCs, because the fibers may be exposed to high stress field after manufacturing. For example, during the curing process, the difference between the coefficients of thermal expansion of the epoxy matrix and the piezoelectric fibers may result in compression of the fibers. In addition, during the fiber poling process, the fibers may extend against the epoxy that surrounds them. In such situation, the fibers may experience additional compression. Exposure to these high electromechanical loads parallel to the material poling direction may result in the depolarization of the material, depending on the material composition and on environmental variables such as temperature, electric field, and stress. In addition, the stress duration effect may influence the depolarization.

Early studies on the effects of static stress on piezoelectric materials have been conducted by Krueger [28] and Zhang [29]. These studies only investigated the low electric field material properties affected by static compressive stresses while many applications operate the material at relatively high electric fields. There may be a possibility that high electric excitation can resist depolarization to some extent. Hence, this section will examine the compressive depolarization of commercial lead zirconate titanate PZT-5A piezoelectric ceramics by evaluating the electric actuation strain at different electric fields, compressive stresses, and compression durations. Varying the combinations of these parameters allows further understanding of the coupling effects among them.

In this section, the detailed data and test procedure of PZT-5A will be presented. The difference between single and multiple loop loading cycles used to investigate the actuation under load will be exhibited. The effect of the compression duration on the residual actuation will be reported.

2.2.1 Actuation under Load

Single Loading Cycle

The objectives of this test were to identify the limit of compression without permanently depolarizing the material and to investigate the possibility that high electric field could avert compressive depolarization of the material. In this test, the compressive load was

monotonically increased up to 150 MPa in 10 MPa increments and then released to 0 MPa also in 10 MPa decrements, as shown in Figure 2-20. The actuation strain was measured five minutes after each change in load. In order to compare the effects of low and high electric fields, the test procedure used by Zhang [29] was modified, and the specimen was excited by 1Hz sinusoidal waves with amplitudes of 9%, 16%, 40%, 70%, 90% and 110% of the coercive field (E_c), which is 1.12 kV/mm for PZT-5A. To evaluate the actuation at high electric field, a generalized piezoelectric constant d^*_{33} was defined as the ratio of peak-to-peak actuation strain to peak-to-peak electric field [44]. To measure the constant d^*_{33} in the low field region and to increase the signal-to-noise ratio of actuation strain measurement, the sinusoidal wave with 9% E_c amplitude was used to represent the low field behavior. 9% E_c was validated to be low enough to represent the low field properties by comparing the measured data with published low field data [29]. The difference between the two sets of data was within $\pm 5\%$ error. A freshly poled specimen that had not been exposed to any compression was tested for each selected electric field. What follows is the detailed test procedure:

1. Measure and record the actuation strain resulting from the selected electric field at zero stress.

2. Compress the sample by 10MPa increments and hold for 5 minutes. The sample electrodes were short-circuited during compression so that the charge generated by the compression could be discharged and balanced. By doing so, it is believed that the material will be more easily depolarized.

3. Measure and record the actuation strain resulting from the selected electric field. The compressive load remained on the sample during the electric actuation.

4. Repeat Steps 2 and 3 until the compressive load is 150MPa.

5. Reduce the compressive load by 10MPa and hold for 5 minutes. Short-circuit the electrodes of the specimen during compression.

6. Measure and record the actuation strain resulting from the selected electric field. The compressive load remained on the sample during the electric actuation.

7. Repeat Steps 5 and 6 until the compressive load was 0MPa.

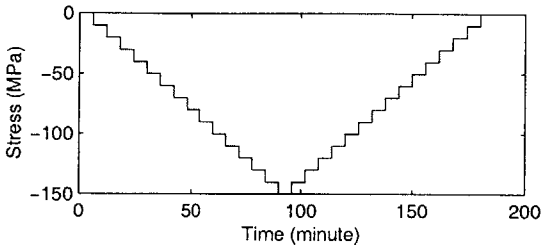

Figure 2-20: The compression profile of the single loading cycle test.

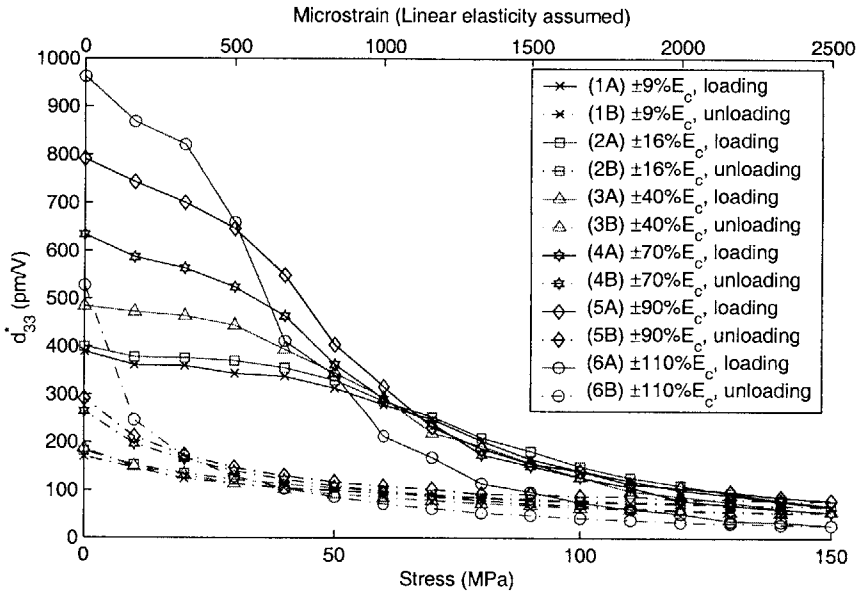

Figure 2-21: Test results of single loading cycle subjected to different electric fields.

Figure 2-21 shows the actuation under load while subject to different electric fields. The low field result at 9% E_c was similar to the one reported by Zhang [29]. Before any compressive load was applied, higher electric field yielded higher actuation. However, higher electric field did not prevent the reduction of actuation when the compressive load was increased. Furthermore, electric fields higher than the coercive field tended to decrease the

actuation more quickly because the negative component of the electric field expedited the depolarization of the material. It was also found that most of the electric actuation did not recover even when the compressive load was totally released except for the slight recovery of the sample using $110\%E_c$. This was because the electric field was higher than the coercive field and would have repolarized the piezoelectric material. In summary, this test result showed that even high electric AC fields had little success in preventing depolarization due to high compressive stresses, although positive DC bias might help achieve this goal.

Multiple Loading Cycles

In the single loading cycle test, the material properties during the unloading cycle were governed by the maximum exposure stress, which was 150MPa. It is also of interest to investigate the unloading material properties determined by different levels of maximum exposure stress less than 150MPa. For this purpose, a new test using multiple loading cycles was designed. In the new test, the total range of 150MPa compression was partitioned into five equal subranges, namely, 30, 60, 90, 120 and 150MPa. Starting from the lowest loading range followed by the higher ones, five loading cycles corresponding to these five subranges were conducted in the test. At each loading cycle, the compression on the specimen was loaded up to the peak of the corresponding loading range in 10MPa increments and then unloaded to zero stress also in 10MPa decrements, as shown in Figure 2-22. Sinusoidal waves with amplitudes of 16%, 40%, 70% and 90% E_c at 1Hz were driven to actuate the specimen 5 minutes after the load was changed. A freshly poled specimen was tested for each selected electric field. The detailed test procedures is:

1. Measure and record the actuation strain resulting from the selected electric field at zero stress.

2. Compress the sample by 10MPa increments and hold for 5 minutes. Short-circuit the electrodes of the specimen during compression.

3. Measure and record the actuation strain resulting from the selected electric field. The compressive load remained on the sample during the electric actuation.

4. Repeat Steps 2 and 3 until the compressive load reached the peak of the loading range corresponding to the current loading cycle.

5. Reduce the compressive load by 10MPa and hold for 5 minutes. Short-circuit the electrodes of the specimen during compression.

6. Measure and record the actuation strain resulting from the selected electric field. The compressive load remained on the sample during the electric actuation.

7. Repeat Steps 5 and 6 until the compressive load was zero.

8. Repeat Steps 2 to 7 for the next loading range which had not yet been applied.

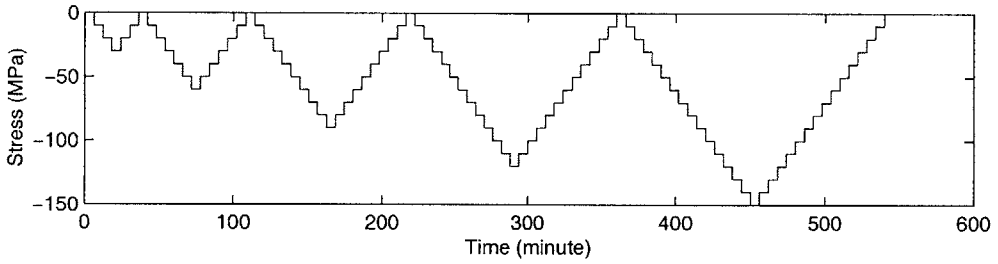

Figure 2-22: The compression profile of the test using multiple loading cycles

Figures 2-23 and 2-24 show the actuation during multiple compressive loading cycles using $\pm 16\%, \pm 40\%, \pm 70\%$ and $\pm 90\%$ E_c electric fields, respectively. In loading cycle 1, under maximum compression of 30MPa, actuation under load shows complete reversibility after reduction of compression. In loading cycle 2, under maximum compression of 60MPa, actuation under load shows slight reversibility after reduction of compression. For the loading cycles 3, 4, and 5, the irreversible behavior shows the obvious depolarization of the material. Figure 2-25 illustrates the reversibility as a function of the electric field and the maximum exposure stress. As shown in Figure 2-25(A), compared to the maximum exposure stress, the applied electric fields are found to be relatively less relevant to the reversibility, although high electric field results in high electric actuation, as shown in Figure 2-25(B). The reversibility clearly indicates the confident operating range of the compression without depolarizing the material. It is also found that the actuation during the multiple loading cycles is clearly enveloped by the actuation under the single loading cycle, as shown in each figure.

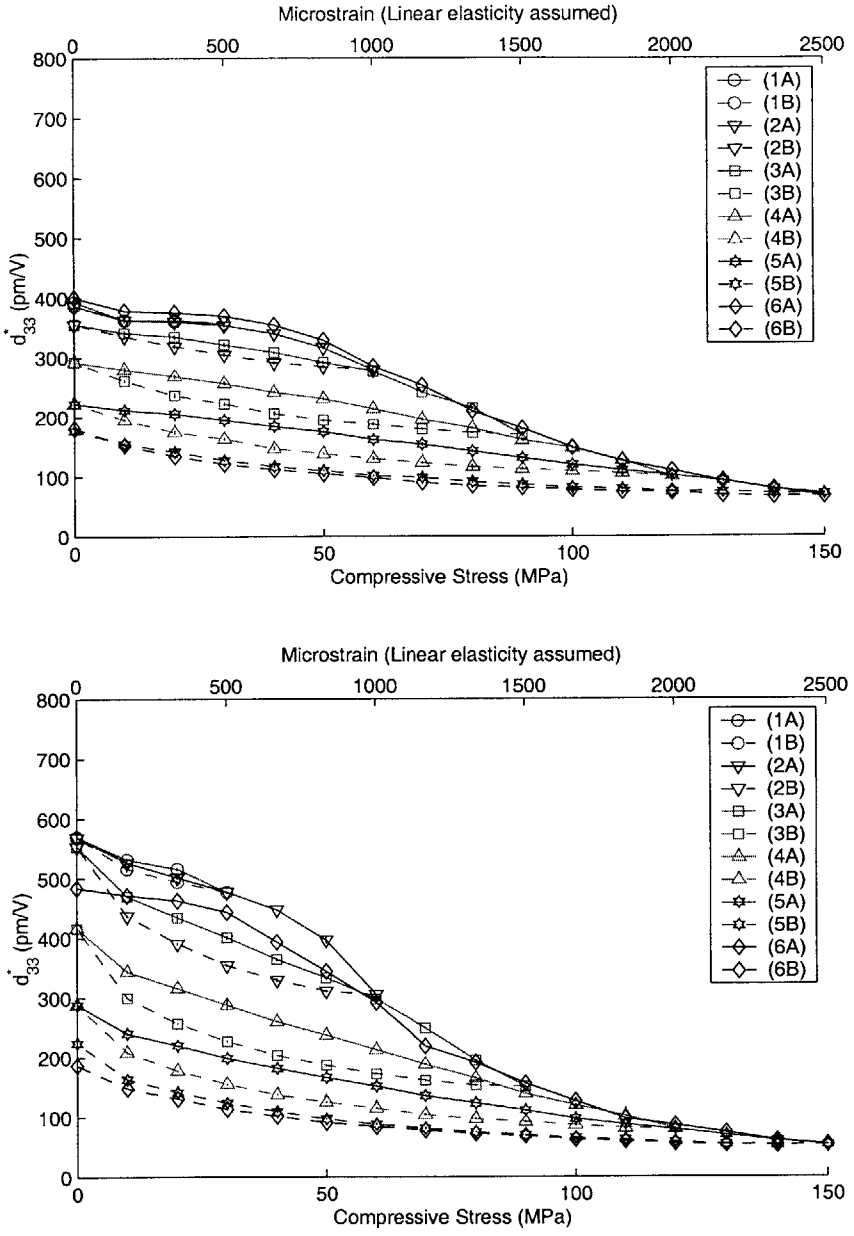

Figure 2-23: Multiple loading cycles with $\pm 16\%$ E_c (upper) and $\pm 40\%$ E_c(lower): (1A) cycle 1, loading, (1B) cycle 1, unloading, (2A) cycle 2, loading, (2B) cycle 2, unloading, (3A) cycle 3, loading, (3B) cycle 3, unloading, (4A) cycle 4, loading, (4B) cycle 4, unloading, (5A) cycle 5, loading, (5B) cycle 5, unloading, (6A) single loading cycle, and (6B) single unloading cycle.

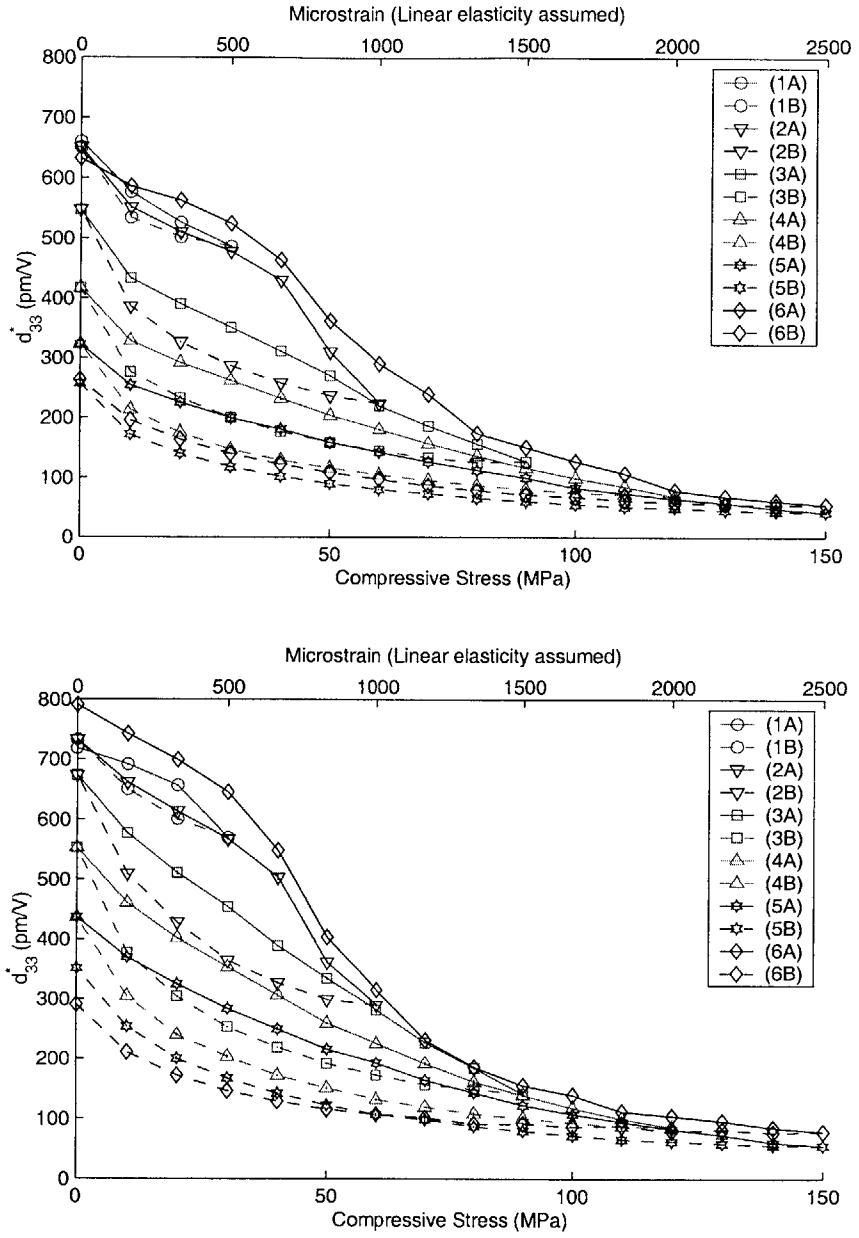

Figure 2-24: Multiple loading cycles with $\pm 70\%$ E_c (upper) and $\pm 90\%$ E_c (lower): (1A) cycle 1, loading, (1B) cycle 1, unloading, (2A) cycle 2, loading, (2B) cycle 2, unloading, (3A) cycle 3, loading, (3B) cycle 3, unloading, (4A) cycle 4, loading, (4B) cycle 4, unloading, (5A) cycle 5, loading, (5B) cycle 5, unloading, (6A) single loading cycle, and (6B) single unloading cycle.

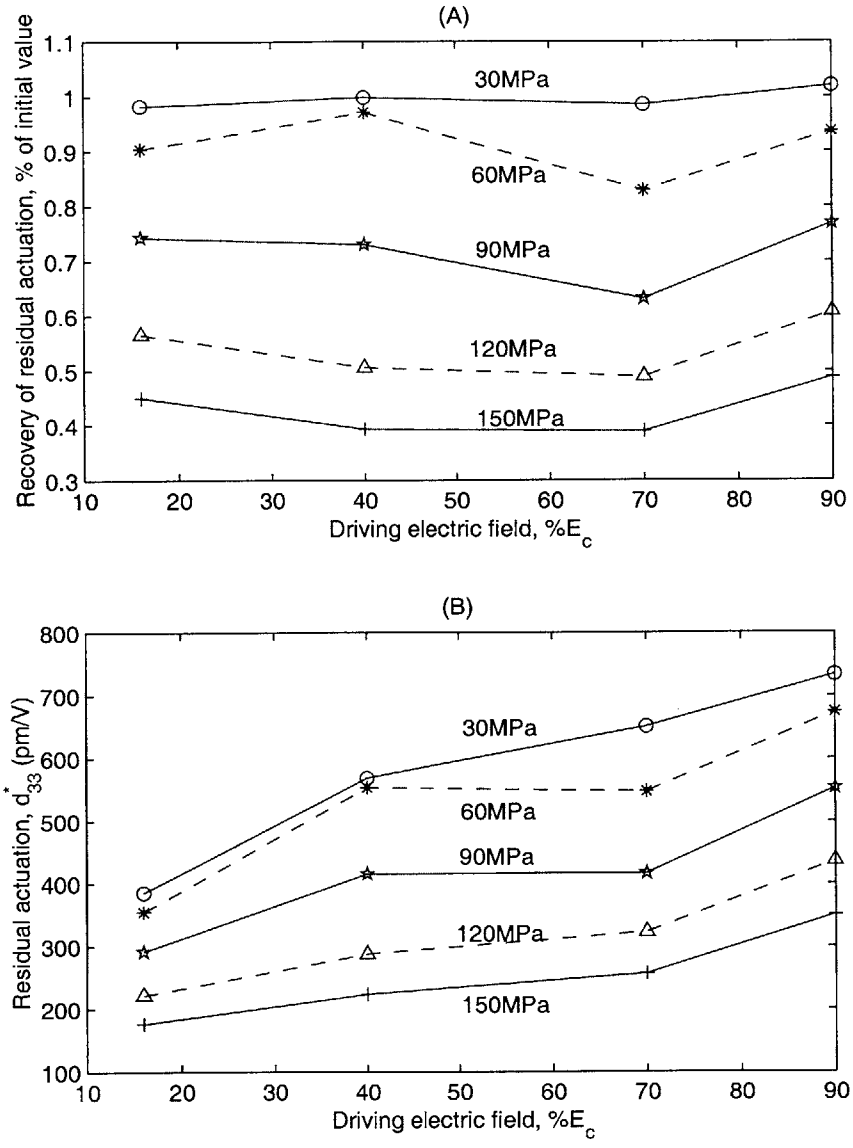

Figure 2-25: Reversibility: (A) Recovery percentage of residual actuation vs. electric field and maximum exposure stress. (B) Residual actuation vs. electric field and maximum exposure stress.

2.2.2 Residual Actuation and Compression Duration

Residual Actuation

In order to characterize the residual actuation at zero stress after a small period of exposure to the compressive load, a test similar to the one conducted on AFCs by Morris *et al.* [56] was performed. It was reported that the AFCs retained their initial actuation at zero stress even after exposure to 150MPa compression stress for 30 seconds. In order to mirror the test performed on AFCs, 30 second compression exposure time was used in this experiment, as shown in Figure 2-26. Sinusoidal waves with the amplitudes of 9%, 17%, 34%, 51% and 68% E_c at 1Hz were selected to actuate the specimen in this experiment. A freshly poled sample was tested for each selected electric field. The detailed procedure is:

1. Measure and record the actuation strain resulting from the selected electric field at zero stress.
2. Compress the sample by 10MPa and hold for 30 seconds. Short-circuit the sample electrodes during compression.
3. Release the load and wait for 30 seconds.
4. Measure and record the residual actuation strain resulting from the selected electric field at zero stress.
5. Repeat steps 2 to 4 with 10MPa load increments until the compressive load was 150MPa.

As shown in Figure 2-27, the residual actuation after exposure to the compression for 30 seconds is normalized by the initial actuation at zero stress. Using lower electric fields ($<$ 50% E_c), the residual actuation reduced as the compressive load was increased. In contrast, using higher electric fields ($>$ 50% E_c), the residual actuation slightly increased even as the compression load was increased. This result correlated with the similar phenomenon observed on AFCs by Morris *et al.* [56] It is of interest to explore this phenomenon further.

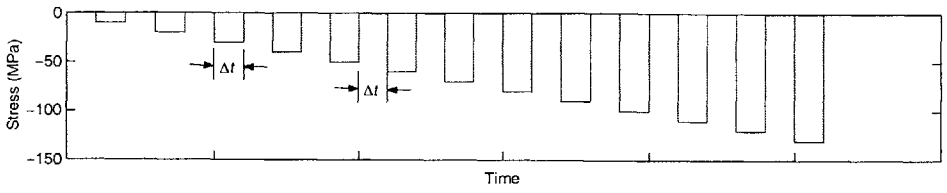

Figure 2-26: The load profile of testing the residual actuation at zero stress after exposure to compressions for a duration of Δt.

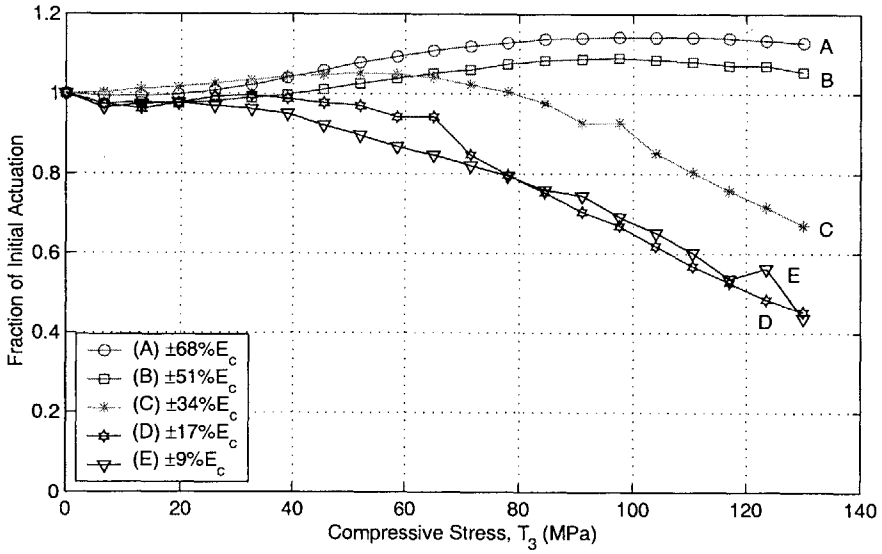

Figure 2-27: The residual actuation after exposure to compressions for 30 seconds is normalized by the initial actuation at zero stress.

Compression Duration Issue

The data of $\pm 70\%$ E_c residual actuation shown in Figure 2-27 slightly increased even as the load increased. However, Figure 2-24 shows the reduction of $\pm 70\%$ E_c residual actuation at zero stress after each of the multiple loading cycles. The only difference between these two data is the compression duration. The data shown in Figure 2-24 used 5 minute duration for each step, and the specimen totally experienced 25 minutes of nonzero compression for the first loading cycle, while the data shown in Figure 2-27 used 30 second duration. Comparison implied the dependency of stress duration. The same phenomenon that actuation is dependent upon compression duration has also been reported by Zhang[29]. In order to study this phenomenon, more tests were conducted by using 5 minute and 30 minute compression durations instead of 30 seconds in the residual actuation test, as shown in Figure 2-26. In addition, in order to exclude the high electric field effect under high compression, two electric excitations distinguished as Types A and B were designed as shown in Figure 2-28. Type A was driving electric actuation at zero stress only, while Type B was driving at both zero and nonzero stress.

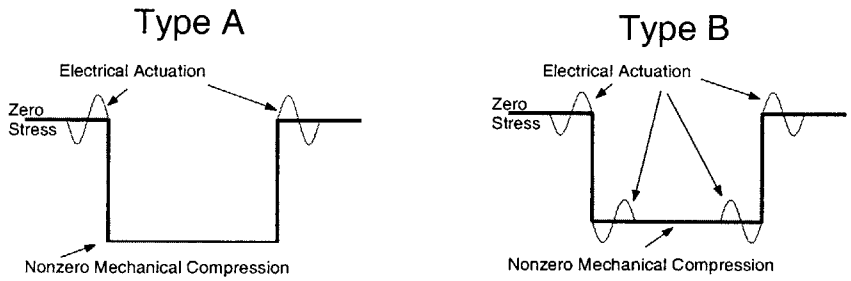

Figure 2-28: Type A was driving electric actuation at zero stress only, while Type B was driving at both zero and nonzero stress.

Figure 2-29(A) shows the test result using Type A actuation and Figures 2-29(B), (C), and (D) show the test result using Type B actuation. Some observations are concluded as the following:

- For Type A actuation using short compression duration, high electric drive can maintain the initial residual actuation even after exposure to high compressive stress, as

illustrated in Lines A1 and A2 in Figure 2-29(A).

- For Type A actuation using high electric drive level, longer compression duration results in reduced residual actuation, as shown in Lines A2 and A3 in Figure 2-29(A).

- Comparing Figures 2-29(A) and (B) shows the difference between Types A and B that the first two statements do not hold for Type B actuation.

- By comparing different durations, Lines C1–C3 in Figure 2-29(C) or Lines D1–D3 in Figure 2-29(D), one can conclude that Type B actuation has little compression duration effect.

- By comparing Line C_i to Line D_i, where i=1...3, for different electric driving fields in Figures 2-29(C) and (D), one can observe that Type B actuation has no ability to resist compressive depolarization, although high electric fields in Figure 2-29(D) result in 10% more actuation than low electric drive in Figure 2-29(C) after exposure to 150MPa.

The mechanism of duration effect on the residual actuation can be explained by the hypothesis that the depoled dipoles can be restituted by the internal electric field induced by unbalanced free charges due to compression until these free charges reach equilibrium. The compression duration matters because it takes time for free charges to reach such equilibrium. Figure 2-30 illustrates how this mechanism works. Before any compression, as shown in Figure 2-30(A), the dipoles in the material align along the poling direction, and the free charges and dipoles stay in equilibrium such that no internal electric field exists. After the compression is applied, the dipoles are flipped, as shown in Figure 2-30(B). At this moment, the unbalanced free charges and the flipped dipoles form internal electric fields which can reorient the dipoles back to the original alignment. This is true until these free charges migrate and compensate with the dipoles such that no more induced internal electric field exists, i.e. reaching equilibrium, as shown in Figure 2-30(C). As a consequence, if the stress is removed before equilibrium, the dipoles will be turned back by the induced internal electric field. This restitution depends on the extent of being in equilibrium that has been achieved by the migrating free charges and the restoring dipoles. In addition, any high electric field applied at this unbalanced state will help restitute the dipoles. This explains

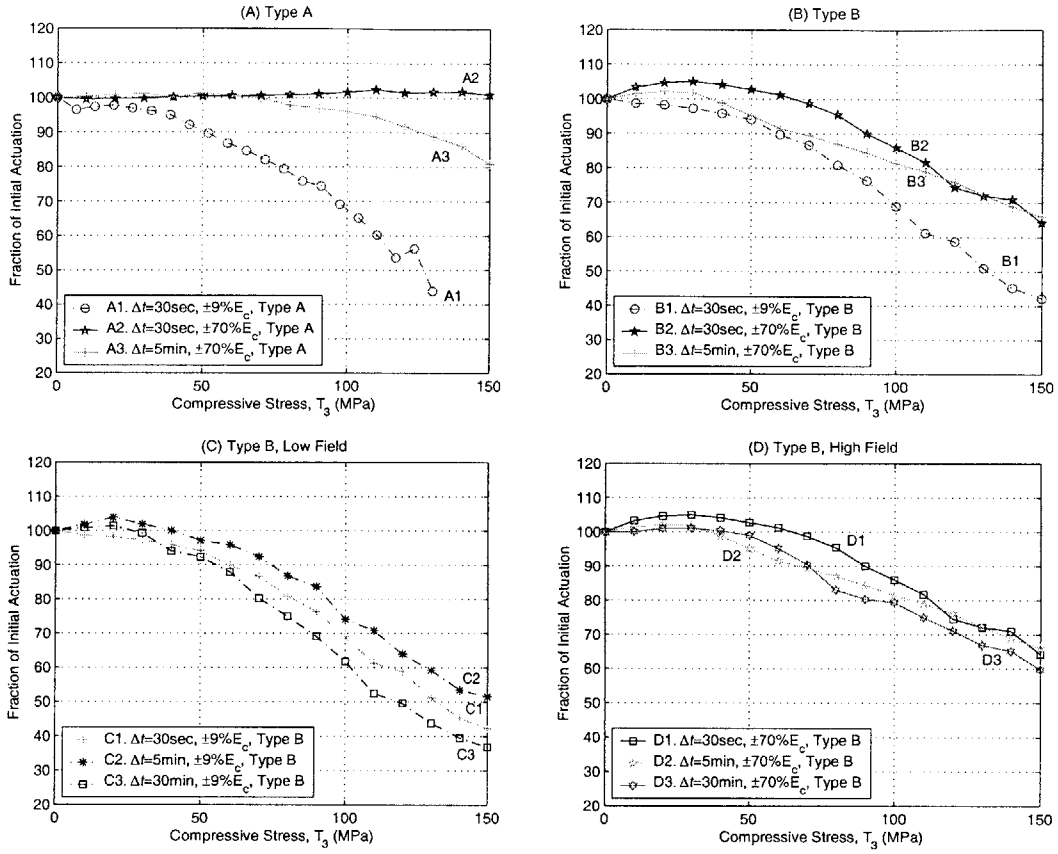

Figure 2-29: Normalized residual actuations for different compression duration and different electric fields: (A) Results using Type A actuation (B) Results using Type B actuation (C) Results using low Type B actuation, $\pm 9\%$ E_c (D)Results using high Type B actuation, $\pm 70\%$ E_c.

why using Type A actuation for short duration and high electric actuation can maintain the original actuation. However, this does not hold for Type B actuation because, in addition to compressive stress, the negative component of the electric field at nonzero compressive stress has further depolarized the material and therefore impedes the restitution of dipoles.

The surprising result that high electric actuation under short duration retains initial actuation provides promising driving conditions for controlled structures. Engineers may take the advantage of this result if short duration of a high compression environment is unavoidable. An example of such a situation is helicopter rotor blades subjected to a sudden gust. High electric actuation with $\pm 70\%$ E_c at zero stress can prevent high compression

depolarization for such short duration. If the high electric actuation under short duration of high compression is necessary, biased electric actuation without negative field is strongly recommended to prevent further depolarization of the material.

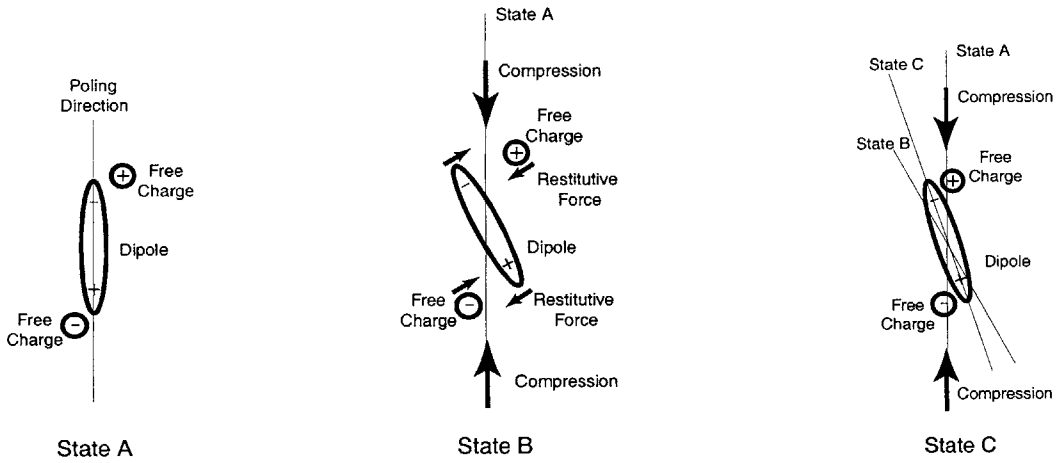

Figure 2-30: Illustration of the dipoles restituted by the internal electric fields induced by the unequilibrium free charges: (A) the original equilibrium state before compression, (B) the unequilibrium state after compression, (C) the equilibrium after compression.

2.2.3 Summary of Actuation Characterization

The compression limit of PZT-5A without depolarizing the material has been investigated in this section by testing the material at different levels and combinations of electric fields, compressive stresses and stress durations. The test results of actuation under load for a single loading cycle showed that the material was depolarized at high compressive stress even for high applied electric field. Once the material was depolarized by 150MPa compressive load, the polarization did not recover even after the complete removal of the load. The reversibility of actuation under load was observed only in the case subjected to the compressive load less than 30 MPa, as indicated by the test results of actuation under load using multiple loading cycles. Slight recovery of electric actuation was observed for the loading case below 60 MPa. The data of actuation under loads higher than 60 MPa indicated that the material suffered severe compressive depolarization and lost most actuation performance even for high electric field.

The properties of the residual actuation at zero stress after removal of the compressive load varied with applied electric field, compression duration, and whether the negative electric field was applied along with the compression. Without negative electric field driven with compressive load, the residual actuation at zero stress by high enough electric field (70% E_c) will remain constant even after exposure to short duration of high compression (less than 30 seconds). However, this is not true for those situations consisting of any combination of low electric field, long duration of compression, and occurrence of high negative electric field along with high compression.

Table 2.2 summarizes a matrix of possible situations leading to material depolarization. This table provides engineers a design guide for active devices under high compression environment. In particular, engineers may take reasonable advantage of certain results observed in this work that indicate that the active devices subjected to short duration of high compression (less than 30 seconds) will retain major actuation performance if high enough electric field(70% E_c) is applied and no compression is applied along with this electric excitation.

Table 2.2: Summary of PZT-5A Compressive Depolarization. (• indicates the test condition.)

	E-Field $\pm 9\% E_c$	E-Field $\pm 70\% E_c$	Compression $\leq 30MPa$	Compression $\geq 30MPa$	Duration $\leq 30sec.$	Duration $t \geq 5min.$	Loss of Actuation	Reversible
Actuation Under Load	•		•			•	little	Yes
	•			•		•	Yes	No
		•	•			•	25% loss	Yes
		•		•		•	Yes	No
Residual Actuation	•		•		•		little	
	•			•	•		Yes	
		•	•		•		No	
		•[4]		•	•		No	
		•[5]		•	•		Yes	
		•	•			•	No	
		•		•		•	Yes	

[4]No negative electric field was applied along with compression

[5]Negative electric field was applied along with compression

2.3 Characterization for Energy Harvesting Application

The most exciting feature of a piezoelectric material is that one can generate electric power by squeezing it very hard and fast. However, it is a major concern that the high compression parallel to the piezoelectric polarization direction may depolarize the materials[47]. Therefore, engineers desire to know the limit of compressive load without degenerating the material. Another concern is the frequency dependency. A previous study by Goldfarb[57] showed that piezoelectric generation using resistive load had low efficiency at high frequency. However, the new study in this work shows that the frequency dependency depends on the use of circuitry. A new test in this work using a rectifying diode circuit demonstrates that the energy can be harvested in a battery and that the efficiency is independent of frequency below the specimen natural frequency.

Hence, this section will fully investigate the frequency and stress effects of the piezoelectric energy harvesting application. Piezoceramics connected with a resistor and diode circuit will be first realized. The material characterization of generalized piezoelectric constants under short and open circuits will then be conducted. Diodes used for power measurement will be selected and characterized. Finally, the power harvested by diode circuitry will be reported. The common commercial piezoceramics PZT-5H[6] was selected for testing because its moderate piezoelectric and elastic constants, availability, and low cost. Other modern engineered materials such as single crystal PZN-PT[7] and PMN-PT[8] were also chosen because of their high piezoelectric constants, as shown in Table 2.1.

2.3.1 Resistive Load vs. Rectifying Circuitry

In order to study the difference between resistive load and rectifying circuitry, a linear electromechanically coupled model was built using SIMULINK^{TM} by Mathworks Inc. In this model, the material constants are assumed independent of stress and frequency. This model can be used to simulate response of the piezoelectric specimen subjected to a mechanical load and connected to circuitry such as resistors and rectifying diodes. More details of the model can be found in Appendix A.

[6] 6.35mm cube supplied by Staveley Sensors Inc, E. Hartford, CT.
[7] PZN-4.5%PT, 5.5mm cube, supplied by TRS Ceramics, Inc., State College, PA.
[8] 6mm × 6mm × 4mm supplied by Crystal Associates Inc., East Hanover, NJ.

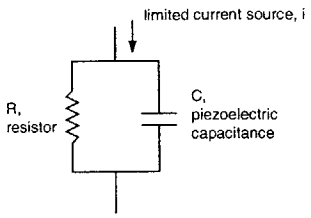

Figure 2-31: Effect of the limited current source on a RC circuit.

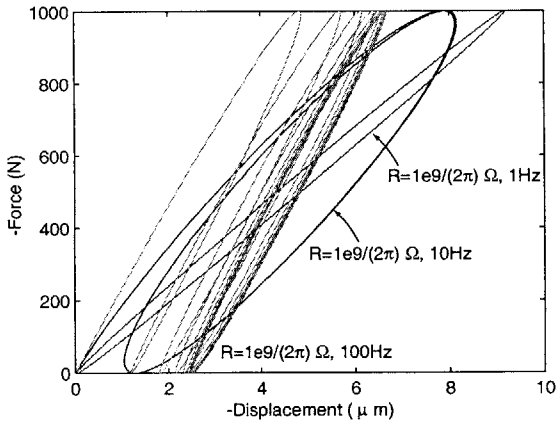

Figure 2-32: Simulation of force-displacement relation of piezoelectric specimen with resistive load.

Before simulating the resistive circuitry, an understanding must be emphasized that only a limited current can be generated by compressing a piezoelectric material. Due to this limited current source and the capacitive impedance of the piezoelectric material itself, the current flowing through the resistor is frequency dependent. As shown in Figure 2-31, in order to maximize the current flowing through the resistor, the value of the resistor (R) must match the impedance of the specimen (C):

$$|R| = \left| \frac{1}{j2\pi fC} \right| \tag{2.3}$$

or

$$R = \frac{1}{2\pi fC} \tag{2.4}$$

where j equals $\sqrt{-1}$ and f is the driving frequency of the mechanical load. Figure 2-32 shows the simulated force-displacement relation of the specimen in the resistor circuit.

The enclosed area by this force-displacement relation represents the mechanical energy transformed into electrical energy. As a result, for a given amplitude of the input force, the larger the enclosed area is, the higher the efficiency is. As shown in the Figure 2-32, for a 100pF specimen with a $1/(2\pi) \times 10^9\Omega$ resistor, the maximum efficiency occurs at 10Hz. This correlates the test result by Goldfarb. However, the same efficiency at different frequency can be obtained by matching the impedance, for instance, using a resistors of $1/(2\pi) \times 10^{10}\Omega$ at 1Hz or a resistor of $1/(2\pi) \times 10^8\Omega$ at 100Hz. This analysis demonstrates that the frequency dependency comes from the mismatch between the resistor and the impedance of the specimen. Unfortunately, the factor of impedance mismatch is not considered by Goldfarb.

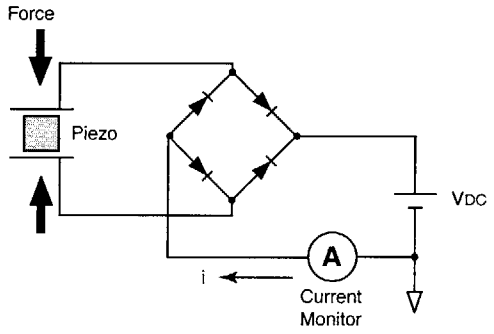

Figure 2-33: Diode bridge circuitry

In contrast to the resistive load, the rectifying circuit shown in Figure 2-33 will result in efficiency that is independent of frequency. Figure 2-34 shows a comparison of the simulated force-displacement relationships for the resistive load and rectifying circuit. Although the maximum efficiency of the rectifying circuit is slightly smaller than that of the resistive circuit, the benefit using the rectifying circuit includes frequency independence and the fact that electric power can be harvested in a battery. As a result, the diode circuit will be used later in this section to characterize the stress effects on the power density generated by piezoelectric materials.

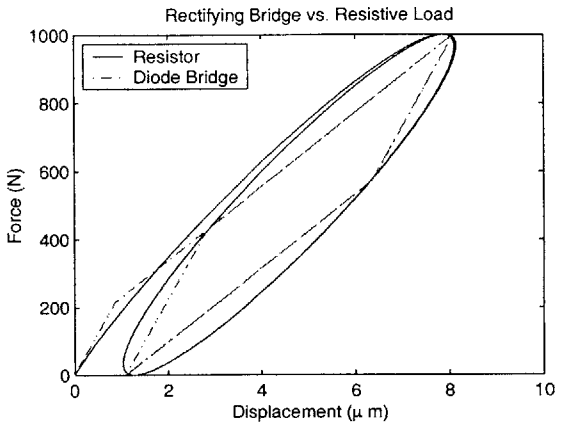

Figure 2-34: Simulation of force-displacement relation of piezoelectric specimen with a resistor or a rectifying diode bridge.

2.3.2 Characterization of Generalized Material Constants

The simulation used in the previous discussion is based on the assumption that the material properties are independent of stress and frequency. This linearity may not be true in practice. As a result, it is of interest to obtain experimental data of material constants as a function of stress and frequency. To do so, a generalized material constant is first defined as the linear slope of material response with respect to the stress at different amplitudes and frequencies of the input stress. These generalized material constants include piezoelectric coupling constants d_{33} and g_{33} and compliances s_{33}^E and s_{33}^D, each a required input of the simulation model. The d_{33} constant determines how much current can be drawn from the specimen at short circuit condition. The g_{33} constant determines how much potential can be generated on the specimen at open circuit condition. The stiffness determines how much displacement the specimen deforms and how much power is delivered into the specimen for a given input force.

The test was performed using the high frequency tester shown in Figure 2-5. Under short circuit condition, strain and charge were measured by the strain gauges and charge amplifier shown in Figure 2-18. Under open circuit condition, strain and voltage were measured by the strain gauges and voltmeter shown in Figure 2-13. Figures 2-35 and 2-36 show the data of s_{33}^E, s_{33}^D, d_{33}, and g_{33} as functions of stress at 10Hz and 400Hz for PZT-5H,

PZN-PT and PMN-PT. As can be seen, the material properties are significant functions of the driving stress but not obvious functions of the driving frequency. The variance of single crystal data at different frequency might be due to the variance of different samples. A slight misalignment of cutting of a single crystal specimen may result in huge variance of material properties, while the cutting has no major effect of a polycrystalline PZT-5H specimen. Each data set can be fitted using a polynomial function of compressive stress T (in MPa):

$$d_{33}^{PZT-5H} = 679.18 + 11.035T - 0.28434T^2 \tag{2.5}$$

$$d_{33}^{PMN-PT} = 958.75 + 17.235T - 0.72036T^2 \tag{2.6}$$

$$d_{33}^{PZN-PT} = 1576.8 + 47.839T - 1.8197T^2 \tag{2.7}$$

$$s_{33}^{E\,PZT-5H} = 23.753 + 0.11773T - 0.0052678T^2 \tag{2.8}$$

$$s_{33}^{E\,PMN-PT} = 39.285 + 0.70661T - 0.0080949T^2 \tag{2.9}$$

$$s_{33}^{E\,PZN-PT} = 78.076 + 0.71686T + 0.0066186T^2 \tag{2.10}$$

$$g_{33}^{PZT-5H} = 0.020196 + 0.00012746T - 0.000041935T^2 + 0.0000023240T^3 - 0.000000057743T^4 \tag{2.11}$$

$$g_{33}^{PMN-PT} = 0.027015 + 0.00051050T - 0.000107110T^2 + 0.0000031697T^3 - 0.000000028433T^4 \tag{2.12}$$

$$g_{33}^{PZN-PT} = 0.036175 + 0.00071800T - 0.00019501T^2 + 0.0000067482T^3 - 0.000000071305T^4 \tag{2.13}$$

$$s_{33}^{D\,PZT-5H} = 10.2763 - 0.035048T + 0.0012802T^2 \tag{2.14}$$

$$s_{33}^{D\,PMN-PT} = 15.525 + 0.59993T + 0.014338T^2 \tag{2.15}$$

$$s_{33}^{D\,PZN-PT} = 15.792 + 0.10766T - 0.15070T^2 + 0.040328T^3 - 0.0017931T^4 + 0.000023619T^5 \tag{2.16}$$

where the units of d_{33} and g_{33} are pC/N and Vm/N, respectively, and s_{33}^E and s_{33}^D are in pm^2/N. Among the four constants, g_{33} decreases most rapidly as the compression is increased. This also results in the sharp degeneration of the coupling coefficients k_{33} shown in Figure 2-37 and defined as:

$$k_{33}^2 = \frac{d_{33}g_{33}}{s_{33}^E} \tag{2.17}$$

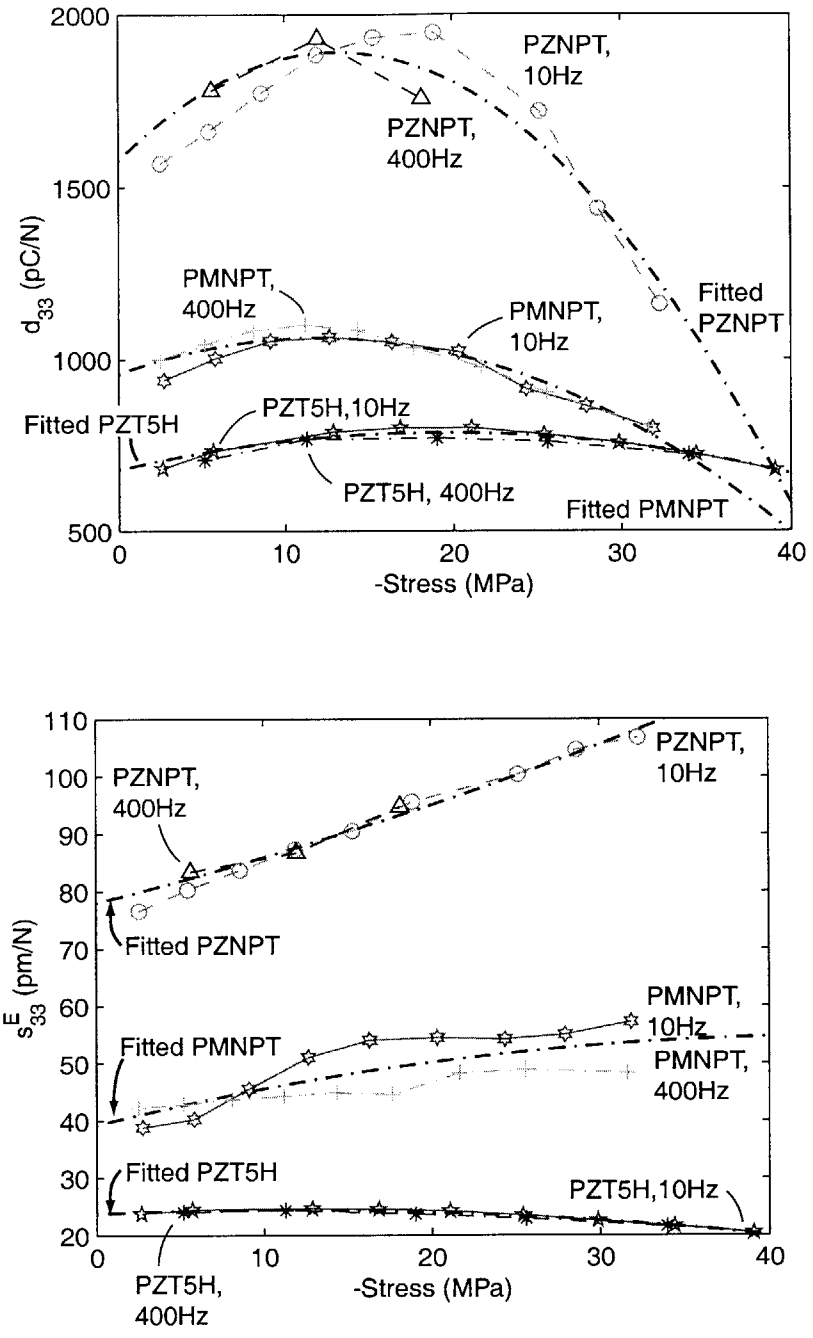

Figure 2-35: Generalized material constants d_{33} and s^E_{33} as functions of stress at 10Hz and 400Hz for PZT-5H, PZN-PT and PMN-PT.

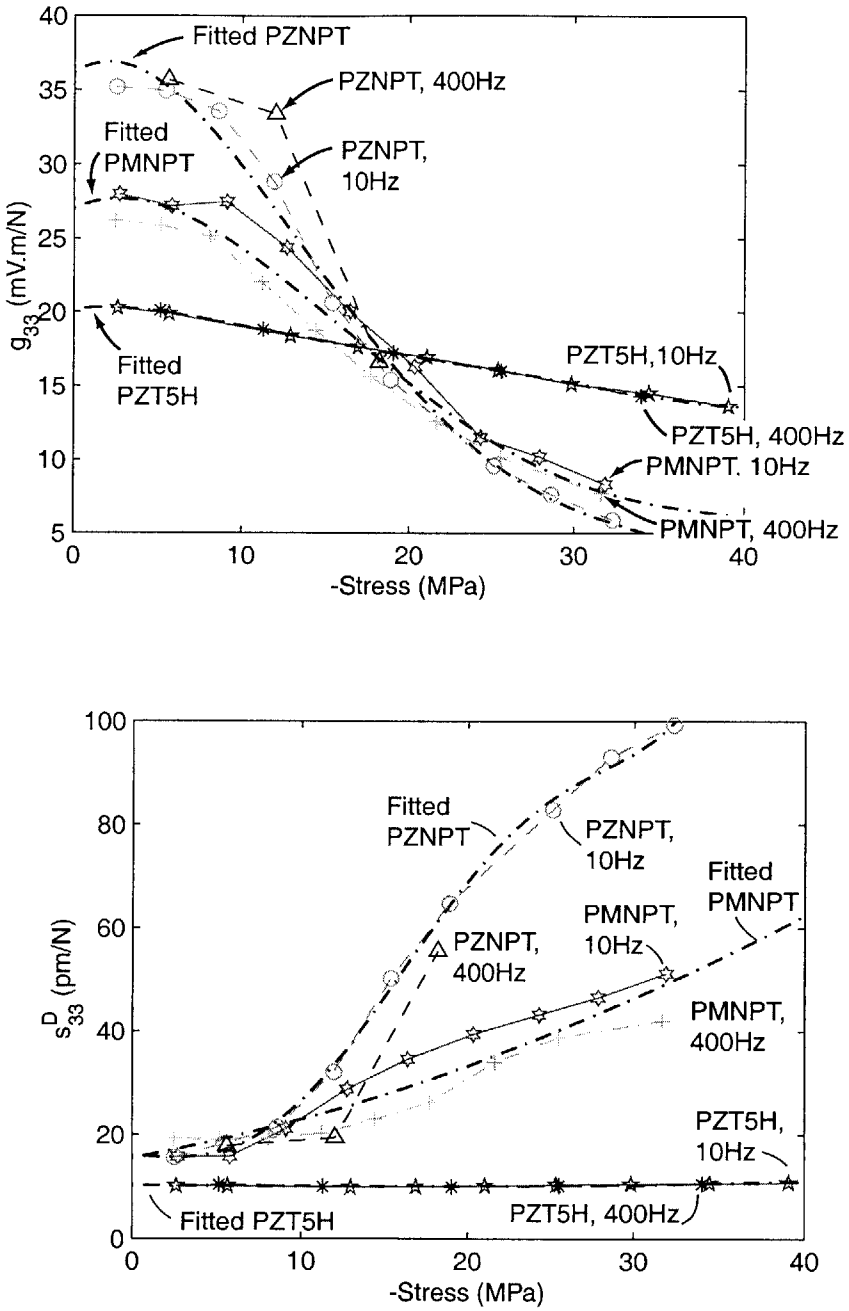

Figure 2-36: Generalized material constants g_{33} and s^D_{33} as functions of stress at 10Hz and 400Hz for PZT-5H, PZN-PT and PMN-PT.

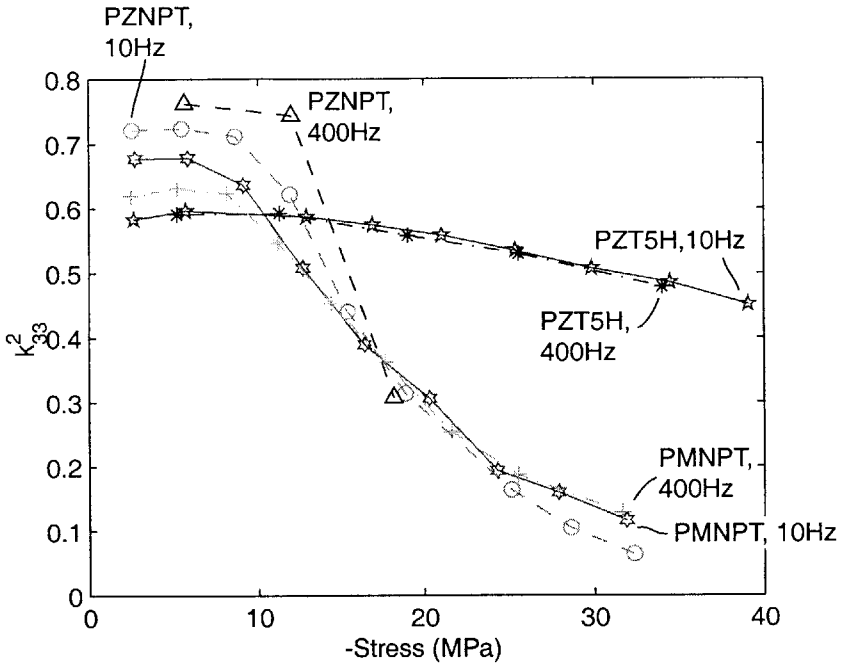

Figure 2-37: k_{33}^2

2.3.3 Diode Selection and Characterization

As mentioned earlier, compressive stress, say up to 20MPa, can easily generate up to 5-15kV/cm open circuit electric field, which corresponds to 3-9kV on a 0.6cm thick specimen. The reverse breakdown voltage of the diode must be higher than the voltage level generated by the piezoelectric materials. The diode CS57-04[9] was therefore chosen to construct a rectifying bridge. A common model can be used to describe the characteristics of the diodes:

$$i = \begin{cases} I_0 \left[exp\left(\frac{qv}{\eta k\theta}\right) - 1 \right], & v \geq 0. \\ 0 & v < 0. \end{cases} \tag{2.18}$$

where $q = 1.60 \times 10^{-19}$(C) is the electron charge, $k = 1.38 \times 10^{-23}$(J/K) is the Boltzmann constant, and θ is the temperature. I_0 and η are material properties to be determined from experiment using the circuit shown in Figure 2-38. For CS57-04 diode, parameters were

[9]Collmer Semiconductor, Inc.

found by fitting the model to the data shown in Figure 2-39:

$$I_0 = 1.35 \times 10^{-11}, \qquad \text{and} \qquad \eta = 5.6.$$

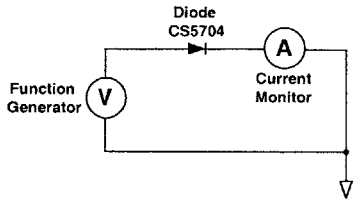

Figure 2-38: Diode forward test circuitry

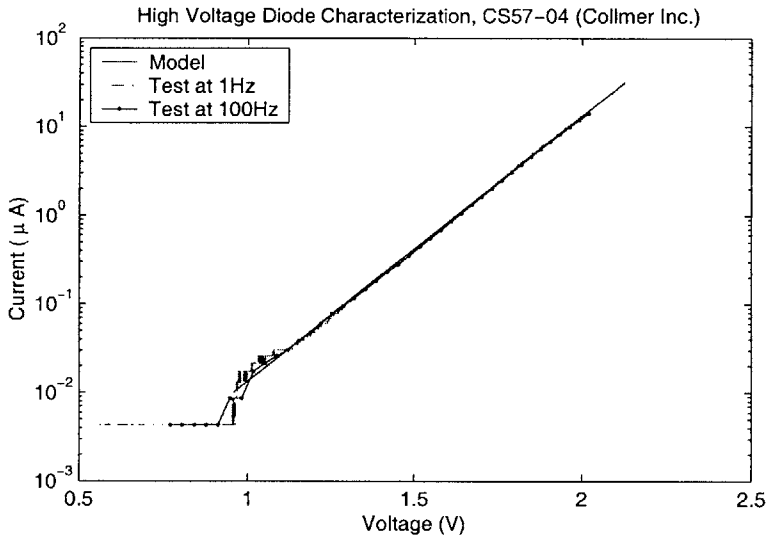

Figure 2-39: Diode characteristics

It is also essential to verify that the reverse current is low enough so that the loss is minimized. This can be done using the test configuration described in Figure 2-40, with current amplifier gain 10^6V/A and reverse voltage up to 4kV. The current in reverse diode mode was found to be less than $0.02\mu A$, which is much less than the forward current range 1 to $100\mu A$ in this thesis work. For convenience, the reverse diode current is therefore assumed zero as in Eq. 2.18.

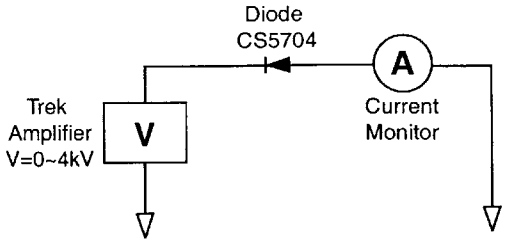

Figure 2-40: Diode reverse test circuitry

2.3.4 Characterization of Material Energy Density

Using the rectifying circuit shown in Figure 2-33, one can obtain the power output by

$$\mathcal{P} = i \times V_{DC} \tag{2.19}$$

where V_{DC} is the DC voltage of the battery, and i is the current flowing into the battery. The specimens of different materials were tested under different frequencies, forces, and battery voltages. Using the generalized material properties measured earlier, one can simulate the response using the Simulink model developed earlier.

Figures 2-41(a), (b), and (c) show good correlation between the measured and simulated response of PZN-PT under low stress at which the material behaves linearly. Unfortunately, the material does not behave linearly under high stress condition. The nonlinear material is the reason why the simulation does not correlate with the measured data very well, as shown in Figures 2-41(c), (d), and (e). Figure 2-42 shows the measured and simulated power as a function of the battery voltage at both low stress and high stress conditions. As can be seen again, the linear simulation predicts the power output much better at low stress than at high stress. In addition, maximum power output occurs approximately when the battery voltage equals one half of the specimen's open circuit voltage.

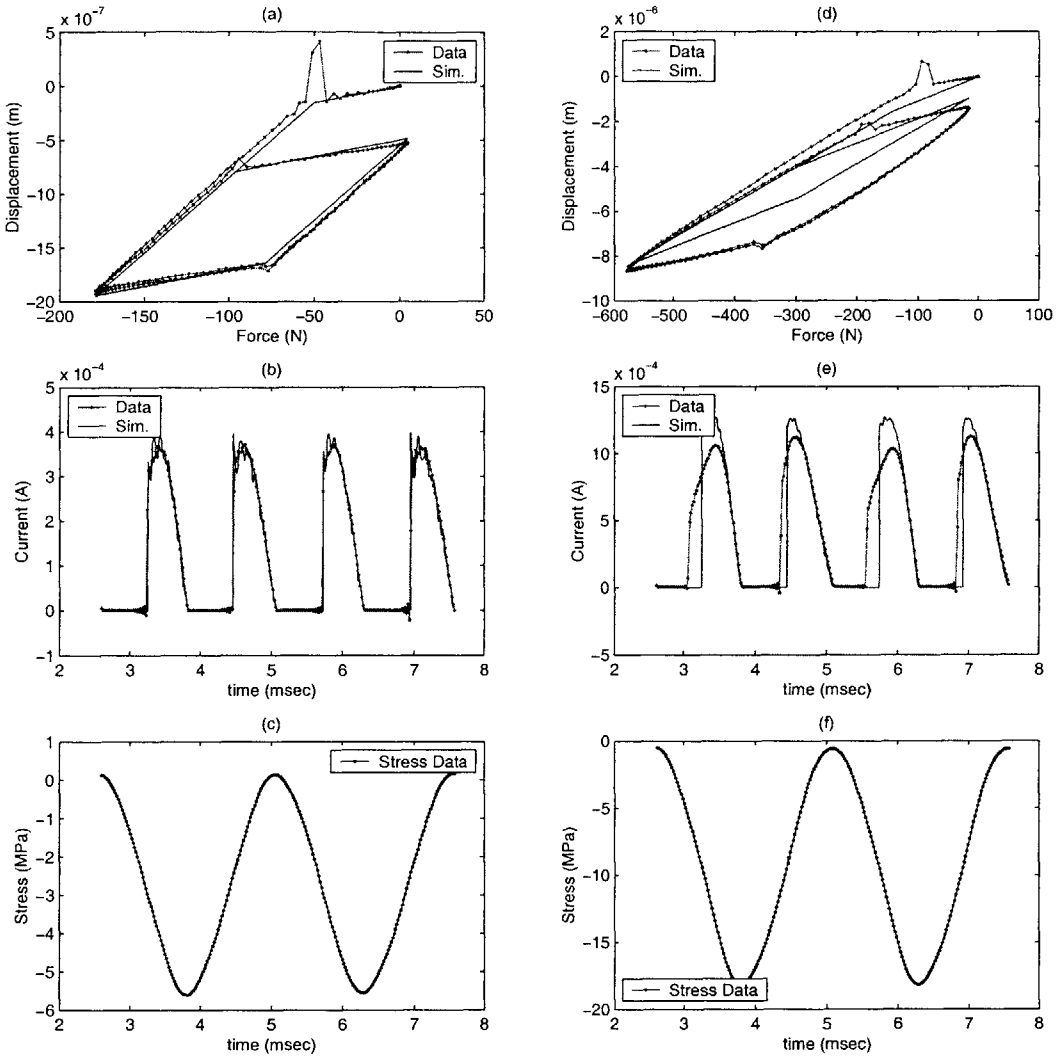

Figure 2-41: Data and simulation of low and high stress response: (a) the force-displacement relation at low stress, 400Hz, V_{DC} =300V; (b) the simulated and measured current at low stress 400Hz, V_{DC} =300V; (c) driving force history of low stress condition; (d) the force-displacement relation at high stress, 400Hz, V_{DC} =400V; (e) the simulated and measured current at high stress 400Hz, V_{DC} =400V; (f) driving force history of high stress condition.

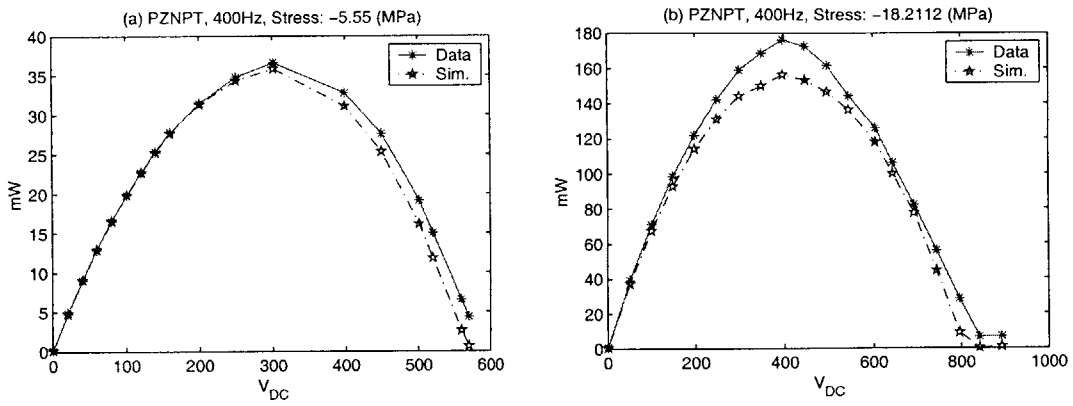

Figure 2-42: Power vs. V_{DC}

In order to compare the harvested electric energy for different sizes of specimens and different driving frequencies, it is convenient to normalize the power $\mathcal{P}$ by the frequency f and specimen volume V and to define an energy density:

$$\Omega = \frac{\mathcal{P}}{fV} \tag{2.20}$$

If the material properties are linear, the maximum energy density obtained using rectifying circuitry is proportional to the square of the stress and is given by[58]

$$\Omega_{max} = \frac{1}{4} k_{33}^2 T_{33}^2 s_{33}^E \tag{2.21}$$

or

$$\Omega_{max} = \frac{1}{4} g_{33} d_{33} T_{33}^2 \tag{2.22}$$

where T_{33} is the compressive stress. Figure 2-43 shows the maximum energy density of different materials as a function of compressive stress using rectifying circuitry. The dashed lines are obtained assuming the materials are linear; however, the experiment shows that the materials degenerate at higher stress. The generalized material constants obtained earlier are also useful to predict this result. Substituting Eq. 2.5, 2.6, 2.7, 2.11, 2.12, and 2.13 into Eq. 2.22 yields a good approximation of maximum energy density, as shown in Figure 2-43.

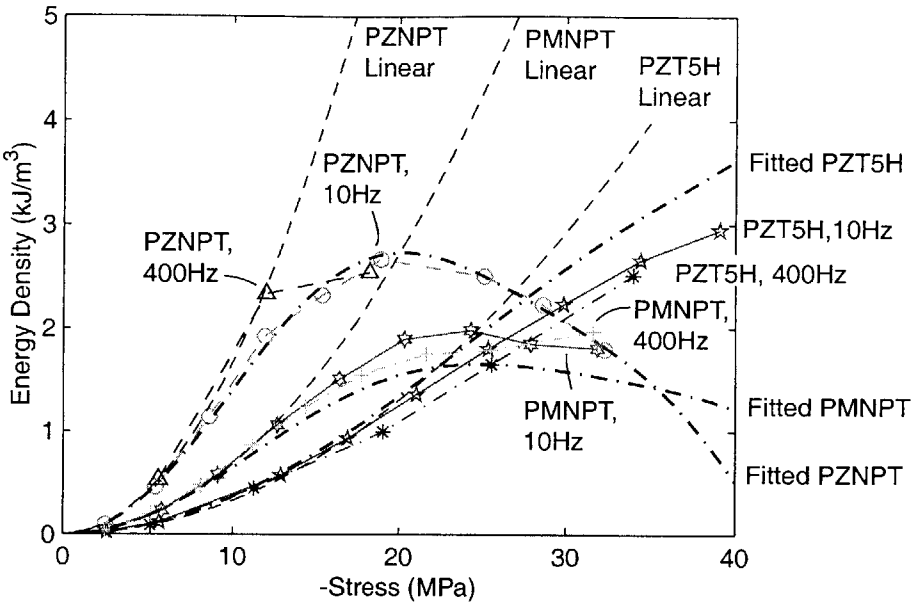

Figure 2-43: Maximum energy density using rectifying circuitry. The curves labeled as "Fitted" are obtained from Eq. 2.22 using generalized material constants described in Eq. 2.5, 2.6, 2.7, 2.11, 2.12, and 2.13. The curve labeled as "Linear" are obtained from Eq. 2.22 assuming constant material coefficients d_{33} and g_{33} at zero stress

2.3.5 Single Crystal vs. Polycrystalline Ceramics

From the data of s_{33}^E as a function of compression, the single crystal PZN-PT and PMN-PT show *softening* phenomenon, while polycrystalline material PZT-5H shows *hardening* behavior. This softening result implies (but not necessarily means) that the material structure of the single crystals might have been damaged by high compression.[10] This damage might be able to explain why the g_{33} constants of the single crystal materials drop more rapidly. For the sake of discussion, it is assumed the undamaged single crystal specimen is perfectly dielectric. When the structure of the single crystal specimen is damaged, the free charge or vacancy might build up, which is the major source of channelling or conductivity. Although the damaged specimen is conductive now, it still has finite resistance. Because of this resistance, the open circuit voltage will decrease and so will the g_{33} constants. In contrast, this resistance has little influence on d_{33} because it is measured under the short circuit con-

[10]Similar damage has also been reported by Lynch[67] that single crystal PZN tends to develop cracks when driving the material with high electric fields.

dition. On the other hand, for the polycrystalline PZT material, the hardening behavior suggests that only domain movement or switching (but little damage) happens while under high compression. This hypothesis qualitatively explains the discrepancies between polycrystalline PZT-5H and single crystal PZNPT and PMN-PT, whereas an additional study using microscopic observation is needed to fully understand this discrepancy.

2.3.6 Summary of Piezoelectric Energy Harvesting

In this work, the material properties for an energy harvesting application were tested and show a significant dependence on applied stress but not a significant dependence on frequency. These material properties can be represented by generalized material constants as functions of stress, as shown in Figures 2-36 and 2-35. For PZT-5H, the material starts to depole when the compression is higher than 22MPa, while the material starts to degenerate at stresses higher than 11MPa for PZN-PT and 15MPa for PMN-PT. Among others, PZN-PT at low stress has the largest energy density which is beneficial. However, this is not necessarily true at higher stress. It might be beneficial if PZT-5H is used at stress higher than 30MPa, according to the result shown in Figure 2-43.

In addition, it is also discovered in this work that both d_{33} and g_{33} are essential to predict the capability of piezoelectric power generation at high compression, according to Eq. 2.22. The literature[54] that only published d_{33} as a function of stress is not sufficient for the purpose of designing a successful energy harvester.

2.4 Characterization for Material Modeling

Although it is possible to characterize each material at each design loading point, the cost is too high. As a result, the ultimate aim of this thesis is to build a full model which can capture the characteristics observed in Sections 2.2 and 2.3. If this can be done, a lot of testing work can be saved. To reach this goal, it is essential to characterize the material under the largest amplitude of practical driving conditions. The approach follows Ghandi's work in which PZT-5H was characterized. In this thesis work, PZT-5A was also tested because it is primarily used in the commercial AFCs. In addition to the study of stress dependency, the study of frequency dependence is also of interest. However, to minimize the number of tests, the effects of frequency and stress are assumed decoupled. By this assumption, only two planes of a three dimensional testing domain needs to be conducted. As shown in Figure 2-44, one is electric field and stress; the other is electric field and frequency.

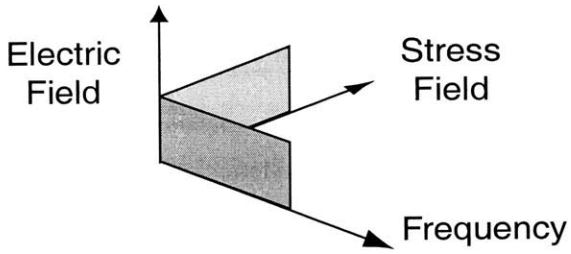

Figure 2-44: The test planes of stress and electric fields versus frequency and electric field

Rate Dependency

Before characterizing the material behavior under compression, one can first examine the rate dependency of the piezoelectric material. To complete the full test matrix, PZT-5H was first driven by electric fields at different frequencies: 0.1Hz, 1Hz and 10Hz. Figures 2-45 shows the result that higher frequency tends to expand the butterfly curves and P-E loops. Figure 2-46 shows the same trends for PZT-5A. Similar phenomena of this expansion have also been found in Magnetic Particle Active Fiber Composites(mpAFC)[73]. These frequency dependent P-E and S-E data will be the basis of the rate dependent model in

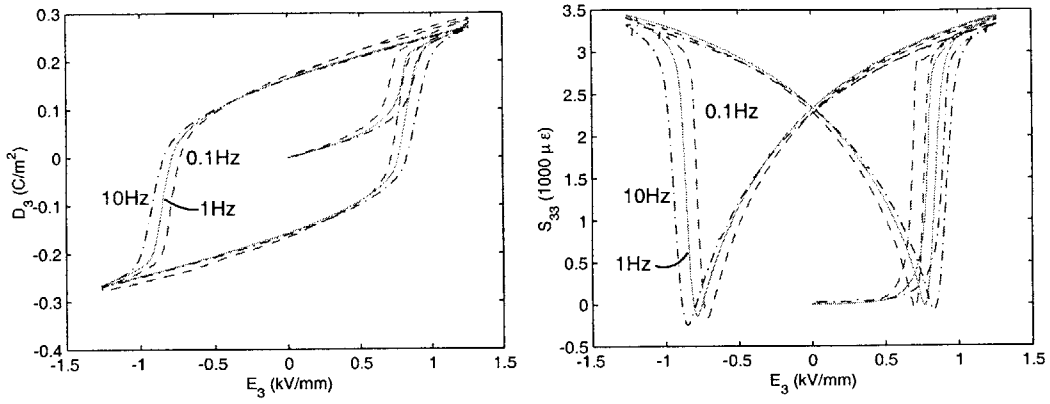

Figure 2-45: Rate dependency of PZT-5H: P-E loops(left) and S-E loops(right)

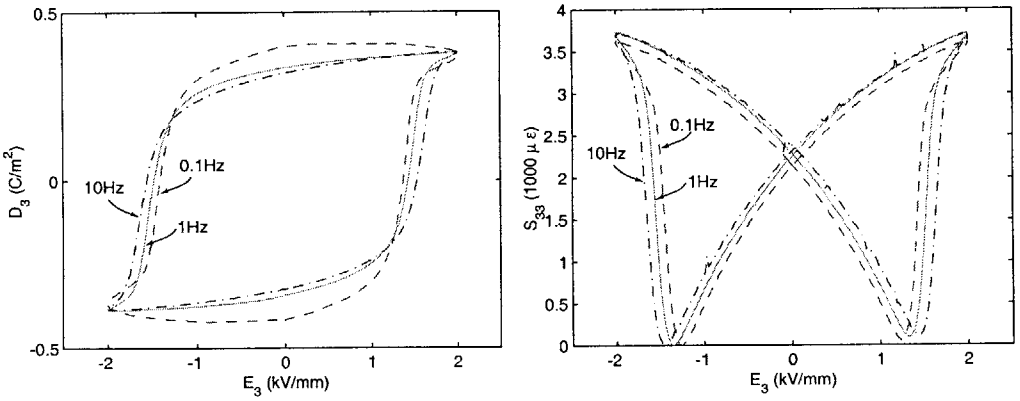

Figure 2-46: Rate dependency of PZT-5A: P-E loops(left) and S-E loops(right)

Stress Dependency

After the test of rate dependence, stress dependence was also of interest in this thesis work. The same test for PZT-5H has been done by Ghandi[35]. Therefore, only PZT-5A will be tested in this thesis. Two configurations, the transverse and the longitudinal tests, shown in Figure 2-2, were used. In the longitudinal test of PZT-5A, the specimen was 6mm by 6mm by 4mm. The buffer blocks were sized 6mm by 6mm by 7mm. By applying T_{33} and E_3, one

can measure the response of $S_{11}(= S_{22})$, S_{33}, and D_3. In the transverse test of PZT-5A, the specimen is 4mm by 4mm by 12mm. By applying T_{11} and E_3, one can measure the response of S_{11}, S_{22}, and S_{33}.

Figures 2-47, 2-48, and 2-49 showed the result of the longitudinal test of PZT-5A (Batch A). Figures 2-50, 2-51, 2-52, and 2-53 showed the result of the transverse test of PZT-5A (Batch B). Unfortunately, these two tests were conducted using two different batches of specimens. Comparing the coercive fields shown in Figure 2-47 and 2-50, the variance of these two batches were very significant. This may cause difficulty in developing the material model later. As a result, an additional longitudinal test using Batch B was repeated, as shown in Figures 2-54, 2-55, and 2-56. The new longitudinal test data of PZT-5A (Batch B) showed a better correlated coercive field.

The tests mentioned above were under compression up to 50MPa. Since the actuation tests in Section 2.2 are under compression up to 150MPa, it was also of interest to perform similar tests under higher compression. However, to avoid the failure of the specimen under high compression and high electric field simultaneously, only the longitudinal tests under compression up to 100MPa were repeated, as shown in Figures 2-57, 2-58, and 2-59. As can be seen, the material was significantly depolarized by higher compression.

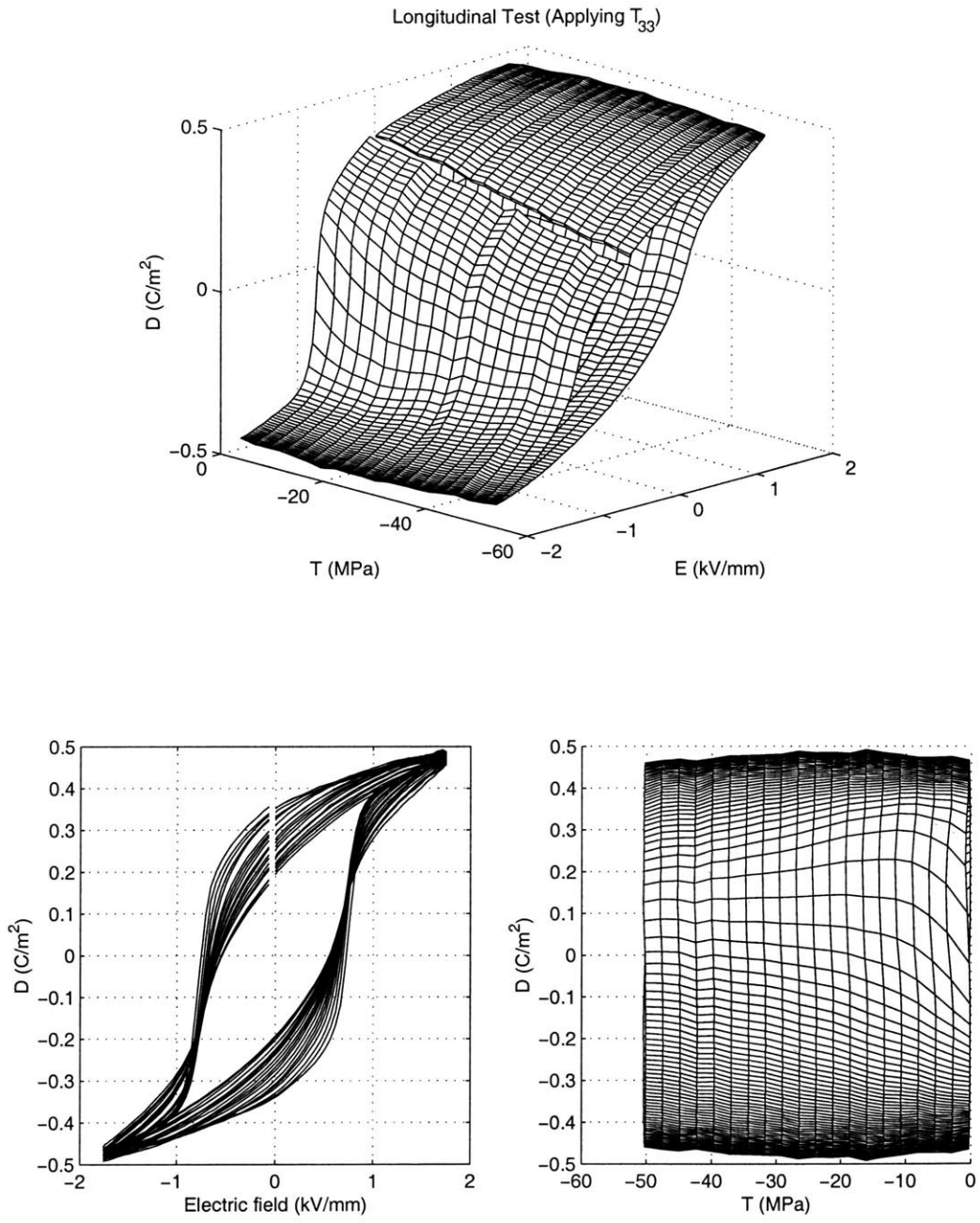

Figure 2-47: The data of repolarizing PZT-5A (Batch A) material behavior under longitudinal compression test.

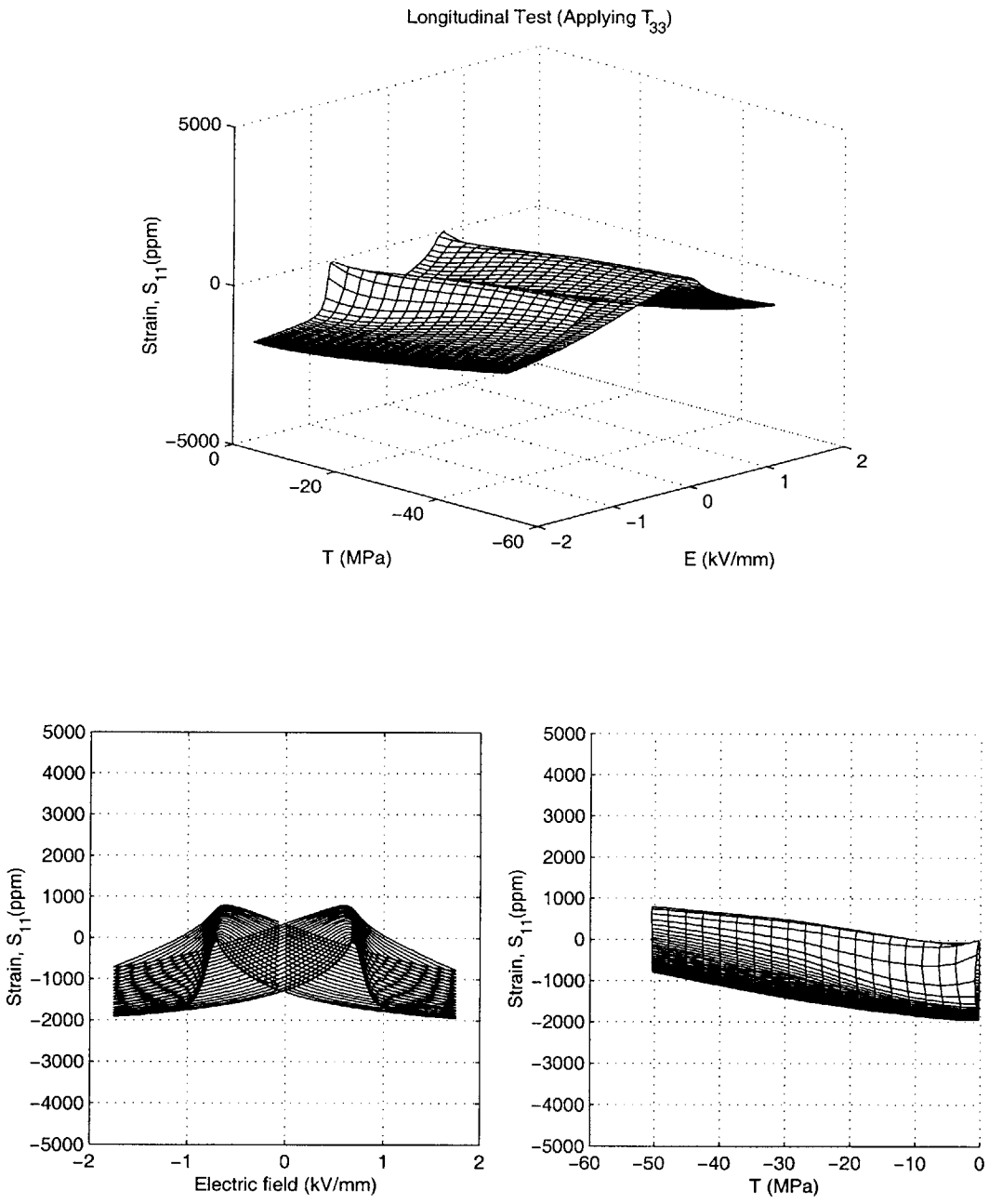

Figure 2-48: The data of repolarizing PZT-5A (Batch A) material behavior under longitudinal compression test.

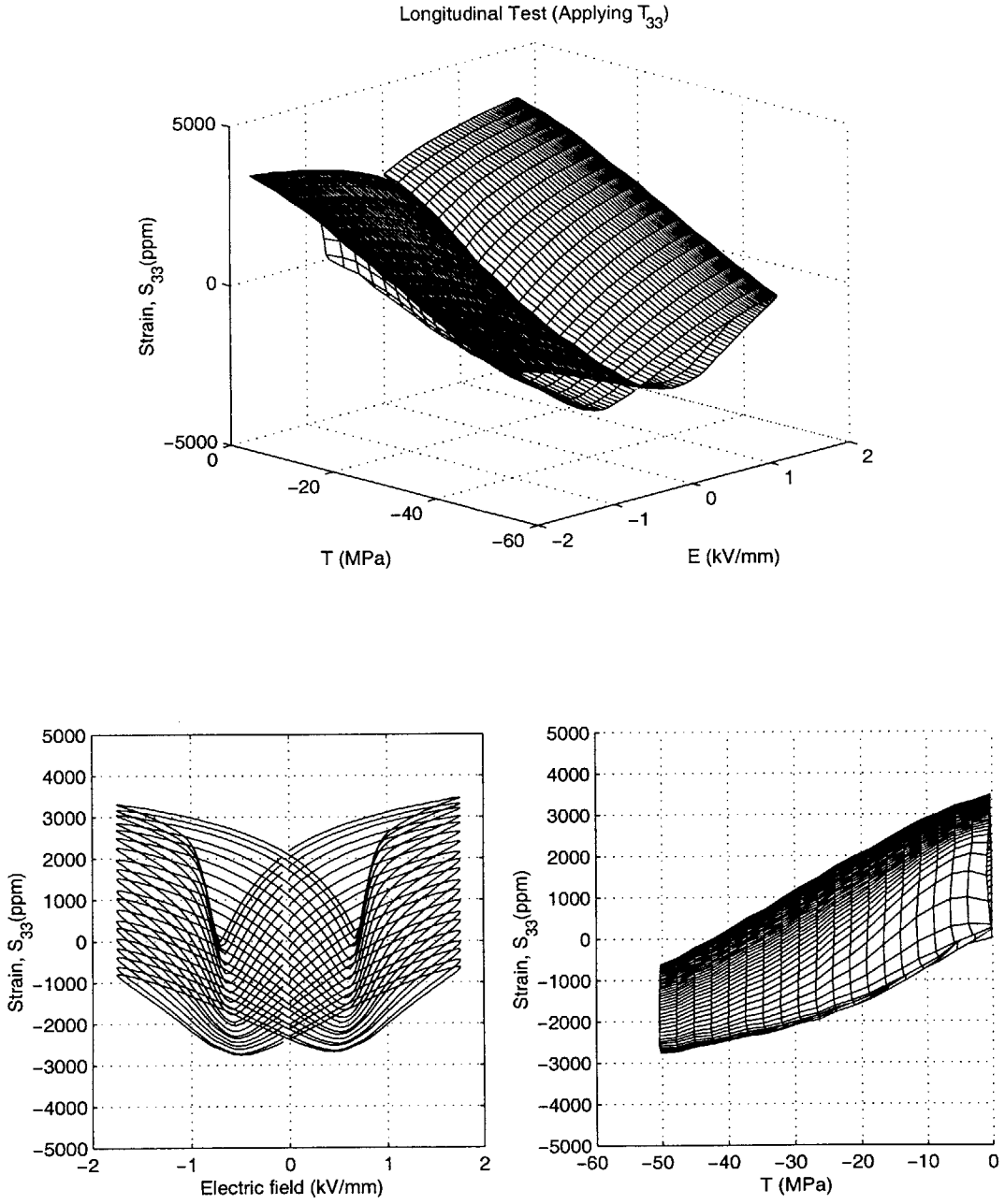

Figure 2-49: The data of repolarizing PZT-5A (Batch A) material behavior under longitudinal compression test.

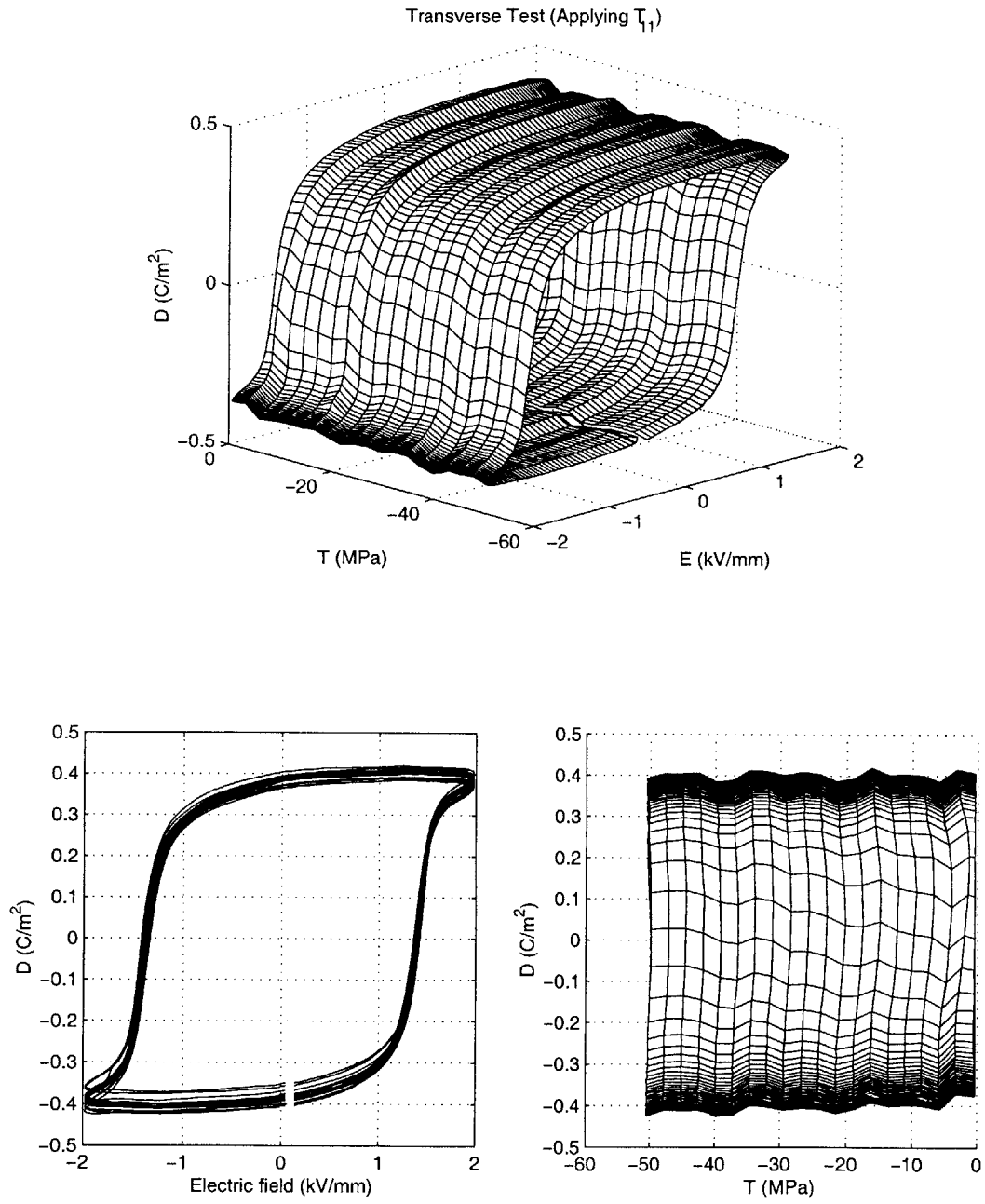

Figure 2-50: The data of repolarizing PZT-5A (Batch B) material behavior under transverse compression test.

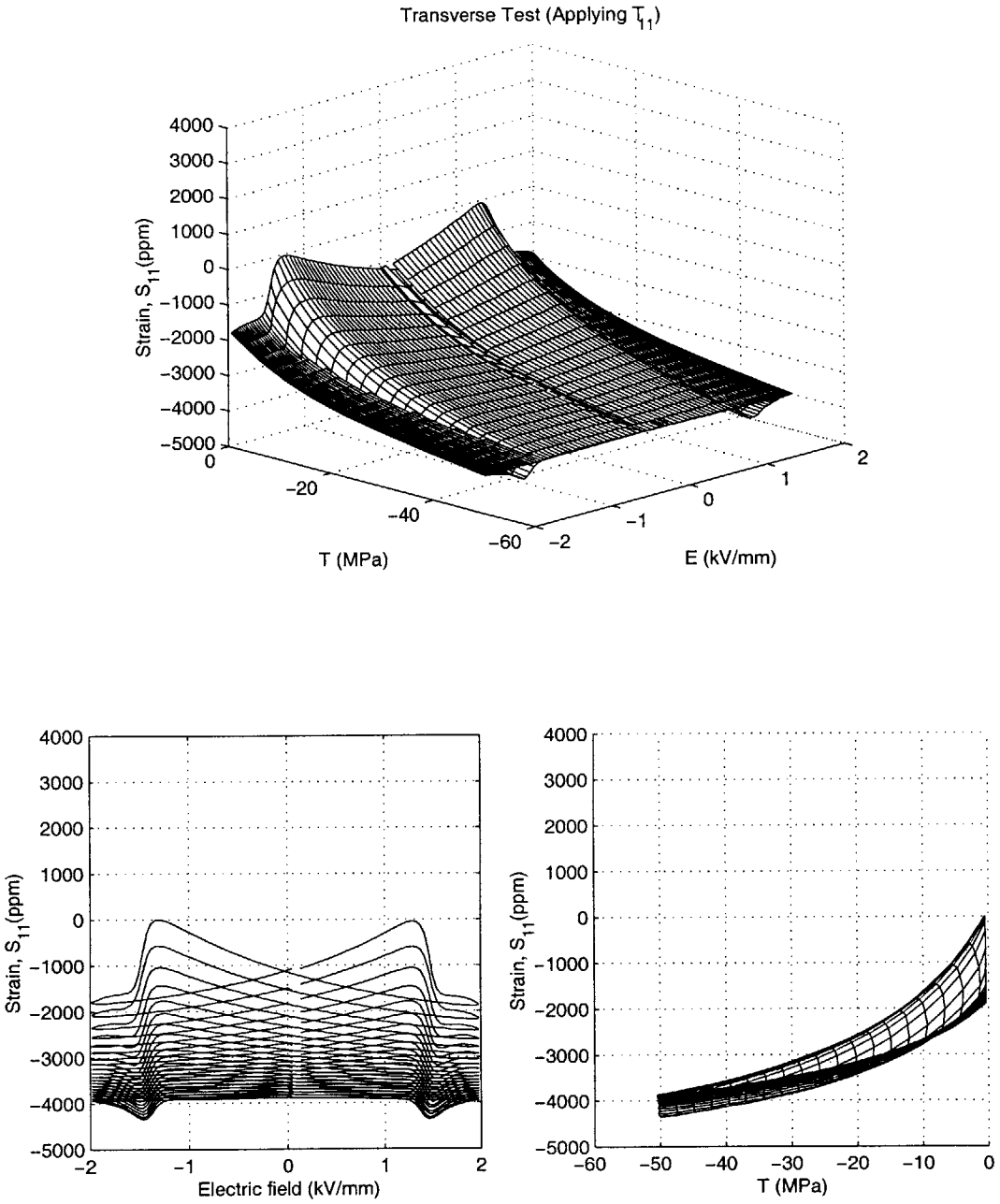

Figure 2-51: The data of repolarizing PZT-5A (Batch B) material behavior under transverse compression test.

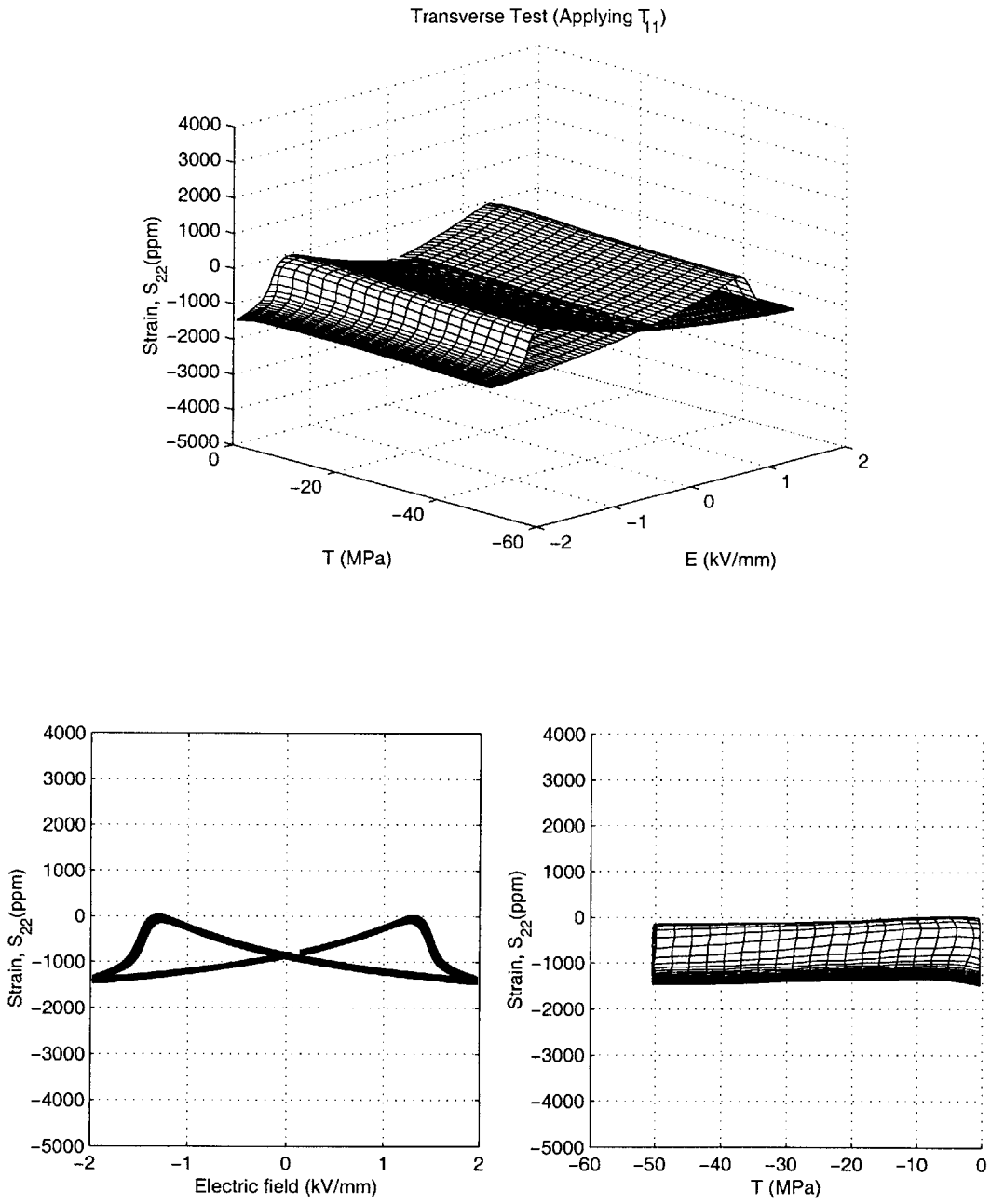

Figure 2-52: The data of repolarizing PZT-5A (Batch B) material behavior under transverse compression test.

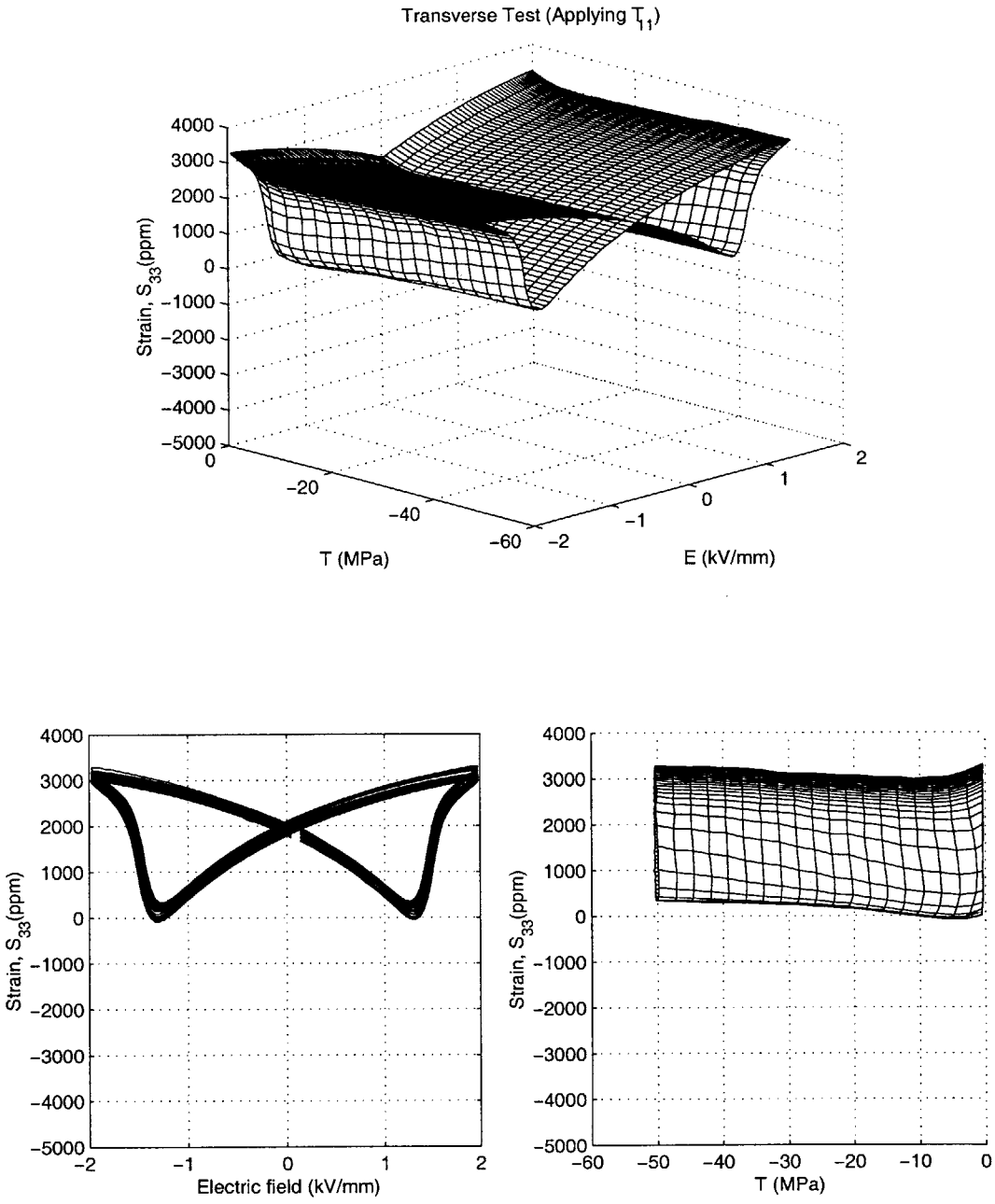

Figure 2-53: The data of repolarizing PZT-5A (Batch B) material behavior under transverse compression test.

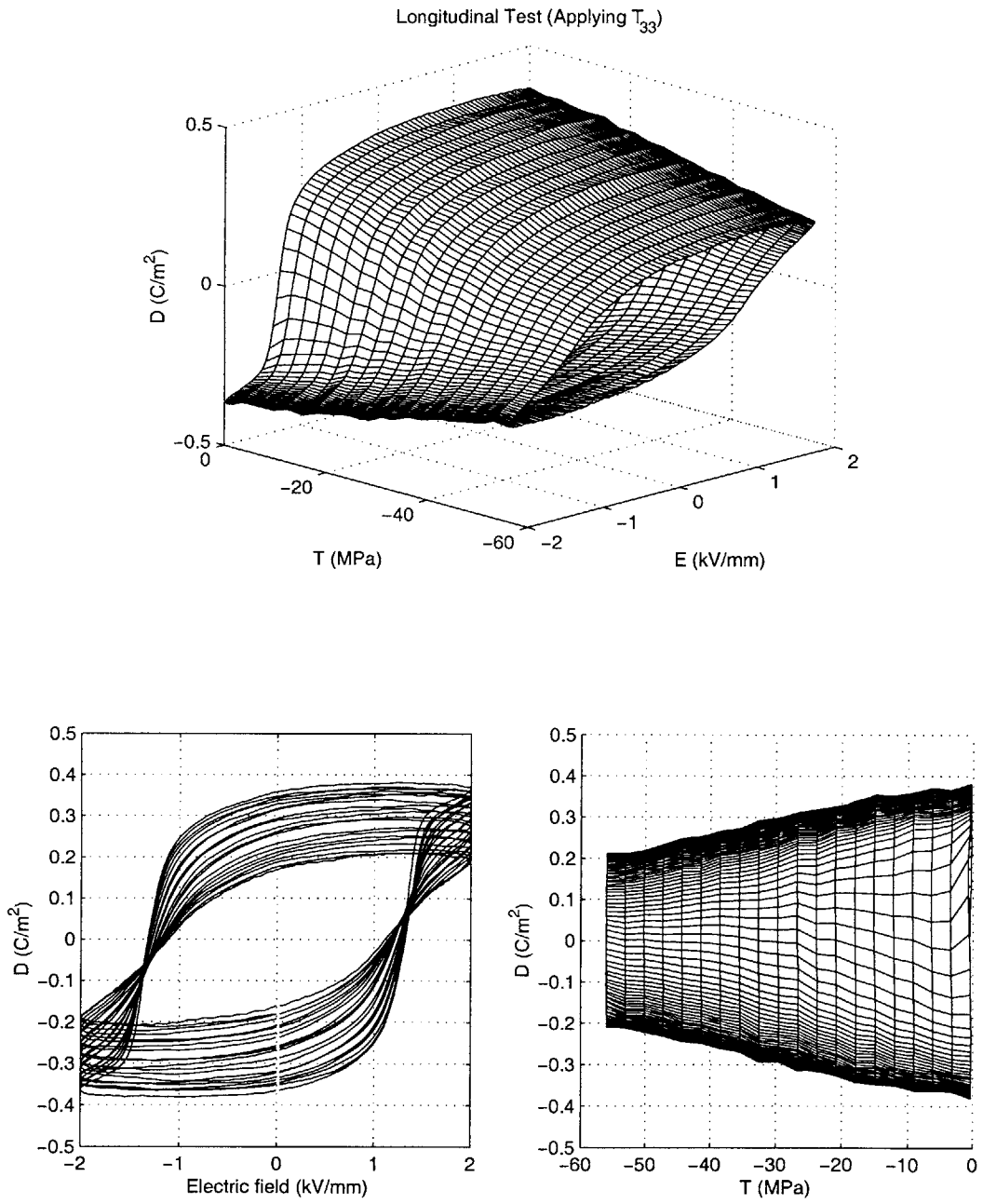

Figure 2-54: The data of repolarizing PZT-5A (Batch B) material behavior under longitudinal compression test (up to 56MPa).

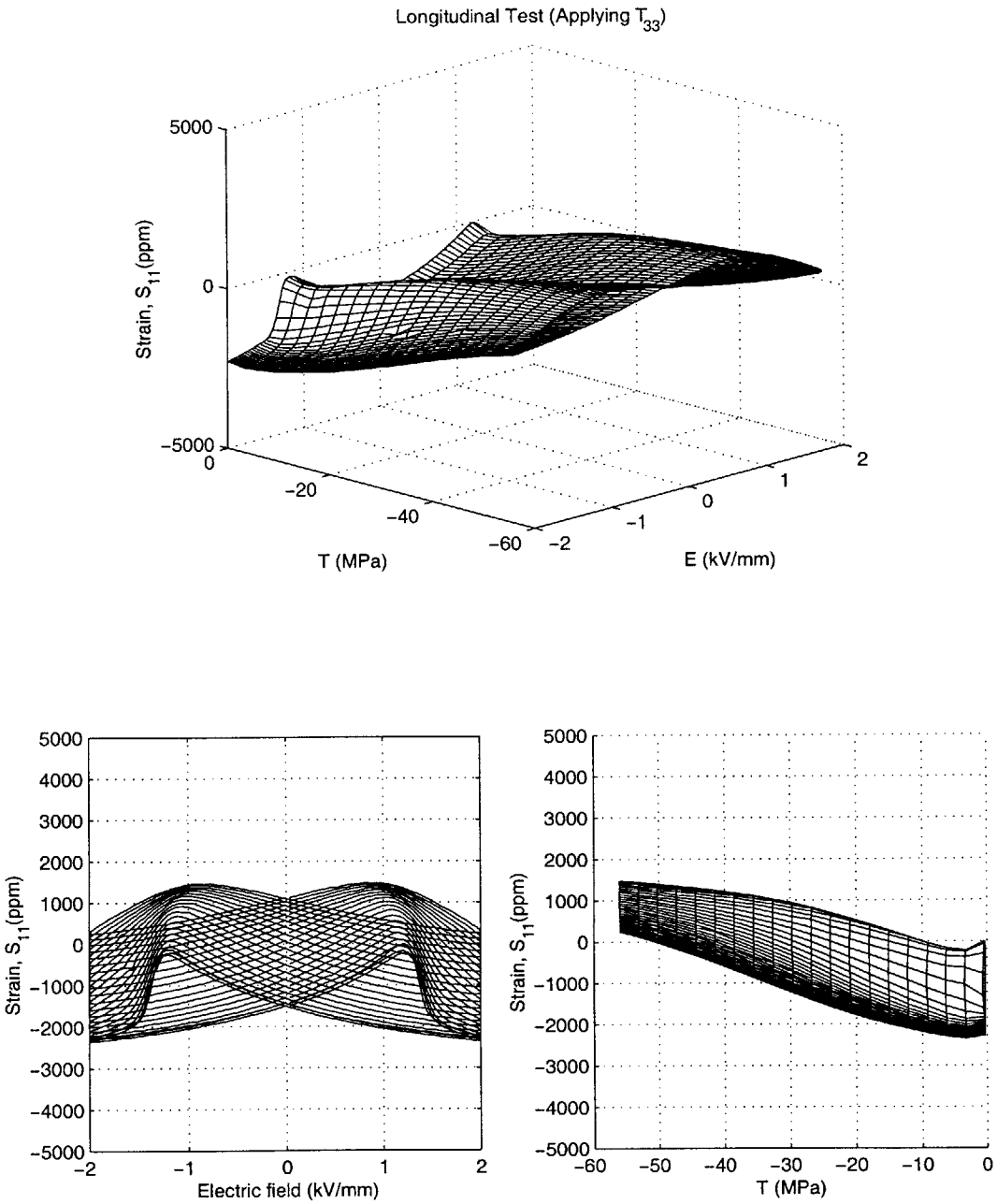

Figure 2-55: The data of repolarizing PZT-5A (Batch B) material behavior under longitudinal compression test (up to 56MPa).

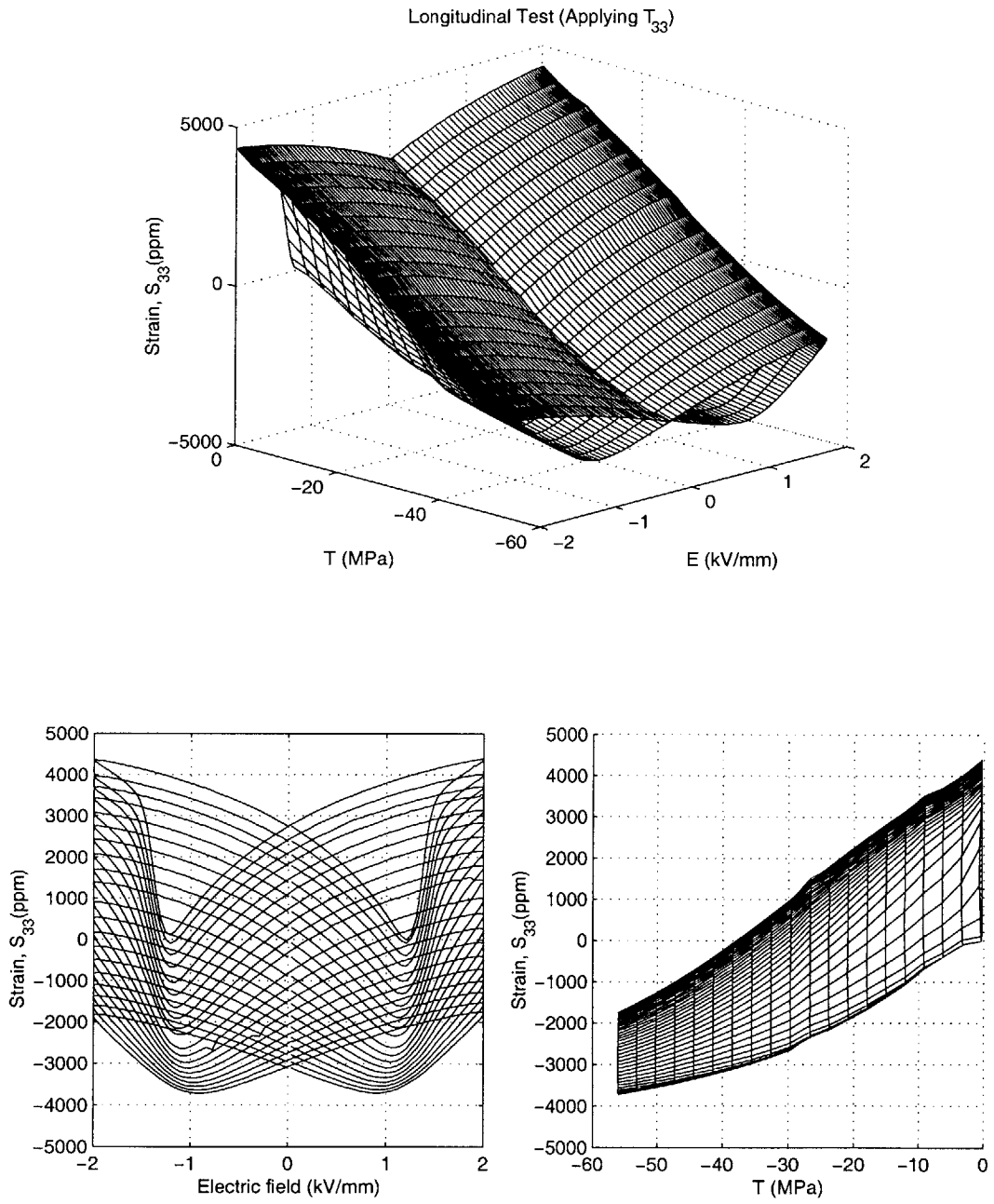

Figure 2-56: The data of repolarizing PZT-5A (Batch B) material behavior under longitudinal compression test (up to 56MPa).

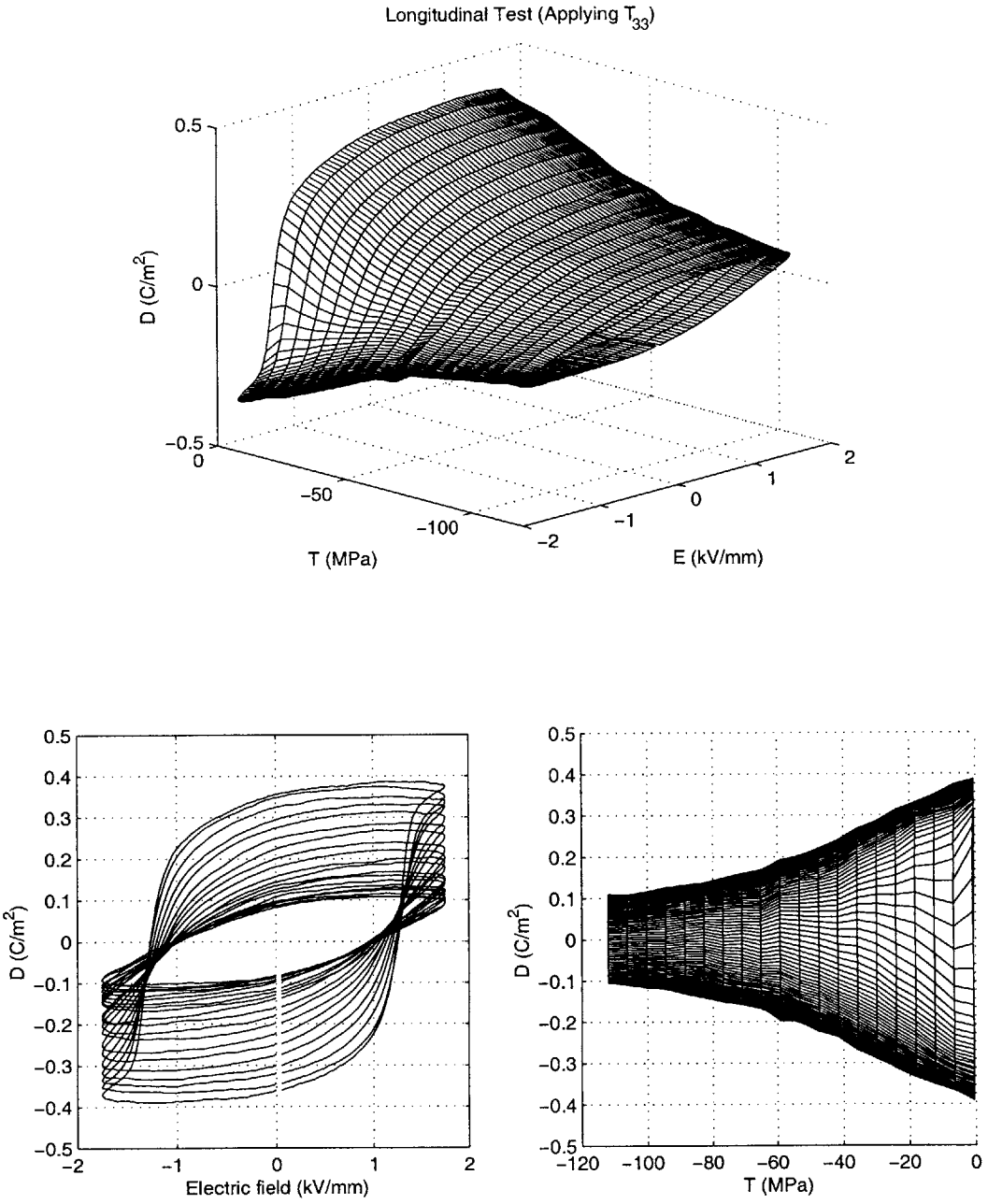

Figure 2-57: The data of repolarizing PZT-5A (Batch B) material behavior under longitudinal test with higher compression (up to 112MPa).

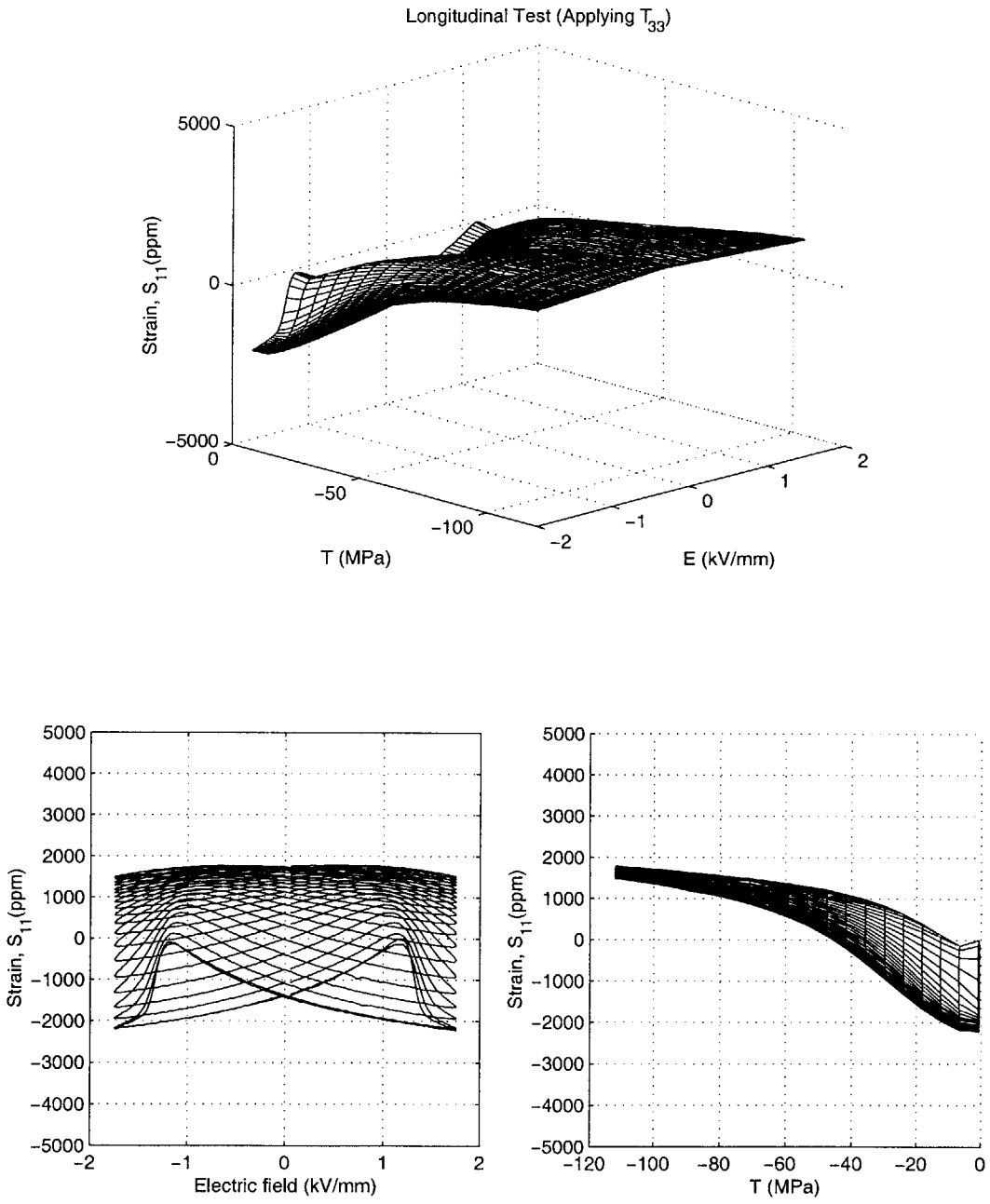

Figure 2-58: The data of repolarizing PZT-5A (Batch B) material behavior under longitudinal test with higher compression (up to 112MPa).

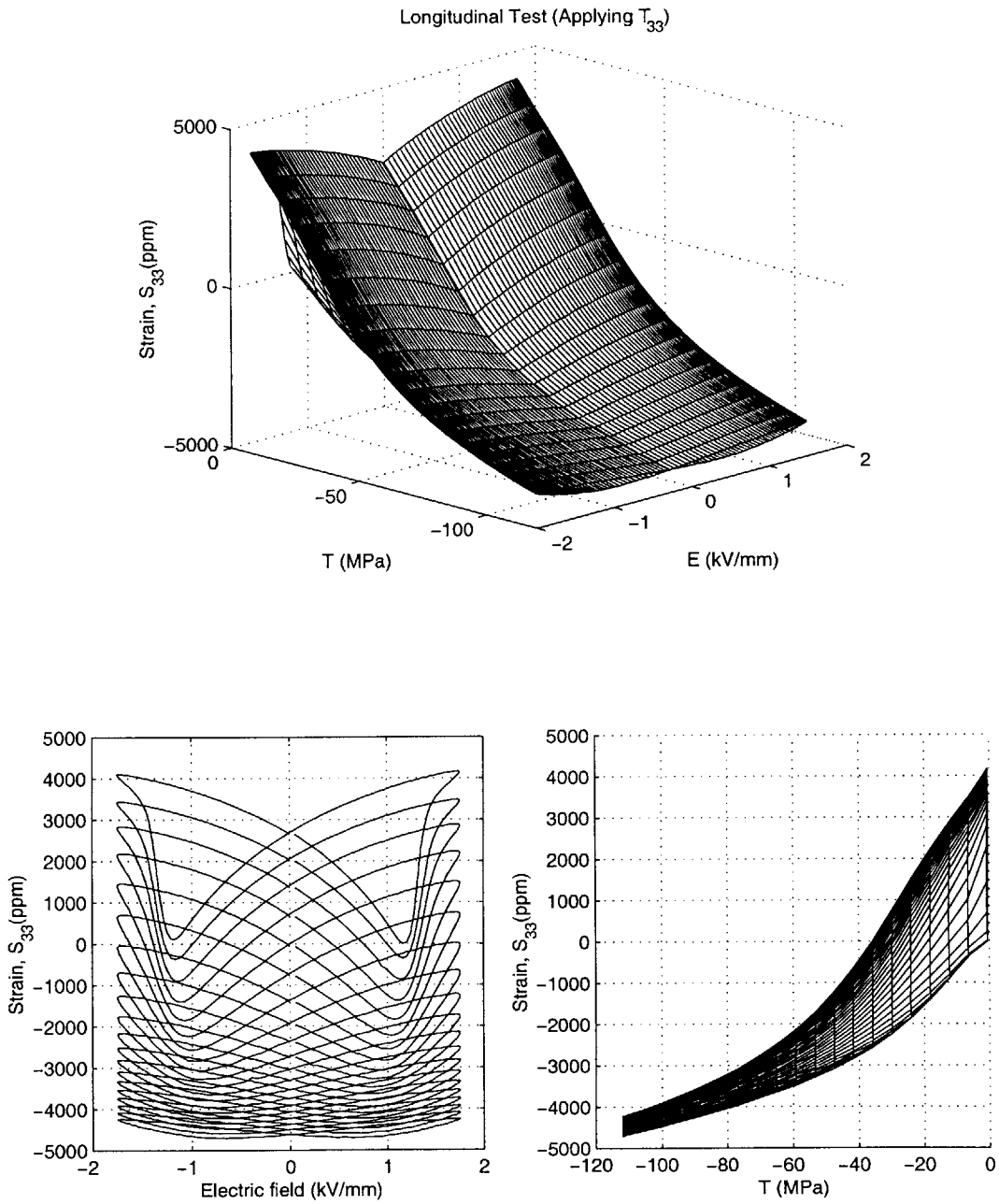

Figure 2-59: The data of repolarizing PZT-5A (Batch B) material behavior under longitudinal test with higher compression (up to 112MPa).

2.5 Summary of Important Material Characteristics

Four major phenomena, electric field dependency, rate dependency, stress dependency, and material composition dependency, have been observed in this chapter. What follows is a summary of these important material characteristics.

Electric Field Dependency

The actuation strongly depends nonlinearly upon the driving level of electric field. In addition, the polarization and strain response show serious hysteresis under high amplitude electric excitation.

Rate Dependency

The rate dependency of piezoelectric materials was found in two conditions. One is the residual actuation caused by varying compression duration (i.e. stress rate); the other is the expansion of butterfly curves and P-E loops caused by higher driving electric field (i.e. electric rate). However, the generalized piezoelectric constants for energy harvesting do not show significant frequency dependency.

Stress Dependency

Compression parallel to the poling direction suppresses the growth of dipoles at high electric field. This makes the butterfly curves or P-E loops look flat at high compression. In addition to electric field, stress field is also a major factor of material nonlinear behavior.

Hard vs. Soft Materials

The difference between hard and soft materials includes: (a) hard material has smaller piezoelectric constant d_{33}, and (b) hard materials tend to have higher coercive field.

It is the goal of this thesis to model these phenomena as accurately as possible. In the next chapter, currently available material models in the literature will be reviewed to examine whether these material models can well predict the material behaviors observed in this chapter. A new model will be developed to improve the accuracy of these models.

Chapter 3

Development of Material Model

The primary objective of this thesis work is to obtain the state equations for the material (constitutive relations) that relate the variables strain (S), stress (T), electric field (E), and electric displacement (D). For instance, the constitutive equations can be written as:

$$\mathbf{D} = \mathbf{D}(\mathbf{E}, \mathbf{T}), \tag{3.1}$$

$$\mathbf{S} = \mathbf{S}(\mathbf{E}, \mathbf{T}). \tag{3.2}$$

In addition to electric and stress fields, the desired model has to be able to simulate the rate dependent material response, as discussed in the previous chapter. To reach this goal, the most advanced material models in the literature will be first examined in this chapter to see whether they meet the requirement of the desired models. After finding the shortcomings of these models, a new model will also be developed in this chapter by improving upon these models.

3.1 Literature Review of Material Models

Two major categories of piezoelectric material models have been proposed since two decades ago. One was based on thermodynamic potentials; the other was based on the phenomenological observation of material response. In this section, a phenomenogical model by Soukhojak and Chiang[2] will first be discussed and followed by an introduction to the theory of thermodynamics. At the end, two thermodynamically consistent models by Devonshire[59] and Ghandi[35] will be examined.

3.1.1 Model by Soukhojak and Chiang

Soukhojak and Chiang expanded Chen and Montgomery's model for anti-ferroelectrics and elasto-ferroelectrics. It is assumed that the total polarization P can be categorized into P_d, the dielectric polarization, and P_F, the polarization due to ferroelectric domain switching:

$$P = P_d + P_F. \tag{3.3}$$

The dielectric polarization accounts for the dynamic hysteresis, while polarization due to ferroelectric domain switching accounts for the static hysteresis. Equilibrium dielectric polarization is given by an odd function of the electric field

$$P_{d,e} = P_{sat} tanh\left(\frac{E}{E_0}\right), \tag{3.4}$$

where P_{sat} is the saturation of polarization, and E_0 is the normalization field. The change rate of dielectric polarization is given by

$$\frac{dP_d}{dt} = \frac{1}{\tau_d}(P_{d,e} - P_d), \tag{3.5}$$

where τ_d is the dielectric time constant. Equations 3.4 and 3.5 solve for P_d as a function of E. Figure 3-1 shows the dielectric polarization as a function of sinusoidal electric field E driving at different frequencies, assuming τ_d=5ms.

Polarization due to ferroelectric switching is given by

$$P_F = nP_s, \tag{3.6}$$

where P_s is the spontaneous polarization, and n is the net fraction of dipoles pointing "up":$-1 \leq n \leq 1$. This parameter exhibits a static hysteresis. The rate equation for n is given by

$$\frac{dn}{dt} = \frac{\beta - n|\beta|}{\tau_{sw}}, \tag{3.7}$$

where β is the ferroelectric domain switching function. β can be expressed analytically as

$$\beta = tanh^3\left(\frac{E}{E_c}\right)^{2m-1}, \tag{3.8}$$

where E_c is the coercive field and m is a positive integer that characterizes the abruptness of the switching function β in the vicinity of E_c. Equations 3.7 and 3.8 solve for the dynamics

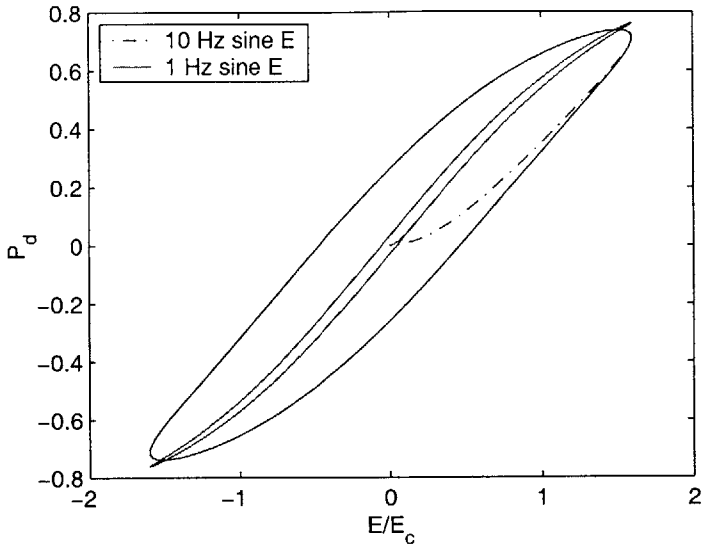

Figure 3-1: The dielectric polarization as a function of sinusoidal electric field E at different frequencies, assuming τ_d= 5ms in Soukhojak's model.

of n as a function of E. Figure 3-2 shows the net fraction of polarization as a function of the sinusoidal electric field E at different frequencies, assuming τ_{sw}=5ms.

Figure 3-3 shows the total polarization as a function of sinusoidal electric field E at different frequencies, assuming τ_{sw}=0.5ms and τ_d=1ms. As can be seen, the model is able to capture the hysteresis of polarization. It can also capture the expansion of polarization at high frequency. However, it is difficult to apply a three dimensional model using this frame work.

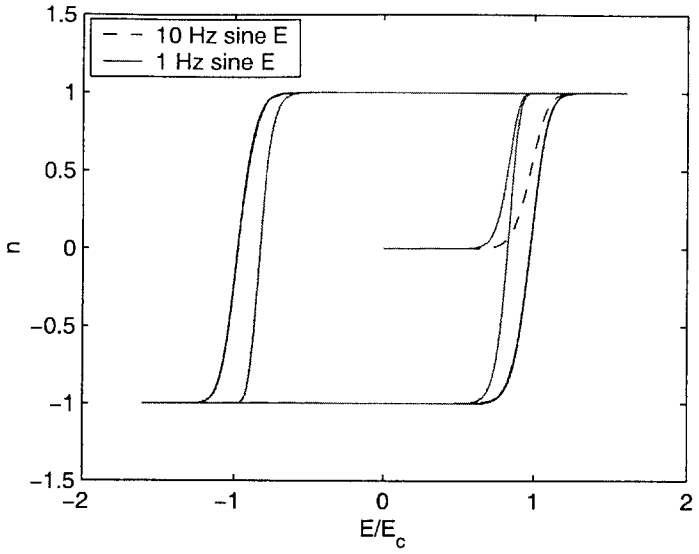

Figure 3-2: The net fraction of polarization as a function of sinusoidal electric field E at different frequencies, assuming τ_{sw}= 5ms in Soukhojak's model.

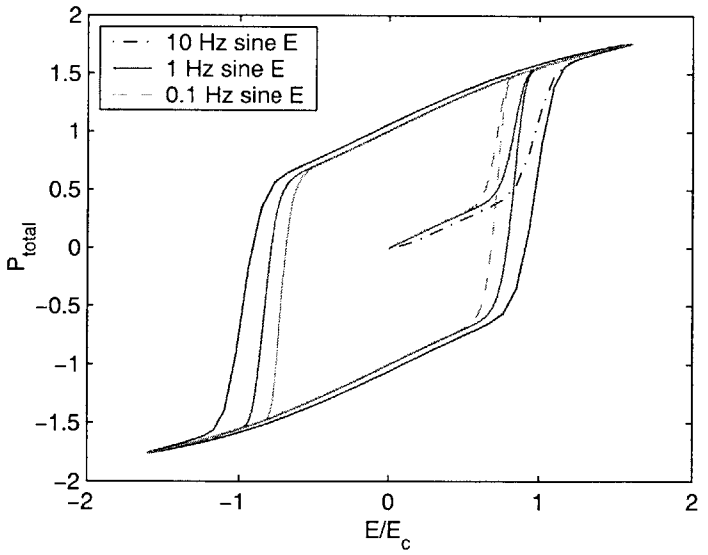

Figure 3-3: The total polarization as a function of sinusoidal electric field E at different frequencies, assuming τ_{sw}= 0.5ms and τ_d= 1ms in Soukhojak's model.

3.1.2 Introduction to Thermodynamic Potential

One can express thermodynamic potentials for the material in terms of any 3 independent variables selected from the conjugate pairs $(\mathbf{S}, \mathbf{T})$, $(\mathbf{D}, \mathbf{E})$, and (σ, θ). Eight possible representations of thermodynamic potentials are listed in Table 3.1. The variables temperature (θ) and entropy (σ) have been included in the list for completeness. They are relevant when the material response is a function of temperature. Selection of the thermal properties (σ, θ) depends on the whether an isothermal or adiabatic condition is considered. In this thesis work, all the tests and models are based on the isothermal condition (i.e. constant θ). To simplify the remaining discussion, the terms associating θ and σ are dropped from the energy expression.

Table 3.1: Thermodynamic potentials

Internal Energy	$dU = \theta d\sigma + \mathbf{T}d\mathbf{S} + \mathbf{E}d\mathbf{D}$
Enthalpy	$dH = \theta d\sigma - \mathbf{S}d\mathbf{T} - \mathbf{D}d\mathbf{E}$
Elastic enthalpy	$dH1 = \theta d\sigma - \mathbf{S}d\mathbf{T} + \mathbf{E}d\mathbf{D}$
Electric enthalpy	$dH2 = \theta d\sigma + \mathbf{T}d\mathbf{S} - \mathbf{D}d\mathbf{E}$
Helmholtz free energy	$dA = -\sigma d\theta + \mathbf{T}d\mathbf{S} + \mathbf{E}d\mathbf{D}$
Gibbs free energy	$dG = -\sigma d\theta + \mathbf{S}d\mathbf{T} - \mathbf{D}d\mathbf{E}$
Elastic Gibbs energy	$dG1 = -\sigma d\theta + \mathbf{S}d\mathbf{T} + \mathbf{E}d\mathbf{D}$
Electric Gibbs energy	$dG2 = -\sigma d\theta + \mathbf{T}d\mathbf{S} - \mathbf{D}d\mathbf{E}$

From each energy function listed in Table 3.1, a set of constitutive relations can be obtained. For instance, given H as a function of the state variables $(\mathbf{T}, \mathbf{E})$, one can obtain the constitutive relations:

$$\mathbf{S} = \frac{\partial H}{\partial \mathbf{T}}. \qquad \mathbf{D} = \frac{\partial H}{\partial \mathbf{E}}. \tag{3.9}$$

These constitutive relations obtained from thermodynamic potentials satisfy the Maxwell relation:

$$\frac{\partial \mathbf{S}}{\partial \mathbf{E}} = \frac{\partial \mathbf{D}}{\partial \mathbf{T}}. \tag{3.10}$$

Formulating a nonlinear model using arbitrary expressions for $\mathbf{T}(\mathbf{S}, \mathbf{D})$ and $\mathbf{E}(\mathbf{S}, \mathbf{D})$ may lead to a system which violates the Maxwell relations and hence the first law of thermodynamics.

The selection of different thermodynamic potentials listed in Table 3.1 depends on the choice of independent variables. Since only isothermal conditions are of interest in this

thesis work, only 4 thermodynamic potentials are possible. Ghandi[35] summarized how these various forms of thermodynamic potentials can be used.

If the strain $\mathbf{S}$ and electric field $\mathbf{E}$ are chosen as independent state variables, electric Gibbs energy G_2 is the appropriate form of thermodynamic potential and results in the constitutive relations:

$$\mathbf{T} = \frac{\partial G_2}{\partial \mathbf{S}}, \qquad \mathbf{D} = -\frac{\partial G_2}{\partial \mathbf{E}}. \tag{3.11}$$

This form is useful for a conventional finite element model that utilizes nodal displacement and voltage degrees of freedom. In such an approach, the strain and electric field are computed from the nodal degrees of freedom. The material model is then used to compute the stress and electric displacement in the material.

If the strain $\mathbf{S}$ and electric displacement $\mathbf{D}$ are chosen as independent state variables, the Helmholtz free energy A is the appropriate form of thermodynamic potential and results in the constitutive relations:

$$\mathbf{T} = \frac{\partial A}{\partial \mathbf{S}}, \qquad \mathbf{E} = \frac{\partial A}{\partial \mathbf{D}}. \tag{3.12}$$

This form is useful for material modeling since electric displacement is the state variable linked directly to the polarization in the material.

If the stress $\mathbf{T}$ and electric field $\mathbf{E}$ are chosen as independent state variables, the Gibbs energy G is the appropriate form of thermodynamic potential and results in the constitutive relations:

$$\mathbf{S} = -\frac{\partial G}{\partial \mathbf{T}}, \qquad \mathbf{D} = -\frac{\partial G}{\partial \mathbf{E}}. \tag{3.13}$$

This form is useful for material testing since it is in general easier to apply a uniaxial stress than a uniaxially constrained strain on a specimen. In addition, using this form, one can test the specimen under voltage control.

If the stress $\mathbf{T}$ and electric displacement $\mathbf{D}$ are chosen as independent state variables, elastic Gibbs energy G_1 is the appropriate form of thermodynamic potential and results in the constitutive relations:

$$\mathbf{S} = -\frac{\partial G_1}{\partial \mathbf{S}}, \qquad \mathbf{E} = \frac{\partial G_1}{\partial \mathbf{D}}. \tag{3.14}$$

This form is useful for material testing if the specimen is tested under current control instead of voltage control.

3.1.3 Thermodynamically Consistent Model

Denvonshire Single Crystal Model

From Section 3.1.2, it is known that constitutive equations can be derived from thermodynamic potentials. The question is how to obtain these energy expansions such that the material behavior can be well-presented by these constitutive relations.

Devonshire presented the first 1-D energy based model for repolarization in single domain crystal ferroelectrics[59]. The free energy is expanded in terms of polynomials of the electric displacement:

$$A = -\frac{1}{2}\alpha D^2 + \frac{1}{4}\beta D^4, \tag{3.15}$$

where α and β are material constants. Two local minima can be found in this potential as a function of electric displacement. These correspond to two possible states of spontaneous polarization. Under an applied electric field, equilibrium is achieved when

$$dA - dW = 0, \qquad dW = EdD. \tag{3.16}$$

This is the first law of thermodynamics, where EdD represents the work done by an applied electric field in causing a change in electric displacement. Equivalently, it can be stated that the system is at equilibrium whenever the energy $A - ED$ is at a local minimum.

Figure 3-4 shows plots of $A - ED$ at different electric fields. As the electric field E is increased, the location of the local minima changes corresponding to a change in the electric displacement of the system. As E is increased beyond a critical level, the system undergoes a phase transition. In other words, the spontaneous polarization of the material changes. If these local minima are plotted as a function of the applied electric field E, as shown in Figure 3-5, one can obtain the electric constitutive relation. This electric constitutive relation can be also obtained by differentiating Eq. 3.15 according to 3.12:

$$E = -\alpha D + \beta D^3. \tag{3.17}$$

To study the mechanical response, one can include the elastic energy in terms of strain S into the free energy expansion:

$$A = \frac{1}{2}cS^2 - hSD^2 - \frac{1}{2}\alpha D^2 + \frac{1}{4}\beta D^4, \tag{3.18}$$

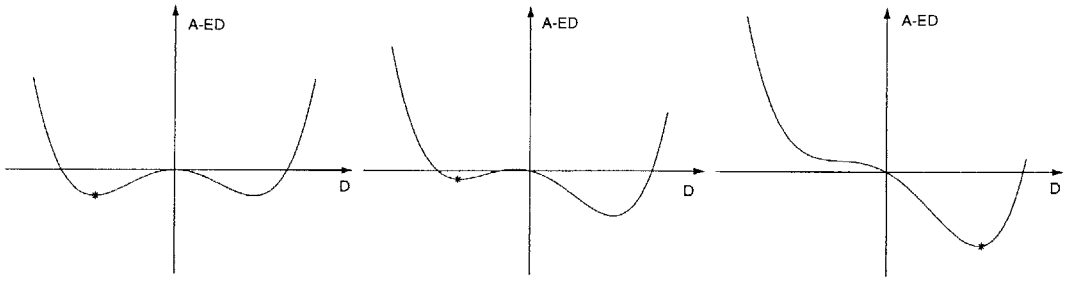

Figure 3-4: Potentials of a ferroelectric material proposed by Devonshire.

[h]

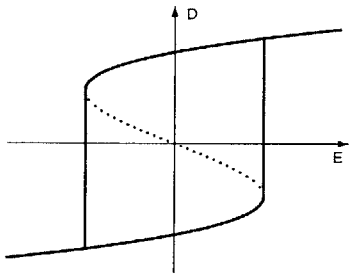

Figure 3-5: Electric constitutive relations. Dotted line indicates the portions of the curve which are thermodynamically unstable.

where the first term represents the elastic energy, and the second term considers the electromechanical coupling. Using this energy expansion, one can obtain the mechanical constitutive relation by differentiating Eq. 3.18 according to Eq. 3.12:

$$T = cS - hD^2. \tag{3.19}$$

Rewriting this equation as

$$S = (T + hD^2)/c, \tag{3.20}$$

and combining with Eq. 3.17 yields

$$E = -(2T/c + \alpha)D + (\beta - 2h/c)D^3. \tag{3.21}$$

Using Eq. 3.20 and 3.21, one can visualize the stress dependence in Figure 3-6. As expected, the applied stress produces a change in the coercive field and the magnitude of the polarization. The applied stress also changes the strain level due to the elasticity of the material.

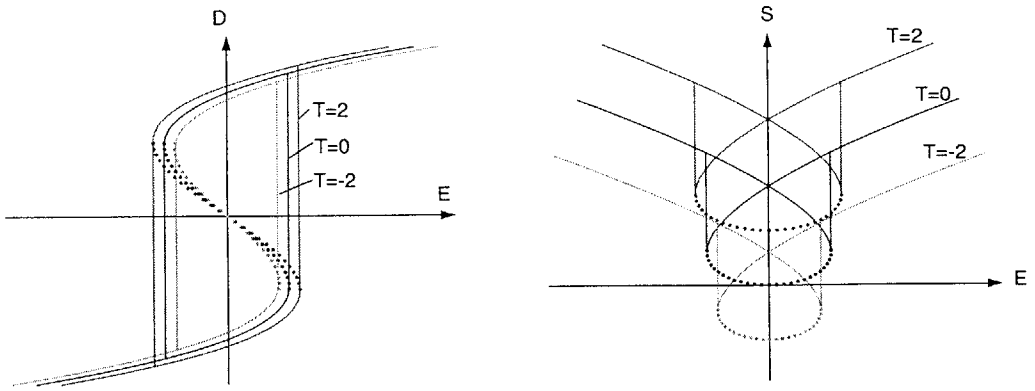

Figure 3-6: Stress dependence of material response using Devonshire model. Dotted line indicates the portions of the curve which are thermodynamically unstable.

Ghandi and Hagood

In general, a polycrystalline piezoelectric can be considered as an assembly of an infinite number of small single domains with randomly oriented polarization. Using this assumption, Chan[60] developed a multiple family model based on Devonshire's single crystal model. One can imagine that quite a few families are required to produce a smooth response in the three-dimensional case. Performing this kind of computation for multiple families for each individual domain is very expensive.

To reduce the computational load, an approximation by Ghandi[35] is used to represent the response of a polycrystalline model. A thermodynamic potential of Helmholtz free energy is first assumed to have the form

$$G_1 = 5D^4 + 10(\Delta D)^2, \tag{3.22}$$

where

$$\Delta D = D - D^*,$$

D is the electric displacement, and D^* is an internal variable representing the net remnant polarization. According to Eq. 3.14, the electric field can then be presented

$$E = \frac{\partial G_1}{\partial D}, \tag{3.23}$$

or

$$E = 20D^3 + 20\Delta D. \tag{3.24}$$

To determine the polarization state, the repolarization rule has to be used:

$$\begin{aligned} &\text{if } |\Delta D| < \Delta D_c, \\ &{}^{t+\Delta t}D^* = {}^{t}D^*, \\ &\text{if } |\Delta D| > \Delta D_c, \\ &{}^{t+\Delta t}D^* = {}^{t}D^* + \Delta D\left(1 - \frac{\Delta D_c}{|\Delta D|}\right), \end{aligned} \tag{3.25}$$

where

$$\Delta D = {}^{t+\Delta t}D - {}^{t}D^*,$$

ΔD_c is the magnitude of the critical difference between the electric displacement and the net remnant polarization. This critical value ΔD_c governs the hysteretic behavior of the system. The response of the system is assumed to be reversible if

$$|\Delta D| < \Delta D_c. \tag{3.26}$$

That is, no repolarization occurs under these conditions. In contrast the system is assumed to undergo repolarization when

$$|\Delta D| = \Delta D_c. \tag{3.27}$$

$|\Delta D| > \Delta D_c$ is considered to be inadmissible. ΔD_c is assumed to be constant. The nonlinear repolarizing system described by Eq. 3.22 and 3.25 can be solved using Newton-Raphson iteration. Figure 3-7 shows the electric displacement and net spontaneous polarization for different ΔD_c. As expected, higher ΔD_c results in expansion of polarization and higher coercive fields.

Although this model captures most of the important phenomena of piezoelectric ceramics, the evolution rule using discrete time step makes it difficult to implement the rate dependence in the model. In addition, due to the discrete time model, it is also difficult to obtain smooth response at the repolarizing region.

3.2 Development of a 1-D Rate and Stress Dependent Piezoelectric Model

The primary goal of this thesis is to develop a rate dependent nonlinear material model based on consistent thermodynamic potentials. The frame work of this material model evolves

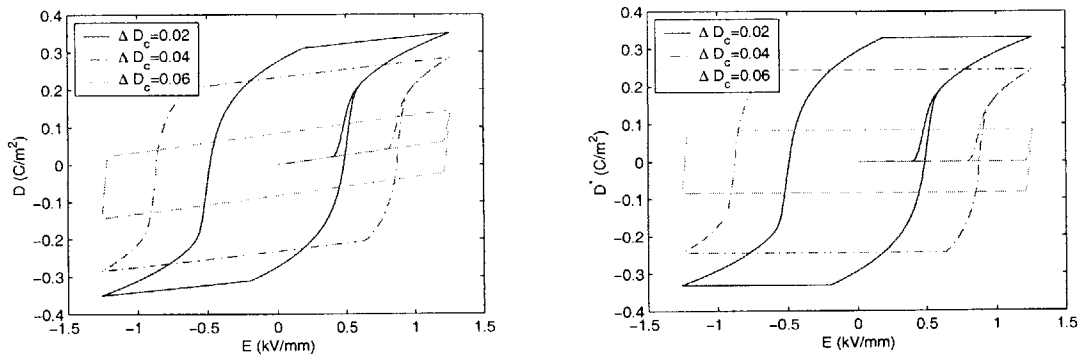

Figure 3-7: The simulated polarization using Ghandi's model

from Ghandi's model and the Weibull probabilistic function. This section will first discuss the assumption of electric conduction effect and then present the derivation of the model in 1-D example. A rate rule mechanism will be introduced to describe the hysteretic behavior of the material. The whole model can also be simplified as a system of differential-algebraic equations (DAE).

3.2.1 Assumption of Electric Conduction Effect

It is important to clarify the conduction effect before developing the material model. A piezoelectric material is not a perfect dielectric material. In other words, the material may be conductive. As shown in Figure 3-8, a piezoelectric material can be simulated by a nonlinear capacitor C_p and a nonlinear resistor R connected in parallel. The conduction through the resistor R may influence the material behavior depending on whether the driving condition is voltage source or charge source control.

Voltage Control vs. Charge Control

An example of voltage control includes the tests for actuation and model development conducted in Section 2.4. In these tests, the specimen is excited by the controlled voltage source from power amplifier. The power amplifier will supply enough current or charge to maintain the voltage commanded by users. Under this voltage source control, the voltage across the specimen is independent of I_r, the current in resistor R. In addition, it is

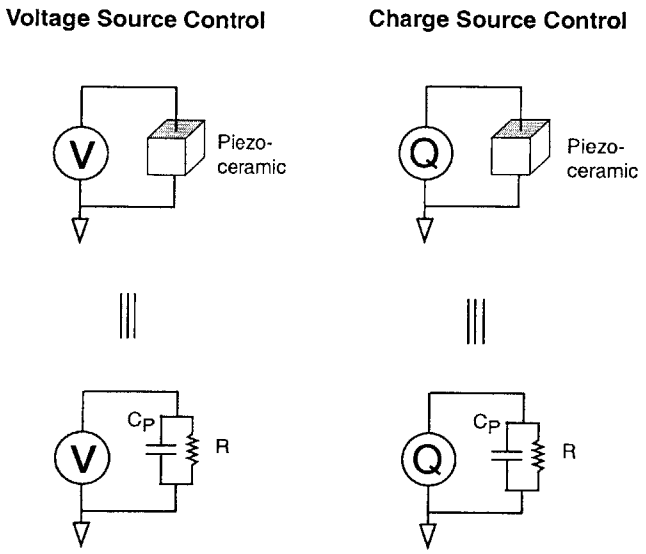

Figure 3-8: Equivalent circuitry of piezoelectric ceramics under voltage source control (left) and charge source control (right).

reported [53] that the volume resistivity is larger than $10^{11}\Omega$M and the time constant is about 2000 seconds assuming the relative dielectric constant($\epsilon_{33}^T/\epsilon_0$) is 3400. This implies that the impedance of R is relatively large compared to dielectrics at frequencies above 0.1Hz at which the rate dependent tests were performed in Section 2.4. Consequently, the conduction effect can be neglected in this thesis work as the specimen is under voltage source control.

In contrast, the voltage across the specimen varies with R if the material is under limited charge source control. Some of the charge will be dissipated in resistor R. This dissipation will cause the voltage to drop. The energy harvester is a good example of charge source control. The finite charge source generated by external compression in the specimen may be dissipated via the conduction. Another example is the active fiber composite shown in Figure 3-9. The piezoelectric fibers are essentially under control of a limited charge source dielectrically generated on the epoxy-fiber interface. In such case, the conduction of the piezoelectric material is important to the overall response of the AFC. This effect has been studied by Harper[36].

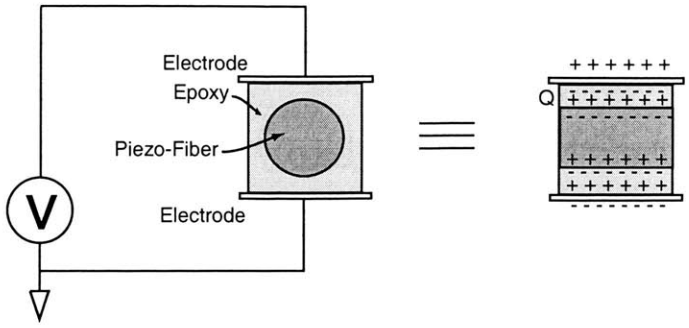

Figure 3-9: Non-contact electrode of AFC makes its piezoelectric fiber under charge source control.

Conclusion

Based on the above arguments, the conduction effect can be neglected in the following discussion of the material model because the model will be developed from the observation of material response under voltage source control. In the case when the driving condition is under charge control, a linear conduction model can be used to supplement the non-conduction material model.

3.2.2 Probabilistic Effect

In Ghandi's model, Equation 3.25 implies that all the dipoles in polycrystalline ceramics repolarize at the same time when $|\Delta D| \geq \Delta D_c$. This simultaneous response can be described using the probability density function and the cumulative probability density function shown in Figure 3-10. With help of this interpretation, one can easily imagine that in practice not all the dipoles in a polycrystalline piezoelectric ceramics will respond to the applied electric field at the same time. Based on this assumption, one can further assume that the reaction of dipoles has a Weibull distribution[61] with respect to ΔD: [1]

$$f(\Delta D) = \frac{\alpha}{\Delta D_c}\left(\frac{\Delta D}{\Delta D_c}\right)^{\alpha-1} exp\left[-\left(\frac{\Delta D}{\Delta D_c}\right)^{\alpha}\right], \text{ for } \Delta D \geq 0, \tag{3.28}$$

[1] Although the Weibull function represents an unsymmetric distribution, it is easier to use the Weibull distribution instead of the normal distribution because of the existence of a closed form of the cumulative Weibull distribution.

where α is a distribution shape parameter. As $\alpha \rightarrow \infty$, the distribution becomes a impulse function, and the cumulative function of the Weibull distribution

$$F(\Delta D) = 1 - exp\left[-\left(\frac{\Delta D}{\Delta D_c}\right)^{\alpha}\right], \text{ for } \Delta D \geq 0 \tag{3.29}$$

becomes a step function. Figure 3-11 shows the Weibull probability density function and the Weibull cumulative probability density function as a function of ΔD for various α.

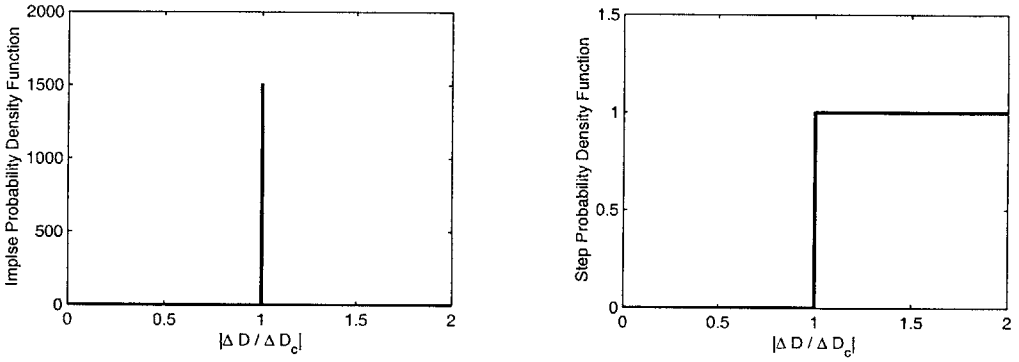

Figure 3-10: Probability density function (left) and cumulative probability density function (right).

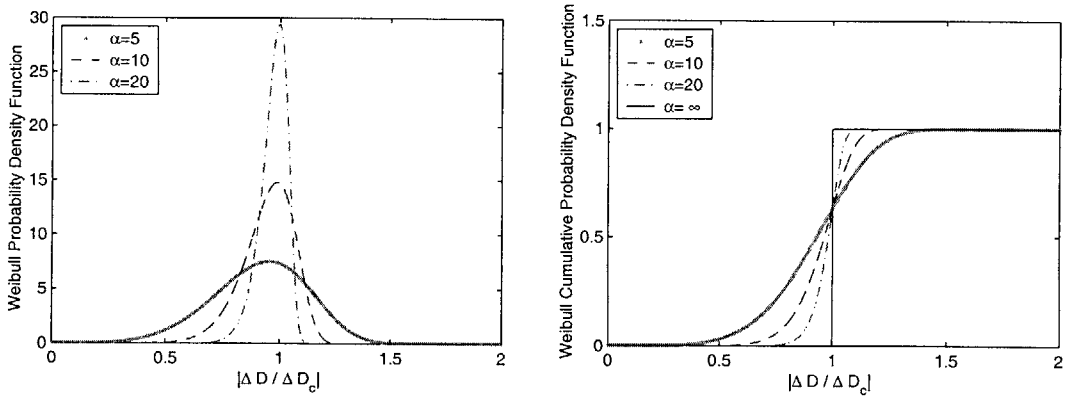

Figure 3-11: Weibull probability density function (left) and its cumulative probability density function (right).

As a consequence, the repolarizing rule, Equation 3.25, can be modified as

$$^{t+\Delta t}D^* = ^t D^* + \Delta D\left(1 - \frac{\Delta D_c}{|\Delta D|}\right)\left\{1 - exp\left[-\left(\frac{|\Delta D|}{\Delta D_c}\right)^{\alpha}\right]\right\}. \tag{3.30}$$

To eliminate the singularity at $\Delta D = 0$ and for convenience, it is desirable to rewrite Equation 3.30 as

$$\Delta D^* = ^{t+\Delta t} D^* - ^t D^* = [\Delta D - sign(\Delta D)\Delta D_c]\left\{1 - exp\left[-\left(\frac{|\Delta D|}{\Delta D_c}\right)^{\alpha}\right]\right\}. \tag{3.31}$$

However, this equation is still not valid because the term $[\Delta D - sign(\Delta D)\Delta D_c]$ has the opposite sign to ΔD when $\Delta D < \Delta D_c$. This was not a problem for Ghandi's original model because ΔD is 0 when $\Delta D < \Delta D_c$. In order to fix this problem, the simplest way is to modify Equation 3.31 as

$$\Delta D^* = ^{t+\Delta t} D^* - ^t D^* = \Delta D\left\{1 - exp\left[-\left(\frac{|\Delta D|}{\Delta D_c}\right)^{\alpha}\right]\right\}. \tag{3.32}$$

Note that the term $\Delta D\left(1 - \frac{\Delta D_c}{|\Delta D|}\right)$ in Equation 3.30 has been simply replaced by ΔD. This simplification may, to some extent, change the characteristics of the original evolution rule (Eq. 3.25), but the difference between Eq.3.25 and 3.32 can be corrected by the parameters in the Weibull function. These parameters can be obtained by comparing the model and experimental data, as will be discussed later.

3.2.3 Rate and Stress Effects of Polarization

Rate Dependency

To account for the rate effect, Equation 3.32 can be modified as

$$\frac{dD^*}{dt} = \frac{\Delta D}{\tau}\left\{1 - exp\left[-\left(\frac{|\Delta D|}{\Delta D_c}\right)^{\alpha}\right]\right\}, \tag{3.33}$$

where τ is a time constant characterizing the change rate of the net remnant polarization D^*. This equation may not be perfect for differentiation because the derivative of the absolute function is not continuous. The purpose of this absolute function is to guarantee a behavior of an even function. As a result, Eq. 3.33 can be further modified by replacing the absolute function with an even function such as

$$\frac{dD^*}{dt} = \frac{\Delta D}{\tau}\left\{1 - exp\left[-\left(\frac{\Delta D}{\Delta D_c}\right)^{2\alpha}\right]\right\}, \tag{3.34}$$

where α now is a positive integer. Again, this modification will not affect the overall development of the model because all the parameters have not been determined yet.

Eq. 3.34 is the final version of the rate rule of the net remnant polarization D^*. This rate rule not only describes the material behavior in continuous time, but also considers the probabilistic response of the domains in polycrystalline ceramics. Using this rate rule and the constitutive relation (Eq. 3.24) derived from thermodynamic potential described in Eq. 3.22, one can well define the polarization response of piezoelectric materials. This system is a set of differential algebraic equations of index-1:

$$\begin{cases} \dot{D}^* = f(D, D^*), \\ 0 = g(D, D^*) - E, \end{cases} \tag{3.35}$$

which can be solved by a number of numerical software package, such as DASPK[46].

Stress Dependency

To model the stress effect of polarization, it is more appropriate to use the elastic Gibbs Energy, as discussed in Section 3.1.2. Adding elastic energy in Eq. 3.22, for instance, one can expand the energy function using Taylor's series in terms of D, D^*, and T:

$$\begin{aligned} G_1 \;=\; & (a_1 D + a_2 D^2 + a_3 D^3 + a_4 D^4 + a_5 D D^* + \ldots) \\ & -(b_0 + b_1 D + b_2 D^2 + b_3 D^3 + b_4 D^4 + b_5 D D^* + \ldots) T \\ & -(c_0 + c_1 D + c_2 D^2 + c_3 D^3 + c_4 D^4 + c_5 D D^* + \ldots) T^2 \\ & +\text{H.O.T.} \end{aligned} \tag{3.36}$$

where the coefficients of this expansion can be obtained by curve fitting to the data obtained in Section 2.4. The detailed procedure will be dicussed in the next section. Consequently, the system can be described using the rate rule (Eq.3.34), the corresponding electric constitutive relation, and the elastic constitutive relations

$$\begin{aligned} E = \frac{\partial G_1}{\partial D} \;=\; & (a_1 + 2a_2 D + 3a_3 D^2 + 4a_4 D^3 + a_5 D^* + \ldots) \\ & -(b_1 + 2b_2 D + 3b_3 D^2 + 4b_4 D^3 + b_5 D^* + \ldots) T \\ & -(c_1 + 2c_2 D + 3c_3 D^2 + 4c_4 D^3 + c_5 D^* + \ldots) T^2 \\ & +\text{H.O.T.} \end{aligned} \tag{3.37}$$

$$S = -\frac{\partial G_1}{\partial T} = (b_0 + b_1 D + b_2 D^2 + b_3 D^3 + b_4 D^4 + b_5 D D^* + \ldots) \\ 2(c_0 + c_1 D + c_2 D^2 + c_3 D^3 + c_4 D^4 + c_5 D D^* + \ldots) T \\ +\text{H.O.T.} \tag{3.38}$$

3.2.4 Parametric Study

Before finding the coefficients in Eq. 3.36, it is essential to investigate how the parameters in the rate rule (Eq. 3.34) influence the model. In addition, it is of interest to understand how the rate and stress affect the materials using this model. To do this in the simplest manner, the following coefficients are first assumed in Eq. 3.36:

$$a_2 = 1, \quad a_4 = 1, \quad a_5 = -2, \quad b_2 = 0.5, \quad c_0 = 0.1, \quad c_1 = 0.001, \tag{3.39}$$

and the others are assumed zero.

Effect of D^*

First it is of interest to see the effect of D^*, which is the major factor of piezoelectric hysteresis. If the rate change of D^* is zero, i.e.

$$\frac{dD^*}{dt} = 0, \tag{3.40}$$

the response shown in Figure 3-12 is non-hysteric as expected. This result can be compared to the hysteretic case where $\frac{dD^*}{dt}$ is not zero as described by Eq. 3.34.

Effect of α

Figure 3-13 shows the effect of α, assuming $f = 1$Hz, $T = 0$, $\Delta D_c = 0.6$, $\tau = 0.001$, and varying $\alpha = \{1,\ 2,\ \text{or}\ 3\}$. As expected from the characteristics of the Weibull function shown in Figure 3-11, the polarization in the beginning starts to increase earlier for smaller α because of the wider distribution for smaller α in Figure 3-11.

Effect of ΔD_c

Figure 3-14 shows the effect of ΔD_c, assuming $f = 1$Hz, $T = 0$, $\alpha = 1$, $\tau = 0.001$, and varying $\Delta D_c = \{0.2,\ 0.5,\ \text{or}\ 0.8\}$. As expected, the polarization in the beginning starts to increase earlier for smaller ΔD_c.

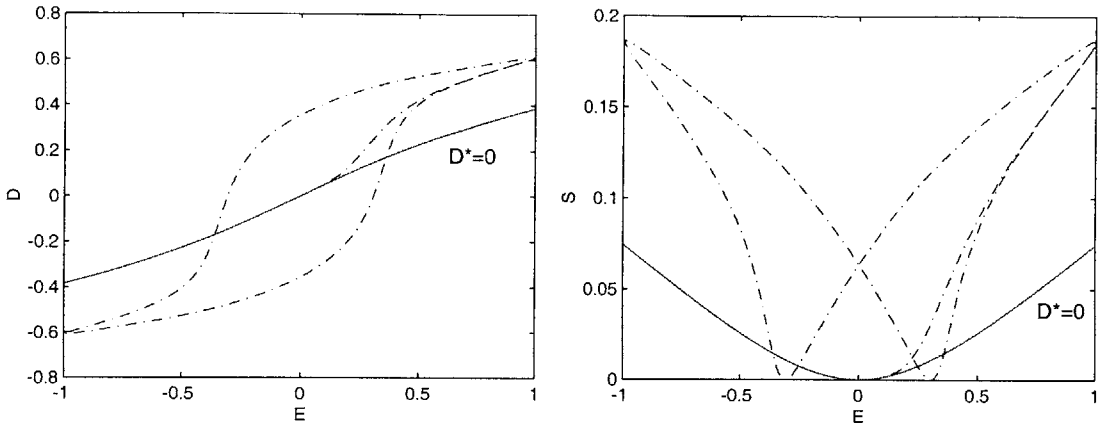

Figure 3-12: Effect of D^* on E-D and E-S relations, assuming $T = 0$ and $f = 1$ Hz. For non zero $D*$ case, $\Delta D_c = 0.5$, $\tau = 0.001$, and $\alpha = 1$ are used in Eq. 3.34.

Effect of τ

Figure 3-15 shows the effect of τ, assuming $f = 1$Hz, $T = 0$, $\Delta D_c = 0.5$, $\alpha = 1$, and varying $\tau = \{0.0005,\ 0.001,$ or $0.0015\}$. As can be seen, a larger time constant τ results in expansion of the polarization and strain response.

Effect of Frequency

Figure 3-16 shows the effect of frequency f, assuming $T = 0$, $\Delta D_c = 0.05$, $\alpha = 3$, $\tau = 0.0005$, and varying $f = \{0.1,\ 1,$ or $10\}$Hz. As can be seen, higher frequency f also results in expansion of the polarization and strain response. This correlates with the observation in Section 2.4.

Effect of Stress

Figure 3-17 shows the effect of T, assuming $f = 1$Hz, $\Delta D_c = 0.05$, $\alpha = 1$, $\tau = 0.001$, and varying $T = \{-1,\ 0,$ or $1\}$. As expected, the compressive stress results in flat polarization and strain response, which correlates with the behavior observed in Section 2.4. Although no experimental data of material in tension is available, the simulated response of material in tension shows reasonable stretch in polarization and strain.

Compared to the data observed in Section 2.4, the parametric study discussed above

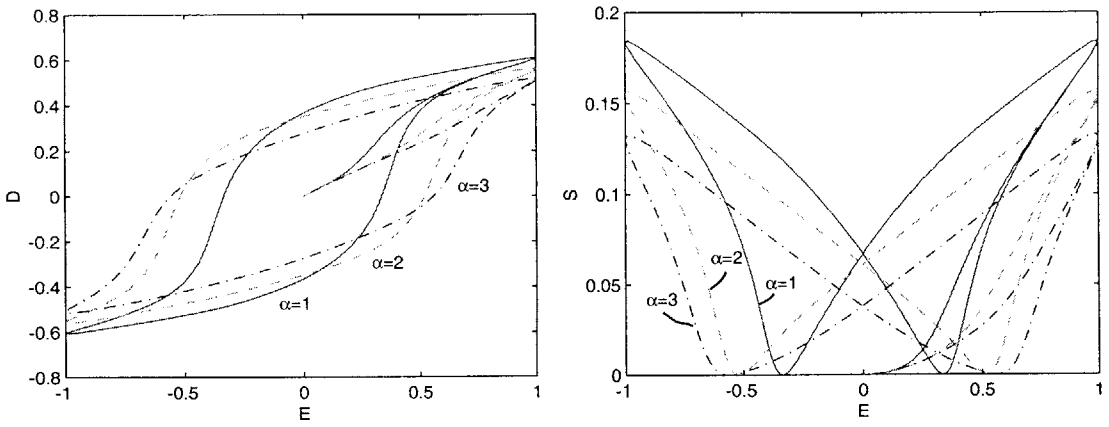

Figure 3-13: Effect of α on E-D and E-S relations, assuming $f = 1\text{Hz}$, $\Delta D_c = 0.6$, $T = 0$, $\tau = 0.001$, and varying $\alpha = \{1,\ 2,\ \text{or}\ 3\}$.

shows that the parameters ΔD_c, α, and τ in the rate rule (Eq.3.34) and the energy expansion (Eq.3.36) are sufficient to describe the rate and stress dependency as well as the major hysteretic behaviors of piezoelectric materials. The next step is to calibrate those coefficients in the energy expansion shown in Eq. 3.36 using a curve fitting technique such that the error between the model and data is minimized.

3.3 1-D Material Parameters

This section will demonstrate how to calibrate the parameters of the material model by fitting the model to the test data obtained in Section 2.4. The optimal parameters for PZT-5A and PZT-5H will be presented with the correlation of data and the model. For the purpose of understanding the mechanisms, the targeted precision is set within an order of magnitude, as discussed in Section 1.3

The parameters of the material model needing to be found include the rate parameters in Eq. 3.34 and the polynomial coefficients in the energy expansion. The polynomial coefficients can be found using standard least squares regression. Unfortunately, the rate parameters appear in the the system in a nonlinear fashion. No efficient algorithm is currently available to optimize these nonlinear parameters. As a result, an intensive simulation for different combinations of rate parameters has to be conducted, and the optimal rate pa-

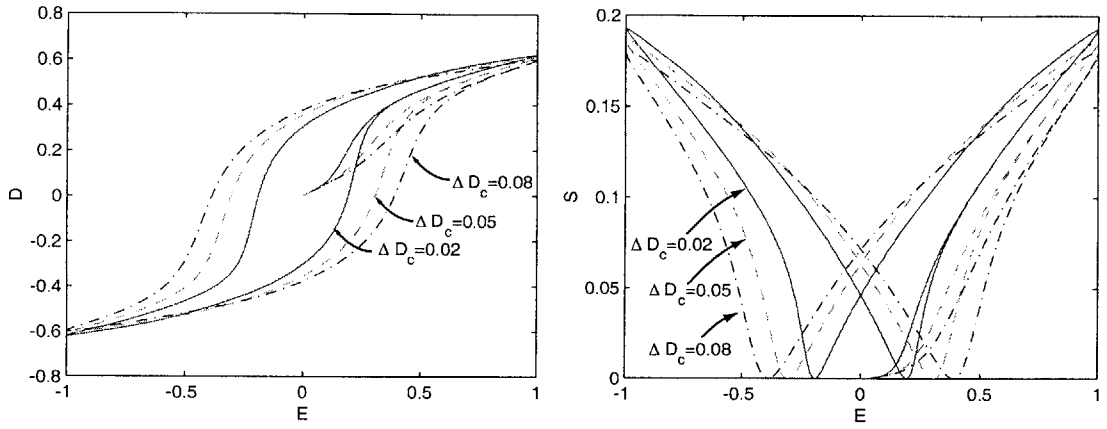

Figure 3-14: Effect of ΔD_c on E-D and E-S relations, assuming $f = 1$Hz, $T = 0$, $\alpha = 1$, $\tau = 0.001$, and varying $\Delta D_c = \{0.2,\ 0.5,$ or $0.8\}$.

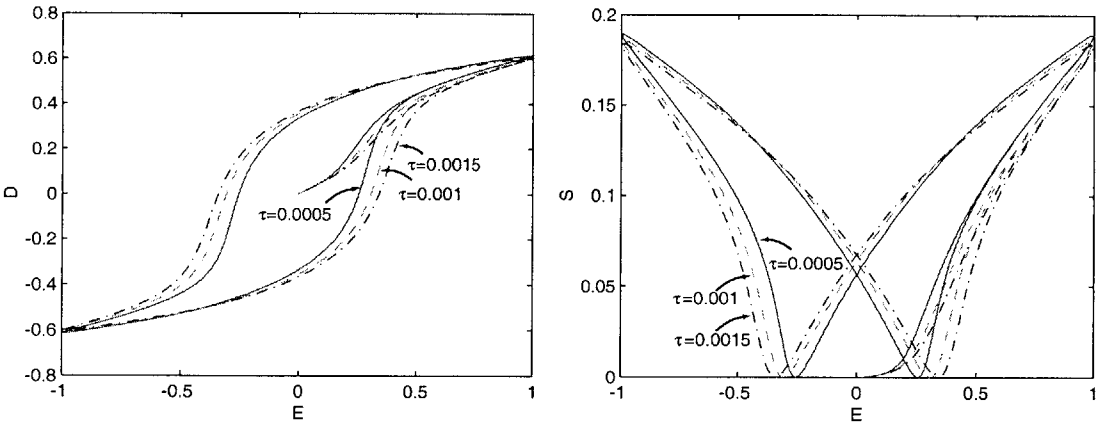

Figure 3-15: Effect of τ on E-D and E-S relations, assuming $f = 1$Hz, $T = 0$, $\Delta D_c = 0.5$, $\alpha = 1$, and varying $\tau = \{0.0005,\ 0.001,$ or $0.0015\}$.

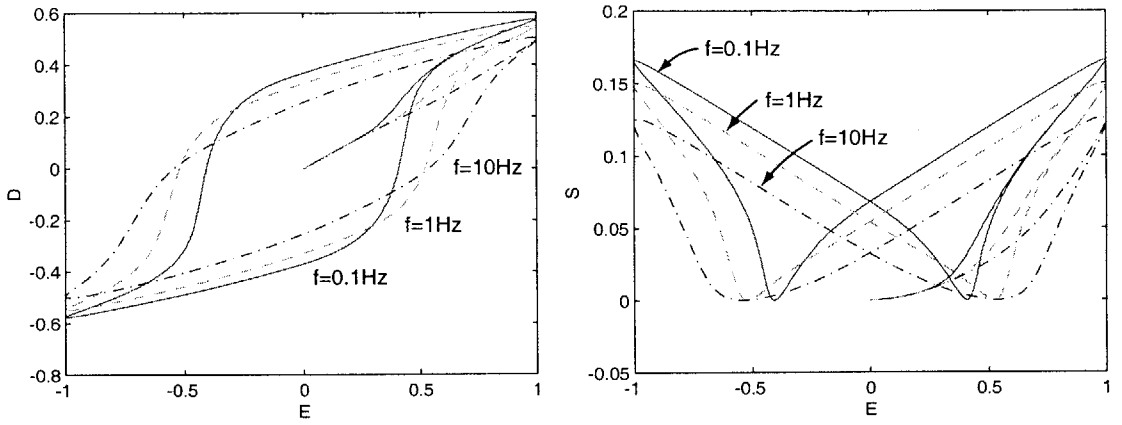

Figure 3-16: Effect of driving frequency on E-D and E-S relations, assuming $T = 0$, $\Delta D_c = 0.05$, $\alpha = 3$, $\tau = 0.0005$, and varying $f = \{0.1,\ 1,\ \text{or}\ 10\} Hz$.

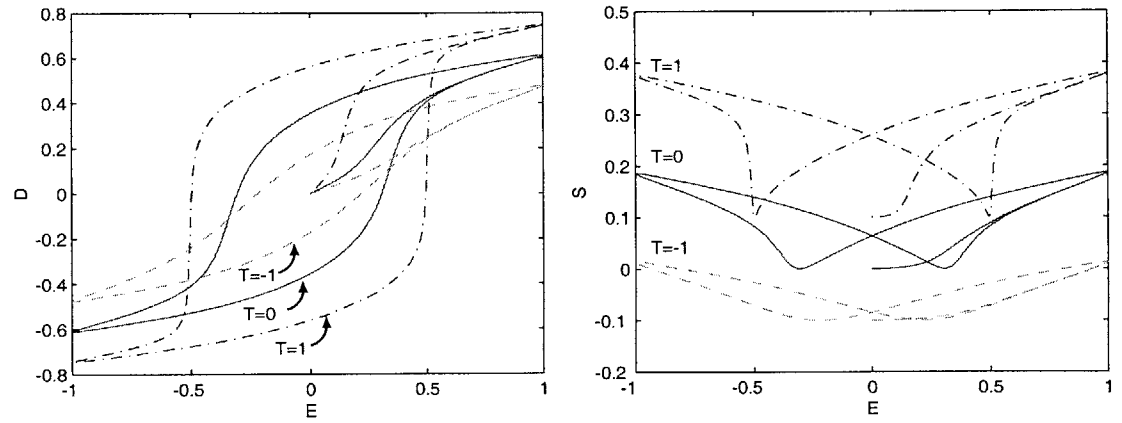

Figure 3-17: Effect of stress on E-D and E-S relations, assuming $f = 1$Hz, $\Delta D_c = 0.05$, $\alpha = 1$, $\tau = 0.001$, and varying $T = \{-1,\ 0,\ \text{or}\ 1\}$.

rameters with minimal error will be found. Below is a summary of the general procedure which is followed by a detailed description.

1. Construct D^* from data of D using Eq. 3.34 with assumed τ, ΔD_c, and α.

2. Assume polynomial terms of energy expansion G_1 as a function of D, D^*, and T.

3. Perform linear least squares regression and calculate the error for optimal coefficients of the assumed polynomial terms and rate rule parameters τ, ΔD_c, and α.

4. Repeat Steps 1 to 3 for different combinations of rate rule parameters τ, ΔD_c, and α. Then compare all the results and find the minimum error for the optimal τ, ΔD_c, and α.

3.3.1 Construction of D^*

As discussed earlier, D^* is a fictitious variables which cannot be measured by any instruments that are currently available. To find the coefficients of the polynomial terms that are functions of D and D^*, D^* must be simulated from measured D.

In this step, a set of rate parameters τ, ΔD_c, and α should be assumed first. The typical range of τ is from 0.1 to 10 millisecond; ΔD_c is from 0.01 to 0.1 C/m^2, and α is from 3 to 10. These values are the conclusion of the parametric study in the previous section. Using these assumed τ, ΔD_c, and α and measured D, one can then find the simulated D^* by solving the differential equation (Eq. 3.34). Two sets of initial conditions of this differential equation are possible: one is zero, and the other is nonzero.

If the material data of polarization D is recorded from the freshly unpoled state, the initial condition of D and D^* are therefore zero. With these initial conditions, the simulated D^* can be solved numerically from Eq. 3.34. Figure 3-18 shows the simulated result and the relation between D and D^*.

Unfortunately, most data for stress dependency study obtained in Section 2.4 did not start from the virgin state of the material, i.e. remanent polarization exists in the material. In other words, the initial values of D and D^* for each cycle are not zero. As a result, iteration for D_0^*, the initial condition of D^*, must be conducted by first assuming $D_0^* = D_0/0.8$ and then solving for D^* for a cycle. The value of D^* at the end of this cycle can

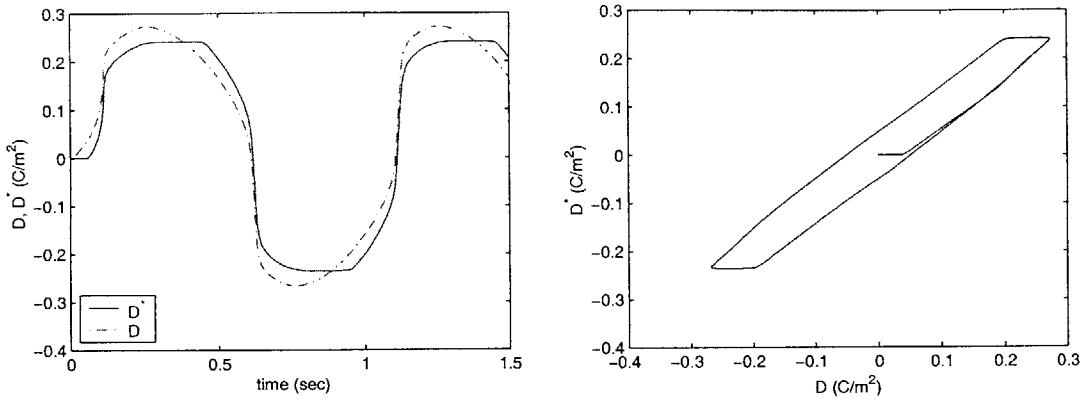

Figure 3-18: Finding D^* for virgin specimen.

be used as the new initial guess of D_0^* for the next integration cycle. This integration process must be continued until the value of D_0^* converges. In general, only two cycles of integration are needed to obtain a converged D_0^* for each stress value. Figure 3-19 shows the time history of measured D, simulated D^{**} with initial guessed D_0^{**}, and simulated D^* with converged D_0^*. The right plot of 3-19 shows the zoomed data that D^{**} converges rapidly to D^*. Figure 3-20 shows the relation between D and D^*. The left plot shows how D^{**} with initial guessed D_0^{**} converges to D^*. The right plot shows the relation between measured D and converged D^*.

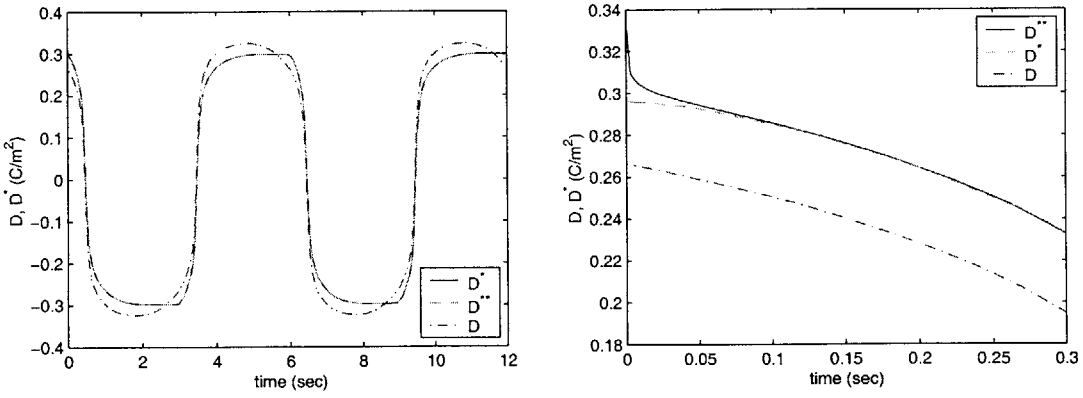

Figure 3-19: Finding D_0^* for poled specimen: (left) time history of measured D, simulated D^{**} with initial guessed D_0^{**}, and simulated D^* with converged D_0^*; (right) zoomed time history.

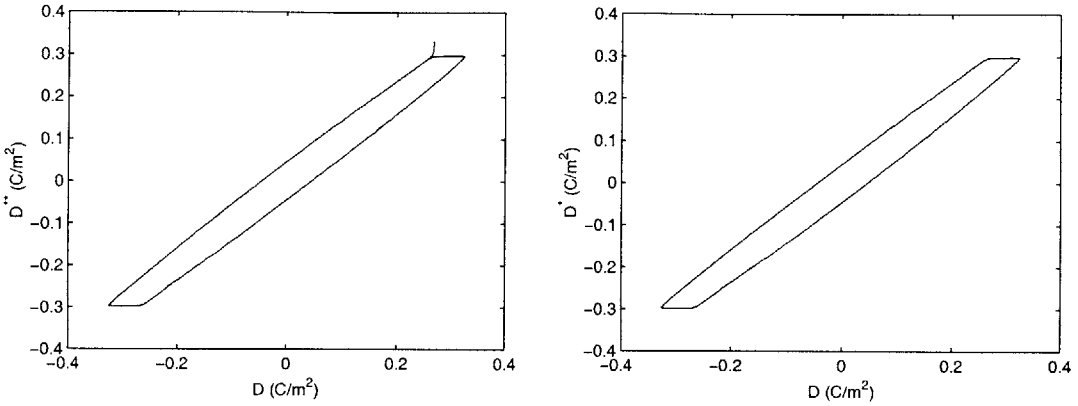

Figure 3-20: Finding D_0^* for poled specimen. (left) initial guessed D_0^{**}, (right) converged D_0^*

3.3.2 Selection of Polynomials

Table 3.2: Polynomial terms of thermodynamic potentials

$\sigma_1 D$	$\sigma_6 D^*$	$\sigma_{11} D D^*$
$\sigma_2 D^2$	$\sigma_7 D^{*2}$	$\sigma_{12} D D^{*2}$
$\sigma_3 D^3$	$\sigma_8 D^{*3}$	$\sigma_{13} D^2 D^{*2}$
$\sigma_4 D^4$	$\sigma_9 D^{*4}$	$\sigma_{14} D^2 D^*$
$\sigma_5 D^5$	$\sigma_{10} D^{*5}$	$\sigma_{15} D^3 D^*$
		$\sigma_{16} D^3 D^{*2}$
		$\sigma_{17} D^3 D^{*3}$
		$\sigma_{18} D^2 D^{*3}$
		$\sigma_{19} D D^{*3}$

First, G_1 is assumed to have a form of

$$G_1 = f_a(D, D^*) - f_b(D, D^*)T - f_c(D, D^*)T^2 - f_d(D, D^*)T^4, \tag{3.41}$$

where the terms related to T^3 are neglected by observing strain (S) is an odd function of stress (T). The corresponding strain and electric field are then

$$S = f_b(D, D^*) + 2f_c(D, D^*)T + 4f_d'(D, D^*)T^3, \tag{3.42}$$

$$E = f_a'(D, D^*) - f_b'(D, D^*)T - f_c'(D, D^*)T^2 - f_d'(D, D^*)T^4, \tag{3.43}$$

where f' denotes the partial derivative of f with respect to D. Table 3.2 shows the polynomial terms used in this work for $f_a(D, D^*)$, $f_b(D, D^*)$, $f_c(D, D^*)$, and $f_d(D, D^*)$. The coefficient corresponding to each term is denoted by σ_i, where σ represents the subscript of f_a, f_b, f_c, and f_d in general. Namely, for instance, f_a is given by

$$f_a(D, D^*) = a_1 D + a2_D^2 + \cdots a_{18} D D^{*3}.$$

Higher order terms can be included in this expansion of the energy function to improve the performance of the model. However, the terms selected in Table 3.2 are found to be sufficient to simulate the observed data. After selection of these polynomial terms, the next step is to obtain the corresponding coefficients using least squares regression such that the error between model and data can be minimized.

3.3.3 Optimization of Polynomial Coefficients

Since the rate parameters are assumed, D^* is simulated from the measured and D, and the polynomial terms of the elastic Gibbs energy are selected, this step is to optimize the coefficients of the energy expansion subjected to the assumed rate parameters. For convenience of discussion, rewriting the elastic Gibbs free energy as

$$G_1 = \sum_k x_k G_1^{(k)}(T, D, D^*) \tag{3.44}$$

yields expressions of E and S as

$$E = \sum_k x_k E^{(k)}(T, D, D^*), \tag{3.45}$$

$$S = \sum_k x_k S^{(k)}(T, D, D^*), \tag{3.46}$$

where x_k includes all the coefficients of a_i, b_i, c_i, and d_i.

With the expression of S and E in Eq. 3.46 and 3.45 and the measured data $\hat{S}$ and $\hat{E}$ from Section 2.4, the weighted cost function for optimization can be defined by summing all the weighted errors for n data points:

$$\mathbf{e} = \sum_{z=1}^{n} w_{E_z}(E_z(\hat{D}_z, \hat{D}_z{}^*, \hat{T}_z) - \hat{E}_z)^2 + \sum_{z=1}^{n} w_{S_z}(S_z(\hat{D}_z, \hat{D}_z{}^*, \hat{T}_z) - \hat{S}_z)^2 \tag{3.47}$$

where n is the number of data points, w_E and w_S are weighting functions, and $\hat{D}$, $\hat{D}^*$, and $\hat{T}$ are the measured values from Section 2.4. This cost function can be also defined from a

weighted linear system

$$\mathbf{WAx} = \mathbf{Wb} \tag{3.48}$$

where $\mathbf{x}$ is the vector of x_k, $\mathbf{W}$ is given by a diagonal matrix of the vector $[\mathbf{w_E}\ \mathbf{w_S}]^T$, and $\mathbf{b}$ is an appended vector of measured $\hat{E}_z$ and $\hat{S}_z$:

$$\mathbf{b} = \begin{bmatrix} \hat{\mathbf{E}} \\ \hat{\mathbf{S}} \end{bmatrix}. \tag{3.49}$$

The corresponding $\mathbf{A}$ can be partitioned as

$$\mathbf{A} = \begin{bmatrix} \mathbf{A^E} \\ \mathbf{A^S} \end{bmatrix}, \tag{3.50}$$

where the respective components of $\mathbf{A^E}$ and $\mathbf{A^S}$ are

$$A^E_{zk} = E^{(k)}(\hat{D}_z, \hat{D}_z{}^*, \hat{T}_z), \tag{3.51}$$

$$A^S_{zk} = S^{(k)}(\hat{D}_z, \hat{D}_z{}^*, \hat{T}_z). \tag{3.52}$$

The vector $\mathbf{x}$ that minimizes the weighted cost function $\mathbf{e}$ or $\mathbf{W}\|\mathbf{Ax} - \mathbf{b}\|$ is the solution to the weighted normal equations[62]:

$$\mathbf{A^T WAx} = \mathbf{A^T Wb} \tag{3.53}$$

i.e. $\mathbf{x} = (\mathbf{A^T WA})^{-1}\mathbf{A^T Wb}$.

3.3.4 Optimization of τ, ΔD_c, and α

In the previous discussion, the coefficients of the energy expansion are optimized for certain assumed rate parameters α, τ and ΔD_c. However, these rate parameters are not optimized yet. Unlike the polynomial coefficients, these rate parameters influence the system in a nonlinear manner, and therefore it is difficult to optimize them using least squares regression. The only possible approach is to intensively repeat the same procedure described in Sections 3.3.1, 3.3.2, and 3.3.3 for different combinations of rate parameters. The optimized rate parameters can be therefore obtained by identifying the minimum value of the cost function. The data of the stress effect as well as the rate effect must be included in this evaluation of the cost function; otherwise, the model may result in unreasonable behavior. For instance,

using the parameters $\alpha = 3$, $\Delta D_c = 0.15\text{C/m}^2$, and $\tau = 1\text{ms}$ and the energy expansion with the coefficients listed in Table 3.3:

$$\begin{aligned}
G_1 &= a_2D^2 + a_4D^4 + a_{11}DD^* + a_{12}DD^{*2} + a_{13}D^2D^{*2} \\
&+ a_{14}D^2D^* + a_{15}D^3D^* + a_{16}D^3D^{*2} + a_{17}D^3D^{*3} + a_{18}D^2D^{*3} \\
&+ a_{19}DD^{*3} + a_{20}D^6 + a_{21}D^4D^* + a_{22}D^4D^{*2} + a_{23}D^4D^{*3} \\
&+ (b_2D^2 + b_4D^4 + b_7D^{*2} + b_9D^{*4} + b_{11}DD^* + b_{12}DD^{*2} \\
&+ b_{13}D^2D^{*2} + b_{14}D^2D^* + b_{15}D^3D^* + b_{16}D^3D^{*2} + b_{17}D^3D^{*3} + b_{18}D^2D^{*3} \\
&+ b_{19}DD^{*3} + b_{20}D^6 + b_{21}D^4D^* + b_{22}D^4D^{*2} + b_{23}D^4D^{*3})T \\
&+ (c_0 + c_2D^2 + c_4D^4 + c_7D^{*2} + c_9D^{*4} + c_{11}DD^* + c_{12}DD^{*2} \\
&+ c_{13}D^2D^{*2} + c_{14}D^2D^* + c_{15}D^3D^* + c_{16}D^3D^{*2} + c_{17}D^3D^{*3} + c_{18}D^2D^{*3} \\
&+ c_{19}DD^{*3} + c_{20}D^6 + c_{21}D^4D^* + c_{22}D^4D^{*2} + c_{23}D^4D^{*3})T^2 \\
&+ (d_0 + d_2D^2 + d_4D^4 + d_7D^{*2} + d_9D^{*4} + d_{11}DD^* + d_{12}DD^{*2} \\
&+ d_{13}D^2D^{*2} + d_{14}D^2D^* + d_{15}D^3D^* + d_{16}D^3D^{*2} + d_{17}D^3D^{*3} + d_{18}D^2D^{*3} \\
&+ d_{19}DD^{*3} + d_{20}D^6 + d_{21}D^4D^* + d_{22}D^4D^{*2} + d_{23}D^4D^{*3})T^4, \qquad (3.54)
\end{aligned}$$

one can correlate the model well with stress dependent data as shown in Figure 3-21. However, this combination of parameter shows a very poor result with respect to rate dependency, as shown in Figure 3-22. As a result, this set of parameters is not valid.

Table 3.3: Coefficients of PZT-5H thermodynamic potential expanded by polynomial terms. This will result in poor rate behavior, despite the good stress dependent response

					$(\times 10^4)$		$(\times 10^5)$
				c_0	0.0035	d_0	-0.0269
a_2	0.1127	b_2	217.1444	c_2	0.3758	d_2	-1.6482
a_4	297.9421	b_4	-13885.0000	c_4	-26.8084	d_4	-207.0929
		b_7	118.4422	c_7	0.3037	d_7	-1.2494
		b_9	-11910.0000	c_9	-25.8064	d_9	-100.2973
a_{11}	-3.6804	b_{11}	-326.2087	c_{11}	-0.7135	d_{11}	3.9120
a_{12}	0.6607	b_{12}	-28.7464	c_{12}	-0.0443	d_{12}	-0.0989
a_{13}	1252.0000	b_{13}	-75620.0000	c_{13}	-157.2291	d_{13}	-723.4826
a_{14}	-0.5245	b_{14}	28.0433	c_{14}	0.0490	d_{14}	-0.3229
a_{15}	-983.0483	b_{15}	52618.0000	c_{15}	105.4464	d_{15}	616.6637
a_{16}	59.0330	b_{16}	-277.7209	c_{16}	0.0469	d_{16}	-22.9987
a_{17}	140.9955	b_{17}	-2712.1000	c_{17}	0.1323	d_{17}	202.0744
a_{18}	-45.1711	b_{18}	264.5240	c_{18}	-0.2842	d_{18}	36.2788
a_{19}	-697.9519	b_{19}	49214.0000	c_{19}	104.7170	d_{19}	394.5847
a_{20}	48.8821						
a_{21}	-17.3723						
a_{22}	-171.4751						
a_{23}	-35.5942						

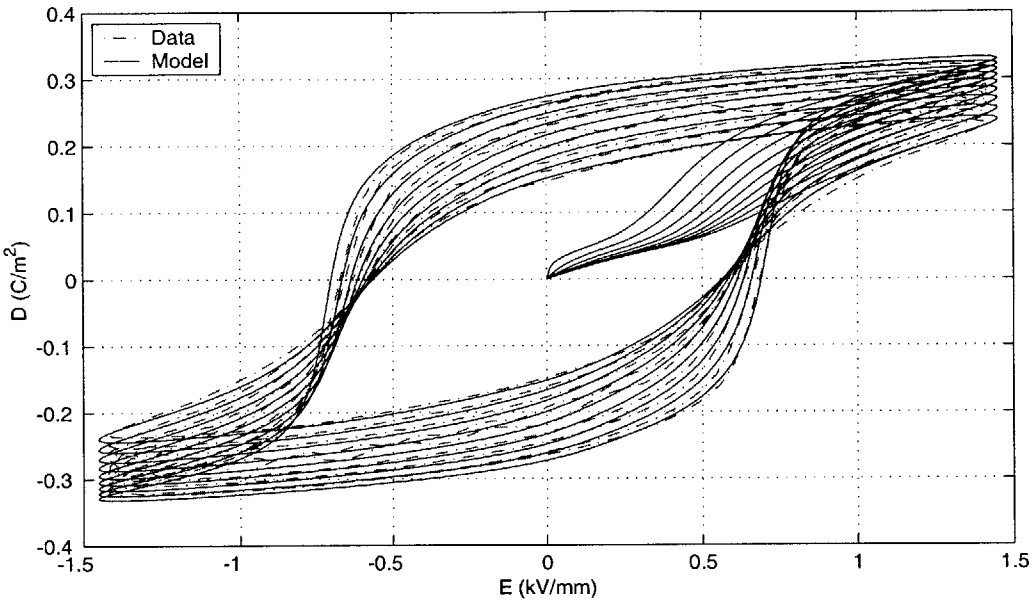

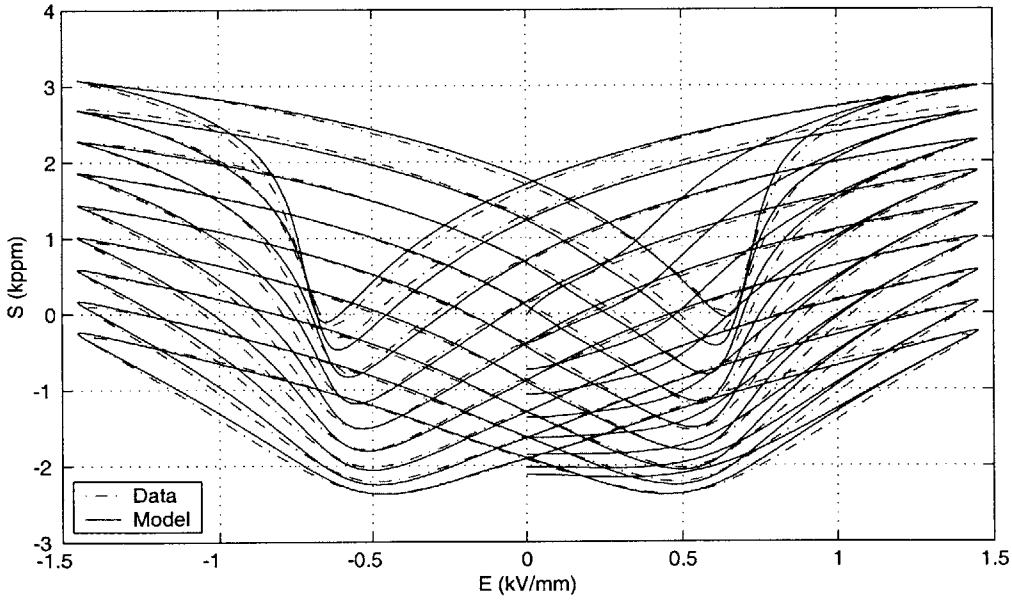

Figure 3-21: Unreasonable strain and polarization response at various stresses using inappropriate parameter optimization. Data was obtained by Ghandi[35].

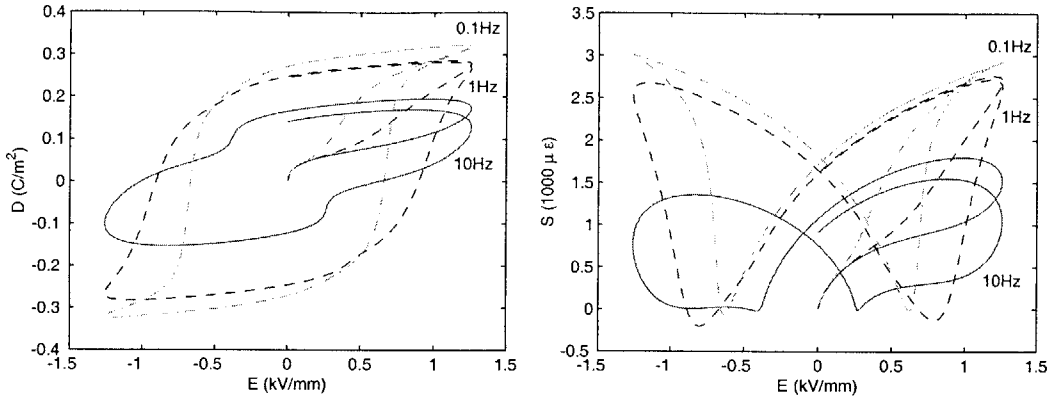

Figure 3-22: Unreasonable strain and polarization response at various frequencies using inappropriate parameter optimization.

3.3.5 Optimized 1-D Model Parameters for PZT-5H

Following the procedures described in Sections 3.3.1–3.3.4 with weight $w_i = 1$, one can find the optimized 1-D rate parameters for PZT-5H: τ=0.1 (ms), ΔD_c=0.03 (C/m^2), α=7. To simplify the model and to avoid the fact that higher order terms may cause unstable solution of the differential algebraic equations at high frequency, only the following terms shall be included in the expansion of the elastic Gibbs free energy G_1:

$$\begin{aligned} G_1 &= a_2D^2 + a_4D^4 + a_{11}DD^* + a_{12}DD^{*2} + a_{13}D^2D^{*2} + a_{14}D^2D^* \\ &+ (b_2D^2 + b_4D^4)T \\ &+ (c_0 + c_2D^2 + c_4D^4)T^2 \\ &+ (d_0 + c_2D^2 + c_4D^4)T^4 \end{aligned} \tag{3.55}$$

Since E is an odd function of D, terms such as D and D^3 are excluded from G_1. In addition, since S is also an odd function of T, terms related with T^3 are excluded from G_1. To increase the performance, cross terms between D and D^* up to second order are included. To scale the system so that the ill-conditioned matrix $\mathbf{A^TWA}$ in Eq. 3.53 can be avoided while performing least square regression, the units of T and D in GPa and C/m^2 are used, respectively. The units of the resulting $E = \partial G_1/\partial D$ and $S = -\partial G_1/\partial T$ are therefore in kV/mm and kppm, respectively.

The corresponding coefficients of the energy expansion are summarized in Table 3.4. Figure 3-23 shows the rate response of the model, which captures the expansion behavior of the rate data shown in Figure 2-45. Figures 3-24, 3-25, and 3-26 show the correlation between the measured data and the simulated material response under different compression levels. As can be seen, the model well-predicts the shrinking effect of compression on the strain and polarization response. In addition, this 1-D PZT-5H model not only achieves the targeted accuracy at Stage 1 but also at Stage 2, as defined in Table 1.1.

Table 3.4: Coefficients of PZT-5H thermodynamic potential expanded in polynomial terms.

				c_0	38.1430	d_0	-2.8570×10^3
a_2	14.4665	b_2	27.4074	c_2	-88.2369	d_2	24.8750×10^3
a_4	-1.5161	b_4	11.6303	c_4	-537.7735	d_4	-351.4483×10^3
a_{11}	-29.2314						
a_{12}	0.3759						
a_{13}	18.1391						
a_{14}	-0.1526						

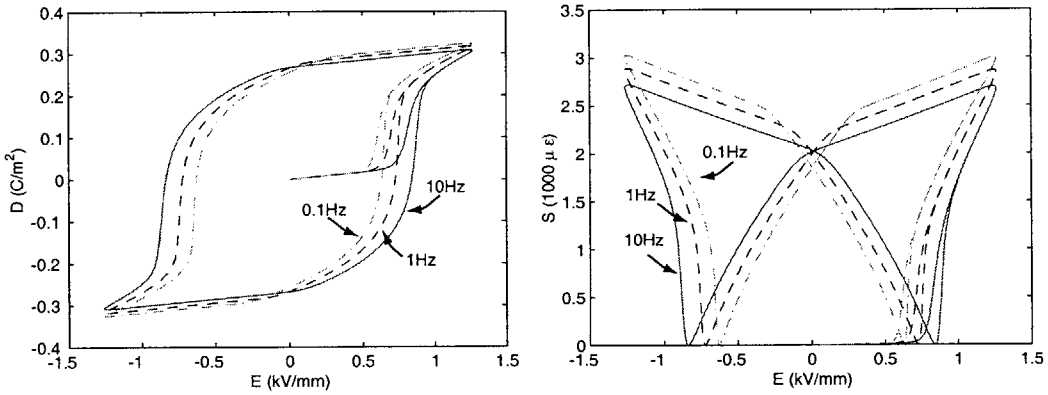

Figure 3-23: Simulated rate dependent behaviors of PZT-5H using 1-D model.

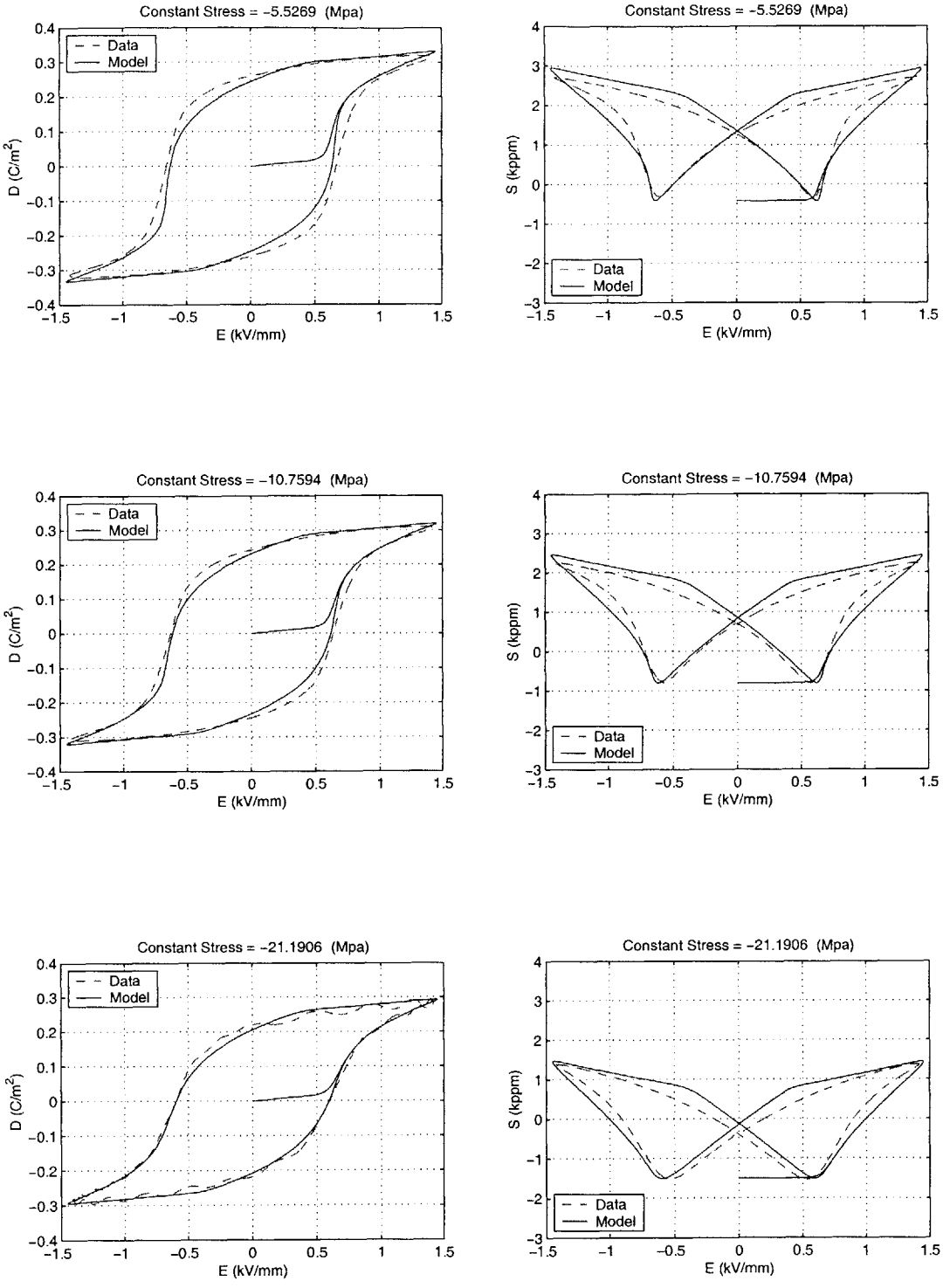

Figure 3-24: Data and simulated stress dependent behaviors of PZT-5H using 1-D model.

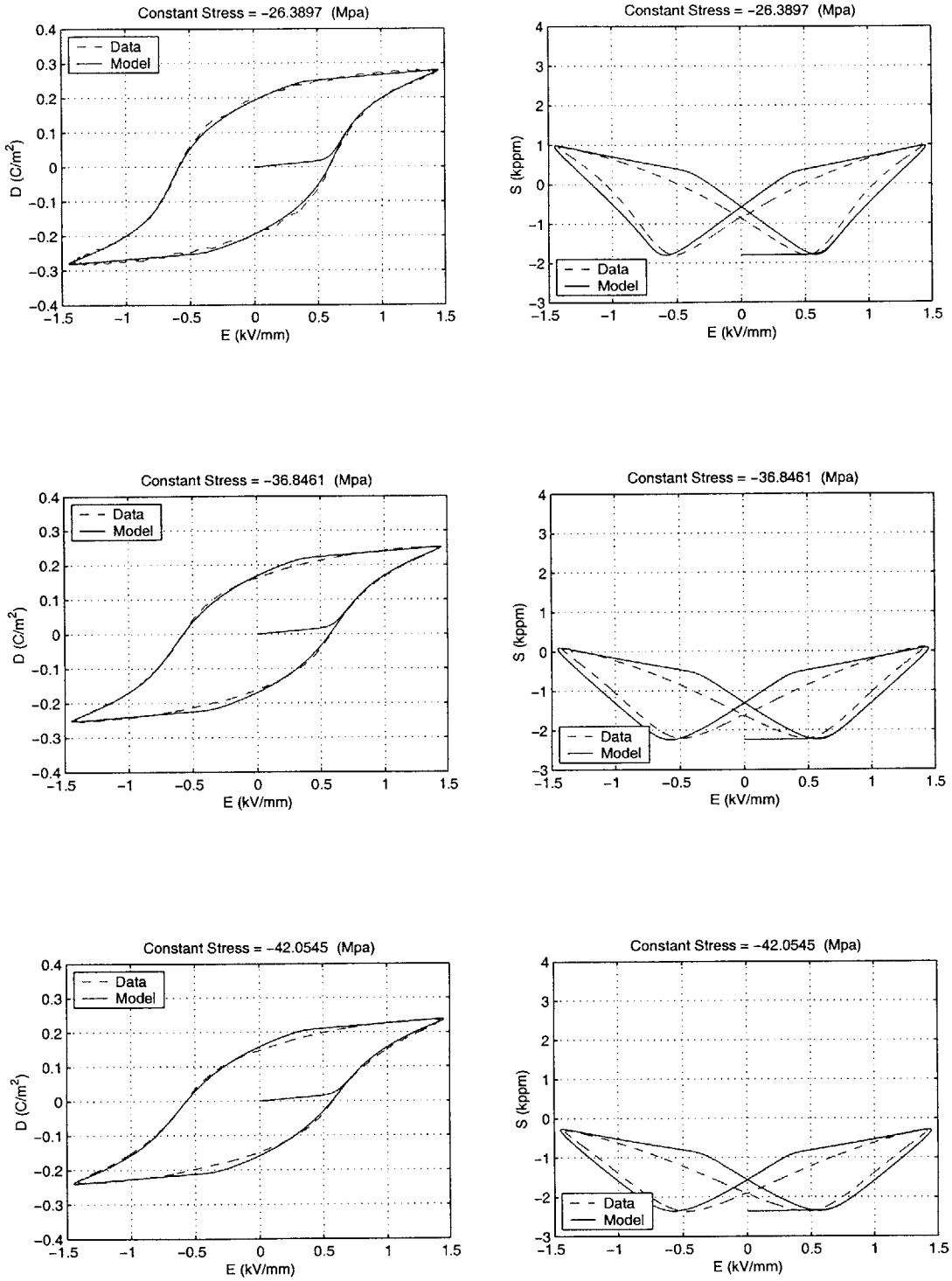

Figure 3-25: Data and simulated stress dependent behaviors of PZT-5H using 1-D model (Cont).

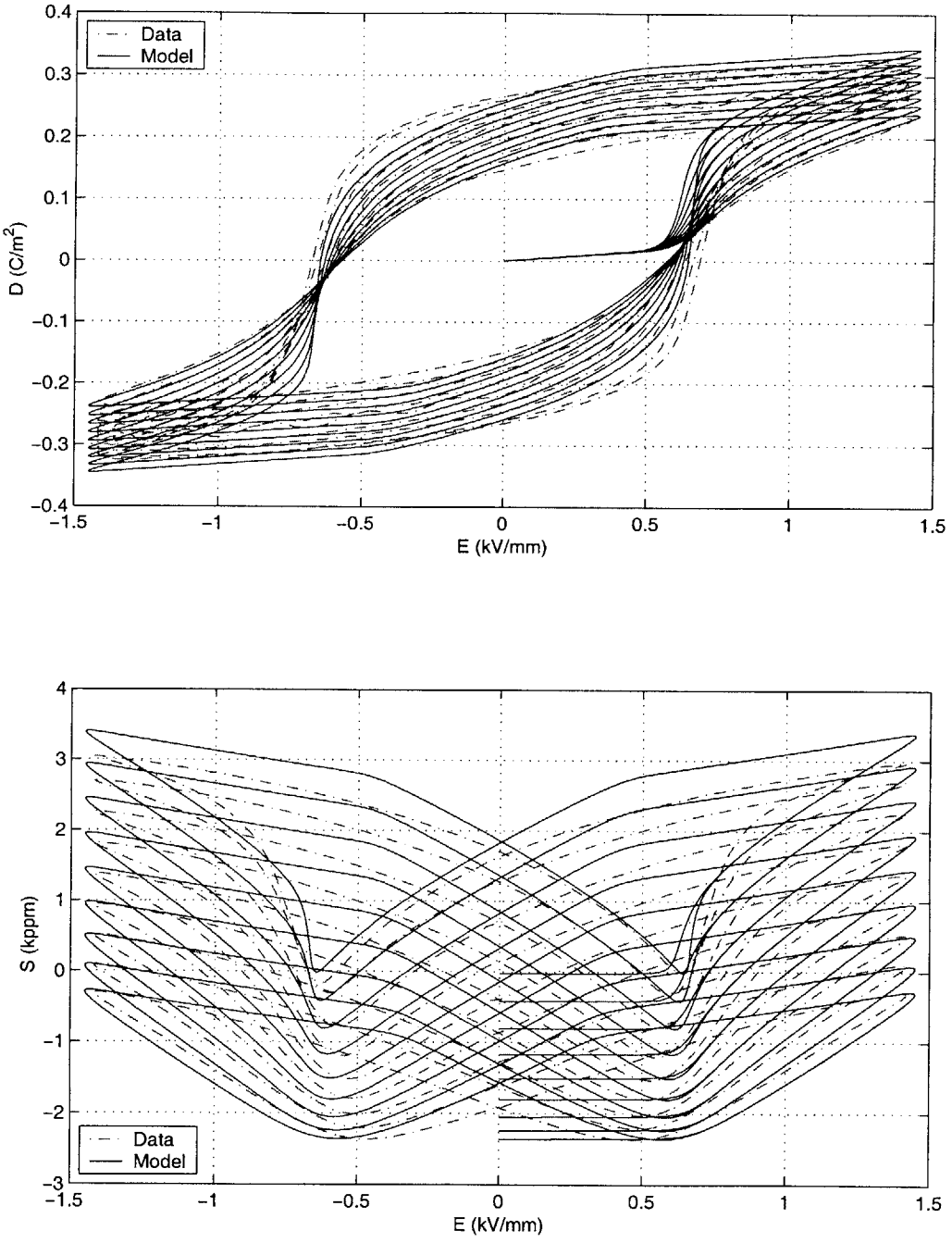

Figure 3-26: Overall data and simulated stress dependent behaviors of PZT-5H using 1-D model.

3.3.6 Optimized 1-D Model Parameters for PZT-5A

As described in Chapter 2, three sets of data under longitudinal test were acquired: (1) Batch A, 0–50MPa; (2) Batch B, 0–50MPa; (3) Batch B, 0–100MPa. Batch A exhibits an abnormal coercive field and therefore is not considered a good batch. In spite of this, it is of interest to see how well the modeling framework developed here can predict a wide range of material behaviors. Based on this motivation, the optimal material parameters defining all sets of data will be obtained using the same procedure and energy expansion for PZT-5H.

PZT-5A (Batch A, 0–50MPa)

As summarized in Table 3.5, the optimized coefficients for this data set can be found using w_i=1 and the optimal rate parameters τ=0.1 (ms), ΔD_c=0.03 (C/m^2), and α=7. Figures 3-27, 3-28, and 3-29 show the correlation between the measured data and the simulated material response under different compression levels. Figure 3-30 shows the rate response of the model, which captures the expansion behavior of the rate data shown in 2-46. In addition, this 1-D PZT-5A model not only achieves the targeted accuracy at Stage 1 but also at Stage 2, as defined in Table 1.1.

Table 3.5: Coefficients of thermodynamic potential expanded by polynomial terms PZT-5A, Batch A.

				c_0	44.7726	d_0	-3.7552×10^3
a_2	8.5107	b_2	20.8161	c_2	7.5421	d_2	32.0817×10^3
a_4	-2.5740	b_4	-26.2853	c_4	-74.7835	d_4	-74.0138×10^3
a_{11}	-17.3906						
a_{12}	-1.9810						
a_{13}	12.1964						
a_{14}	0.9194						

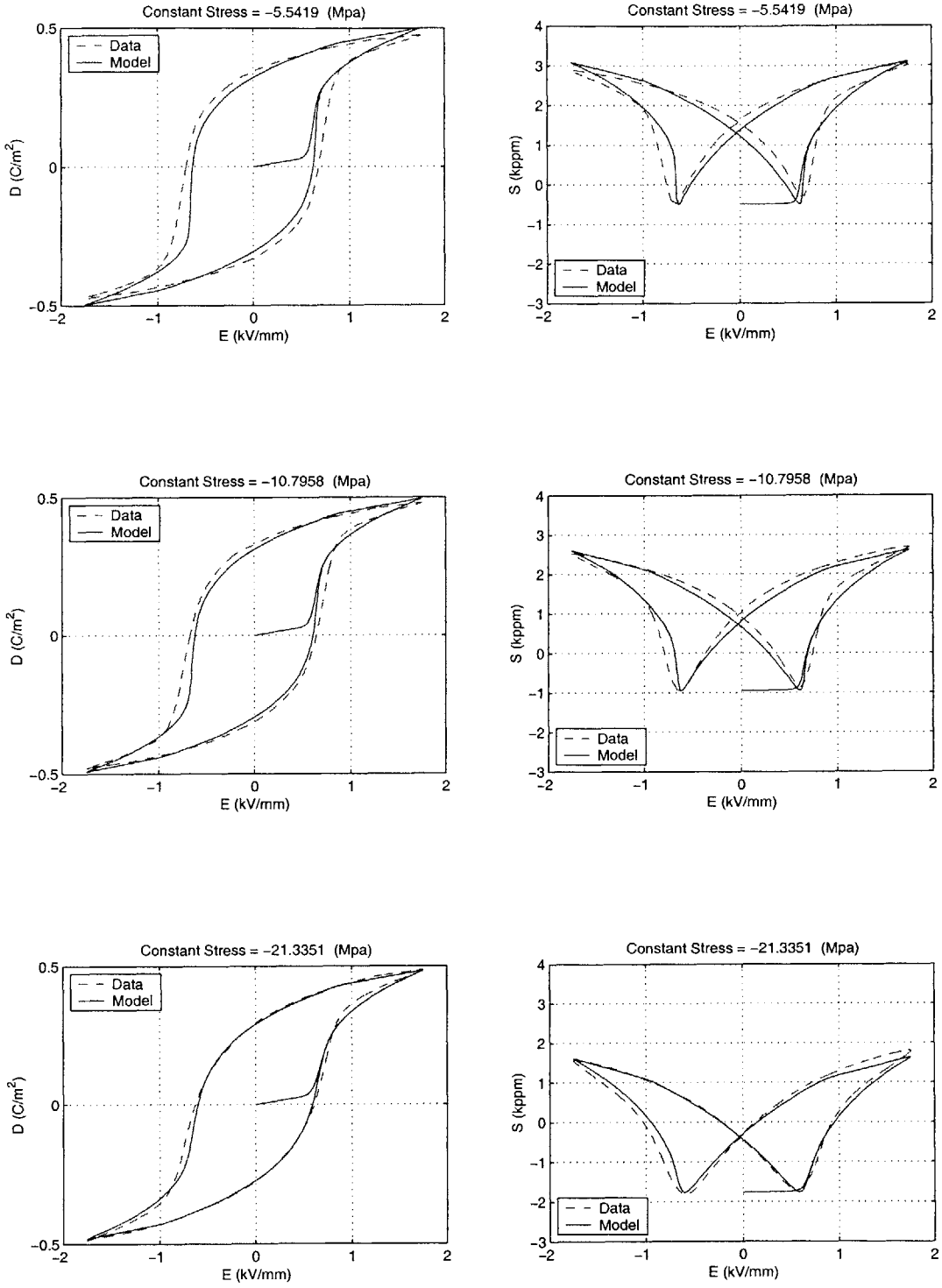

Figure 3-27: Data and simulated stress dependent behaviors of PZT-5A, Batch A, using 1-D model.

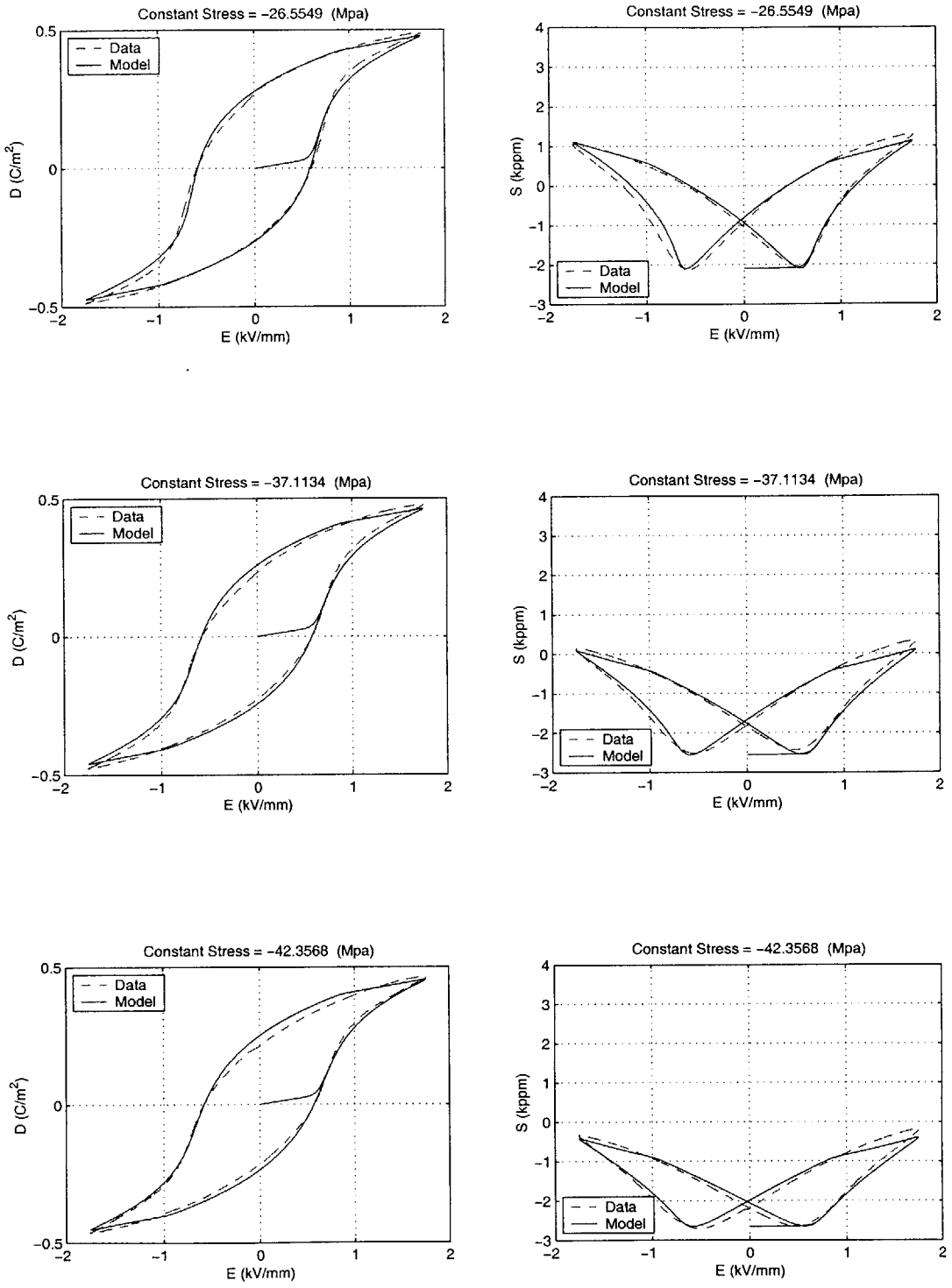

Figure 3-28: Data and simulated stress dependent behaviors of PZT-5A, Batch A, using 1-D model(Cont).

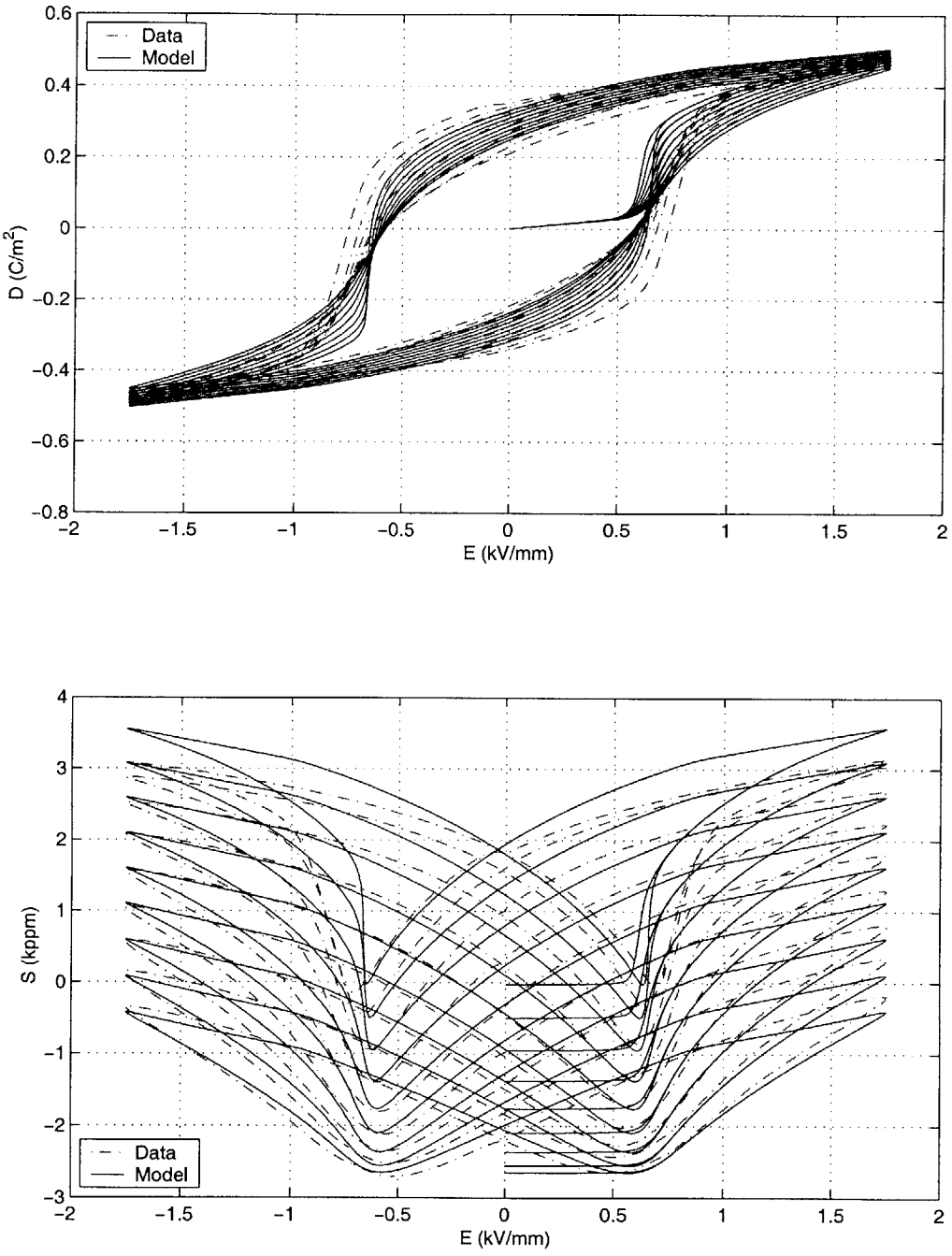

Figure 3-29: Overall data and simulated stress dependent behaviors of PZT-5A, Batch A, using 1-D model.

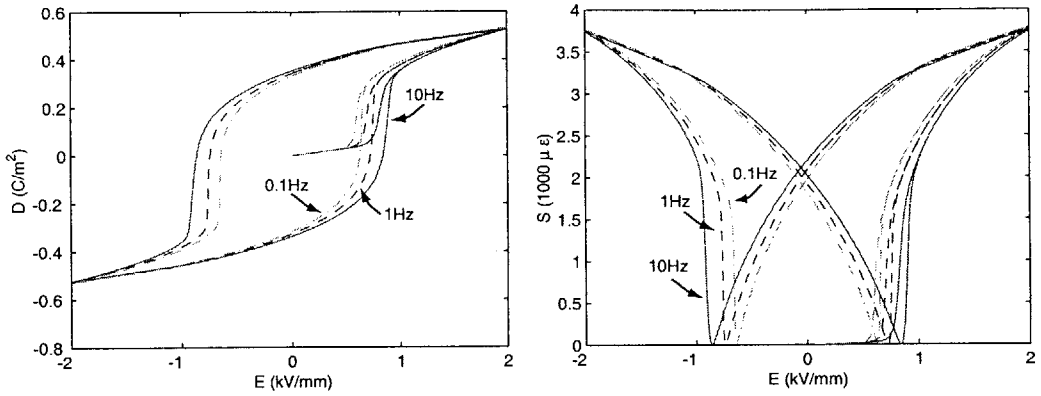

Figure 3-30: Simulated rate dependent behaviors of PZT-5A, Batch A, using 1-D model.

PZT-5A (Batch B, 0–50MPa)

Similarly, using w_i=1 and the optimal rate parameters τ=0.1 (ms), ΔD_c=0.01 (C/m^2), and α=7, the optimized coefficients for this data set can be found as summarized in Table 3.6. Figure 3-31 shows the rate response of the model, which captures the expansion behavior of the rate data shown in 2-46. Figures 3-32, 3-33, and 3-34 show the correlation between the measured data and the simulated material response under different compression levels. In addition, this 1-D PZT-5A model not only achieves the targeted accuracy at Stage 1 but also at Stage 2, as defined in Table 1.1.

Table 3.6: Coefficients of thermodynamic potential expanded in polynomial terms for PZT-5A, Batch B, 0–50MPa

				c_0	33.5042	d_0	57.0187
a_2	86.0048	b_2	33.7068	c_2	52.9584	d_2	-2.1257×10^4
a_4	-29.4160	b_4	-33.2464	c_4	-1.2124 ×10^3	d_4	-2.9374 ×10^4
a_{11}	-171.7265						
a_{12}	9.9571						
a_{13}	66.3547						
a_{14}	-4.8116						

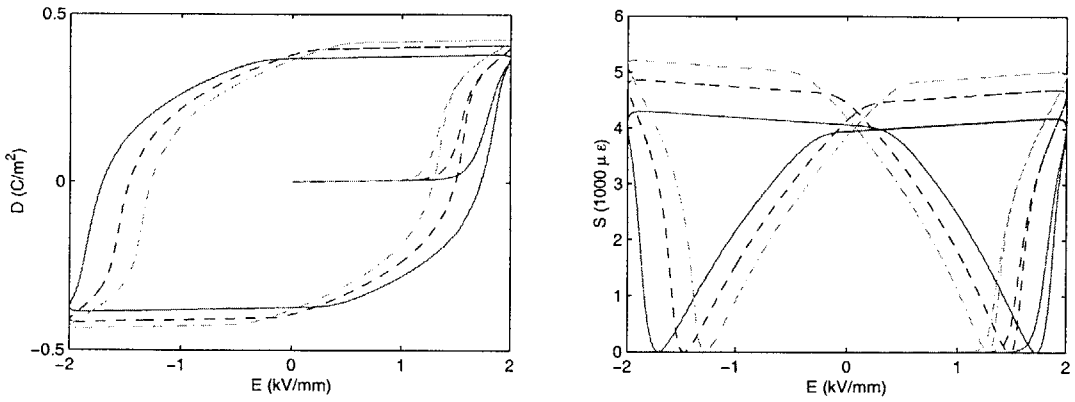

Figure 3-31: Simulated rate dependent behaviors of PZT-5A, Batch B, 0–50MPa, using 1-D model.

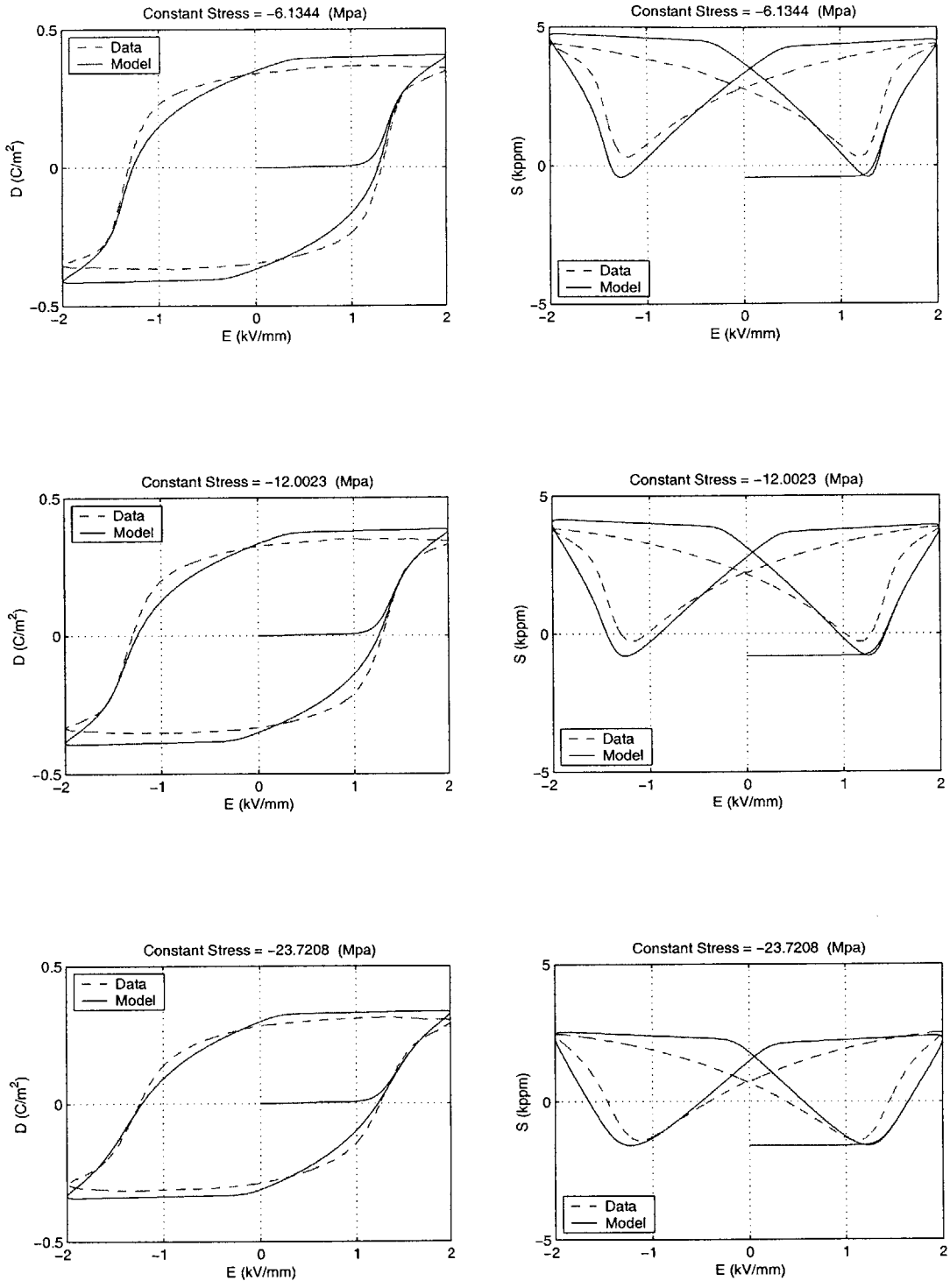

Figure 3-32: Data and simulated stress dependent behaviors of PZT-5A, Batch B, 0–50MPa, using 1-D model.

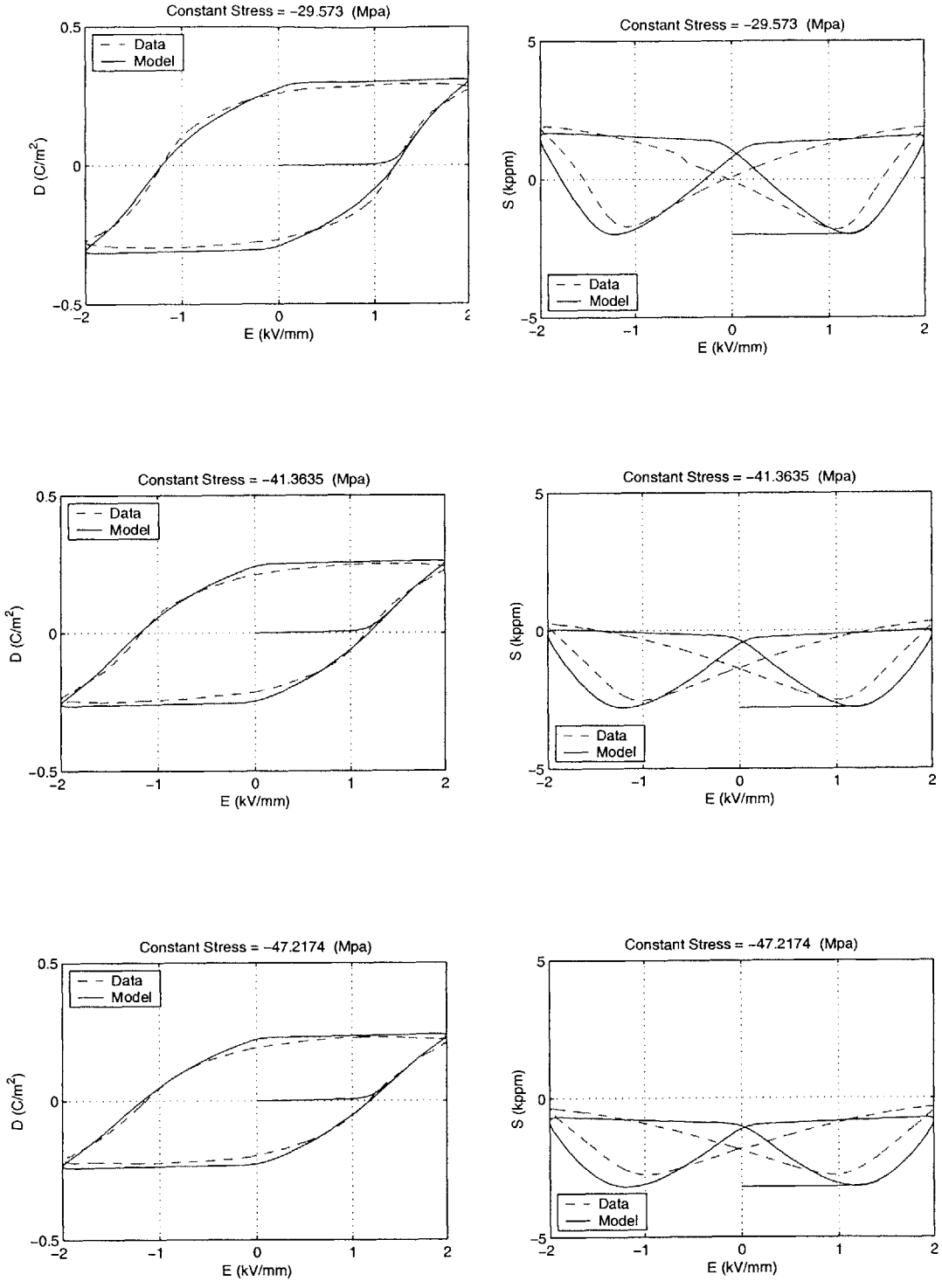

Figure 3-33: Data and simulated stress dependent behaviors of PZT-5A, Batch B, 0–50MPa, using 1-D model (Cont).

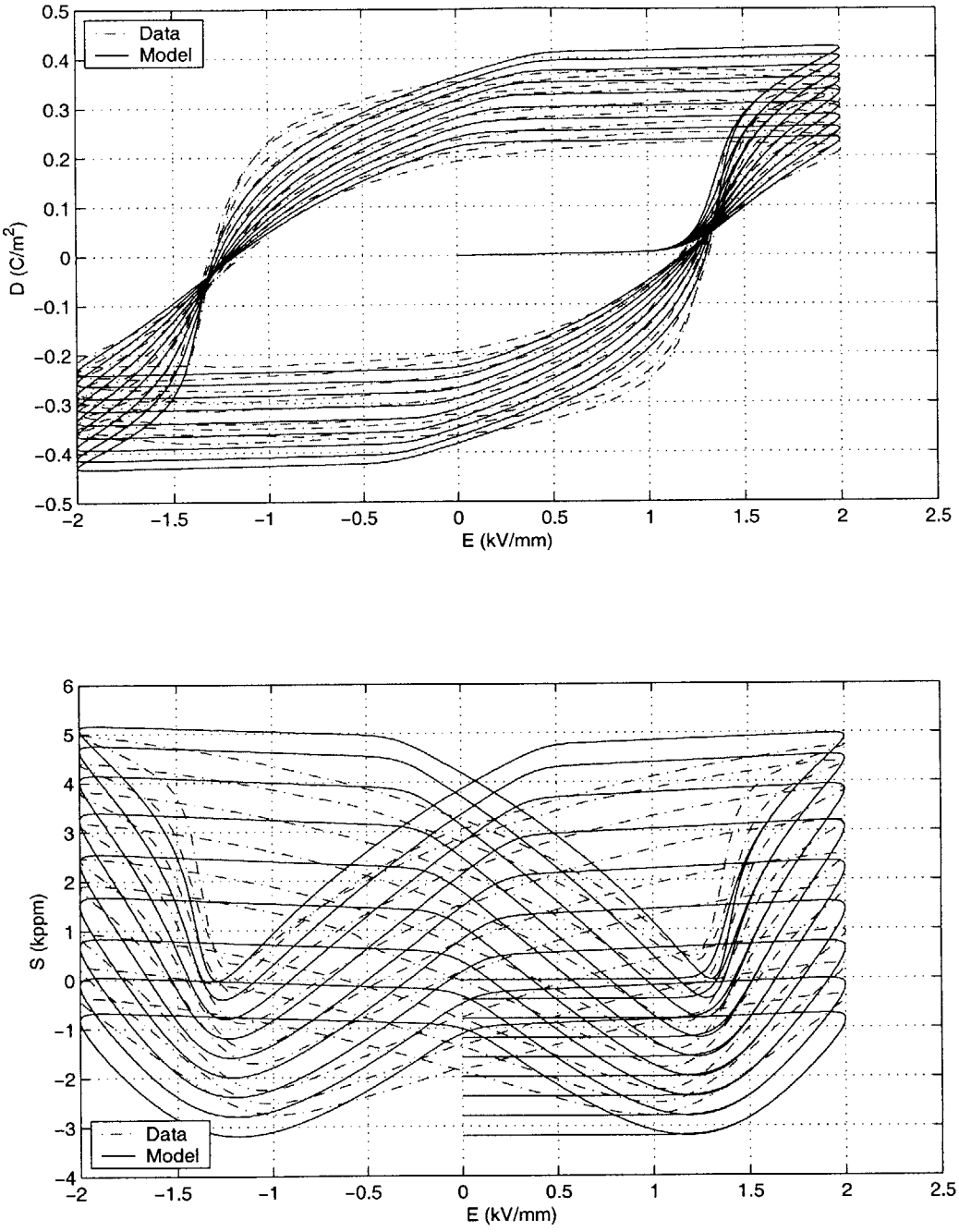

Figure 3-34: Overall data and simulated stress dependent behaviors of PZT-5A, Batch B, 0–50MPa, using 1-D model.

PZT-5A (Batch B, 0–100MPa)

Similarly, using w_i=1 and the optimal rate parameters τ=0.1 (ms), ΔD_c=0.01 (C/m^2), and α=7, the optimized coefficients for this data set can be found as summarized in Table 3.7. Figure 3-35 shows the rate response of the model, which captures the expansion behavior of the rate data shown in 2-46. Figures 3-36, 3-37, and 3-38 show the correlation between the measured data and the simulated material response under different compression levels. In addition, this 1-D PZT-5A model not only achieves the targeted accuracy at Stage 1 but also at Stage 2, as defined in Table 1.1.

Table 3.7: Coefficients of thermodynamic potential expanded in polynomial terms for PZT-5A, Batch B, 0–100MPa

				c_0	37.9313	d_0	-764.8502
a_2	72.2932	b_2	16.4705	c_2	-169.0589	d_2	1.7444×10^3
a_4	-26.6186	b_4	56.4527	c_4	377.5831	d_4	-4.2211×10^4
a_{11}	-143.1599						
a_{12}	-7.4087						
a_{13}	55.6369						
a_{14}	3.6222						

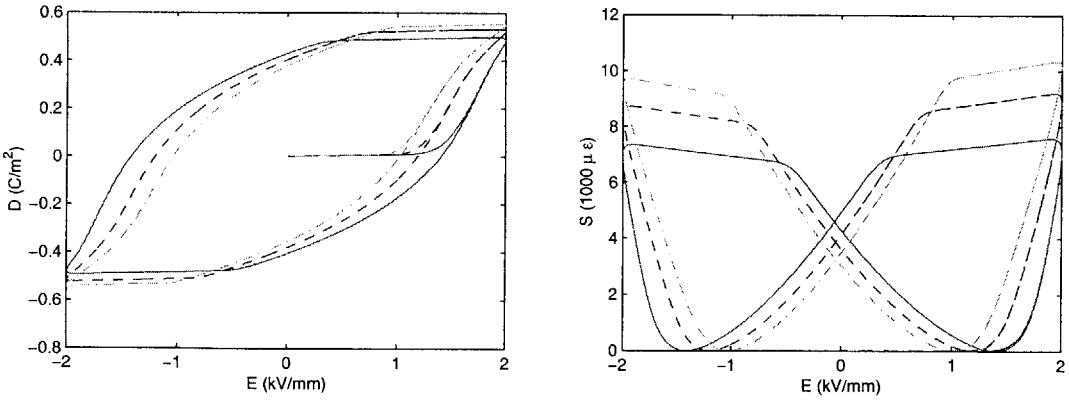

Figure 3-35: Simulated rate dependent behaviors of PZT-5A, Batch B, 0–100MPa, using 1-D model.

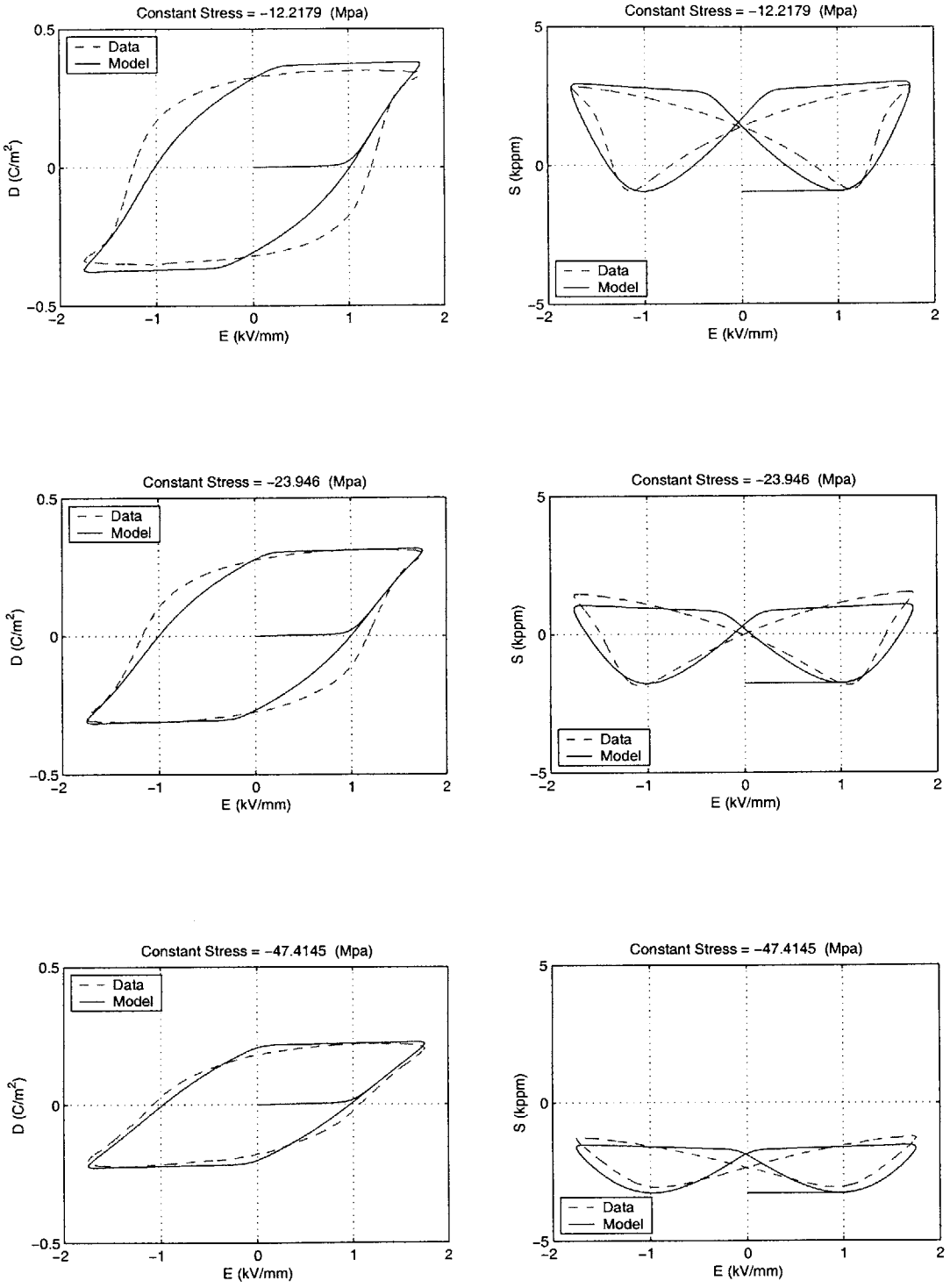

Figure 3-36: Data and simulated stress dependent behaviors of PZT-5A, Batch B, 0–100MPa, using 1-D model.

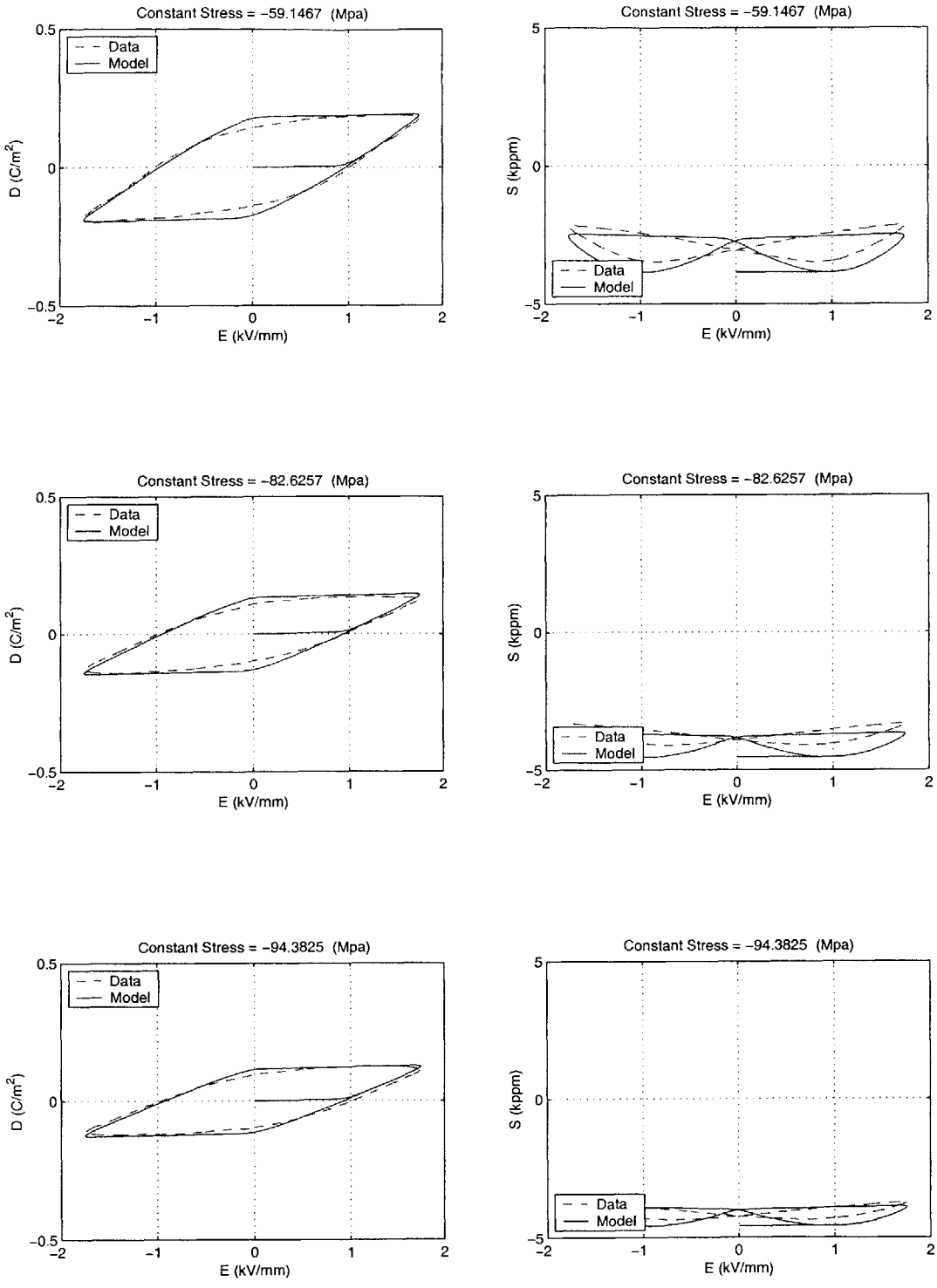

Figure 3-37: Data and simulated stress dependent behaviors of PZT-5A, Batch B, 0–100MPa, using 1-D model (Cont).

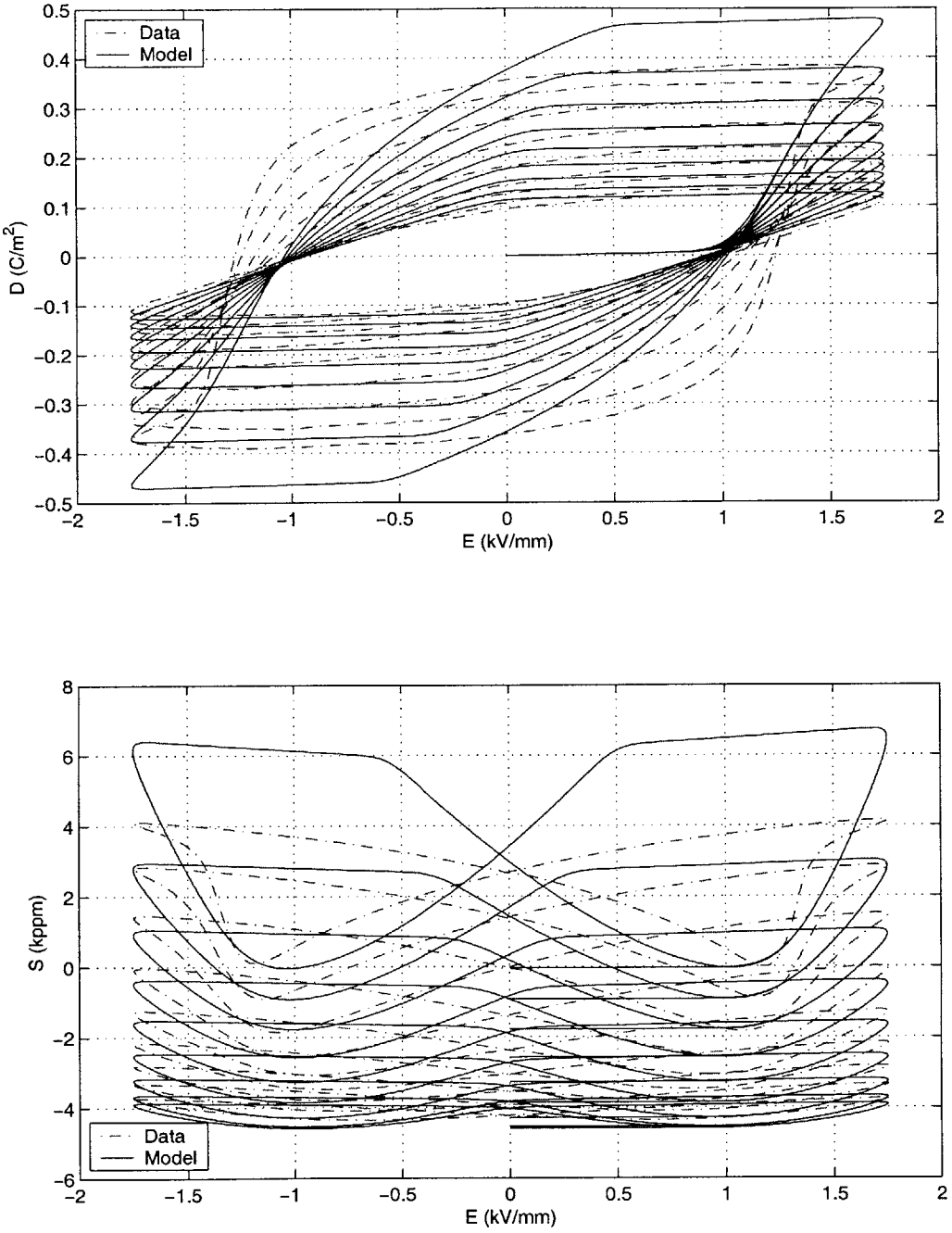

Figure 3-38: Overall data and simulated stress dependent behaviors of PZT-5A, Batch B, 0–100MPa, using 1-D model.

3.3.7 Discrepancy of Domain Switching Process between PZT-5A and PZT-5H

Compared to the models of PZT-5H and Batch A of PZT-5A, the model for Batch B of PZT-5A shows worse correlation with the data. This can be explained by the special relationship between strain (S) and electric displacement (D) of PZT-5A[2]. If S is plotted versus D, an important discrepancy between PZT-5H and PZT-5A can be found, as shown in Figure 3-39. The S-D relationship of PZT-5A shows more hysteretic behavior than that of PZT-5H, while a simple non-hysteretic parabolic function can be used to approximate the S-D curve of PZT-5H. Similar phenomena have also been reported by Zhou *et al.* [65], except that the discrepancy was found for a single material at different frequencies. He also proposed a 90°/180° domain switching hypothesis to explain this phenomenon. The hysteresis of the S-D curve is due to two successive 90° domain switching processes, instead of an instantaneous 180° process.

It is well known that PZT ceramics in the tetragonal phase state have two kinds of domain structures: 180° domains and 90° domains. Strong electric fields (higher than E_c) induce switching of the 180° domains and the reorientation of 90° domains (ferroelectric switching).[3] 180° domain reversal does not contribute to the induced strain, only 90° rotation does, whereas the 180° domain reversal contributes mainly to the polarization[66][65].

The domain switching process of PZT-5A is illustrated in Figure 3-40(c). Most of the domains undergo a 90° switching from points A and a to B for the first time due to the increasing electric field (still less than E_c), but there are still some domains remaining at the previous poling direction. Hence, the polarization is still negative and the strain reaches its minimum value at point B, but it may not be zero. From point B to b, part of the domains experiences a second 90° reorientation. Domains with an opposite poling direction make the net polarization zero, but the strain has already started to increase. At point b, most of the domains undergo a 90° switch for the second time. From points b to C and c, both 90° and 180° switching processes may happen, since the electric field is larger than E_c. At points C and c, nearly all the domains have been aligned to the direction of a positive electric field. Hence, both polarization and strain are saturated. The domain switching

[2]For convenience, Batch B of PZT-5A will represent PZT-5A in the rest of the discussion, unless it is specified.

[3]90° domain reorientation can also be induced by stress (ferroelastic switching).

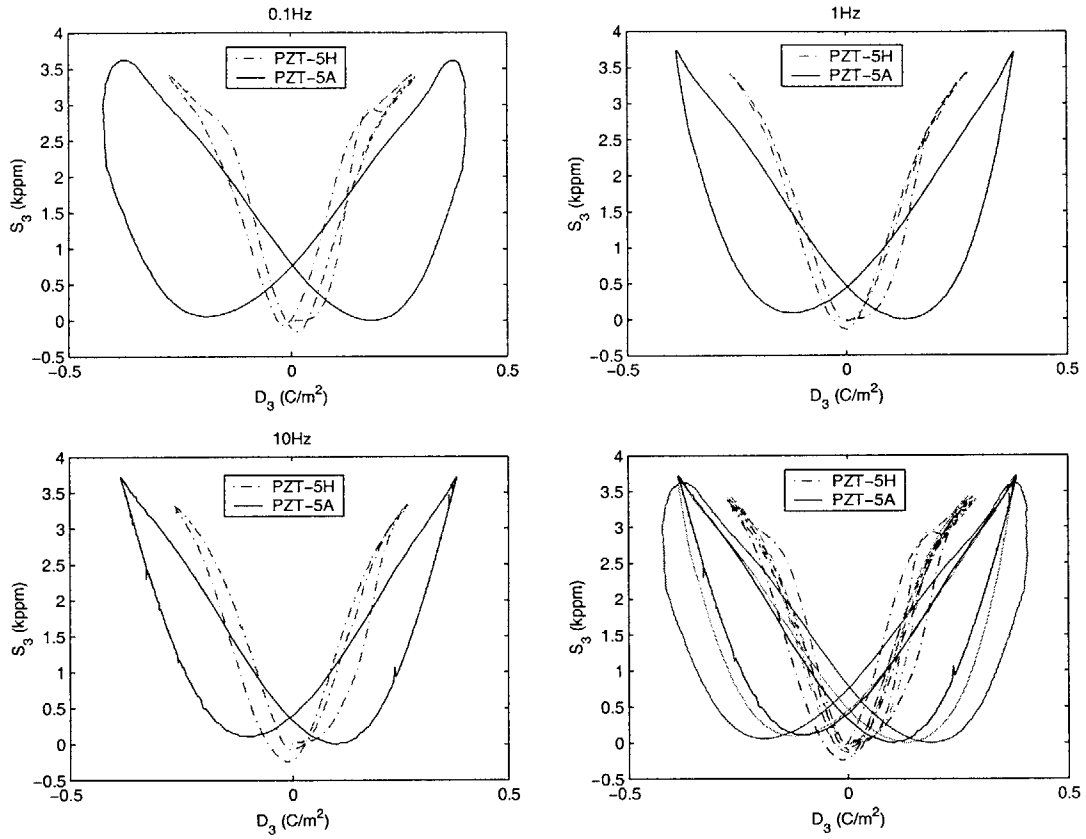

Figure 3-39: Comparison between S-D curves of PZT-5H and PZT-5A. Right lower plot shows all data.

process of the following sequence of D, d-E-e-F, f-G, g is nearly the same, just that the direction is opposite.

The domain switching process of PZT-5H is illustrated in Figure 3-40(f). Some domains still keep their negative polarization direction from points A and a to points B and b. In the meantime, unlike PZT-5A, a small number of PZT-5H domains have completed their 180° reversals and changed their polarization to the positive direction. This is because PZT-5H is considered "softer" than PZT-5A and therefore both 90° and 180° switching processes may occur even though the electric field is smaller than E_c. Since the number of domains with opposite polarization is the same, the net polarization of the specimen is zero. From points b to C and c, PZT-5H domains undergo the same switching process as PZT-5A domains do.

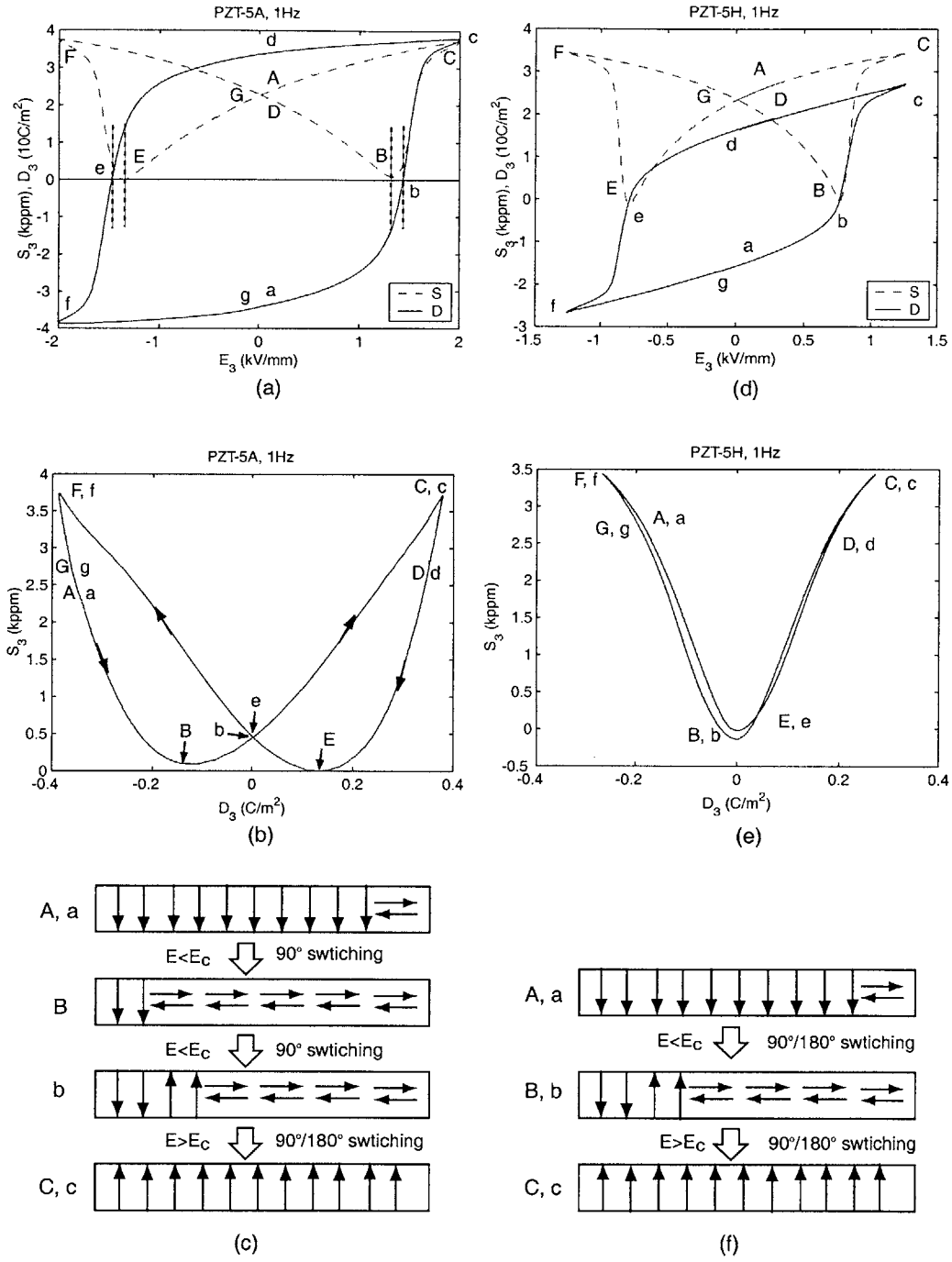

Figure 3-40: Discrepancy of domain switching between PZT-5A((a),(b),(c)) and PZT-5H((d),(e),(f)).

The key discrepancy between PZT-5A and PZT-5H is that PZT-5A requires two successive 90° reorientations to fulfill a domain reversal, which can be accomplished by an instantaneous 180° reversal for a softer material, such as PZT-5H. For hard material(PZT-5A), this is because only 90° reorientation is allowed when electric field is smaller than E_c. In contrast, both 90° and 180° switching processes may occur for soft material (PZT-5H) even though electric field is smaller than E_c. In addition, experimental results reported by Tsurumi *et al.*[68] also indicated that the velocity of the 90° domain wall motion was relatively low. As a result, the hysteresis of PZT-5A S-D curve is due to this slower 90° domain wall motion.

According to the findings by Zhou *et al.*[65], significant hysteresis was observed in the S-D curves at low frequencies, while simple parabolic S-D curves were observed at high frequencies. This is because there is enough time for the two-step 90° domain switching to take place at low frequencies. Although this phenomenon is not detected in each data of PZT-5A and PZT-5H in this work, as shown in Figure 3-39, similar observation can be found in the rate data of PZT-5A: the S-D curves at low frequency (0.1Hz or 1Hz) show more hysteretic behavior than that at high frequency (10Hz).

In summary, in order to improve the material model for PZT-5A, the hysteresis observed in the S-D curve must be included in the model. Although it may not be difficult to describe this hysteresis by a differential equation or a new internal variable, making the model thermodynamically consistent is the key obstacle. As a result, this modification will be left as a recommendation for future work.

3.4 Development of a 3-D Rate and Stress Dependent Piezoelectric Model

In the previous section, a rate dependent model of a piezoelectric material in one dimension has been developed. Although the 1-D models achieve second level accuracy, a fully 3-D model is still absent. In order to reach the second level goal, as defined in Table 1.1, the approach of the 1-D model is extended to three dimensions in this section.

3.4.1 Introduction to Ghandi's Tensor Invariants

It is natural to expand the energy function in three dimensions in terms of classic tensors proposed by Lines and Glass[63]:

$$A = \frac{1}{2}c^D_{ijkl}S_{ij}Skl - \frac{1}{2}h_{ijkl}S_{ij}D_kD_l + \frac{1}{2}\beta^S_{ij} + \frac{1}{4}\xi^S_{ijkl}D_jD_jD_kD_l. \tag{3.56}$$

This expression depends on the choice of coordinates and is only useful for single crystal materials because this expression is dependent on the choice of the coordinate system. However, piezoelectric ceramics have no preferred orientation because they are composed of various domains with arbitrary orientations. Consequently, the internal energy expression for ceramics shall be invariant with respect to rotations. To do so, Ghandi proposed an expression of free energy in terms of invariant inner products of the internal variables in the expansion. For example, consider the term $c^D_{ijkl}S_{ij}S_{kl}$ in Eq. 3.56. The tensor contains 81 elements which may be reduced to two independent quantities for an isotropic material. This term can be replaced by two terms with scalar coefficients:

$$c_{ijkl}S_{ij}S_{kl} \Rightarrow aS_{ii}S_{jj} + bS_{ij}S_{ji}. \tag{3.57}$$

Thus, the invariant form of Eq. 3.56 may be written as

$$U = aS_{ii}S_{jj} + bS_{ij}S_{ji} + cS_{ii}D_jD_j + dS_{ij}D_iD_j + eD_iD_i + fD_iD_iD_jD_j. \tag{3.58}$$

Transversely Isotropic Tensor Invariants

Since a poled piezoelectric material is transversely isotropic, a unit vector along the direction of polarization of the material a_i is used in addition to the strain S_{ij} and the electric displacement D_i in the expansion of the energy function. It is essential to specify an

expression for the energy in terms of S_{ij} and D_i which satisfies rotational symmetry about the polarization axis a_i. From an integrity basis for the isotropic functions by Zhang[64] and using the fact that any complete representation for isotropic functions of S_{ij}, D_i, and a_i may be regarded as a complete representation for a function of S_{ij} and D_i under the symmetry group characterized by rotation about a_i, Ghandi summarized a complete set of the corresponding tensor invariants :

$$\begin{array}{lll} S_{ii}, & S_{ij}S_{ji}, & S_{ij}S_{jk}S_{ki}, \\ D_iD_i, & S_{ij}D_iD_j, & S_{ij}S_{jk}D_iDk, \\ a_ia_i, & D_{ij}a_iaj, & S_{ij}S_{jk}a_iak, \\ a_iD_i, & (S_{ij}+S_{ji})a_iDj, & (S_{ij}S_{jk}+S_{kj}S_{ji})a_iD_k. \end{array} \tag{3.59}$$

Ghandi also presented these invariants in terms of T_{ij} and D_i:

$$\begin{array}{llll} & I_1 = a_ia_i, & I_2 = a_iD_i, & I_3 = D_iD_i, \\ J_0 = T_{ii}, & J_1 = T_{ij}a_ia_j, & J_2 = T_{ij}(a_iD_j + a_jD_i), & J_3 = T_{ij}D_iD_j, \\ K_0 = T_{ij}T_{ji}, & K_1 = T_{ik}T_{kj}a_ia_j, & K_2 = T_{ik}T_{kj}(a_iD_j + a_jD_i), & K_3 = T_{ik}T_{kj}D_iD_j, \\ L_1 = T_{ij}T_{jk}T_{ki}. & & & \end{array} \tag{3.60}$$

Using these tensor invariants, Ghandi suggested that a Taylor series expansion of the energy may be presented as:

$$\begin{aligned} G_1 &= f + f_0J_0 + f_1J_1 + f_3J_3 + f_{00}J_0J_0 + f_{01}J_0J_1 + f_{02}J_0J_2 + f_{03}J_0J_3 \\ &+ f_{11}J_1J_1 + f_{12}J_1J_2 + f_{13}J_1J_3 + f_{22}J_2J_2 + f_{23}J_2J_3 + f_{33}J_3J_3 \\ &+ g_0K_0 + g_1K_1 + g_2K_2 + g_3K_3 + \ldots, \end{aligned} \tag{3.61}$$

where each f and g is a function of the electric invariants (I_1, I_2, I_3) to an arbitrary order. Selection of the terms to be included is determined by the availability of experimental data when conducting the least squares regression for model optimization.

Matrix Implementation of Tensor Invariants and their Derivatives

To implement the model in the finite element code, Ghandi also expressed these tensor invariants and their derivatives in matrix notation as summarized in Table 3.8 where T

denotes stress in Voigt notation and $\hat{\mathbb{T}}$ denotes stress as a 3×3 matrix. That is:

$$\hat{\mathbb{T}} = \begin{bmatrix} T_{11} & T_{12} & T_{13} \\ T_{12} & T_{22} & T_{23} \\ T_{13} & T_{23} & T_{33} \end{bmatrix}, \qquad T = \begin{bmatrix} T_{11} & T_{22} & T_{33} & T_{23} & T_{13} & T_{12} \end{bmatrix}^{\top}. \tag{3.62}$$

An additional operator $(\ )^{\times}$ was introduced by Ghandi to map a 3×1 vector into a 3×6 matrix as follows:

$$\mathbf{v}^{\times} = \begin{bmatrix} v_1 & 0 & 0 & 0 & v_3 & v_2 \\ 0 & v_2 & 0 & v_3 & 0 & v_1 \\ 0 & 0 & v_3 & v_2 & v_1 & 0 \end{bmatrix}. \tag{3.63}$$

Using this operator, one can express the tensor inner product of a symmetric tensor and a vector $(T_{ij}D_j)$ in two various notations:

$$T_{ij}D_j \qquad \Leftrightarrow \qquad \hat{\mathbb{T}}\mathbf{D} = \mathbf{D}^{\times}\mathbf{T}. \tag{3.64}$$

The first notation is useful for differentiating the invariant with respect to $\mathbf{D}$, while the second notation is appropriate for the derivatives with respect to $\mathbf{T}$.

Relationship between a_i and D_i^*

The invariant tensors listed in Eq. 3.60 show a complete representation for a function of S_{ij} and D_i under the symmetry group characterized by rotation about a_i. The vector a_i used to specify the direction of transverse isotropy in the energy expansion is exactly the same vector as the net remnant polarization of the ceramics, D_i^*. Hence, all occurrences of a_i in the three dimensional model shall be substituted by D_i^*.

Table 3.8: Derivatives of various invariants of symmetric tensor T_{ij} and vectors D_i and a_i, where $\mathbf{e} = [1\ 1\ 1\ 0\ 0\ 0]^\top$ and $\mathbf{R} = \text{diag}([1\ 1\ 1\ 2\ 2\ 2])$.

	G_1	G_1	$\partial G_1/\partial \mathbf{T}$	$\partial^2 G_1/\partial \mathbf{T}^2$	$\partial G_1/\partial \mathbf{D}$	$\partial^2 G_1/\partial \mathbf{D}^2$	$\partial^2 G_1/(\partial \mathbf{T}\partial \mathbf{D})$
I_1	$a_i a_i$	$\mathbf{a}^\top\mathbf{a}$	$\mathbf{0}$	0	$\mathbf{0}$	0	0
I_2	$D_i a_i$	$\mathbf{D}^\top\mathbf{a}$	$\mathbf{0}$	0	$\mathbf{a}$	0	0
I_3	$D_i D_i$	$\mathbf{D}^\top\mathbf{D}$	$\mathbf{0}$	0	$\mathbf{2D}$	$2\mathbf{I}$	0
J_0	T_{ii}	$\mathbf{T}^\top\mathbf{e}$	$\mathbf{e}$	0	$\mathbf{0}$	0	0
K_0	$T_{ij}T_{ji}$	$\mathbf{T}^\top\mathbf{R}\mathbf{T}$	$\mathbf{2RT}$	$\mathbf{2R}$	$\mathbf{0}$	0	0
J_1	$T_{ij}a_i a_j$	$\mathbf{a}^\top\hat{\mathbb{T}}\mathbf{a}$	$\mathbf{a}^{\times\top}\mathbf{a}$	0	$\mathbf{0}$	0	0
J_2	$T_{ij}(D_i a_j + a_i D_j)$	$\mathbf{a}^\top\hat{\mathbb{T}}\mathbf{D} + \mathbf{a}^\top\hat{\mathbb{T}}\mathbf{a}$	$\mathbf{a}^{\times\top}\mathbf{D} + \mathbf{D}^{\times\top}\mathbf{a}$	0	$\mathbf{2}\hat{\mathbb{T}}\mathbf{a}$	0	$\mathbf{2a}^\times$
J_3	$T_{ij}D_i D_j$	$\mathbf{D}^\top\hat{\mathbb{T}}\mathbf{D}$	$\mathbf{D}^{\times\top}\mathbf{D}$	0	$\mathbf{2}\hat{\mathbb{T}}\mathbf{D}$	$2\hat{\mathbb{T}}$	$\mathbf{2a}^\times$
K_1	$T_{ik}T_{kj}a_i a_j$	$\mathbf{a}^\top\hat{\mathbb{T}}^2\mathbf{a}$	$\mathbf{2a}^{\times\top}\mathbf{a}^\times\mathbf{T}$	$\mathbf{2a}^{\times\top}\mathbf{a}^\times$	$\mathbf{0}$	0	0
K_2	$T_{ik}T_{kj}(D_i a_j + a_i D_j)$	$\mathbf{a}^\top\hat{\mathbb{T}}^2\mathbf{D}$ $+\mathbf{D}^\top\hat{\mathbb{T}}^2\mathbf{a}$	$\mathbf{2a}^{\times\top}\mathbf{D}^\times\mathbf{T}$ $+\mathbf{2D}^{\times\top}\mathbf{a}^\times\mathbf{T}$	$\mathbf{a}^{\times\top}\mathbf{D}^\times$ $+\mathbf{D}^{\times\top}\mathbf{a}^\times$	$\mathbf{2}\hat{\mathbb{T}}^2\mathbf{a}$	0	$2(\hat{\mathbb{T}}\mathbf{a}^\times + (\hat{\mathbb{T}}\mathbf{a})^\times)$
K_3	$T_{ik}T_{kj}D_i D_j$	$\mathbf{D}^\top\hat{\mathbb{T}}^2\mathbf{D}$	$\mathbf{2D}^{\times\top}\mathbf{D}^\times\mathbf{T}$	$\mathbf{2D}^{\times\top}\mathbf{D}^\times\mathbf{T}$	$\mathbf{2}\hat{\mathbb{T}}^2\mathbf{D}$	$2\hat{\mathbb{T}}^2$	$2(\hat{\mathbb{T}}\mathbf{D}^\times + (\hat{\mathbb{T}}\mathbf{D})^\times)$

3.4.2 3-D Rate Rules

After expanding the energy in terms of tensor invariants, the next step is to specify the evolution rule of $\mathbf{D}^*$ for three dimensional problems. This can be done by modifying the rate rule in Eq. 3.34 as

$$\frac{d\mathbf{D}^*}{dt} = \frac{\mathbf{D} - \mathbf{D}^*}{\tau} \left\{ 1 - exp\left[- \left(\frac{\|\mathbf{D} - \mathbf{D}^*\|}{\Delta D_c} \right)^{2\alpha} \right] \right\}, \tag{3.65}$$

where $\mathbf{D}$ and $\mathbf{D}^*$ are vectors in three dimensions, i.e.

$$\mathbf{D} = [D_1,\ D_2,\ D_3]^\top, \qquad \mathbf{D}^* = [D_1^*,\ D_2^*,\ D_3^*]^\top,$$

and $\|\mathbf{D} - \mathbf{D}^*\|$ is the ℓ_2 norm of the vector $(\mathbf{D} - \mathbf{D}^*)$.

3.5 Finding 3-D Material Parameters

The procedure for finding optimized 1-D material parameters can be modified to find 3-D material parameters. To do so, the elastic Gibbs free energy shall be first expanded in terms of tensor invariants:

$$G_1 = \sum_k x_k G_1^{(k)}(\mathbf{T}, \mathbf{D}, \mathbf{D}^*), \tag{3.66}$$

where x_k is the coefficient of the selected energy function. This expression yields the electric field and strain as

$$\mathbf{E} = \sum_k x_k \mathbf{E}^{(k)}(\mathbf{T}, \mathbf{D}, \mathbf{D}^*), \tag{3.67}$$

$$\mathbf{S} = \sum_k x_k \mathbf{S}^{(k)}(\mathbf{T}, \mathbf{D}, \mathbf{D}^*), \tag{3.68}$$

where $\mathbf{E}$ is a 3×1 vector and $\mathbf{S}$ is a 6×1 vector. Next, the strain and polarization response subjected to both longitudinal and transverse tests shall be included in the cost function such that Eq. 3.47 becomes:

$$\mathbf{e} = \sum_{z=1}^{n} w_{E_z} (E_{3z}(\hat{\mathbf{D}}_z, \hat{\mathbf{D}}_z^*, \hat{\mathbf{T}}_z) - \hat{E}_{3z})^2 + \sum_{z=1}^{n} \sum_{i=1}^{3} w_{S_z} (S_{iz}(\hat{\mathbf{D}}_z, \hat{\mathbf{D}}_z^*, \hat{\mathbf{T}}_z) - \hat{S}_{iz})^2, \tag{3.69}$$

where $\hat{}$ denotes the measured data. E_{3z} and S_{iz} are the corresponding components in Eq. 3.67 and 3.68. Since only E_3, S_1, S_2, and S_3 are measured in Chapter 2, only these components in Eq. 3.67 and 3.68 are included in the cost function, Eq. 3.69.

After defining this cost function, one can then obtain the optimized material model in three dimensions by minimizing the cost function subjected to various rate parameters of the 3-D rate rule in Eq. 3.65. The detailed procedure has been described in Section 3.3.1–3.3.4 except that the cost function (Eq. 3.69), the rate rule (Eq. 3.65), and the energy expansion (Eq. 3.66) shall be used instead.

3.5.1 Optimized 3-D PZT-5H Model Parameters

Using this modification for the 3-D model and following the procedure described in Section 3.3.1 –3.3.4, one can obtain the optimized material parameters for PZT-5H as characterized in Chapter 2. To fit the data, weights w_E=50 and w_S=1 were used, and the Gibbs energy function was expanded in 27 terms as suggested by Ghandi. Table 3.9 lists these terms and their optimal coefficients. The optimized rate parameters are found to be τ=0.1(ms), ΔD_c=0.03 (C/m^2), and α=7.

Table 3.9: Energy expansions for PZT-5H in 3-D and their optimal coefficients.

$G_1^{(k)}$	x_k	$G_1^{(k)}$	x_k	$G_1^{(k)}$	x_k
I_2	-29.0122	J_3	-73.7834	K_0	-34.7323
I_3	14.4313	J_3I_2	-2.8420×10^3	K_0I_1	-1.7861×10^3
I_3I_3	7.1147	J_3I_3	1.8671×10^3	K_0I_2	2.8609×10^3
J_0I_1	9.3314	J_0J_0	9.6466	K_0I_3	-810.6531
J_0I_2	3.5402	$J_0J_0I_1$	1.6667×10^3	K_1	4.7744×10^3
J_0I_3	3.2426	$J_0J_0I_2$	-2.3131×10^3	K_2	-4.0868×10^3
$J_0I_3I_3$	-9.9131	$J_0J_0I_3$	606.0236	K_3	3.3175×10^3
J_1	-55.1078	J_0J_1	-5.1591×10^3		
J_1I_2	1.0125×10^3	J_0J_2	4.1821×10^3		
J_2	40.8231	J_0J_3	-3.3173×10^3		

Figures 3-41–3-44 show the correlation between the data and the model for PZT-5H. As can be seen, the material model effectively captures the significant trends of the piezoelectric behaviors under various mechanical loading conditions. In addition, compared to the data shown in Figure 2-45, this 3-D model is able to simulate the rate dependency of PZT-5H as shown in Figure 3-45. Finally, this 3-D PZT-5H model also achieves the targeted precision of Stage 2, as defined in Table 1.1.

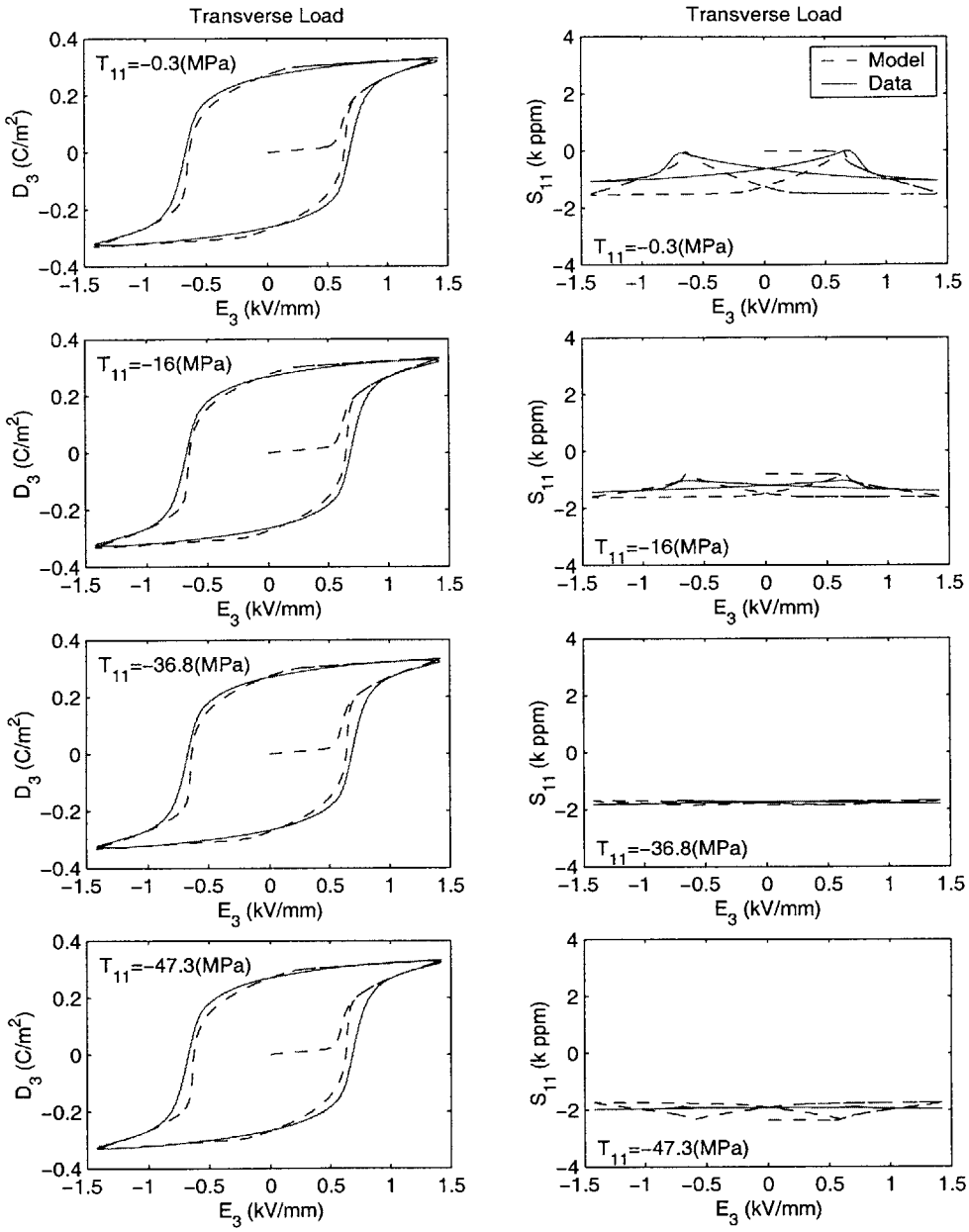

Figure 3-41: Correlation between 3-D model and data of PZT-5H transverse tests.

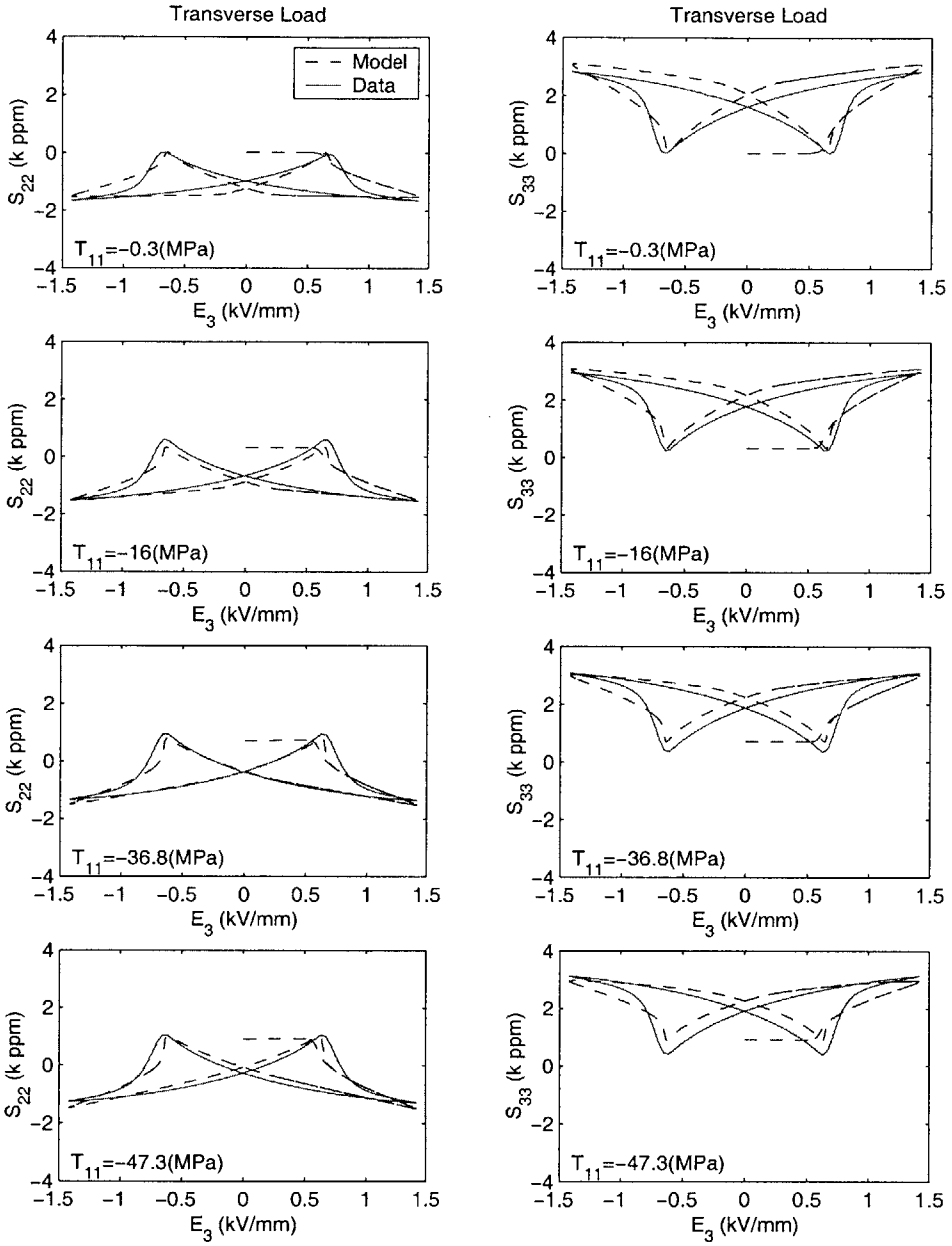

Figure 3-42: Correlation between 3-D model and data of PZT-5H transverse tests (Cont.)

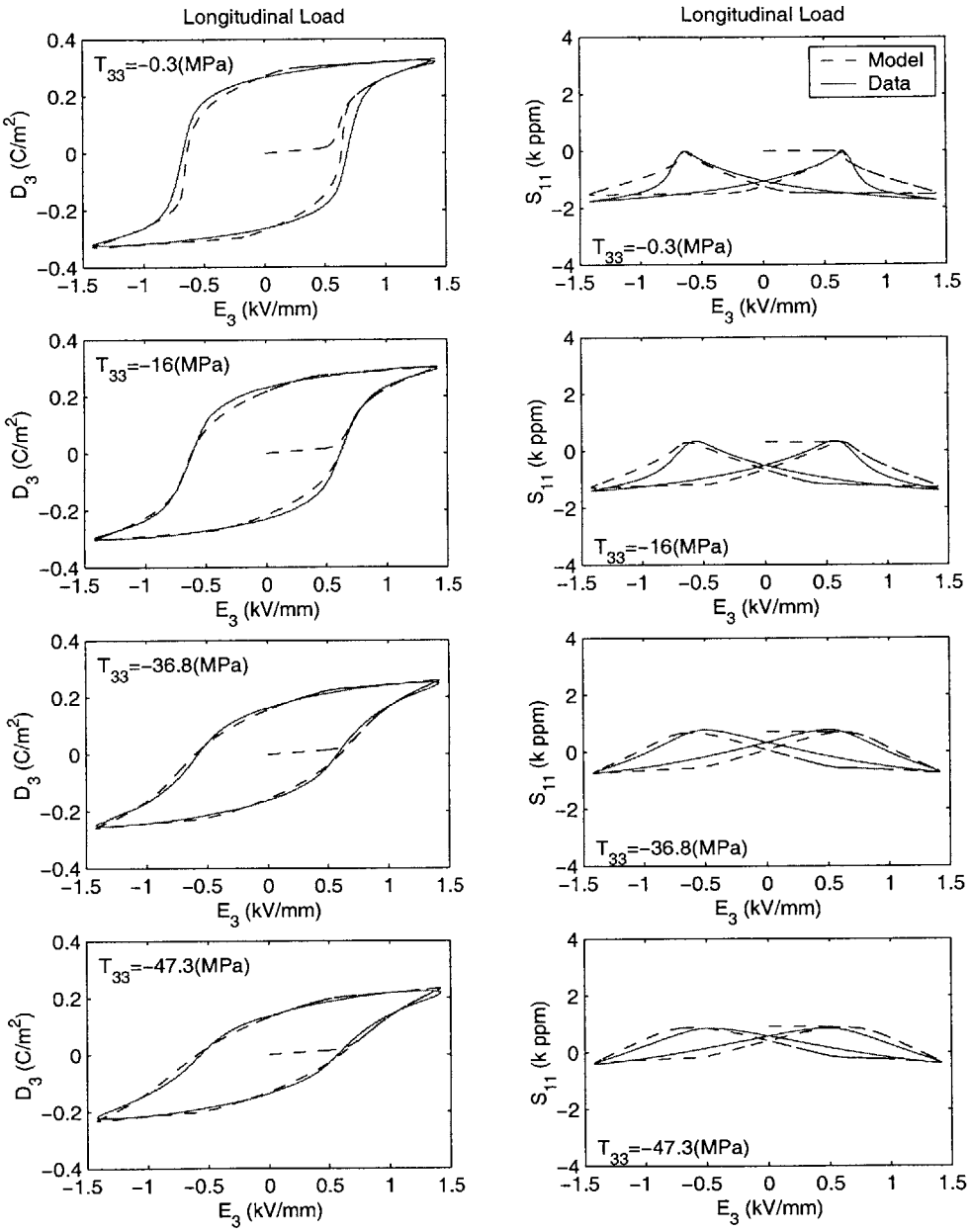

Figure 3-43: Correlation between 3-D model and data of PZT-5H longitudinal tests.

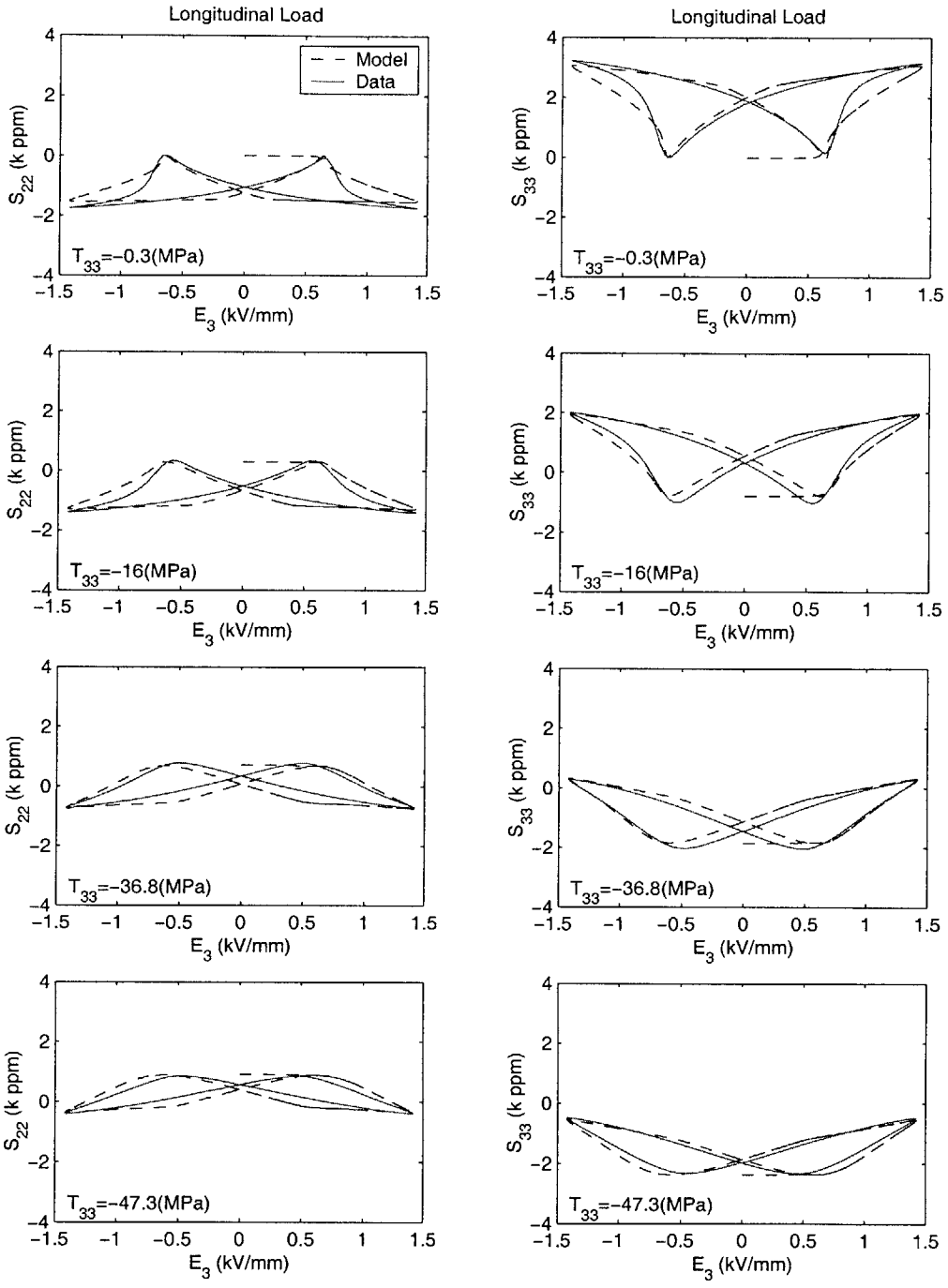

Figure 3-44: Correlation between 3-D model and data of PZT-5H longitudinal tests (Cont.)

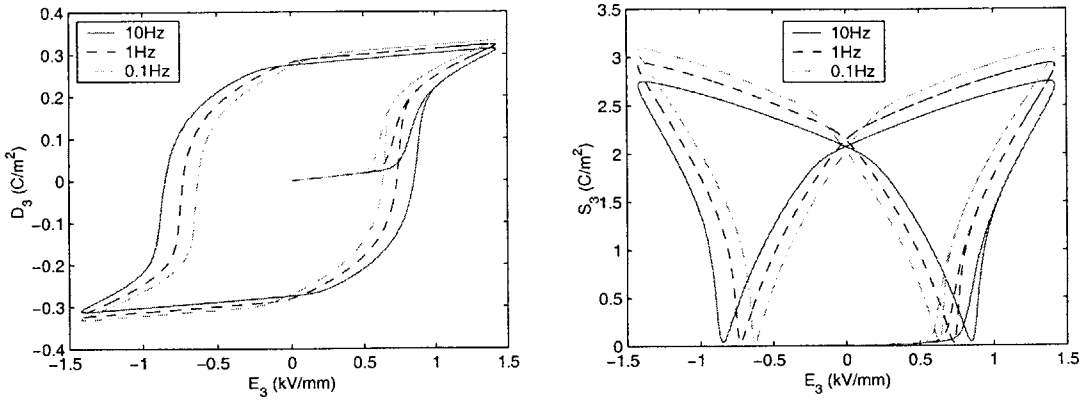

Figure 3-45: Simulated rate dependency of PZT-5H using 3-D model

3.5.2 Optimized 3-D PZT-5A Model Parameters

As presented in Chapter 2, Batch A and Batch B of PZT-5A specimens show inconsistent coercive fields. This inconsistency may cause difficulty in optimizing the material properties. To avoid this problem, the data of both transverse and longitudinal tests for the least squares regression shall be chosen from the same specimen batch. As a result, Batch-B data under compression up to 50MPa, shown in Figures 2-50–2-56, were used to obtain the optimized parameters. With the weights w_E=50 and w_S=1 and the same energy expansion for PZT-5H, one can find the optimized coefficients of energy functions as listed in Table 3.10. These results are based on the following optimized rate parameters: τ=0.1(ms), ΔD_c=0.01 (C/m^2), and α=7.

Figures 3-46–3-49 show the correlation between the data and the model for PZT-5A. As can be seen, the material model effectively captures the significant trends of piezoelectric behaviors under various mechanical loading conditions. In addition, compared to the data shown in Figure 2-46, this 3-D model is able to simulate the rate dependency of PZT-5A as shown in Figure 3-50. However, this 3-D PZT-5A model barely accomplishes the targeted accuracy and does not perform as well as the 3-D PZT-5H model. This can be explained by the same reason as discussed in Section 3.3.7, specifically that PZT-5A exhibits a special hysteretic relation between strain and electric displacement that simple Taylor expansion

cannot simulate well. To improve the model, a new internal variable must be defined, and its rate rule must be also derived to specify the S-D hysteresis of PZT-5A.

Table 3.10: Energy expansions for PZT-5A in 3-D and their optimal coefficients.

$G_1^{(k)}$	s_k	$G_1^{(k)}$	s_k	$G_1^{(k)}$	s_k
I_2	-169.2308	J_3	-565.8915	K_0	-43.7857
I_3	85.0693	J_3I_2	-12967	K_0I_1	152930
I_3I_3	2.4812	J_3I_3	8627.7	K_0I_2	-308880
J_0I_1	-81.0137	J_0J_0	11.5568	K_0I_3	156050
J_0I_2	178.1540	$J_0J_0I_1$	-155280	K_1	-237990
J_0I_3	-77.2817	$J_0J_0I_2$	313630	K_2	242210
$J_0I_3I_3$	-28.2338	$J_0J_0I_3$	-158360	K_3	-246150
J_1	-572.5728	J_0J_1	228990		
J_1I_2	4378.9	J_0J_2	-233590		
J_2	543.0814	J_0J_3	238000		

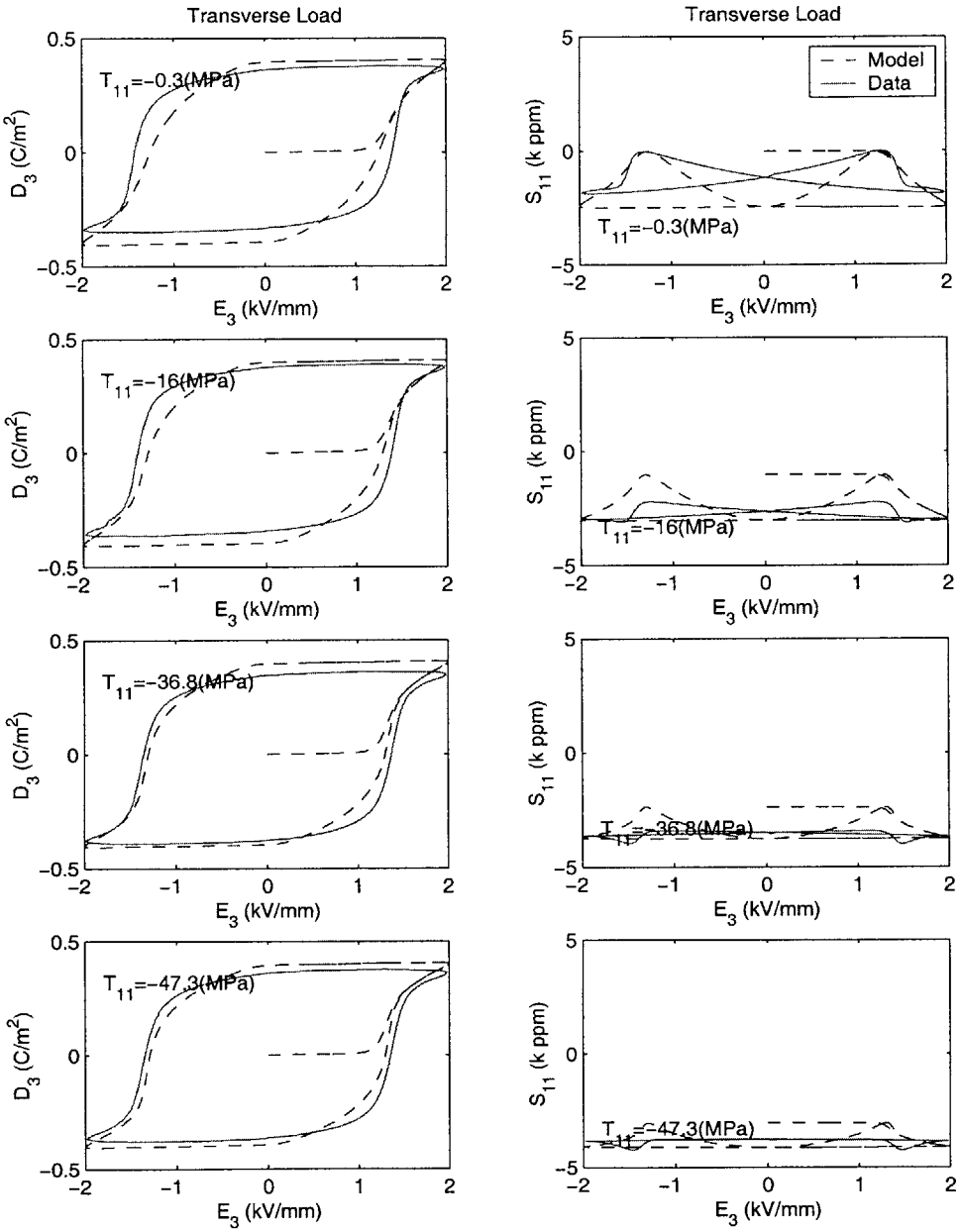

Figure 3-46: Correlation between 3-D model and data of PZT-5A transverse tests.

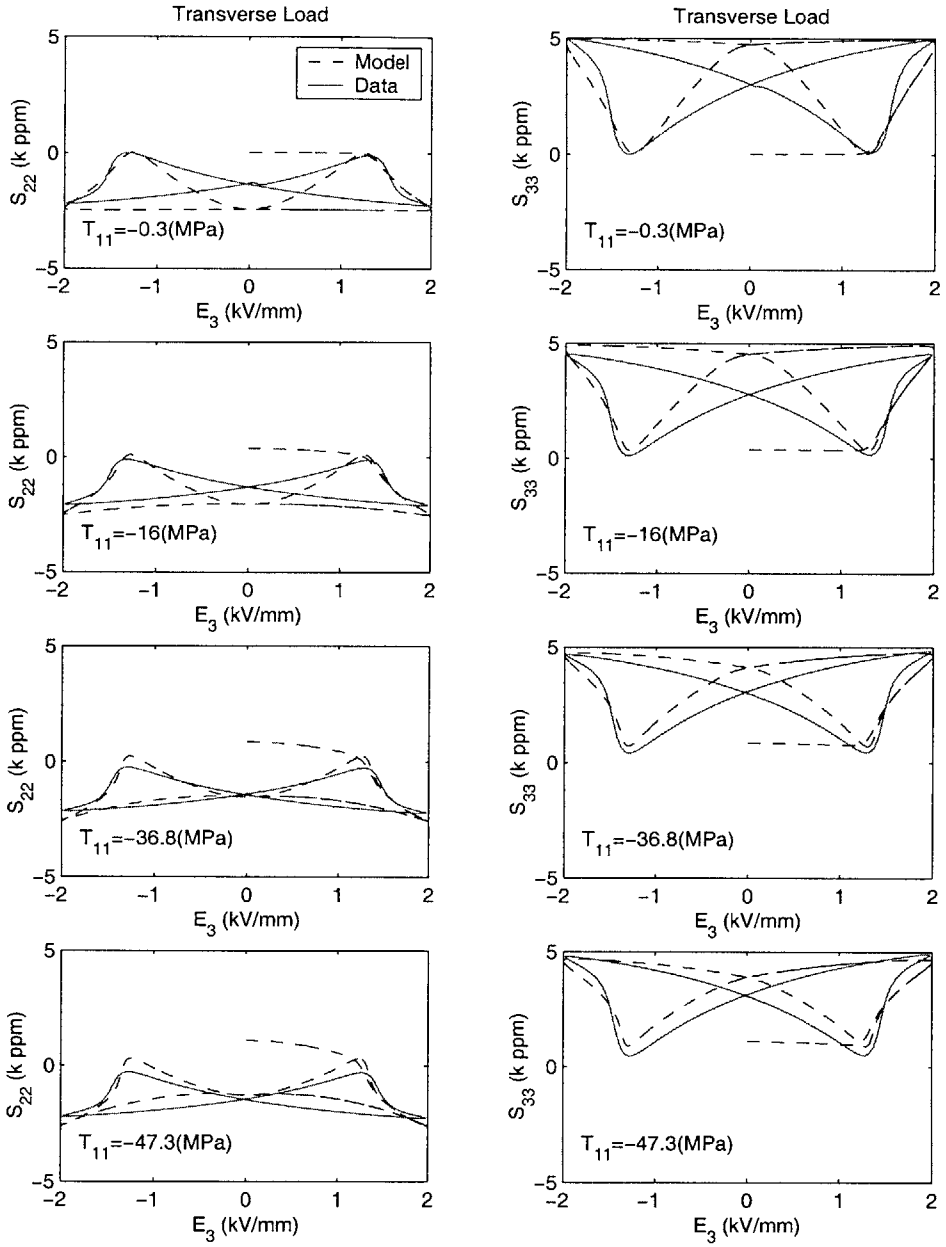

Figure 3-47: Correlation between 3-D model and data of PZT-5A transverse tests (Cont.)

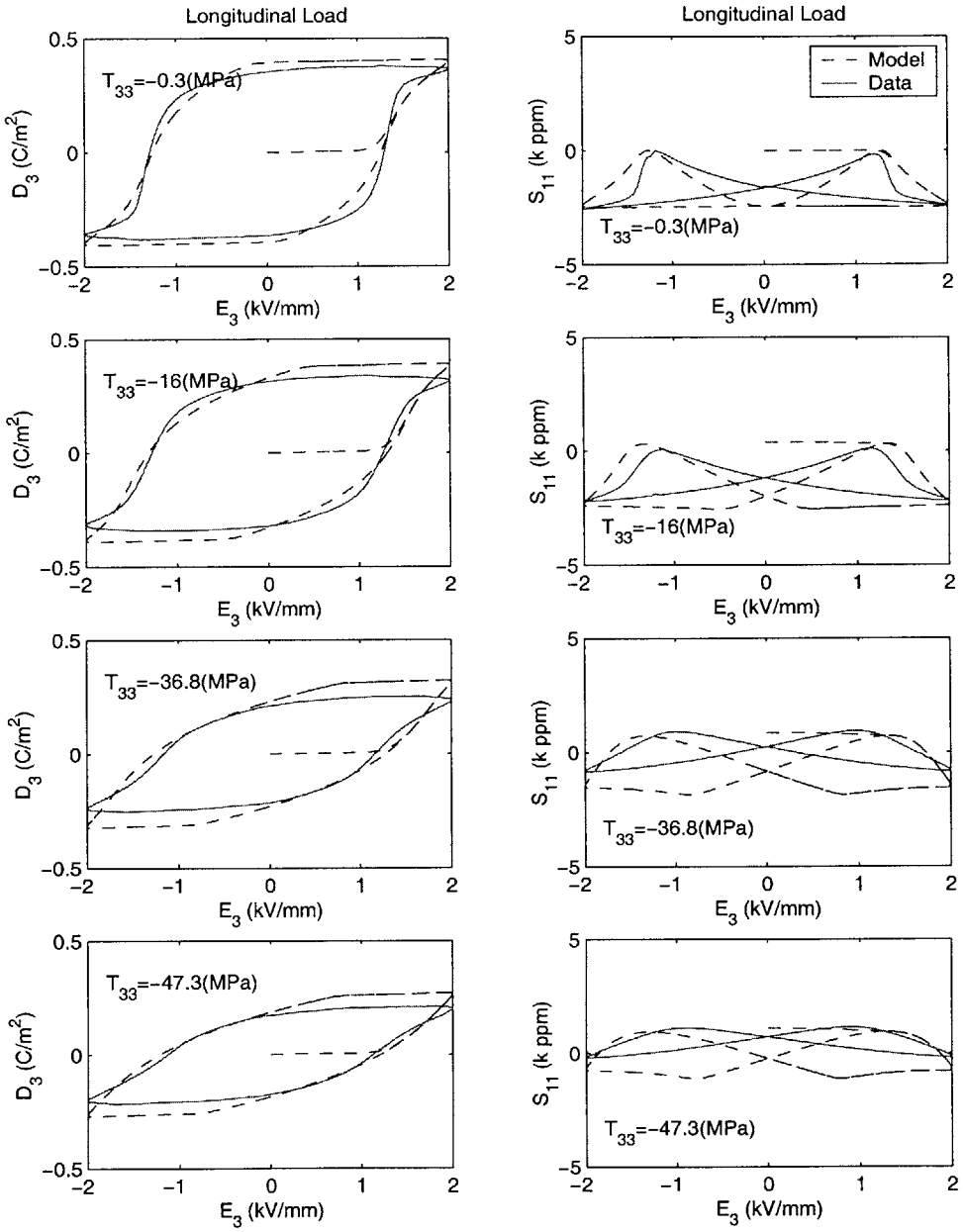

Figure 3-48: Correlation between 3-D model and data of PZT-5A longitudinal tests.

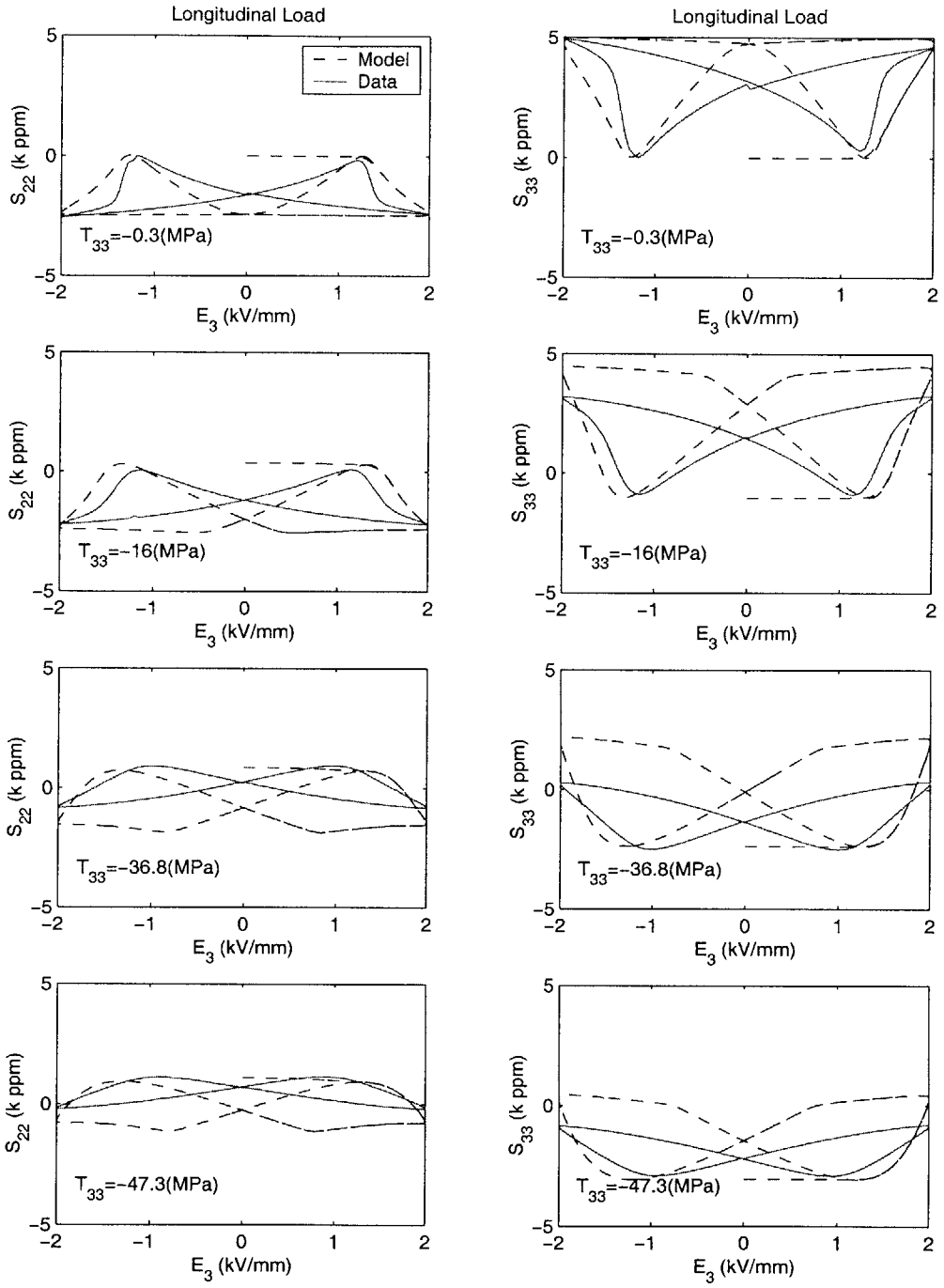

Figure 3-49: Correlation between 3-D model and data of PZT-5A longitudinal tests (Cont.)

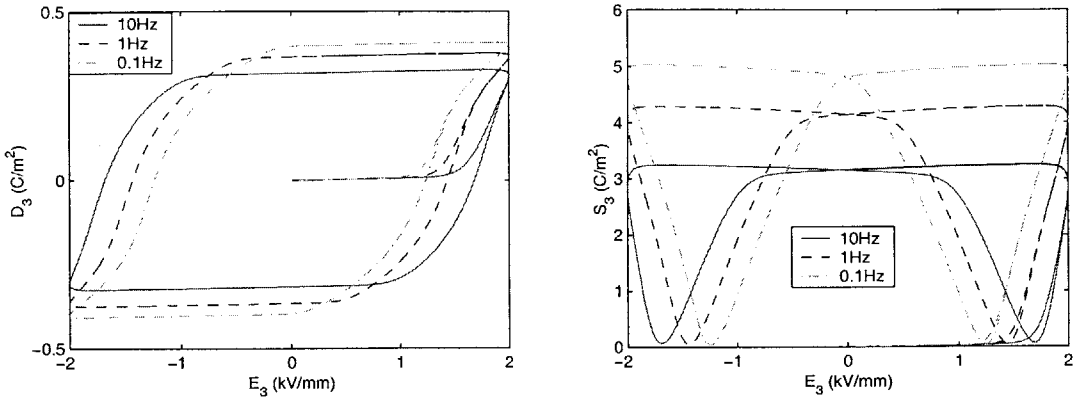

Figure 3-50: Simulated rate dependency of PZT-5A using 3-D model

3.6 Summary of Model Development

In this chapter, models for one and three dimensional piezoelectric response under various loading conditions have been developed using a thermodynamic framework and an evolution rule of the internal variable D^*. The model parameters for PZT-5A and PZT-5H have been optimized by minimizing the error between model fits and measured data. In general, the models are capable of predicting major trends of the material response, such as stress dependency and rate dependency, within the targeted accuracy of Stages 1 and 2, as defined in Table 1.1. However, it is found that the PZT-5H model performs much better than the PZT-5A model. This is because of the special hysteric relationship between strain and polarization of PZT-5A, which can be explained by the variance between 90° and 180° domain switching processes. In order to improve the material model for PZT-5A, a new rate rule is required that incorporates a new internal variable to describe this S-D hysteresis. Although it may not be difficult to do so, making the model thermodynamically consistent is the key obstacle. As a result, this modification will be left as a future work for the successors. Despite this, it is also of interest to test the models developed in this chapter against the criteria of Stage 3. This examination will be discussed in the next chapter.

Chapter 4

Model Validation for Application at Stage 3

In the previous chapter, the model correlated well with the data within the targeted precision of Stages 1 and 2. It is also of interest to test the models against the criteria of Stage 3. The task of Stage 3 is to condense the data into a material library or a design guide for material selection. This includes the information for actuation and energy harvesting applications. Since this information is obtained from the minor loop test, this chapter will first examine the minor loop performance. This will be followed by the model validation for PZT-5H power generation. The PZT-5A actuation predicted by the model will then be evaluated. Finally, the model performance against Stage 3 criteria will be summarized.

4.1 PZT-5H Minor Loop Validation

The purpose of the minor loop test is to examine the response while subject to moderate electric fields, usually below the coercive field so that the material will not be re-polarized by high electric fields. To validate the minor loop behavior, a test in addition to those in Chapter 2 was also conducted. Figure 4-1 shows the driving command of the electric field E_3 of this test. During the test, behaviors of strain S_3 and electric displacement D_3 were recorded and have been compared to the simulated response by the 1-D and 3-D models developed in the previous section. In order to facilitate the simulation for different loading conditions, graphical simulation block diagrams using SIMULINK were built and documented

in detail in Appendix A. Since the test was performed by exciting an electric field, the short circuit simulations in Appendices A.3 and A.4 shall be used for 1-D and 3-D, respectively.

Figures 4-2 and 4-3 show the time history correlation between data and simulation. Figures 4-4 and 4-5 also present the modeled and measured relations between electric field and electric displacement and electric field and strain. As can be seen, both 1-D and 3-D models are capable of simulating the minor loop response including the small hysteretic loops shown in the data. However, the values predicted by the models are not accurate. This is not surprising because the models are not perfectly flawless as discussed in the previous chapter. In addition, the PZT-5H specimen of this minor loop test is not from the same batch as those test specimens used by Ghandi [35]. Compared to the test data shown by Ghandi [35], the peak strain and electric displacement of this minor loop test specimen are higher. Nevertheless, the models are able to predict the minor loop behaviors within the factor of 2.

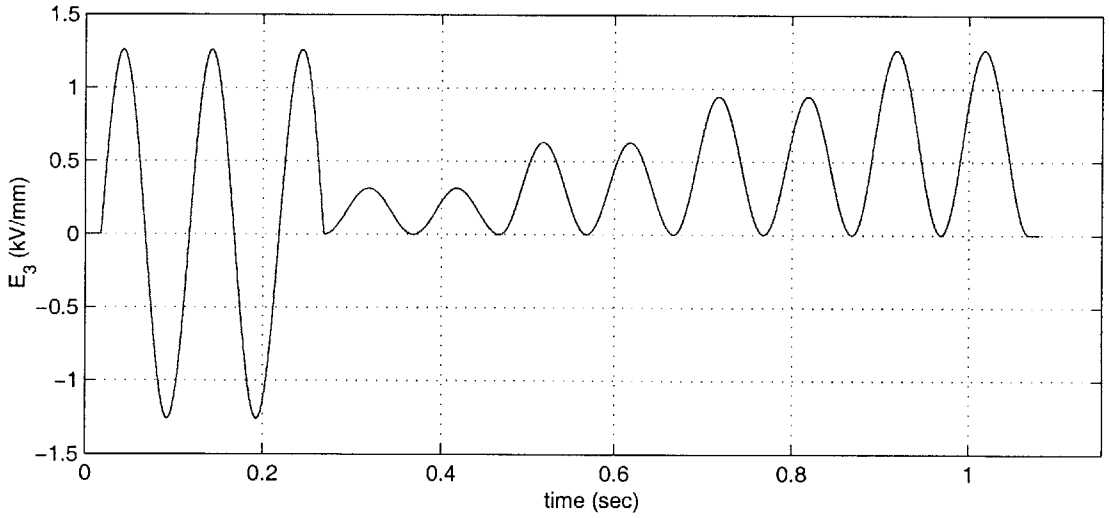

Figure 4-1: Electric driving command for minor loop test.

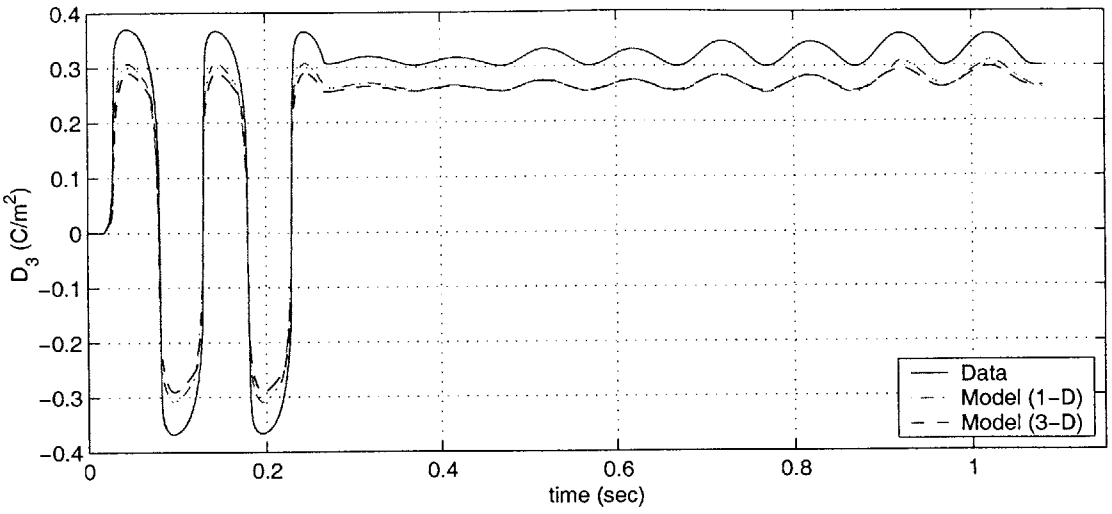

Figure 4-2: Time history correlation between modeled and measured electric displacement of minor loop test for PZT-5H.

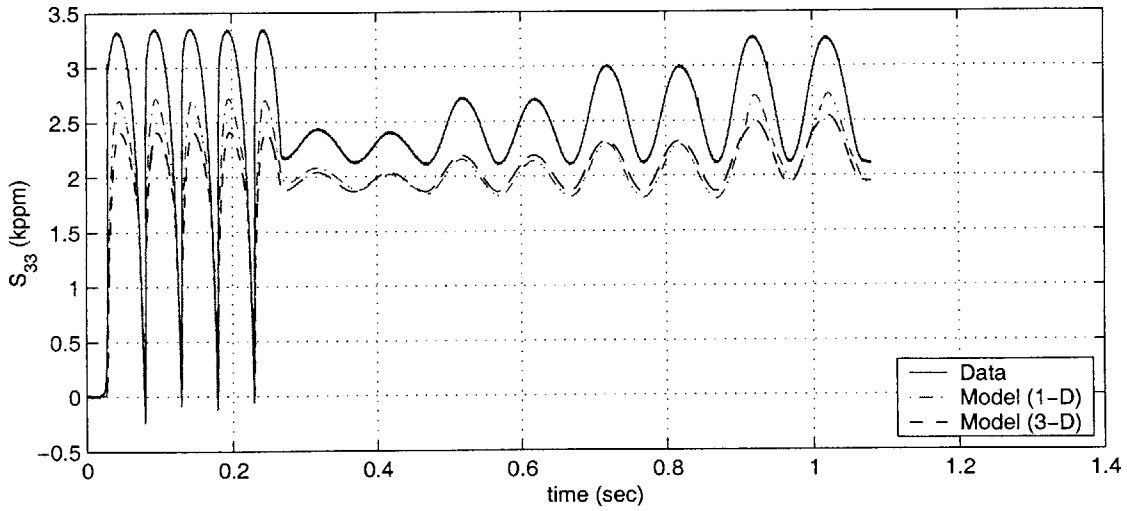

Figure 4-3: Time history correlation between modeled and measured strain of minor loop test for PZT-5H.

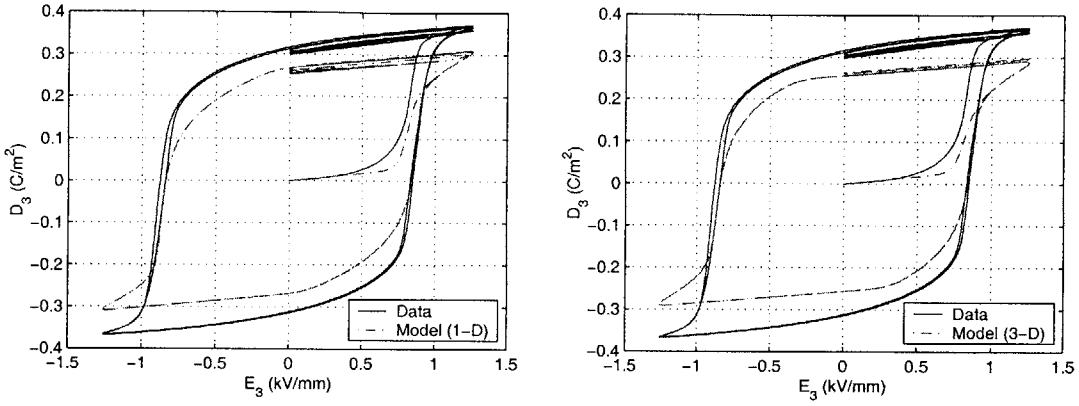

Figure 4-4: Correlation between modeled and measured electric displacement of minor loop test for PZT-5H. Left: 1-D model; right: 3-D model.

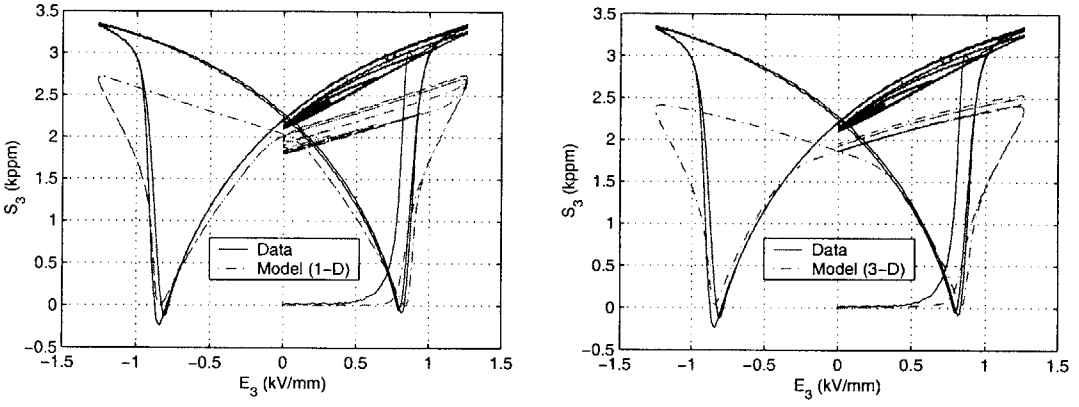

Figure 4-5: Correlation between modeled and measured strain of minor loop test for PZT-5H. Left: 1-D model; right: 3-D model.

4.2 Model Validation for PZT-5H Power Generation

It is also of interest to investigate if both 1-D and 3-D models are capable of predicting the material properties of PZT-5H for piezoelectric energy harvesting application. To do so, generalized piezoelectric constants including those under short circuit and open circuit tests shall be examined first. In addition, the response of piezoelectric specimens subjected to compression and shunted by the diode circuit shall be analyzed.

4.2.1 Validation of Generalized Piezoelectric Constants under Short Circuit

In order to simulate the generalized piezoelectric constant under short circuit, the same SIMULINK block diagram for the minor loop test discussed in the previous section can be used without change. To produce a poled piezoelectric specimen in the model, half a cycle of a 0.1Hz sinusoidal wave can be used as the polarizing signal. The final values of simulated D and D^* during this excitation represent the states of the poled material.

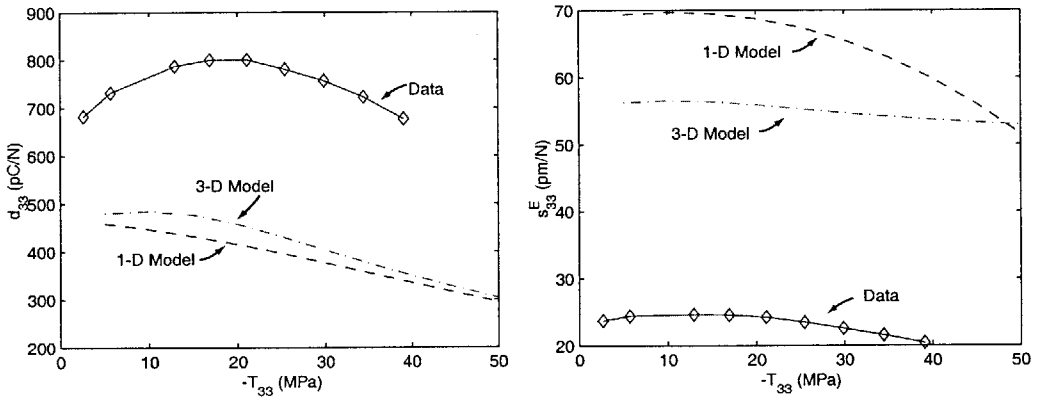

Figure 4-6: Comparison between the predicted and measured generalized d_{33} (left) and s^E_{33} (right).

To predict the generalized d_{33} and s^E_{33} constants, a 10Hz sinusoidal compression wave was used as a driving signal under the condition that electric field is constrained to be zero. The generalized constants were extracted using the same definition in Chapter 2. Figure 4-6 presents the comparison between the predicted and measured generalized d_{33} and s^E_{33}

constants. Unfortunately, the models fail to predict accurate values of the generalized constants under the short circuit condition. The explanation of this bad correlation will be discussed at the end of this section. However, the models do show the trend that the generalized constants decrease as compression increases. In addition, as can be seen, the 3-D model performs better than the 1-D model.

4.2.2 Validation of Generalized Piezoelectric Constants under Open Circuit

In order to simulate the generalized piezoelectric constant under open circuit, new SIMULINK models were built and are shown in detail in Appendices A.5 and A.7. Values of D and D^* which represent the poled states of the materials are also required as the initial conditions of the models. To predict the generalized g_{33} and s_{33}^D constants, a 10Hz sinusoidal compression wave was used as a driving signal under the condition that electric displacement is constrained to be constant. The generalized constants were extracted using the same definition in Chapter 2. Figure 4-7 presents the comparison between the predicted and measured generalized g_{33} and s_{33}^D constants, respectively.

Unfortunately, both the 1-D and 3-D models fail to predict accurate values of the generalized constants under open circuit condition. The explanation of this bad correlation will be discussed at the end of this section. In addition, the models do not capture the decreasing trend of g_{33} as compression increases. This is because no conduction effect is considered in the models. Recall the discussion in Section 3.2.1 that the electric conduction plays a significant role in the material behavior if it is under charge source control. This is the same situation with the measurement of g_{33}. During the test, two paths of conduction are possible: one is the internal resistance of the material itself, and the other is the finite impedance of the voltage meter. The former has been measured by Harper [36], and its corresponding resistance is converted to be 1.87GΩ. The latter is exactly known as 10GΩ for the 10Hz test. To account for the loss due to this electric conduction, the SIMULINK models were modified by including a resistor R, as shown in Appendices A.6 and A.8. Although this modification does not improve the capability of predicting an accurate g_{33} constant, both the 1-D and 3-D models have been improved to capture the phenomenon shown in Figure 4-7 that the g_{33} constant decreases as the compression increases.

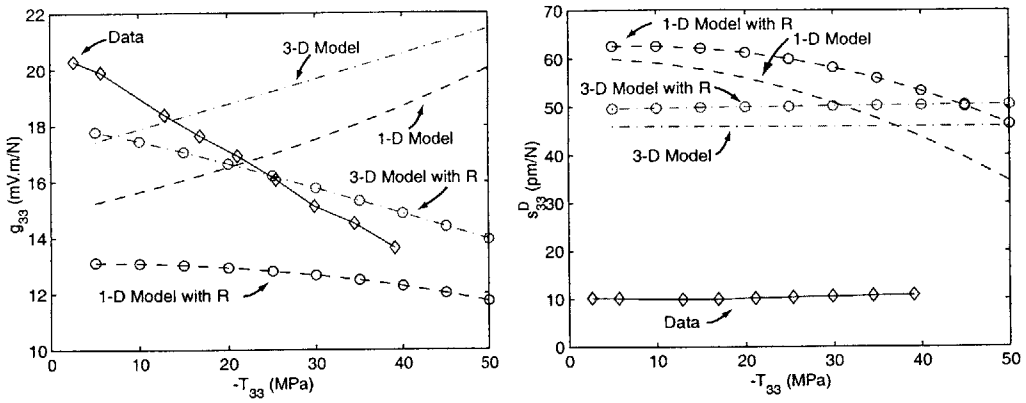

Figure 4-7: Comparison between the predicted and measured generalized g_{33} (left) and s^D_{33} (right).

4.2.3 Validation of Diode Circuit Response

To simulate the nonlinear response of a piezoelectric specimen subjected to compression and connected to the diode circuit, approriate SIMULINK models were built and are shown in detail in Appendices A.9 and A.10. Figures 4-8, 4-9, and 4-10 show the comparison of the simulated response and data of the current flowing through the battery in the diode circuit shown in Figure 2-33 for 2.62MPa, 16.8MPa, and 39MPa compressions, respectively. As can be seen, neither the 1-D nor the 3-D model can predict the response well because both models have difficulty simulating accurately the generalized piezoelectric constants. Ironically, the linear piezoelectric model using measured generalized piezoelectric constants outperforms the nonlinear models.

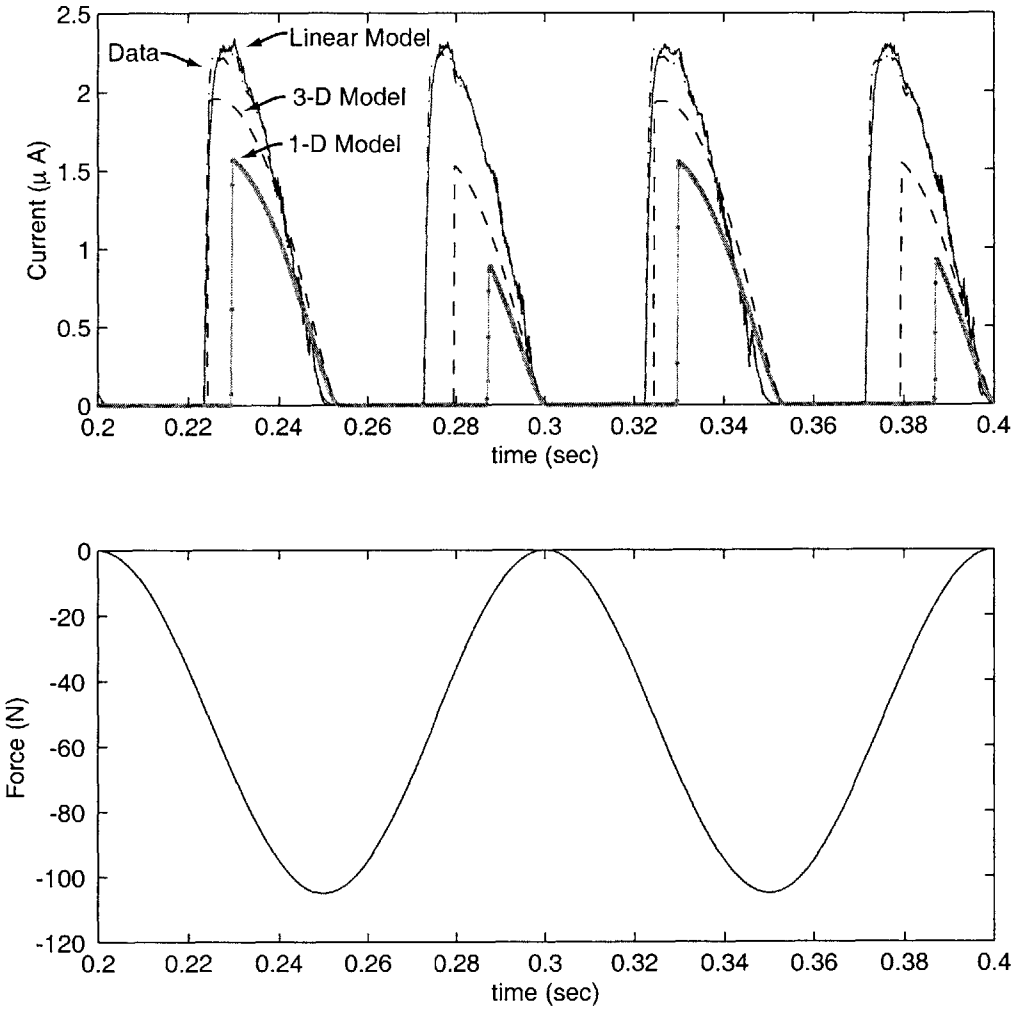

Figure 4-8: The current output of the diode circuit. The piezoelectric specimen is under 105N compression. Upper plot shows the time history of current. Lower plot shows the time history of input force.

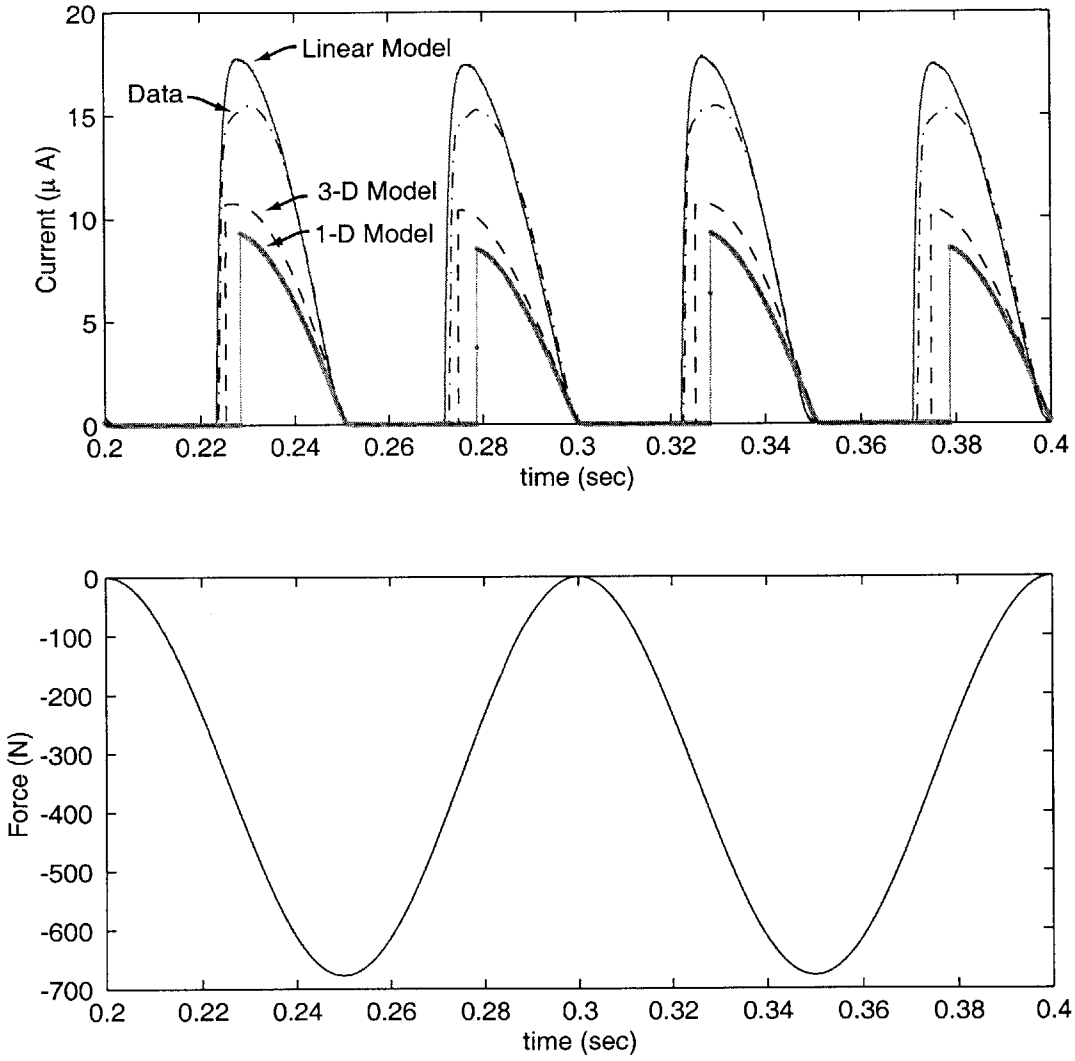

Figure 4-9: The current output of the diode circuit. The piezoelectric specimen is under 677N compression. Upper plot shows the time history of current. Lower plot shows the time history of input force.

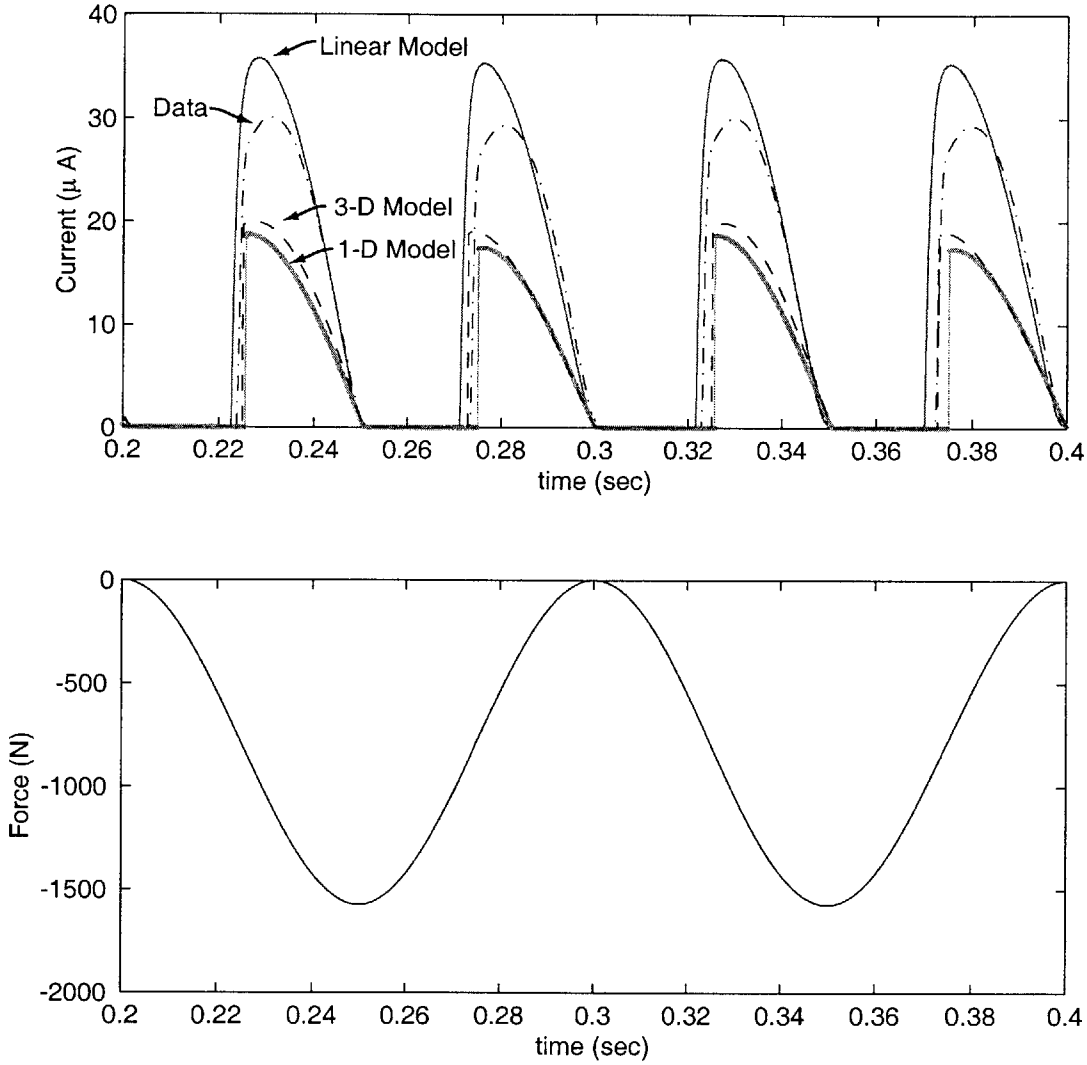

Figure 4-10: The current output of the diode circuit. The piezoelectric specimen is under 1573N compression. Upper plot shows the time history of current. Lower plot shows the time history of input force.

4.2.4 Explanation of Poor Correlation: Stress Rate Dependency

As discussed above, the nonlinear models developed in the previous chapter fail to predict the response accurately within the targeted precision. This might be due to the neglect of the stress rate dependency in the material model. To explain this, the remnant strain of a PZT-5H specimen at zero electric field in Figures 3-24 and 3-25 are first plotted as a function of stress as shown in Figure 4-11 (right). Using this plot, s_{33}^E can be approximated as 88pm/N. Note that the stress rate of this data is very low as shown in Figure 4-12.

The stress rate dependence can be found by comparing two data sets of s_{33}^E: one is for PZT-5H power generation as shown in Figure 4-11 (left) and the other is extracted from PZT-5H butterfly curve under various stresses shown in Figure 4-11 (right). The former s_{33}^E is approximately 25pm/N and is obtained by exciting 10Hz compression at zero electric field (i.e. short circuit condition) while the latter is approximately 88pm/N and is obtained at very low stress rate as shown in Figure 4-12. In addition, the latter s_{33}^E is closer to the model prediction because the model is built by the data set of the same stress rate.

As a result, it is obvious that stress rate dependence can be inferred from Figure 4-11. This stress rate dependence therefore contributed to the bad correlation of s_{33}^E shown in Figure 4-11 (left) as well as the other piezoelectric and elastic constants for power generation (d_{33}, g_{33}, and s_{33}^D).

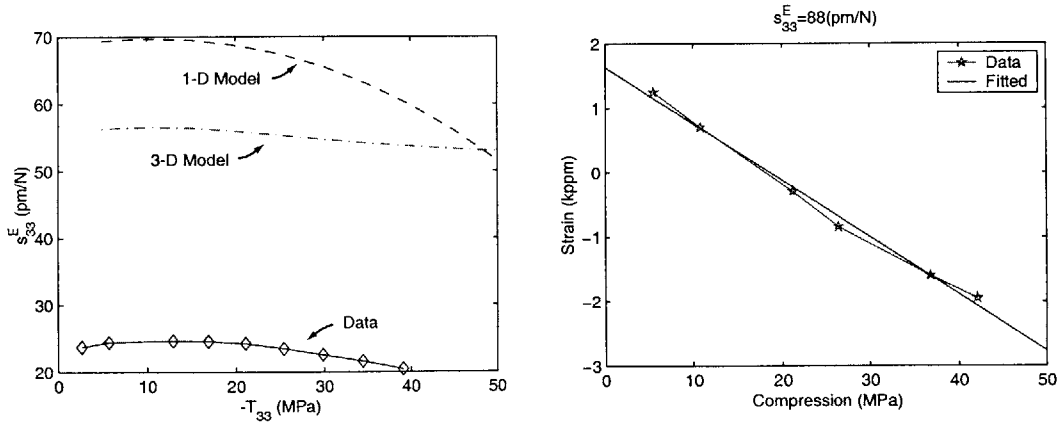

Figure 4-11: Comparison between the predicted and measured generalized s_{33}^E of PZT-5H.

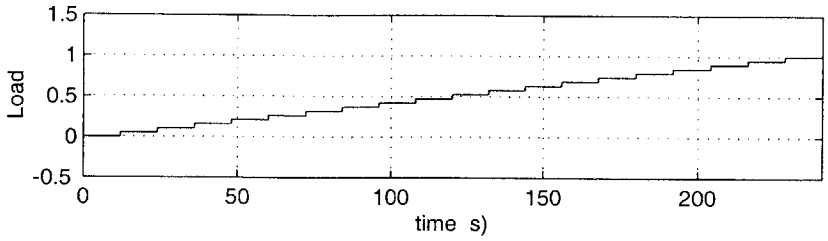

Figure 4-12: Load rate of butterfly curve test at various stresses.

4.3 Model Validation for PZT-5A Actuation

It is also of interest to investigate if the nonlinear model is capable of predicting the material properties of PZT-5A for piezoelectric actuation. This includes the behaviors of the single loop and multiple loop tests presented in Section 2.2. The compression of these data ranges from 0 to 150MPa, while none of the nonlinear model developed in the previous chapter is valid up to 150MPa compression.

Although the 1-D model for PZT-5A (Batch B) is valid up to 112MPa, the bad correlation might not be good enough to simulate the test result of actuation. Among the three 1-D models of PZT-5A developed in Chapter3, the model for PZT-5A (Batch A) shows better correlation and therefore will be chosen to simulate the piezoelectric actuation test in the following. For comparison, the driving electric field is normalized by the coercive field which is 0.75kV/mm for PZT-5A (Batch A). The same simulink simulation block diagram used for the minor loop test in Section 4.1 can be used for this type of simulation, except that the material parameters must be replaced by the coefficients listed in Table 3.5.

4.3.1 Validation of Single Loop Test

Figure 4-13 shows the converse generalized d_{33}^* subjected to electric fields of $\pm 9\%$ E_c, $\pm 16\%$ E_c and $\pm 40\%$ E_c, respectively. As can be seen, the model fails to predict correct values of the converse generalized d_{33}^* because of the difficulty in finding the exact parameters for the model, as discussed in the previous chapter. In spite of this flaw, the model well describes the decreasing d_{33}^* of the material under high compression.

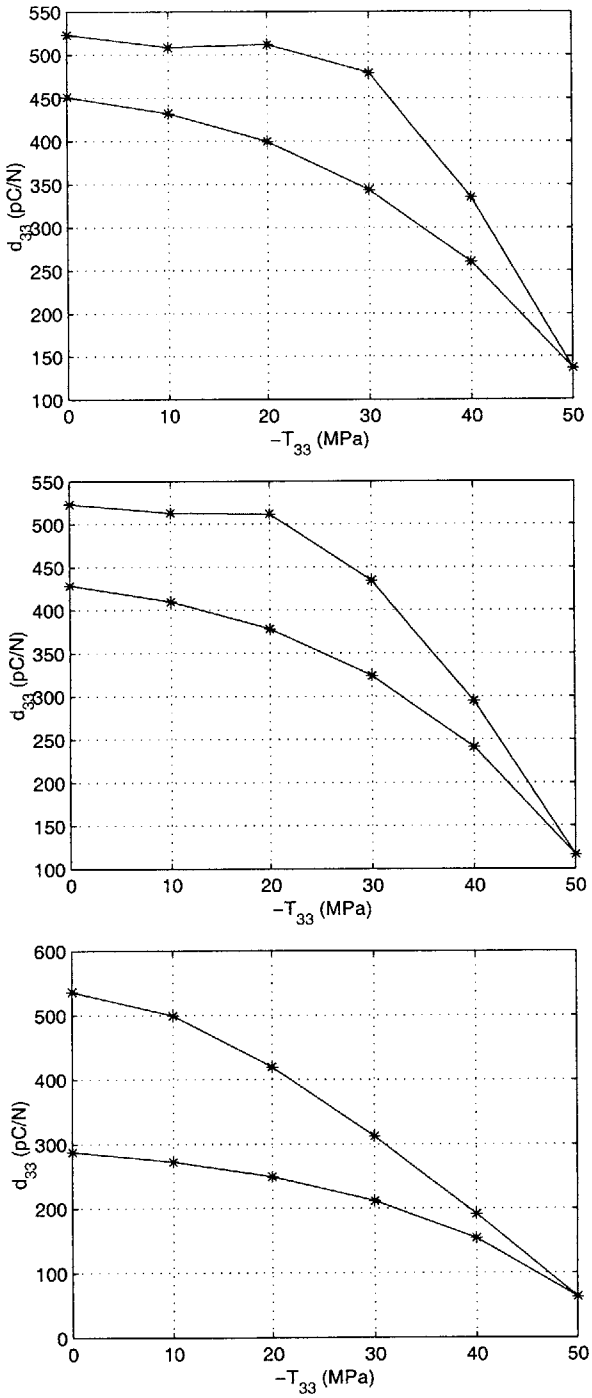

Figure 4-13: Simulation of single loop test with $\pm 0.09 E_c$ (upper), $\pm 0.16 E_c$ (middle), and $\pm 0.40 E_c$ (lower) driving electric field.

4.3.2 Validation of Multiple Loop Test

Because the material model is only valid up to 50MPa, the simulated multiple loop test uses the peak load first up to 30MPa and then to 50MPa. As shown in Figure 4-14, the actuation slightly recovers from the first peak load but not as completely as the data shown in Section 2.2. In addition, the material begins to exhibit compressive depolarization after the compression up to 50MPa, which correlates with the data shown in Section 2.2.

To see if the material actuating properties can recover after slight compression, an additional set of tests is done by using the first peak load only up to 20MPa and then to 50MPa for the second one. As shown in Figure 4-15, the actuation completely recovers from the first peak load if the negative driving electric field is low enough (less than $\pm 16\%$ E_c). In contrast, high enough negative driving electric field may result in incomplete recovery of actuation after experiencing the first peak load. This is because the high electric field in negative polarization also tends to depolarize the material. These simulated results show qualitatively that the model is capable of describing the phenomenon observed in Section 2.2, although the value is not accurate.

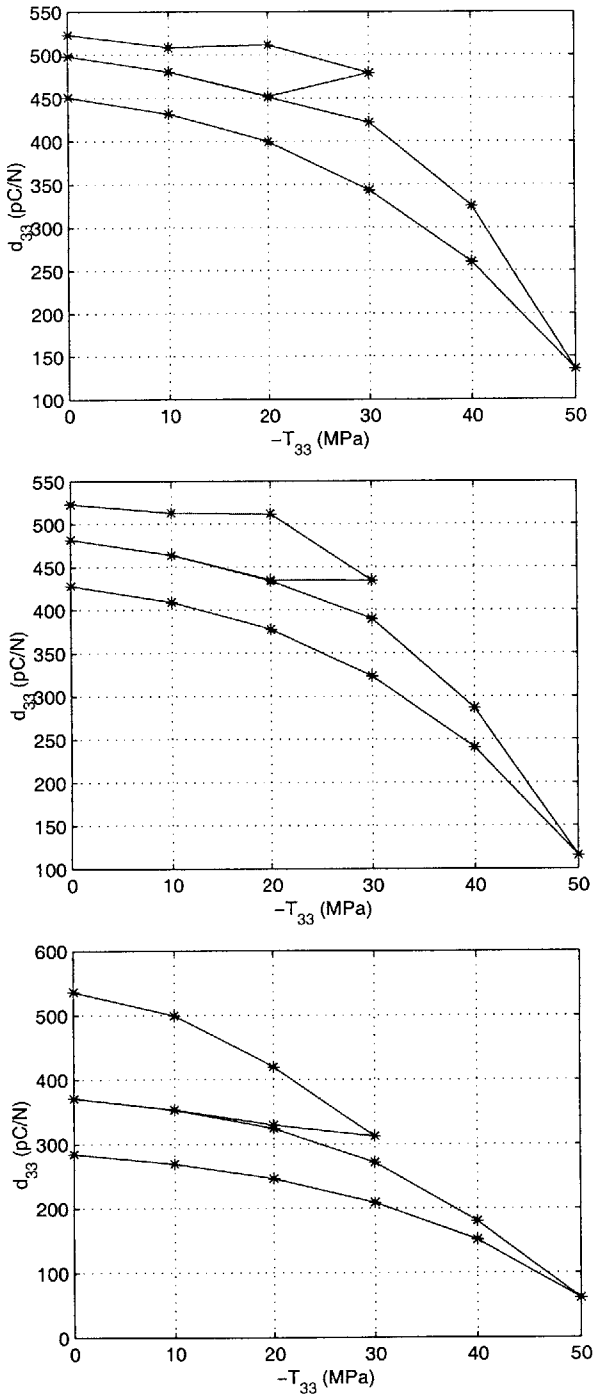

Figure 4-14: Simulation of single loop test with $\pm 0.09 E_c$ (upper), $\pm 0.16 E_c$ (middle), and $\pm 0.40 E_c$ (lower) driving electric field. Maximum compression of first loop is 30MPa.

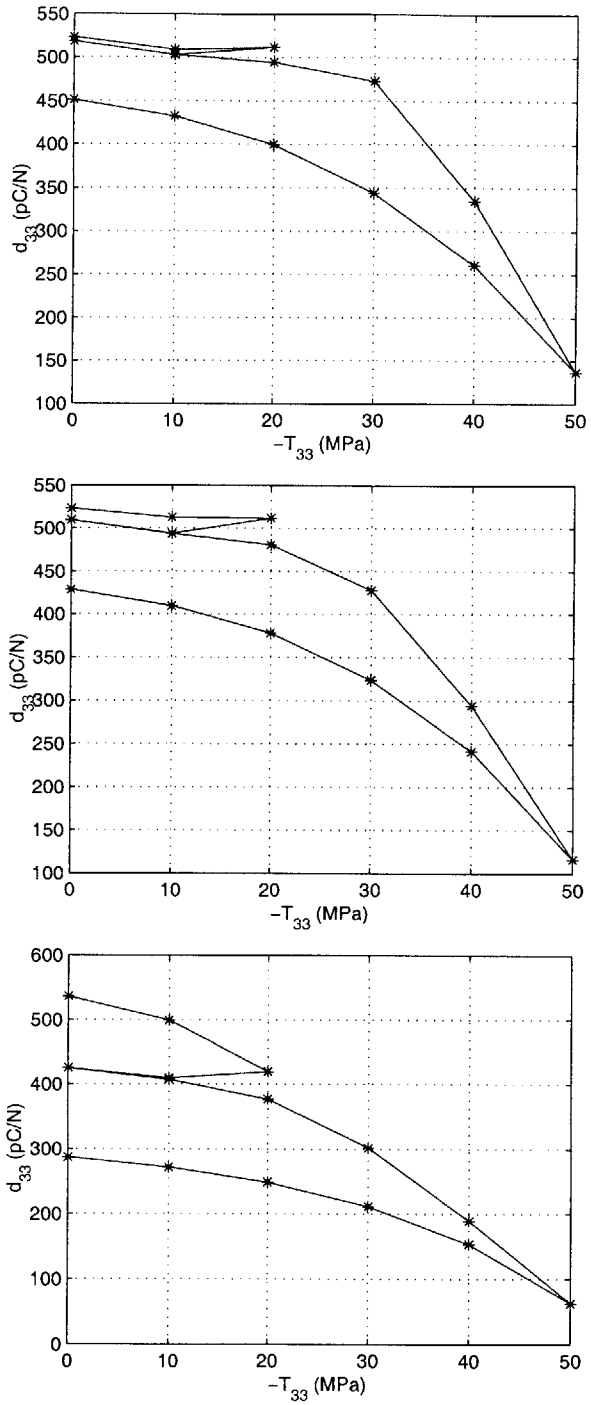

Figure 4-15: Simulation of single loop test with $\pm 0.09 E_c$ (upper), $\pm 0.16 E_c$ (middle), and $\pm 0.40 E_c$(lower) driving electric field. Maximum compression of first loop is 20MPa.

4.4 Summary of Model Validation at Stage 3

This chapter examined the capability of the material models in predicting the minor loop behaviors and the material constants. Although the material models are able to capture major trends of material behaviors under various stresses and driving frequencies, they fail to forecast accurate piezoelectric constants for actuation and energy harvesting applications, which is the required task at Level 3. Several reasons contribute to this deficiency:

1. There was significant variance among the material batches.
2. S-D hysteresis was not modeled.
3. Stress rate effect was neglected in the material model.
4. The material parameters were obtained by fitting the model with the wide range data. However, this methodology may not be efficient in predicting local derivatives of the response.

To improve the model, it is recommended to include two new internal variables: one is to describe the S-D hysteresis of PZT-5A; the other is to specify the stress rate dependency. In addition, higher order terms in the energy expansion may help improve the local derivative of the material response.

Chapter 5

3-D Analysis Using Finite Element Method

It is the goal of this thesis to develop a method to analyze electromechanically coupled devices with irregular geometries or boundary conditions. Finite element method has been used to solve this type of problem for a long time. The first linear piezoelectric finite element method was formulated by Allik and Hughes [8]. This linear formulation was later commercialized in the finite element software package ANSYS. Unfortunately, none of the currently available software packages are capable of analyzing or implementing the nonlinearity and hysteresis of piezoelectric materials.

The most advanced work in finite element analysis of nonlinear piezoelectric materials was done by Ghandi [35]. Unlike the conventional formulation used by Allik [8], Ghandi developed a mixed formulation using electric displacement D as an additional degree of freedom, in addition to the potential V and displacement u. However, the solution technique described in [35] is only appropriate for the rate independent nonlinear piezoelectric material model, i.e. discrete time model. Since a new rate dependent material model has been developed in this thesis work, the mixed finite element formulation by Ghandi as well as its solution technique shall be modified to implement the system in the continuous time domain. It is therefore the objective of this chapter to demonstrate the feasibility of a rate dependent mixed finite element analysis of nonlinear piezoelectric materials.

This chapter will start with a complete summary of the rate dependent mixed formula-

tion, followed by the implementation of the material model and the spatial discretization. The techniques of the numerical solution will then be addressed. In the end, element tests and case studies will be shown to demonstrate the solution technique.

5.1 Mixed Formulation

5.1.1 Problem Statement of an Electroelastic Continuum

The goal of this thesis is to calculate the response of an electroelastic continuum subjected to different boundary conditions and loading. To do so, the problem shall be specified first as the following. A material volume V bounded by surface $S = S_f + S_u$ is subject to mechanical surface traction $f_i^{S_f}$ on S_f and mechanical displacement constraints $u_i^{S_u}$ on S_u. These are the essential and natural mechanical boundary conditions, respectively:

$$u_i = u_i^{S_u} \text{ on } S_u, \tag{5.1}$$

$$T_{ij}n_j = f_i^{S_f} \text{ on } S_f. \tag{5.2}$$

Within the body of this continuum, applied body forces must balance the internal stresses:

$$T_{ij,j} + f_i^B = 0. \tag{5.3}$$

Portions of the surface may be covered by electrical conductors. On such portions, S_ϕ, the electric potential is specified. The remainder of the surface, S_q, is insulated, and a surface charge is specified. These are the essential and natural electrical boundary conditions, respectively:

$$\phi = \phi^{S_\phi} \text{ on } S_\phi, \tag{5.4}$$

$$D_i n_i = -q^{S_q} \text{ on } S_q. \tag{5.5}$$

Gauss's equation for charge equilibrium can be written as

$$D_{i,i} - q^B = 0. \tag{5.6}$$

In addition, strain-displacement and electric field-potential relations can be written as

$$S_{ij} = \frac{1}{2}(u_{i,j} + u_{j,i}), \tag{5.7}$$

$$E_i = -\phi_{,i}. \tag{5.8}$$

Finally, the stress and electric field are related to strain and electric displacement by the material constitutive equation developed in Chapter 3:

$$T_{ij}(S_{kl}, D_m), \tag{5.9}$$

$$E_n(S_{kl}, D_m). \tag{5.10}$$

5.1.2 Equations of Equilibrium

The first step in solving the problem stated above using the finite element method is to discretize the body into numerous elements and to describe the degrees of freedom on each element in terms of shape functions:

$$\begin{aligned} \mathbf{u} &= \mathbf{H_u}\hat{\mathbf{U}}, \\ \phi &= \mathbf{H_v}\hat{\mathbf{V}}, \\ \mathbf{D} &= \mathbf{H_D}\hat{\mathbf{D}}, \end{aligned} \tag{5.11}$$

where $\hat{\mathbf{U}}$ is the vector of nodal displacement degrees of freedom for the element, $\hat{\mathbf{V}}$ is the vector of nodal voltage degrees of freedom, and $\hat{\mathbf{D}}$ is the vector of electric displacement. The matrices $\mathbf{H_u}$, $\mathbf{H_v}$, and $\mathbf{D}$ contain the shape functions for displacement, potential, and electric displacement, respectively. In addition, the strain $\mathbf{S}$ and electric potential gradient $\nabla\phi$ can also be described in terms of derivatives of the shape functions:

$$\begin{aligned} \mathbf{S} &= \mathbf{B_u}\hat{\mathbf{U}}, \\ \nabla\phi &= \mathbf{B_v}\hat{\mathbf{V}}, \end{aligned} \tag{5.12}$$

where the matrices $\mathbf{B_u}$ and $\mathbf{B_v}$ contain the shape functions of strain and gradient of potential. These shape functions are determined by the spatial discretization of the problem which will be discussed later. The mixed formulation of equations of equilibrium for finite element analysis using this approximation has been derived by Ghandi [35]:

$$\int_V \mathbf{B}_u^T \mathbf{T}(\mathbf{S}, \mathbf{D}, \mathbf{D}^*) dV - \int_V \mathbf{H}_u^T \mathbf{f}^B dV - \int_{S_f} \mathbf{H}_u^T \mathbf{f}^{S_f} dS = 0, \tag{5.13}$$

$$\int_V \mathbf{B}_v^T \mathbf{D} dV + \int_V \mathbf{H}_v^T q^B dV + \int_{S_q} \mathbf{H}_v^T q^{S_q} dS = 0, \tag{5.14}$$

$$\int_V \mathbf{H}_D^T (\mathbf{E}(\mathbf{S}, \mathbf{D}, \mathbf{D}^*) + \nabla\phi) dV = 0. \tag{5.15}$$

The first equation is the equilibrium of mechanical force, and the second equation is an expression of Gauss's equation. The third equation describes the constraint between electric displacement $\mathbf{D}$ and the gradients of potential ϕ. The detailed derivation of these equations can be found in Ghandi's work [35].

Generalized Degrees of Freedom

To simplify the discussion of the solution algorithm, Ghandi has defined generalized degree of freedom $\hat{\mathbf{X}}$, generalized internal loads $\mathbf{F_I}$, and generalized external loads $\mathbf{F_E}$ as

$$\hat{\mathbf{X}} = \begin{bmatrix} \hat{\mathbf{U}} \\ \hat{\mathbf{D}} \\ \hat{\mathbf{V}} \end{bmatrix}, \qquad \mathbf{F_I}(\hat{\mathbf{X}}) = \begin{bmatrix} \mathbf{R_I}(\hat{\mathbf{X}}) \\ \mathbf{L}(\hat{\mathbf{X}}) \\ -\mathbf{Q_I}(\hat{\mathbf{X}}) \end{bmatrix}, \qquad \mathbf{F_E} = \begin{bmatrix} \mathbf{R_E} \\ \mathbf{0} \\ -\mathbf{Q_E} \end{bmatrix}, \tag{5.16}$$

where equivalent nodal forces due to internal stress ($\mathbf{R_I}$), equivalent nodal forces due to external loads ($\mathbf{R_E}$), equivalent nodal charges corresponding to the internal electric field ($\mathbf{Q_I}$), equivalent nodal charges due to distributed body and surface charges ($\mathbf{Q_E}$), and the constraint equation ($\mathbf{L}$) are

$$\mathbf{R_I}(\hat{\mathbf{X}}) = \int_V \mathbf{B}_u^T \mathbf{T}(\mathbf{S}, \mathbf{D}, \mathbf{D}^*) dV, \tag{5.17}$$

$$\mathbf{Q_I}(\hat{\mathbf{X}}) = -\int_V \mathbf{B}_v^T \mathbf{D} dV, \tag{5.18}$$

$$\mathbf{L}(\hat{\mathbf{X}}) = \int_V \mathbf{H}_D^T \mathbf{E}(\mathbf{S}, \mathbf{D}, \mathbf{D}^*) dV + \int_V \mathbf{H}_D^T \nabla\phi dV, \tag{5.19}$$

$$\mathbf{R_E} = \int_V \mathbf{H}_u^T \mathbf{f}^B dV + \int_{S_f} \mathbf{H}_u^T \mathbf{f}^{S_f} dS, \tag{5.20}$$

$$\mathbf{Q_E} = \int_V \mathbf{H}_v^T q^B dV + \int_{S_q} \mathbf{H}_v^T q^{S_q} dS. \tag{5.21}$$

Thus the finite element equilibrium equations (Eq. 5.13, 5.14, and 5.15) may be written as:

$$\mathbf{F}(\hat{\mathbf{X}}) = \mathbf{F_I}(\hat{\mathbf{X}}) - \mathbf{F_E} \tag{5.22}$$

However, this is not considered a complete representation of the system yet. There are four variables ($\mathbf{D}$, $\mathbf{D}^*$, $\mathbf{U}$, and $\mathbf{V}$) but only three equations in the defined system. The equation for the internal variables $\mathbf{D}^*$ has not been specified. For the discrete time material model, the evolution of $\mathbf{D}^*$ is implicitly specified in the 3-D version of Eq. 3.25 in Ghandi's

work [35], while for the continuous time material model developed in this thesis work, $\mathbf{D}^*$ is explicitly described in Eq. 3.65 or can be simplified as:

$$\dot{\hat{\mathbf{D}}}^* = \mathbf{f}(\hat{\mathbf{D}}, \hat{\mathbf{D}}^*) \tag{5.23}$$

where $(\dot{})$ is the derivative with respect to time t.

In summary, the complete set of system equations includes Eq. 5.22 and 5.23, and the nonlinearity of the material response enters through the functions $\mathbf{T}(\mathbf{S}, \mathbf{D}, \mathbf{D}^*)$ and $\mathbf{E}(\mathbf{S}, \mathbf{D}, \mathbf{D}^*)$. This system is essentially a set of differential-algebraic equations (DAE). Unlike the discrete system by Ghandi, which is just a set of nonlinear equations, the differential-algebraic formulation of the continuous system has a special feature that the initial conditions must be consistent. As a result, the objective of the FEM code is to compute nodal displacement/potentials and elemental electric displacement such that Eq. 5.22 and Eq. 5.23 are satisfied at all time.

5.2 Implementation of Material Model

In the material model, the strain and electric fields are functions of the electric displacement and stress

$$\begin{aligned} \mathbf{S} &= \mathbf{S}(\mathbf{D}, \mathbf{D}^*, \mathbf{T}), \\ \mathbf{E} &= \mathbf{E}(\mathbf{D}, \mathbf{D}^*, \mathbf{T}). \end{aligned} \tag{5.24}$$

However, to implement the finite element method, the constitutive law must be in the form of

$$\begin{aligned} \mathbf{T} &= \mathbf{T}(\mathbf{D}, \mathbf{D}^*, \mathbf{S}), \\ \mathbf{E} &= \mathbf{E}(\mathbf{D}, \mathbf{D}^*, \mathbf{S}). \end{aligned} \tag{5.25}$$

Since the strain is restricted as a first order function of stress when the tensor invariants were chosen, one can rewrite the equations as

$$\mathbf{S} = \mathbf{s}^{\mathbf{D}}\mathbf{T} + \mathbf{S}^{\mathbf{0}}, \tag{5.26}$$

where

$$\mathbf{s}^{\mathbf{D}} = \frac{\partial \mathbf{S}}{\partial \mathbf{T}}, \tag{5.27}$$

and

$$\mathbf{S}^{\mathbf{0}} = \mathbf{S}(\mathbf{T} = \mathbf{0}, \mathbf{D}, \mathbf{D}^*).$$

Note that $\mathbf{s^D}$ and $\mathbf{S^0}$ now are functions of $\mathbf{D}$ and $\mathbf{D^*}$ only and are independent of $\mathbf{T}$. The stress can be represented as a function of $\mathbf{S}$, $\mathbf{D}$, and $\mathbf{D^*}$:

$$\mathbf{T} = (\mathbf{s^D})^{-1}(\mathbf{S} - \mathbf{S^0}) \tag{5.28}$$

Substituting Eq. 5.28 into Eq. 5.24, one can represent electric field as a function of $\mathbf{D}$, $\mathbf{D^*}$, and $\mathbf{S}$. Hence, by transforming the material model from the form of Eq. 5.24 into the form of Eq. 5.25, one can implement the material model in the finite element analysis.

5.3 Implementation of Spatial Discretization

Detailed convergence tests of various element types have been discussed by Ghandi [35]. Among those convergeable element types, tetrahedral elements are most attractive because they can easily mesh complex geometry. Both the 4-node and 10-node tetrahedral elements shown in Figure 5-1 have been considered in this thesis work to demonstrate the finite element analysis. The 4-node element represents uniform fields for each element, while the 10-node element represents linearly distributed fields for each element. Apparently, higher order elements such as 10-node show faster converging rates than lower order elements. However, due to the nonlinear material model implemented in the finite element formulation, the integration in Eq. 5.13 and 5.14 might be a problem. These integrations are usually carried out by summing up the functionals at the Guassian points. According to Gellert [45], 20 numerical integration points are required to meet the degree of precision of 5. This means 20 times the computational effort compared to that of the 4-node element. In addition, the way that the material model is formulated needs a degree of precision of at least 6. More derivation is needed to obtain the formula for degree higher than 5. Based on the purpose of demonstration only, the derivation of a new formula is out of the scope of this thesis work. As a result, only 4-node elements are used in the rest of the discussion.

5.3.1 4-node Tetrahedra

Although the shape functions of the 4-node tetrahedon can be easily found in any text of finite element analysis, they are summarized here for completeness. First, the isoparametric

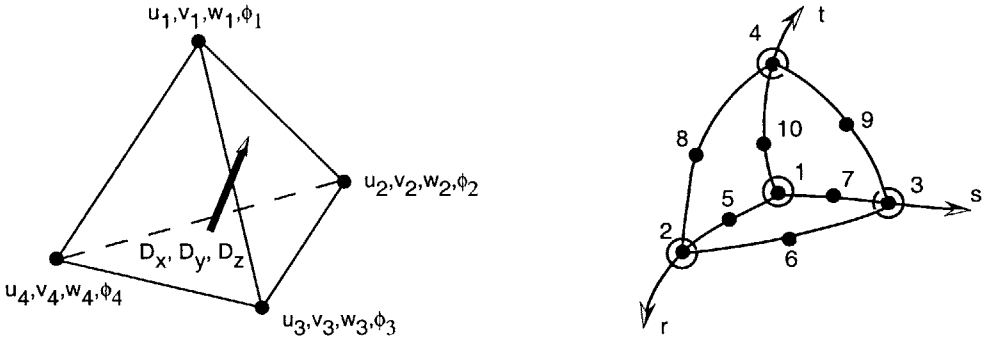

Figure 5-1: 4-node (left) and 10-node (right) tetrahedral elements.

shape functions are defined as:

$$\begin{aligned} h_1 &= 1 - r - s - t, \\ h_2 &= r, \\ h_3 &= s, \\ h_4 &= t. \end{aligned} \tag{5.29}$$

Hence, the shape function for the displacement degrees of freedom on each element is

$$\mathbf{H_u}^{(e)} = \begin{bmatrix} h_1 & 0 & 0 & h_2 & 0 & 0 & \cdots & h_4 & 0 & 0 \\ 0 & h_1 & 0 & 0 & h_2 & 0 & \ddots & 0 & h_4 & 0 \\ 0 & 0 & h_1 & 0 & 0 & h_3 & \cdots & 0 & 0 & h_4 \end{bmatrix}, \tag{5.30}$$

the shape function for the potential degrees of freedom on each element is

$$\mathbf{H_v}^{(e)} = \begin{bmatrix} h_1 & h_2 & h_3 & h_4 \end{bmatrix}, \tag{5.31}$$

and the shape function for the electric displacement degrees of freedom on each element is

$$\mathbf{H_D}^{(e)} = \begin{bmatrix} 1 & 0 & 0 \\ 0 & 1 & 0 \\ 0 & 0 & 1 \end{bmatrix}. \tag{5.32}$$

Since the strain is the spatial derivative of the displacement

$$\mathbf{S} = \begin{bmatrix} u_{,x} & v_{,y} & w_{,z} & v_{,z} + w_{,y} & u_{,z} + w_{,x} & u_{,y} + v_{,x} \end{bmatrix}^T, \tag{5.33}$$

the shape function of strain on each element is

$$\mathbf{B_u}^{(e)} = \begin{bmatrix} h_{1,x} & 0 & 0 & h_{2,x} & 0 & 0 & \cdots & h_{4,x} & 0 & 0 \\ 0 & h_{1,y} & 0 & 0 & h_{2,y} & 0 & \ddots & 0 & h_{4,y} & 0 \\ 0 & 0 & h_{1,z} & 0 & 0 & h_{2,z} & \ddots & 0 & 0 & h_{4,z} \\ 0 & h_{1,z} & h_{1,y} & 0 & h_{2,z} & h_{2,y} & \ddots & 0 & h_{4,z} & h_{4,y} \\ h_{1,z} & 0 & h_{1,x} & h_{2,z} & 0 & h_{2,x} & \ddots & h_{4,z} & 0 & h_{4,x} \\ h_{1,y} & h_{1,x} & 0 & h_{2,y} & h_{2,x} & 0 & \cdots & h_{4,y} & h_{4,x} & 0 \end{bmatrix}, \tag{5.34}$$

and the shape function of electric field on each element is

$$\mathbf{B_v}^{(e)} = \begin{bmatrix} h_{1,x} & h_{2,x} & h_{3,x} & h_{4,x} \\ h_{1,y} & h_{2,y} & h_{3,y} & h_{4,y} \\ h_{1,z} & h_{2,z} & h_{3,z} & h_{4,z} \end{bmatrix}. \tag{5.35}$$

Note that

$$\mathbf{J} = \begin{bmatrix} \frac{\partial x}{\partial r} & \frac{\partial y}{\partial r} & \frac{\partial z}{\partial r} \\ \frac{\partial y}{\partial s} & \frac{\partial y}{\partial s} & \frac{\partial z}{\partial s} \\ \frac{\partial z}{\partial t} & \frac{\partial y}{\partial s} & \frac{\partial z}{\partial t} \end{bmatrix}, \tag{5.36}$$

and therefore

$$\begin{bmatrix} \frac{\partial}{\partial x} \\ \frac{\partial}{\partial y} \\ \frac{\partial}{\partial z} \end{bmatrix} = \mathbf{J}^{-1} \begin{bmatrix} \frac{\partial}{\partial r} \\ \frac{\partial}{\partial s} \\ \frac{\partial}{\partial t} \end{bmatrix}, \tag{5.37}$$

and the matrix $\mathbf{B_v}$ is

$$\mathbf{B_v}^{(e)} = \mathbf{J}^{-1} \begin{bmatrix} h_{1,r} & h_{2,r} & h_{3,r} & h_{4,r} \\ h_{1,s} & h_{2,s} & h_{3,s} & h_{4,s} \\ h_{1,t} & h_{2,t} & h_{3,t} & h_{4,t} \end{bmatrix}. \tag{5.38}$$

In addition, the element in matrix $\mathbf{B_u}^{(e)}$ can be extracted from matrix $\mathbf{B_v}^{(e)}$ in Eq. 5.38. Since the shape function for the 4-node tetrahedron is a first-order function, the Jacobian matrix is just a function of nodal coordinates but not a function of isoparametric natural coordinates:

$$\mathbf{J} = \begin{bmatrix} x_2 - x_1 & y_2 - y_1 & z_2 - x_1 \\ x_3 - x_1 & y_3 - y_1 & z_3 - z_1 \\ x_4 - x_1 & y_4 - y_1 & z_4 - z_1 \end{bmatrix}. \tag{5.39}$$

Numerical Integration

Since all the functions are constant along each element, the integration on the volume of each element can be carried out easily.

Assembly

To assemble all the elements into the global finite element system, a connectivity matrix $\mathbf{N}$ which attributes the element nodal index to global nodal index is needed. The connectivity matrix $\mathbf{N}$ has size of $m \times n$, where m is the number of total elements, and n is the number of nodes per element. In addition, two index vectors $\mathbf{I_v}$ and $\mathbf{I_u}$ are needed to indicate the prescribed potential and displacement degrees of freedom, respectively.

5.4 Solution Techniques

5.4.1 Differential Algebraic Formulation

The variables that need to be solved include $\hat{\mathbf{U}}$, $\hat{\mathbf{V}}$, $\hat{\mathbf{D}}$, and $\hat{\mathbf{D}}^*$, which are defined by Eq. 5.22 and 5.23. Using the numerical integration or so called Gaussian-Quadrature which transforms the spatial integration into summation $\sum$, one can rewrite the system as

$$\dot{\hat{\mathbf{D}}}^* - \mathbf{f}(\hat{\mathbf{D}}, \hat{\mathbf{D}}^*) = 0, \tag{5.40}$$

$$\sum \mathbf{J}\mathbf{B}_\mathbf{u}^\mathbf{T}\mathbf{T}(\mathbf{B_u}\hat{\mathbf{U}}, \mathbf{H_D}\hat{\mathbf{D}}, \hat{\mathbf{D}}^*) - \mathbf{R_E} = 0, \tag{5.41}$$

$$\sum \mathbf{J}\mathbf{H}_\mathbf{D}^\mathbf{T}\mathbf{E}(\mathbf{B_u}\hat{\mathbf{U}}, \mathbf{H_D}\hat{\mathbf{D}}, \hat{\mathbf{D}}^*) + \sum \mathbf{J}\mathbf{H}_\mathbf{D}^\mathbf{T}\mathbf{B_v}\hat{\mathbf{V}} = 0, \tag{5.42}$$

$$\sum \mathbf{J}\mathbf{B}_\mathbf{v}^\mathbf{T}\mathbf{H_D}\hat{\mathbf{D}} - \mathbf{Q_E} = 0. \tag{5.43}$$

Eq. 5.40, 5.41, 5.42, and 5.43 can be further renamed and simplified, respectively, as

$$\dot{\hat{\mathbf{D}}}^* - \mathbf{F}_1(\hat{\mathbf{D}}, \hat{\mathbf{D}}^*) = 0, \tag{5.44}$$

$$\mathbf{F_U}(\hat{\mathbf{U}}, \hat{\mathbf{D}}, \hat{\mathbf{D}}^*) - \mathbf{R_E} = 0, \tag{5.45}$$

$$\mathbf{F_D}(\hat{\mathbf{U}}, \hat{\mathbf{D}}, \hat{\mathbf{D}}^*, \hat{\mathbf{V}}) = 0, \tag{5.46}$$

$$\mathbf{F_V}(\hat{\mathbf{D}}) - \mathbf{Q_E} = 0. \tag{5.47}$$

With this representation, one can easily trace the dependent variables in the equations. If some of the displacement and potential degrees of freedom are prescribed, one can partition

them as

$$\hat{\mathbf{U}} = \begin{bmatrix} \hat{\mathbf{U}}_\mathbf{a} \\ \hat{\mathbf{U}}_\mathbf{b} \end{bmatrix}, \qquad \hat{\mathbf{V}} = \begin{bmatrix} \hat{\mathbf{V}}_\mathbf{a} \\ \hat{\mathbf{V}}_\mathbf{b} \end{bmatrix}, \tag{5.48}$$

where $\hat{\mathbf{U}}_\mathbf{a}$ and $\hat{\mathbf{V}}_\mathbf{a}$ are the unknown displacement and potential degrees of freedom, and $\hat{\mathbf{U}}_\mathbf{b}$ and $\hat{\mathbf{V}}_\mathbf{b}$ are the prescribed displacement and potential degrees of freedom, respectively. Similarly, $\mathbf{R_E}$ and $\mathbf{Q_E}$ can be partitioned into

$$\mathbf{R_E} = \begin{bmatrix} \mathbf{R_{E_a}} \\ \mathbf{R_{E_b}} \end{bmatrix}, \qquad \mathbf{Q_E} = \begin{bmatrix} \mathbf{Q_{E_a}} \\ \mathbf{Q_{E_b}} \end{bmatrix}, \tag{5.49}$$

where $\mathbf{R_{E_a}}$ is the prescribed force on the unknown displacement $\hat{\mathbf{U}}_\mathbf{a}$, and $\mathbf{R_{E_b}}$ is the reaction force on the prescribed displacement $\hat{\mathbf{U}}_\mathbf{b}$. Similarly, $\mathbf{Q_{E_a}}$ is the prescribed charge on the unknown voltage degree of freedom $\hat{\mathbf{V}}_\mathbf{a}$, and $\mathbf{Q_{E_b}}$ is the reaction charge on the prescribed voltage degree of freedom $\hat{\mathbf{V}}_\mathbf{b}$. These partitions can be conducted in the computer program using the vectors $\mathbf{I_u}$ and $\mathbf{I_v}$. Although $\hat{\mathbf{D}}$ and $\hat{\mathbf{D}}^*$ are degrees of freedom, in general they are difficult to be prescribed.

With these partitions, Eq. 5.45 can be rearranged into

$$\mathbf{F_2}(\hat{\mathbf{U}}_\mathbf{a}, \hat{\mathbf{U}}_\mathbf{b}, \hat{\mathbf{D}}, \hat{\mathbf{D}}^*) - \mathbf{R_{E_a}} = 0, \tag{5.50}$$

$$\mathbf{F_3}(\hat{\mathbf{U}}_\mathbf{a}, \hat{\mathbf{U}}_\mathbf{b}, \hat{\mathbf{D}}, \hat{\mathbf{D}}^*) - \mathbf{R_{E_b}} = 0, \tag{5.51}$$

and Eq. 5.46 can be rewritten as

$$\mathbf{F_4}(\hat{\mathbf{U}}_\mathbf{a}, \hat{\mathbf{U}}_\mathbf{b}, \hat{\mathbf{D}}, \hat{\mathbf{D}}^*, \hat{\mathbf{V}}_\mathbf{a}, \hat{\mathbf{V}}_\mathbf{b}) = 0. \tag{5.52}$$

In addition, Eq. 5.47 can be partitioned into

$$\mathbf{F_5}(\hat{\mathbf{D}}) - \mathbf{Q_{E_a}} = 0, \tag{5.53}$$

$$\mathbf{F_6}(\hat{\mathbf{D}}) - \mathbf{Q_{E_b}} = 0. \tag{5.54}$$

To make it clear, the equations to be solved are recollected again from Eq. 5.40, 5.50,

5.51,5.52, 5.53, and 5.54:

$$\dot{\hat{\mathbf{D}}}^* - \mathbf{F_1}(\hat{\mathbf{D}}, \hat{\mathbf{D}}^*) = 0, \tag{5.55}$$

$$\mathbf{F_2}(\hat{\mathbf{U}_a}, \hat{\mathbf{U}_b}, \hat{\mathbf{D}}, \hat{\mathbf{D}}^*) - \mathbf{R_{E_a}} = 0, \tag{5.56}$$

$$\mathbf{F_3}(\hat{\mathbf{U}_a}, \hat{\mathbf{U}_b}, \hat{\mathbf{D}}, \hat{\mathbf{D}}^*) - \mathbf{R_{E_b}} = 0, \tag{5.57}$$

$$\mathbf{F_4}(\hat{\mathbf{U}_a}, \hat{\mathbf{U}_b}, \hat{\mathbf{D}}, \hat{\mathbf{D}}^*, \hat{\mathbf{V}_a}, \hat{\mathbf{V}_b}) = 0, \tag{5.58}$$

$$\mathbf{F_5}(\hat{\mathbf{D}}) - \mathbf{Q_{E_a}} = 0, \tag{5.59}$$

$$\mathbf{F_6}(\hat{\mathbf{D}}) - \mathbf{Q_{E_b}} = 0. \tag{5.60}$$

The input of these equations are $\hat{\mathbf{U}_b}$, $\hat{\mathbf{V}_b}$, $\mathbf{R_{E_a}}$, and $\mathbf{Q_{E_a}}$. The unknown variables to be solved are $\hat{\mathbf{V}_a}$, $\hat{\mathbf{U}_a}$, $\hat{\mathbf{D}}$, $\hat{\mathbf{D}}^*$, $\mathbf{R_{E_b}}$, and $\mathbf{Q_{E_b}}$. Since $\mathbf{R_{E_b}}$ and $\mathbf{Q_{E_b}}$ are the reaction force and charge, to solve this system, it is convenient to solve for $\hat{\mathbf{V}_a}$, $\hat{\mathbf{U}_a}$, $\hat{\mathbf{D}}$, and $\hat{\mathbf{D}}^*$ first from Eq. 5.55, 5.56, 5.58, and 5.59. Once $\hat{\mathbf{V}_a}$, $\hat{\mathbf{U}_a}$, $\hat{\mathbf{D}}$, and $\hat{\mathbf{D}}^*$ are solved, the reaction force ($\mathbf{R_{E_b}}$) and charge ($\mathbf{Q_{E_b}}$) can be obtained easily from Eq. 5.57 and 5.60. As a result, the final set of equations to be solved includes Eq. 5.55, 5.56, 5.58, and 5.59, which shall be recollected here again for convenience:

$$\dot{\hat{\mathbf{D}}}^* - \mathbf{F_1}(\hat{\mathbf{D}}, \hat{\mathbf{D}}^*) = 0, \tag{5.61}$$

$$\mathbf{F_2}(\hat{\mathbf{U}_a}, \hat{\mathbf{U}_b}, \hat{\mathbf{D}}, \hat{\mathbf{D}}^*) - \mathbf{R_{E_a}} = 0, \tag{5.62}$$

$$\mathbf{F_4}(\hat{\mathbf{U}_a}, \hat{\mathbf{U}_b}, \hat{\mathbf{D}}, \hat{\mathbf{D}}^*, \hat{\mathbf{V}_a}, \hat{\mathbf{V}_b}) = 0, \tag{5.63}$$

$$\mathbf{F_5}(\hat{\mathbf{D}}) - \mathbf{Q_{E_a}} = 0. \tag{5.64}$$

This is essentially a set of differential algebraic equations(DAE) again, which can be rewritten in the general form

$$F(t, \mathbf{z}, \dot{\mathbf{z}}) = 0. \tag{5.65}$$

where $\mathbf{z}$ is a vector of state variables to be solved:

$$\mathbf{z} = \begin{bmatrix} \hat{\mathbf{D}}^* \\ \hat{\mathbf{U}_a} \\ \hat{\mathbf{D}} \\ \hat{\mathbf{V}_a} \end{bmatrix}. \tag{5.66}$$

5.4.2 Time-stepping Numerical Algorithm

The basic idea for solving a DAE system is to replace the solution and its derivative in Eq. 5.65 by a finite difference approximation and to solve the resultant equations for the solution at the current time t_n using Newton's method. For example, replacing the derivative by the backward difference in Eq. 5.65 gives the first order formula

$$F(t_n, \mathbf{z}_n, \frac{\mathbf{z}_n - \mathbf{z}_{n-1}}{h_n}) = 0, \tag{5.67}$$

where $h_n = t_n - t_{n-1}$. This equation can be solved at each time step using a modified Newton method:

$$\mathbf{z}_n^{(m+1)} = \mathbf{z}_n^{(m)} - \left(\frac{1}{h_n}\frac{\partial F}{\partial \dot{\mathbf{z}}} + \frac{\partial F}{\partial \mathbf{z}}\right)^{-1} F\left(t, \mathbf{z}_n^{(m)}, \frac{\mathbf{z}_n^{(m)} - \mathbf{z}_{n-1}}{h_n}\right), \tag{5.68}$$

where m is the iteration index. Solving this requires solution of the linear system

$$\mathbf{A}\mathbf{x} = \mathbf{b}, \tag{5.69}$$

where

$$\mathbf{A} = \left(\frac{1}{h_n}\frac{\partial F}{\partial \dot{\mathbf{z}}} + \frac{\partial F}{\partial \mathbf{z}}\right) \tag{5.70}$$

is an $N \times N$ iteration matrix, $\mathbf{x} = \mathbf{z}_n^{(m+1)} - \mathbf{z}_n^{(m)}$ is an N-vector, and

$$\mathbf{b} = -F\left(t, \mathbf{z}_n^{(m)}, \frac{\mathbf{z}_n^{(m)} - \mathbf{z}_{n-1}}{h_n}\right)$$

is an N-vector. N is the total number of the degrees of freedom to be solved.

Calculation of Iteration Matrix A

The iteration matrix (Eq. 5.70) can be calculated numerically using a finite difference scheme. However, to improve the convergence, it is recommended to calculate the iteration matrix analytically if possible. From Eq. 5.55, the term $\frac{\partial F}{\partial \dot{\mathbf{z}}}$ can be written as

$$\frac{\partial F}{\partial \dot{\mathbf{z}}} = \begin{bmatrix} \mathbf{I} & 0 \\ 0 & 0 \end{bmatrix}, \tag{5.71}$$

where $\mathbf{I}$ is a $q \times q$ identity matrix. q is the size of the vector $\hat{\mathbf{D}}^*$. From Eq. 5.61, 5.62, 5.63 and 5.64, the term $\frac{\partial F}{\partial \mathbf{z}}$ can be written as

$$\frac{\partial F}{\partial \mathbf{z}} = \begin{bmatrix} \mathbf{K_{ss}} & 0 & \mathbf{K_{sd}} & 0 \\ \mathbf{K_{us}} & \mathbf{K_{uu}} & \mathbf{K_{ud}} & 0 \\ \mathbf{K_{ds}} & \mathbf{K_{du}} & \mathbf{K_{dd}} & \mathbf{K_{dv}} \\ 0 & 0 & \mathbf{K_{vd}} & 0 \end{bmatrix}, \tag{5.72}$$

where

$$\mathbf{K_{ss}} = \frac{\partial \mathbf{F_1}}{\partial \hat{\mathbf{D}}^*},$$

$$\mathbf{K_{sd}} = \frac{\partial \mathbf{F_1}}{\partial \hat{\mathbf{D}}},$$

$$\mathbf{K_{us}} = \frac{\partial \mathbf{F_2}}{\partial \hat{\mathbf{D}}^*} = \int_V \mathbf{B_u}^T \frac{\partial \mathbf{T}}{\partial \mathbf{D}^*} \mathbf{H_D} dV,$$

$$\mathbf{K_{uu}} = \frac{\partial \mathbf{F_2}}{\partial \hat{\mathbf{U}}} = \int_V \mathbf{B_u}^T \frac{\partial \mathbf{T}}{\partial \mathbf{S}} \mathbf{B_u} dV,$$

$$\mathbf{K_{ud}} = \frac{\partial \mathbf{F_2}}{\partial \hat{\mathbf{D}}} = \int_V \mathbf{B_u}^T \frac{\partial \mathbf{T}}{\partial \mathbf{D}} \mathbf{H_D} dV,$$

$$\mathbf{K_{ds}} = \frac{\partial \mathbf{F_3}}{\partial \hat{\mathbf{D}}^*} = \int_V \mathbf{H_D}^T \frac{\partial \mathbf{E}}{\partial \mathbf{D}^*} \mathbf{H_D} dV,$$

$$\mathbf{K_{du}} = \frac{\partial \mathbf{F_3}}{\partial \hat{\mathbf{U}}} = \int_V \mathbf{H_D}^T \frac{\partial \mathbf{E}}{\partial \mathbf{S}} \mathbf{B_u} dV,$$

$$\mathbf{K_{dd}} = \frac{\partial \mathbf{F_3}}{\partial \hat{\mathbf{D}}} = \int_V \mathbf{H_D}^T \frac{\partial \mathbf{E}}{\partial \mathbf{D}} \mathbf{H_D} dV,$$

$$\mathbf{K_{dv}} = \frac{\partial \mathbf{F_3}}{\partial \hat{\mathbf{V}}} = \int_V \mathbf{H_D}^T \mathbf{B_v} dV,$$

$$\mathbf{K_{vd}} = \frac{\partial \mathbf{F_4}}{\partial \hat{\mathbf{D}}} = \int_V \mathbf{B_v}^T \mathbf{H_D} dV.$$

As can be seen, the matrices $\mathbf{K_{us}}$, $\mathbf{K_{uu}}$, $\mathbf{K_{ud}}$, $\mathbf{K_{ds}}$, and $\mathbf{K_{du}}$ are dependent upon the material properties. To calculate these matrices, one must first change the variables as the following:

$$\frac{\partial \mathbf{T}}{\partial \mathbf{D}^*} = \frac{\partial \mathbf{T}}{\partial \mathbf{S}} \frac{\partial \mathbf{S}}{\partial \mathbf{D}^*}, \tag{5.73}$$

$$\frac{\partial \mathbf{T}}{\partial \mathbf{D}} = \frac{\partial \mathbf{T}}{\partial \mathbf{S}} \frac{\partial \mathbf{S}}{\partial \mathbf{D}}, \tag{5.74}$$

$$\frac{\partial \mathbf{E}}{\partial \mathbf{S}} = \frac{\partial \mathbf{E}}{\partial \mathbf{T}} \frac{\partial \mathbf{T}}{\partial \mathbf{S}}, \tag{5.75}$$

where $\frac{\partial \mathbf{S}}{\partial \mathbf{D}^*}$, $\frac{\partial \mathbf{S}}{\partial \mathbf{D}}$, $\frac{\partial \mathbf{E}}{\partial \mathbf{D}^*}$, and $\frac{\partial \mathbf{E}}{\partial \mathbf{T}}$ can be obtained symbolically from the material model (Eq. 5.24), and $\frac{\partial \mathbf{T}}{\partial \mathbf{S}}$ can be obtained by inverting Eq. 5.27.

In summary, Eq. 5.71 and 5.72 give the iteration matrix $\mathbf{A}$. With this iteration matrix, Eq. 5.65 can be solved numerically.

5.4.3 Software Implementation

Solving a large scale system of DAEs such as the one in Eq. 5.65 is not a trivial problem. A well-known DAE solver, DASSL, has been developed by Pezold[46]. A sophisticated version of DASSL called DASPK scales and preconditions the iteration matrix ($\mathbf{A}$) so that the system $\mathbf{Ax} = \mathbf{b}$ is solved with $\mathbf{A}$ virtually close to an identity matrix. For this reason, this thesis work implemented the DASPK solver to solve the system defined in Eq. 5.65.

5.5 Case Study

This section will demonstrate the capability of the nonlinear finite element code developed above. It is important to study how these elements perform before emulating real problems. Hence, this section will first examine a simple element under various loading conditions to assure the result. After the element tests, large scale problems, such as a chunk of material under uniform and skewed loading, will be simulated to demonstrate the contribution of this nonlinear finite element code.

5.5.1 Element Tests

Test 1. Single element with complete prescribed voltage

It is the intention to see how the polarization in the element responds to the applied electric fields. The first test case, as shown in Figure 5-2, examines the response of an element with four nodes subjected to prescribed voltage. Node 1, 2, and 3 are ground, while Node 4 is driven with a 1.4kV cyclic voltage at 0.1Hz. In addition, the following displacements are constrained to be zero: $u_x^{(1)}$, $u_y^{(1)}$, $u_z^{(1)}$, $u_x^{(2)}$,$u_y^{(3)}$, $u_x^{(4)}$, and $u_y^{(4)}$, where the number in ( ) denotes the nodal number. In this case, all the voltage degrees of freedom are prescribed; that is, $\mathbf{V} = \mathbf{V_b}$. This means that $\mathbf{V_a}$ and $\mathbf{Q_{E_a}}$ are actually null vectors in the system. As a result, the system of Eq. 5.61, 5.62, 5.63, and 5.64 becomes

$$\dot{\hat{\mathbf{D}}}^* - \mathbf{F_1}(\hat{\mathbf{D}}, \hat{\mathbf{D}}^*) = 0, \tag{5.76}$$

$$\mathbf{F_2}(\hat{\mathbf{U}_a}, \hat{\mathbf{U}_b}, \hat{\mathbf{D}}, \hat{\mathbf{D}}^*) - \mathbf{R_{E_a}} = 0, \tag{5.77}$$

$$\mathbf{F_4}(\hat{\mathbf{U}_a}, \hat{\mathbf{U}_b}, \hat{\mathbf{D}}, \hat{\mathbf{D}}^*, \hat{\mathbf{V}_b}) = 0. \tag{5.78}$$

Therefore, only $\hat{\mathbf{D}}$, $\hat{\mathbf{U}}_\mathbf{a}$, and $\hat{\mathbf{D}}^*$ need to be solved. Figure 5-3 shows the polarization and displacement response of different nodes versus applied cyclic voltage signal. The polarization direction and deformed body can be visualized in Figure 5-2.

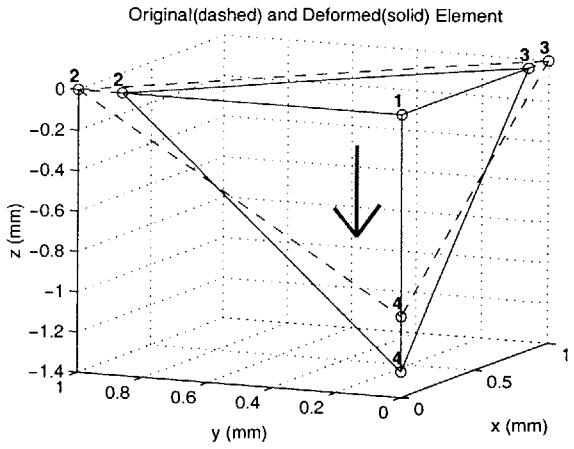

Figure 5-2: Test 1. Results: deformed body. Displacement is not in scale.

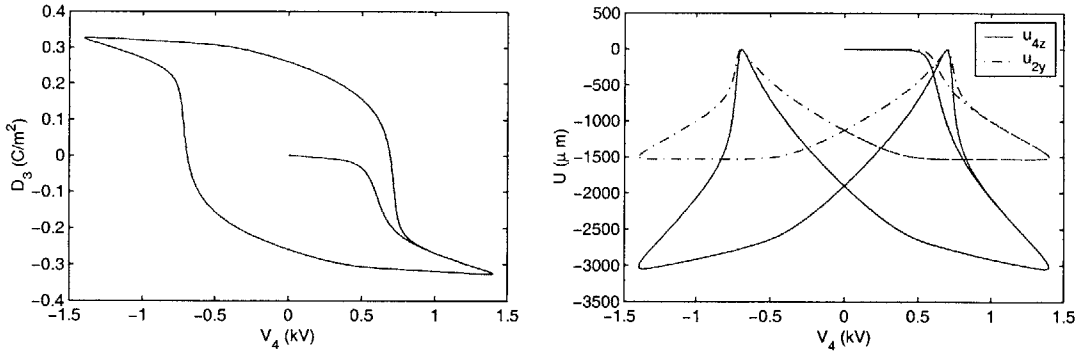

Figure 5-3: Test 1. Results: polarization (left) and displacement (right) vs. driving voltage.

Test 2. Single element with incomplete prescribed voltage

It is also important to investigate if the FEM code can solve for unprescribed nodal voltages on the element. As illustrated in Figure 5-4, Node 4 is prescribed with a 0.1Hz and 1.4kV cyclic voltage, and Node 1 is ground , while voltage on Nodes 2 and 3 are left undetermined. In addition, the following displacements are constrained to be zero: $u_x^{(1)}$, $u_y^{(1)}$, $u_z^{(1)}$, $u_x^{(2)}$,$u_y^{(3)}$, $u_x^{(4)}$, and $u_y^{(4)}$. Compared to the applied voltage, Figure 5-5 shows the voltage solved by the FEM code. Due to the boundary condition prescribed on the nodal displacement, the element may undergo stress as the electric field increases. This induced stress will cause the nodal potential to decrease as shown in Figure 5-5. Figure 5-6 shows the polarization and displacement response of different nodes versus applied voltage. The polarization direction and deformed body can be visualized in Figure 5-4.

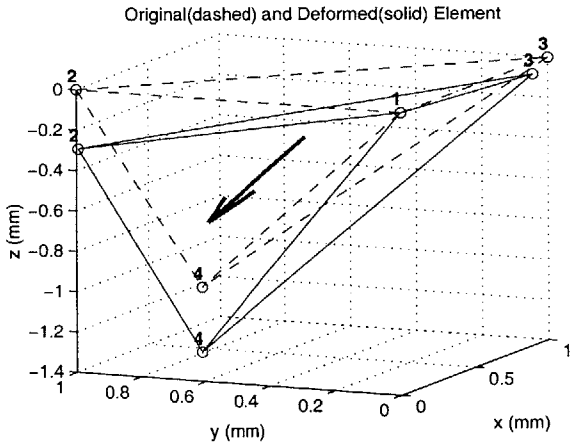

Figure 5-4: Test 2. Results

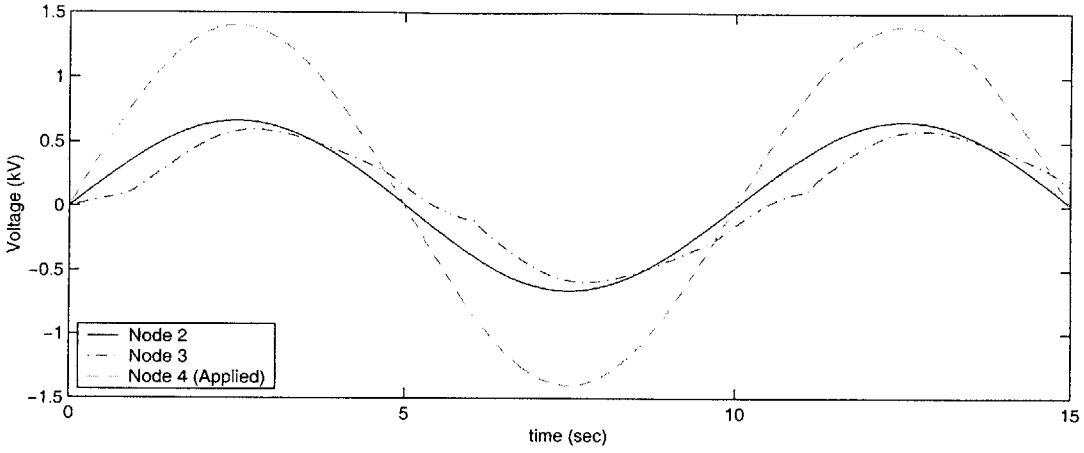

Figure 5-5: Test 2 result: comparison between nodal voltage and driving voltage.

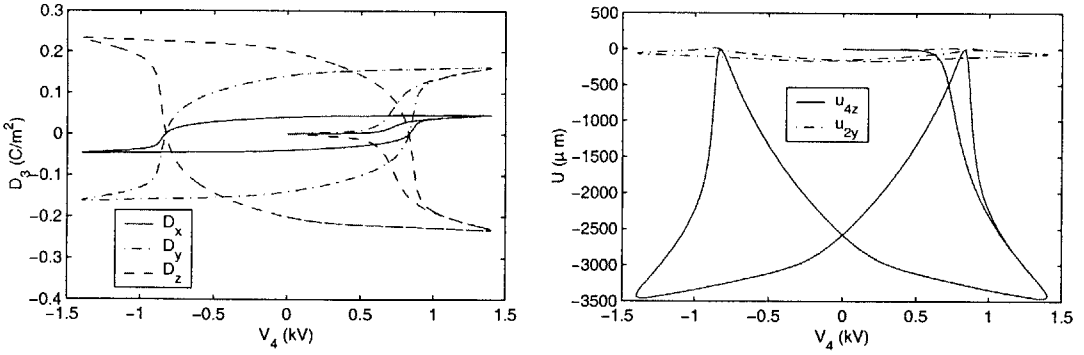

Figure 5-6: Test 2. results: polarization (left) and displacement (right) vs. driving voltage.

5.5.2 Piezoelectric Response under Uniform Loading

Before solving the problem with irregular boundary conditions or geometries, it is also essential to examine the case under uniform electric field, as shown in Figure 5-7. By symmetry, one can re-define the case with the representative volume shown in Figure 5-7 under the following boundary conditions:

$$\begin{aligned} \phi &= V\sin(\omega t), \quad \text{at } z = H, \\ \phi &= 0, \quad \text{at } z = 0, \\ u_x &= 0, \quad \text{at } x = 0, \\ u_y &= 0, \quad \text{at } y = 0, \\ u_z &= 0, \quad \text{at } z = 0. \end{aligned}$$

For demonstration purposes, the dimensions of the representative volume are a=1mm, b=1mm, and H=3mm, and its driving voltage is a 1Hz cyclic wave with an amplitude of 4.35kV. The representative volume is meshed into 36 elements by 19 nodes, shown in Figure 5-8 (left).

Figure 5-8 (right) shows the simulated results of the deformed body and the polarization direction on each element at time = 1.5s. As can be seen, the representative volume extends along the polarization direction while it shrinks in the transverse directions. Figure 5-9 shows the time history of the nodal voltages solved by the code. As can be seen, the potentials on the nodes are proportional to their z-coordinates because the volume is under uniform electric field along the z-direction. For the same reason, the whole volume exhibits a uniform polarization as shown in Figure 5-10 (right), and the displacements are also proportional to their z-coordinates as shown in Figure 5-10 (left).

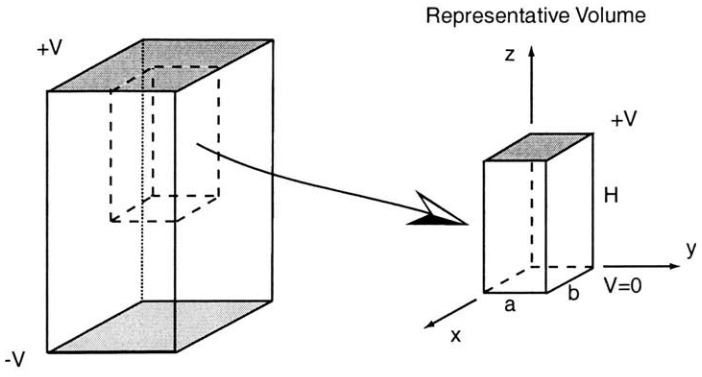

Figure 5-7: Representative volume of specimen under uniform electric field.

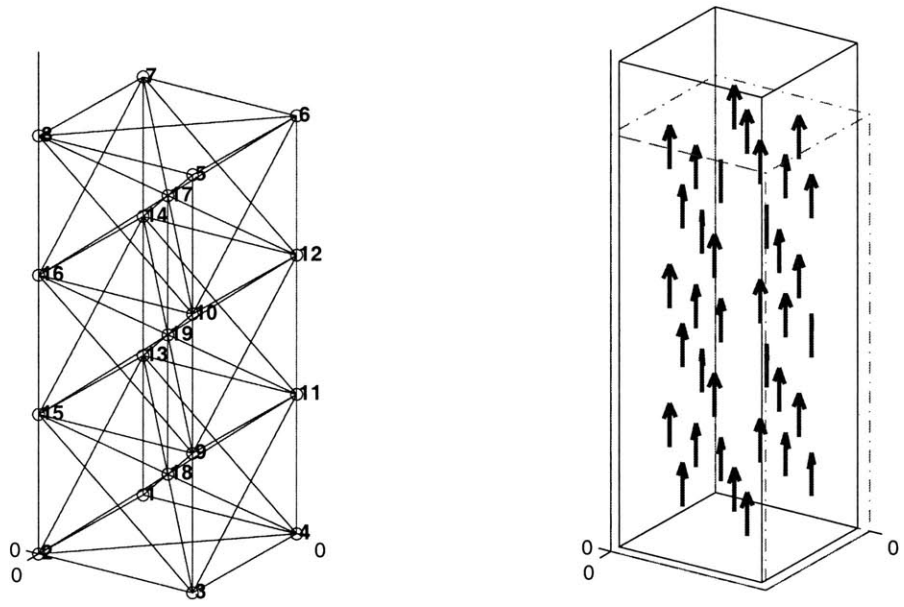

Figure 5-8: Mesh of representative volume for the case under uniform electric field.

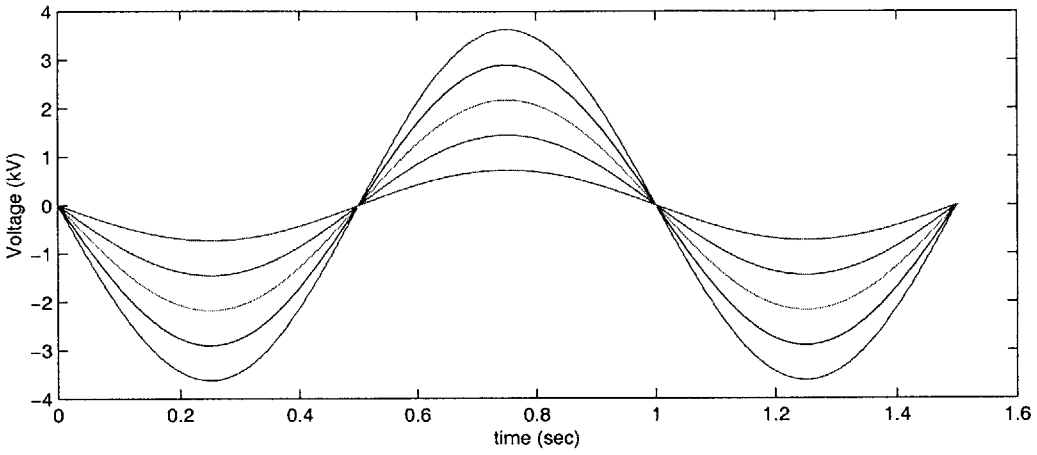

Figure 5-9: Solved voltage on the nodes.

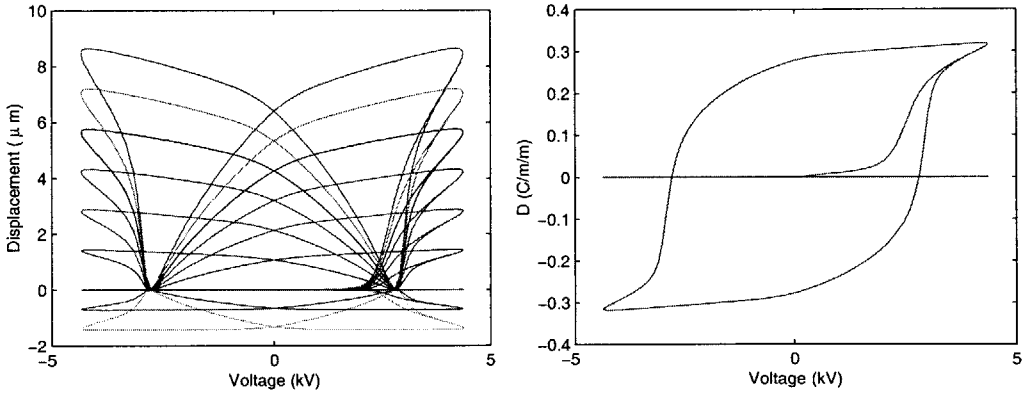

Figure 5-10: Solution of displacement on the nodes (left) and electric displacement on the elements (right).

5.5.3 Piezoelectric Response under Skewed Loading

It is the ultimate goal of this thesis to simulate the material response for irregular geometry or non-uniform boundary conditions. To demonstrate this capability of this code, a chunk of material with four electrodes on its edges is used, as illustrated in Figure 5-11. By symmetry, one can re-define the case with the representative volume shown in Figure 5-11 under the following boundary conditions:

$$\begin{aligned} \phi = V\sin(\omega t), \quad & \text{at } z = b,\ d < x < c + d, \\ \phi = 0, \quad & \text{at } x = 0, \\ u_x = 0, \quad & \text{at } x = 0, \\ u_y = 0, \quad & \text{at } y = 0, \\ u_z = 0, \quad & \text{at } z = 0. \end{aligned}$$

For demonstration purposes, the dimensions of the representative volume are a=1mm, b=1mm, c=1mm, and d=2mm, and its driving voltage is a 0.126Hz cyclic wave with an amplitude of 2.8kV. The representative volume is also meshed into 36 elements by 19 nodes, shown in Figure 5-12.

Figures 5-13 and 5-14 first show the results of the simulated potentials on the nodes compared to the cyclic driving voltage. As can be seen, some of the nodal potentials are not exactly proportional to the the driving voltage. This is because some of the element is experiencing stress while other elements are polarized. This phenomenon is very severe for the coarsely meshed volume especially when meshed by the 4-node tetrahedral element like the one used in this case, because this type of element exhibits very stiff characteristics[1]. For the same reason, the polarizations and displacements of some of the elements exhibit strange behavior, as shown in Figures 5-15 and 5-16. The polarization direction of each element and the deformed body compared to the original volume at various time steps are shown in Figure 5-17. As can be seen, the representative volume exhibits slight shear deformation due to the skewed electric field. Despite this, the deformation of the body shows significant elongation along the x-direction after 1.5 cycles of driving voltage. This is exactly the case for the actuator with interdigitated electrodes introduced in Chapter 1.

[1]The strain field and electric displacement are assumed uniform on the element. As a result, it shows little flexibility of its response

Unfortunately, the results discussed above are not converged to the real problem yet because of the coarse mesh used in this problem. In order to increase the accuracy, a much finer mesh must be used to relieve the stiff characteristics of the 4-node tetrahedral element.

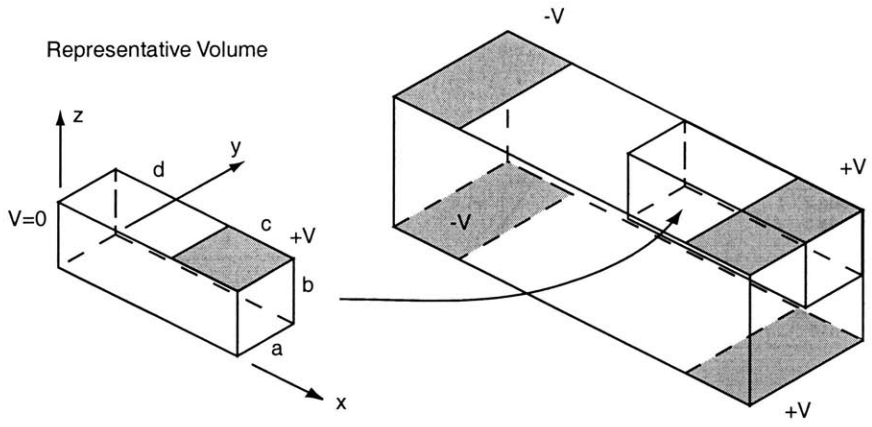

Figure 5-11: Representative volume of specimen under skewed electric field.

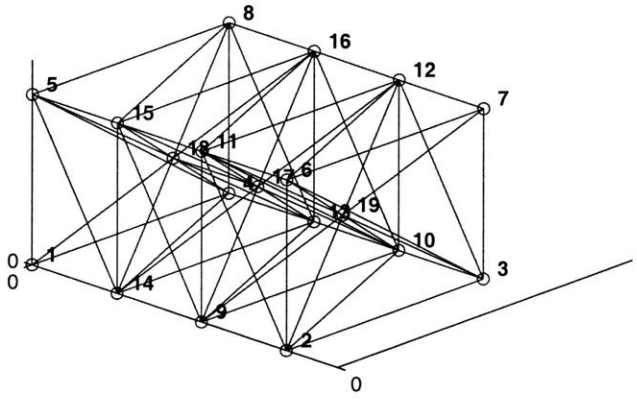

Figure 5-12: Mesh of representative volume for the case under skewed electric field.

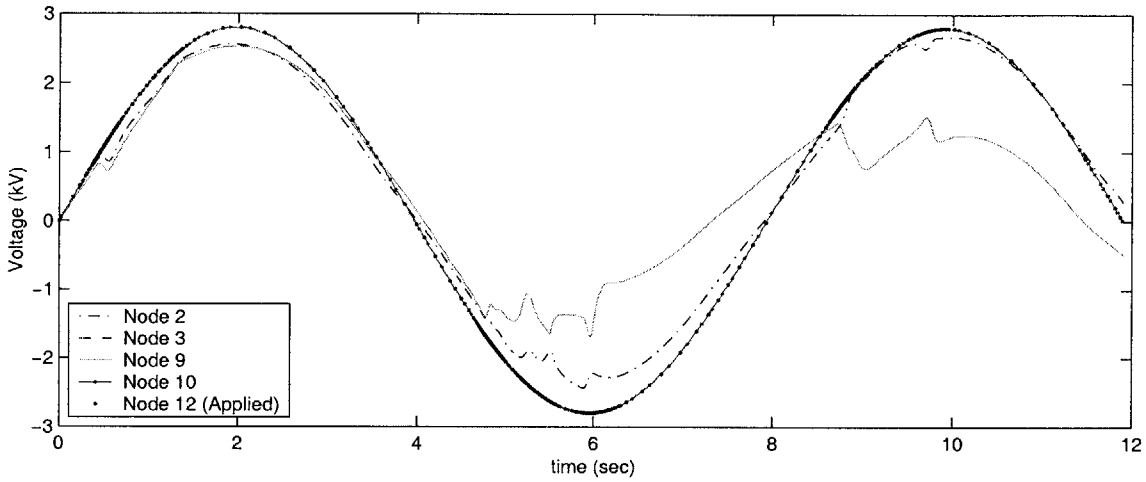

Figure 5-13: Solved voltage on the nodes.

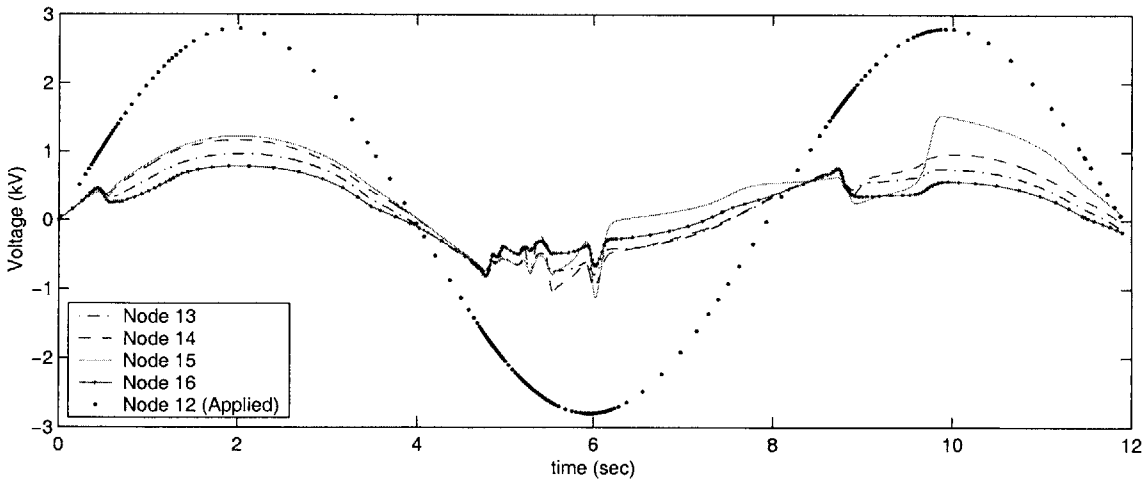

Figure 5-14: Solved voltage on the nodes.

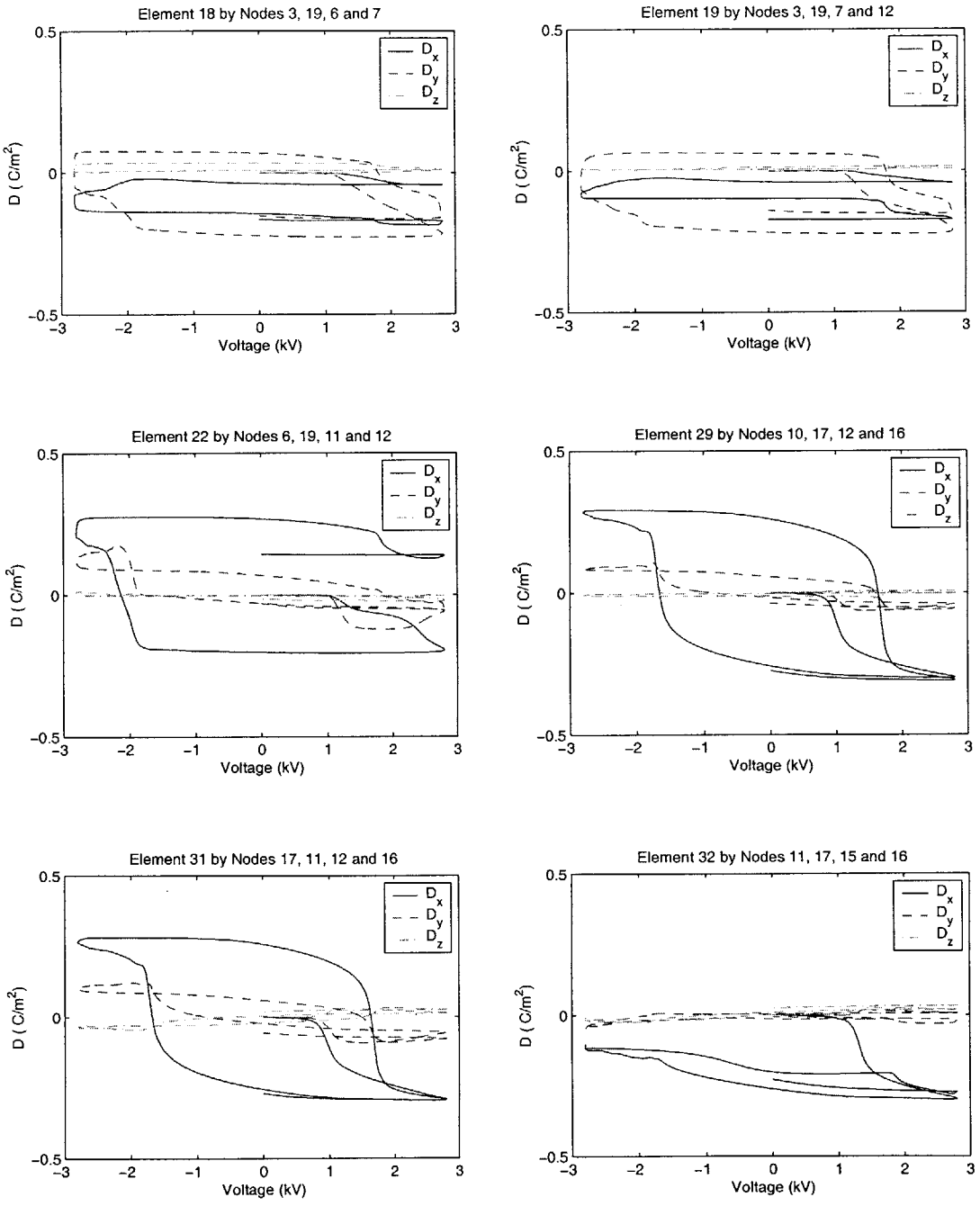

Figure 5-15: Electric displacement vs. driving voltage under skewed electric field on various elements.

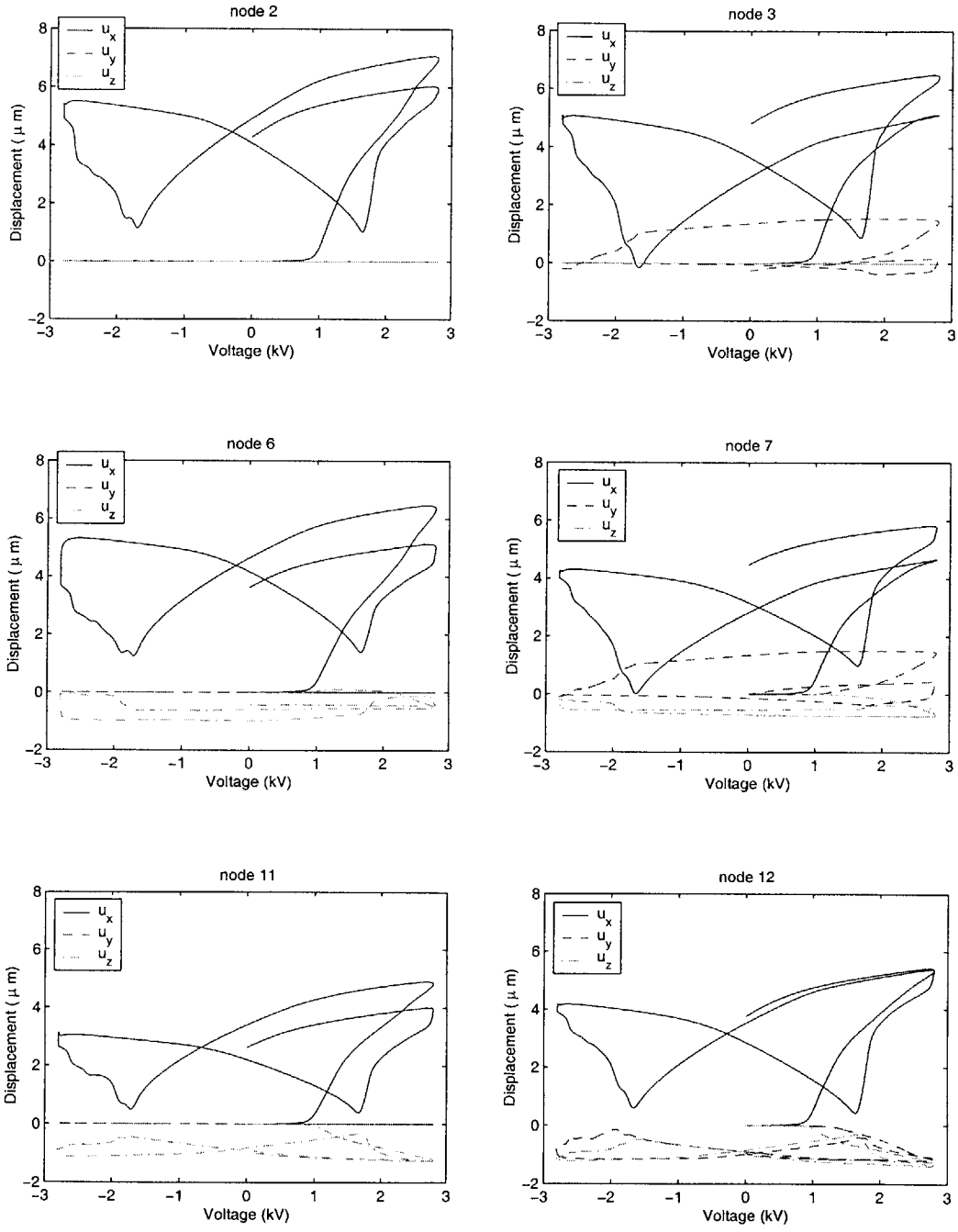

Figure 5-16: Displacement vs. driving voltage under skewed electric field on various nodes.

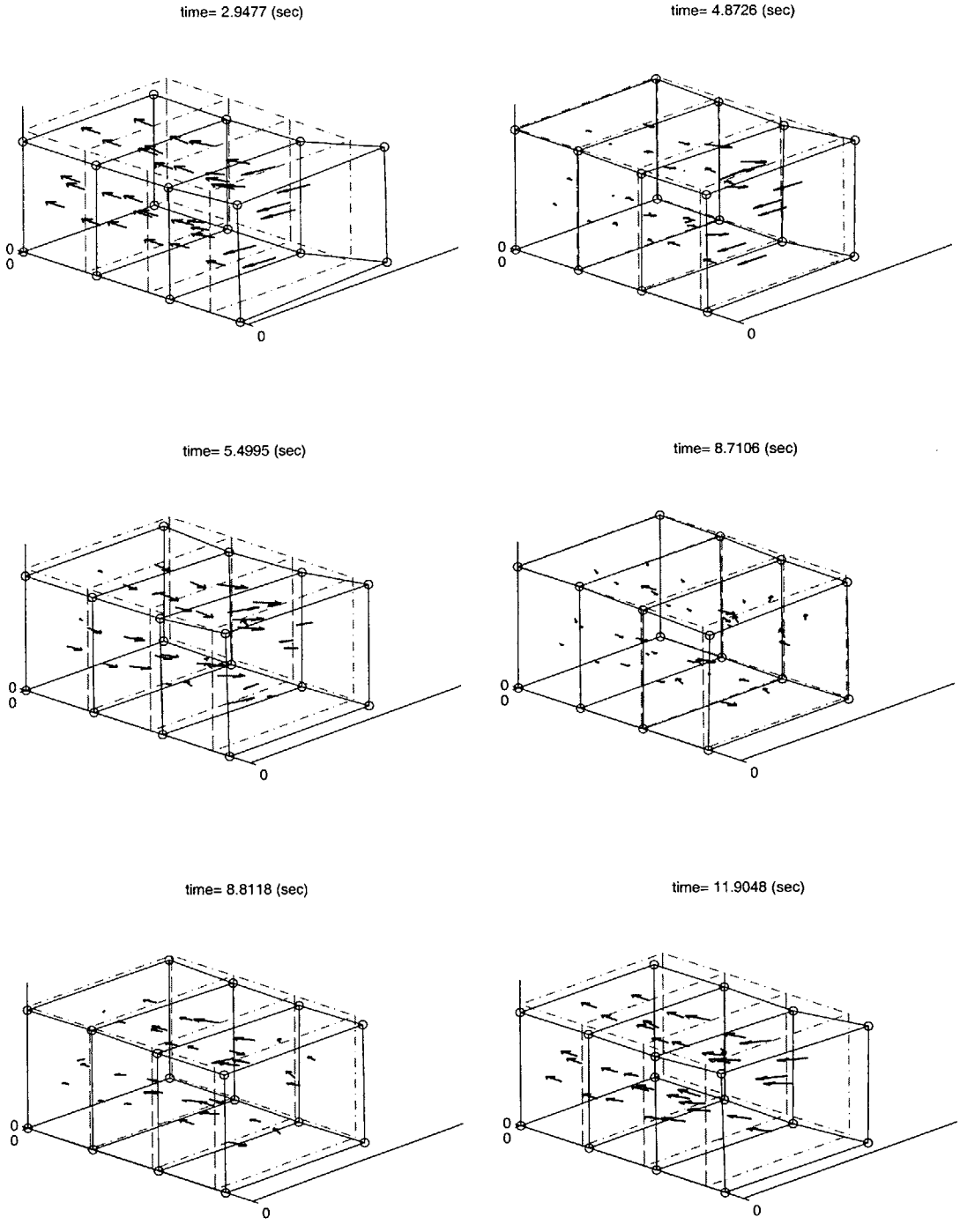

Figure 5-17: Deformed body under skewed electric field at various time steps.

5.5.4 Limitation of Large Scale Problem

As mentioned earlier, in order to increase the accuracy of the simulation, a much finer mesh must be used to eliminate the stiff characteristics of the 4-node tetrahedral element. This refined mesh will result in rapid growth of the degrees of freedom. As the scale of the problem grows, the tolerance control of iteration becomes very important for the DAE code to reach the converged solution.

An attempt has been made to simulate the previous case under skewed loading with a finer mesh. Unfortunately, the finite element code using the DASPK solver fails to converge the solution under the specified tolerance. This failure is believed to be caused by the inefficient tolerance control used by the DASPK solver. In DASPK, the tolerance is controlled by the root-mean-square norm of the residues of the algebraic-differential equations:[46]

$$\|\mathbf{x}\|_{RMS} = \left[N^{-1} \sum_{i}^{N} (x_i)^2 \right]^{1/2} \tag{5.79}$$

where N is the degree of freedom. This algorithm shows no difficulty in solving small scale problems. However, as the degree of freedom increases, the error seen by the solver decreases because the error has been divided by N. To remedy this problem, it is recommended that the tolerance should be controlled by the ℓ_2 norm

$$\|\mathbf{x}\|_2 = \left[\sum_{i}^{N} (x_i)^2 \right]^{1/2} \tag{5.80}$$

or by the ℓ_∞ norm

$$\|\mathbf{x}\|_\infty = max(x_i) \tag{5.81}$$

instead of root-mean-square norm.

Unfortunately, it is impossible to modify the DASPK solver without violating its copyright, and developing a new solver is beyond the scope of this thesis work. The only thing that can be done is to tighten the tolerance manually according to the size of the problem, N. However, by doing so, more computational efforts are required to solve the problem. Due to the limitation of the current computing capability, a large scale problem cannot be solved within the schedule of this thesis. As a result, solving for a large scale problem shall be left as future work. Nevertheless, the study in the previous case that is under skewed loading has successfully demonstrated the formulation and the solution technique of the 3-D rate dependent piezoelectric finite element analysis.

5.6 Summary of 3-D Nonlinear Rate Dependent Finite Element Analysis

To provide a compatible analysis tool for problems with irregular geometries using the material model developed in this thesis, based on the mixed FEM formulation by Ghandi[35], a differential algebraic formulation of finite element method was derived, coded, and solved using the DASPK DAE solver in this chapter. The computer code successfully demonstrated simple examples with uniform and skewed loadings. However, the size of solvable problem was limited by the tolerance control algorithm and speed of computing machines.

Chapter 6

Conclusions

This chapter summarizes the critical data of the piezoelectric material properties and the development of the material models. The limitations of the model and finite element analysis are revealed. Possible future work is also recommended. Finally, the essential contributions advanced by this thesis are detailed.

6.1 Summary and Future Work

Nonlinearity and hysteresis make it difficult to analyze and design a piezoelectric device for smart structures applications, such as actuating and sensing components as well as energy harvesters. In addition, compressive depolarization is a major concern in terms of performance. Most actuators, sensors, and even energy harvesters operate at high compression. This compression, which is usually parallel to the poling direction, will depolarize the material and degenerate the performance. Moreover, frequency dependence is a well-known characteristic of piezoelectric materials. As a result, this thesis is motivated by these obstacles to characterize in details the nonlinear and hysteric behaviors while subject to various loading conditions. It is also the goal to develop an analytical model and a finite element analysis tool to predict these behaviors.

Since PZT-5A has been used as fibers in commercial active fiber composites, and it has moderate piezoelectric constant and stiffness, PZT-5A was selected for the actuation tests in this work. Single crystal PZN-PT and PMN-PT were chosen for the power generation tests because of their high piezoelectric constants. PZT-5H was also tested for energy harvesting

because of its low cost and moderate piezoelectric constants. In addition to these tests, repolarizing material behaviors of both PZT-5A and PZT-5H subjected to high electric excitations and under static compression were also characterized to obtain a full range of information for material modeling.

To study the actuation performance of PZT-5A, several tests were designed: a single loop test was aimed at depicting the envelope of actuation during compressive loading and unloading situations, a multiple loop test was aimed at identifying the reversibility of the actuation after various intermediate levels of compressive, and a residual test with various compression duration was aimed at revealing the stress rate effects. The tests unveiled the following facts:

1. Compression starts to depolarize the PZT-5A material at 30 MPa.
2. PZT-5A actuation capability can fully recover after 30MPa compression and slightly rebound after 60MPa. However, after 90MPa, PZT-5A loses approximately 70% of its actuation, depending on the level of electric excitation.
3. High electric field cannot prevent the depolarization.
4. Short compression duration with positive high electric excitation can result in actuation recovery.

To measure the energy harvesting capability of PZT-5H and single crystal PZN-PT and PMN-PT, an open circuit voltage divider and a short circuit charge amplifier were designed, built and calibrated. To apply high frequency force, the piezo-actuating component testers developed by Lutz and Shi were modified to obtain accurate and sufficient compression. The piezoelectric and elastic constants, g_{33}, d_{33}, s_{33}^{E}, and s_{33}^{D} while subject to various amplitudes of compression were first measured and curve-fitted as polynomial functions of the compression. The electrical power generated by various amplitudes of compression was then obtained using a rectifying diode circuit and correlated with the estimated power output using the fitted piezoelectric constants.

An essential trend was found for single crystal PZN-PT and PMN-PT that g_{33} decreased drastically as the compression was increased. This significantly degenerated the electric power output at high compression. In addition, unlike PZT-5H, single crystal showed softening tendency as the compression was enhanced. This implied that the single crystal structure might be damaged by the high compression. Lessons learned from this test include:

both g_{33} and d_{33} are the critical material properties with regard to the energy harvesting capability; PZT-5H starts to deteriorate at 22MPa, while single crystal materials start to degenerate at 11MPa for PZN-PT and 15MPa for PMN-PT; using PZN-PT at low compression for energy harvesters is beneficial, while using PZT-5H is more profitable at compression higher than 30MPa.

To develop a material model, which was targeted to capture full-range nonlinear and hysteretic behaviors as well as material constants, repolarizing responses of PZT-5A were also characterized using longitudinal and transverse tests. These tests were originally developed for PZT-5H by Ghandi but were modified in this work specially for PZT-5A. In addition, rate dependent repolarizing data of both PZT-5A and PZT-5H under stress free conditions were acquired.

Another goal of this thesis is to develop a material model by establishing a physical framework within which empirical descriptions of the behavior of some of the variables are embedded. The development of the model consists of three stages: to gain understanding and insight of material behaviors; to capture major effects into equations and computer codes for the use of finite element method; to condense material data as constants to establish a material library or design guide for material selection. The description of these stages follows the guideline by Ashby[70]. Each stage has its objective task and corresponding precision. Additional mechanisms shall be taken into consideration to proceed to the more accurate level.

The goal of the first stage was to understand the electric rate and static stress dependent effects. At this stage, only the 1-D model was considered and the precision was targeted within an order of magnitude. The model was formulated using the thermodynamically consistent framework developed by Ghandi who introduced an internal variable D^*, a net remnant polarization, to govern the material hysteresis. An additional evolution law of D^* was proposed using the Weibull function to describe the electric rate dependence in this work. A parametric study was performed to evaluate the influence of the rate rule constants: ΔD_c controls the initiation of repolarization, α governs abruptness of repolarizing transition, and both α and τ determine the rate dependence of coercive field. The material models for PZT-5H and PZT-5A were determined by optimizing the coefficients of energy expansion and by tuning the rate rule constants. At this first stage, this 1-D model successfully

offered significant insights into rate dependence and stress dependence of the materials and achieved the targeted precision.

In order to formulate the model for the use of the full 3-D finite element analysis at the second stage with the targeted precision factor of 2, 3-D tensor invariants originally proposed by Ghandi were included in the 1-D model developed in the first level. The 1-D evolution law of D^* was modified into three dimensions. 3-D models for PZT-5H and PZT-5A were also obtained by optimizing the coefficients of energy expansion and by tuning the rate rule constants. This 3-D model also achieves the targeted precision of Stage 2 .

The model developed at Stage 2 was tested directly against the criteria of the third stage without adding new mechanisms. Unfortunately, the model failed to achieve the targeted precision of 1.1 due to the following factors:

1. Stress rate dependence is absent.

2. Unlike PZT-5H, a special rate rule describing the hysteresis between S and D is required to improve the PZT-5A model.

3. Least squares fit using large amplitude data makes it difficult to predict the small signal response accurately, unless the data is perfectly fit by the model.

These factors are recommended as future work for a better material model. Although it may not be difficult to derive a new rate rule managing the hysteresis between S and D, the major obstacle is to guarantee the model to be thermodynamically consistent.

To provide a compatible analysis tool for problems with irregular geometries using this material model, based on the mixed FEM formulation by Ghandi[35], a differential algebraic formulation of the finite element method was derived, coded, and solved using the DASPK DAE solver. The computer code successfully demonstrated simple examples with uniform and skewed loadings. However, the size of the solvable problem was limited by the tolerance control algorithm and the speed of the available computing machines. To improve the stability of convergence, a new tolerance control algorithm using ℓ_∞ norm of the residues of the algebraic-differential equations was proposed for future work,

$$\|\mathbf{x}\|_\infty = max(x_i), \tag{6.1}$$

instead of original root-mean-square norm used by DASPK:

$$\|x\|_{RMS} = \left[N^{-1} \sum_{i}^{N} (x_i)^2 \right]^{1/2}, \tag{6.2}$$

where N is the number of the degrees of freedom, and $\mathbf{x}$ is the residue vector of the differential algebraic equations. To facilitate the computation, parallel computing is feasible and recommended.

The combination of the nonlinear mixed FEM model and the material model provides a useful tool for modeling the response of active devices with complicated geometries and irregular boundary conditions. This tool permits investigation of the nonuniform polarization in such devices and its effect of the phenomenological response of the system. This tool also permits analysis of internal stress originated by nonuniform spontaneous strain in the material which can cause actuator failure.

6.2 Contributions

Piezoelectric Actuation Constants

Piezoelectric actuation constants d_{33} under various stresses have been reported by Zhang [29] and Krueger [28]. However, these data were obtained using small electric excitation.

In this work, piezoelectric actuation constants d_{33} under various static stresses were measured using various levels of electric signals. In addition, new methodologies such as the multiple loop test and the residual actuation test were conducted to identify how the material recovers from the degeneration of compressive depolarization. Moreover, the compression duration issues were discovered and tested.

Piezoelectric Power Generation Constants

Both g_{33} and d_{33} are essential to determine the electric energy output of piezoelectric materials. In addition, s_{33}^E and s_{33}^D are essential to determine the required mechanical input energy and coupling coefficients.

Although these data of PZT-5H have been measured and published by the vendor[53], the test conditions were limited to low stress. d_{33} constants of PZN-PT at high stress have also been published by the vendor[54], but the data was obtained from the actuation test

and therefore is not valid for an energy harvesting application. In addition, no complete sets of single crystal PZN-PT and PMN-PT data are available in the literature.

In this work, systematic material characterization for power generation was performed under various amplitudes and frequencies of compression. d_{33}, g_{33}, s_{33}^D, and s_{33}^E constants are extracted from the experiments and fitted as functions of compression. These results successfully correlate with the measured power data using the rectifying circuit. Comparison between polycrystalline PZT-5H and single crystal PZN-PT and PMN-PT were performed.

This work also found that g_{33} plays an important role in determining the maximum electric power output under high stress because g_{33} decreases drastically as compression is increased. Moreover, from the data of s_{33}^E as a function of compression, the single crystal PZN-PT and PMN-PT show ***softening*** phenomenon, while polycrystalline material PZT-5H shows ***hardening*** behavior. This result implies that the material structure of the single crystal specimens might have been damaged by high compression. This might explain why g_{33} of the single crystals drops more rapidly. Additional study is needed to fully understand this discrepancy.

Demonstration of Piezoelectric Power Generation at High Frequency

It is a goal of this thesis to demonstrate that piezoelectric power generation can still work at high frequency. Although the piezoelectric power generation was first demonstrated by Umeda [32][33] using a diode circuit and a ball drop as the mechanical input, it is difficult to examine the result as a function of stress and frequency. The recent study by Goldfarb [57] reported that the efficiency of piezoelectric power generation is frequency dependent and that the efficiency is very low at high frequency.

However, a further study in this work shows that the frequency dependency depends upon the impedance of the circuit that is used to characterized the power. In Goldfarb's result, the test was implemented using a resistor whose impedance will cause problems, especially at high frequency. Unlike Goldfarb's approach but similar to Umeda's, this work systematically designed a test procedure using the high frequency tester and demonstrated frequency independency which disproved Goldfarb's statement. In addition, this work also identified the limitation caused by high compression.

3-D Repolarizing Material Behavior of PZT-5A

The 3-D repolarizing material behavior of PZT-5H under various stresses has been reported by Ghandi[35]. However, data of PZT-5A, which is used in the commercial AFCs, would be essential to improve the performance of AFCs but is absent in the literature. As a result, one of the goals in this work is to obtain sufficient material data of PZT-5A for analyzing AFCs.

The challenge of testing PZT-5A is the preparation of the specimen. The higher coercive field of PZT-5A makes it difficult to obtain fully repolarizing behavior with saturation. Due to the 8kV isolation limitation of the strain gauge conditioner, the specimen has to be small enough to obtain high enough electric driving field. On the other hand, the specimen has to be large enough to accommodate the strain gauges and to prevent electric arcing. This work has overcome these obstacles and has successfully obtained the 3-D repolarizing data of PZT-5A. In addition, rate dependent data of both PZT-5A and PZT-5H were acquired.

3-D Rate Dependent Model

Table 6.2 shows a comparison of various models found in the literature. None of the models in the literature are capable of simulating 3-D nonlinear repolarizing material behavior under various stresses and frequencies. For instance, Ghandi[35] developed a 3-D thermodynamically consistent model. Ghandi's model only considers stress dependency but not frequency dependency. Another example is the model by Soukhojak and Chiang[2] who has modeled 1-D behavior of materials under various stresses and frequencies. But it is difficult to expand this framework into a 3-D model.

Based on the 3-D model developed by Ghandi, a new 3-D rate dependent model was developed in this work. To do so, a novel evolution law was derived to describe the rate dependency of the materials. In addition, a material model library of PZT-5A and PZT-5H was established.

Discrepancy of Domain Switching Process between PZT-5A and PZT-5H

A major discrepancy between hard and soft materials was found by comparing the S-D curves of PZT-5A and PZT-5H. The hysteresis of the PZT-5A S-D curve was the reason why the PZT-5A model did not perform as well as PZT-5H's. In addition, this hysteresis

Table 6.1: Model comparison with literatures

	1-D	3-D	Rate dependent	Stress dependent	Strain response	Polarization response	Comment
Tikare et. al.[1]	•		•			•	Monte Carlo
Fan et. al.[6]	•			•	•		Nonlinear spring
Chen and Lynch[24]	•			•	•	•	
Hwang et. al.[22]	•			•	•	•	
Smith and Ounaies[7]	•		•			•	ODE
Bassinouny et.al.[11]	•		•	•		•	
Chen and Montgomery[13]	•		•		•	•	
Chen and Tucker[15]	•					•	
Soukhojak and Chiang[2]	•		•	•	•	•	ODE
Ghandi and Hagood[35]	•	•		•	•	•	Tensor invariants
This work	•	•	•	•	•	•	DAE

was explained by a $90°/180°$ domain switching hypothesis modified from Zhou's theory[65]. Although Zhou has reported similar hysteretic behavior in an S-D curve, his results were limited to a single material at various frequencies. In contrast, the result shown in this work covers two distinguishable materials at various frequencies.

This finding also shows the significance of the PZT-5A characterization accomplished in this work. Without this, the flaw in Ghandi's framework[35] and in this material model would not have been revealed.

Differential Algebraic Formulation of Finite Element Analysis

Because the 3-D rate dependent material model was newly developed, none of commercial finite element software packages could can support this model. To provide a compatible analysis tool, based on the mixed FEM formulation by Ghandi[35], a differential algebraic formulation of the finite element method was derived, coded, and demonstrated successfully by simple examples. Although the performance of this code was limited by the current computing facility, this code is expected to contribute to solving real problems when advanced computing machines are made available.

Appendix A

Simulink Graphical Model

This appendix documents the simulation of the Simulink models used in this thesis. These models include:

1. Linear piezoelectricity with resistive load[1].
2. Linear piezoelectricity with diode bridge[2].
3. 1-D nonlinear short circuit piezoelectricity.
4. 3-D nonlinear short circuit piezoelectricity.
5. 1-D nonlinear open circuit piezoelectricity.
6. 1-D nonlinear open circuit piezoelectricity with conduction.
7. 3-D nonlinear open circuit piezoelectricity.
8. 3-D nonlinear open circuit piezoelectricity with conduction.
9. 1-D nonlinear piezoelectricity with diode circuit.
10. 3-D nonlinear piezoelectricity with diode circuit.

The reader is encouraged to consult the manual of Simulink[71]. Some graphical simulation blocks make use of S-functions[72], which will be listed in Appendix B.

[1]Linear piezoelectric block was constructed with help from K. Ghandi.
[2]Diode bridge block was constructed with help from Y.-H. Su.

A.1 Linear Piezoelectricity with Resistive Load

Figure A-1 shows the graphical simulation of linear piezoelectricity with resistor R. The block "Piezo" in Figure A-1 is detailed in Figure A-2. The matrix gain "K "in Figure A-2 describes the constitutive relation between the inputs (force and charge) and outputs (voltage and displacement):

$$\frac{L}{A}\begin{bmatrix} \beta_{33}^{T} & -g_{33} \\ g_{33} & s_{33}^{D} \end{bmatrix}, \tag{A.1}$$

where L is the thickness of the specimen, and A is the area of the cross section.

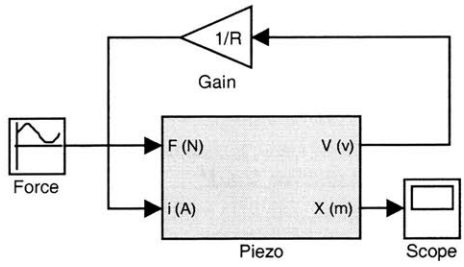

Figure A-1: Linear piezoelectricity with resistive load

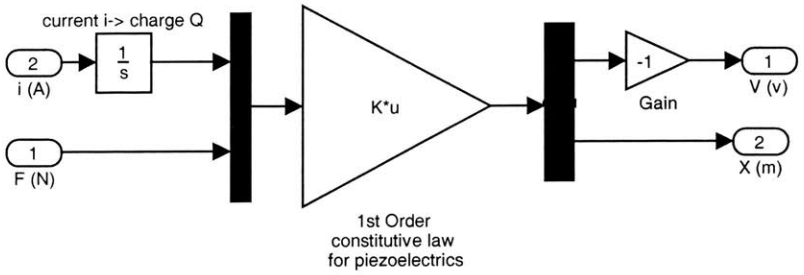

Figure A-2: The block "Piezo" shown in Figure A-1.

A.2 Linear Piezoelectricity with Diode Bridge

Figure A-3 shows the graphical simulation of linear piezoelectricity with a rectifying diode bridge whose voltage and current are labeled in Figure A-4: the voltages and currents at four junctions are V_k and I_k, $k = 1 \cdots 4$, respectively; the voltages across the diodes and the currents through the diodes are v_k and i_k, $k = 1 \cdots 4$, respectively.

The block "Piezo" in Figure A-3 is the same as the one specified in Figure A-2. The gain matrix in Figure A-3 relates the voltage differences between the piezoceramics and the battery:

$$\begin{bmatrix} 0.5 & 0.5 \\ 1.0 & 0.0 \\ 0.5 & -0.5 \end{bmatrix}. \tag{A.2}$$

The block "Rectifying Diode Bridge" in Figure A-3 is detailed in Figure A-5. The first gain matrix in Figure A-5, labeled as "Voltages(Junction->Diode)", links the global nodal voltage to the local diode voltages:

$$\begin{Bmatrix} v_1 \\ v_2 \\ v_3 \\ v_4 \end{Bmatrix} = \begin{bmatrix} 1 & -1 & 0 & 0 \\ 0 & -1 & 1 & 0 \\ 0 & 0 & -1 & 1 \\ -1 & 0 & 0 & 1 \end{bmatrix} \begin{Bmatrix} V_1 \\ V_2 \\ V_3 \\ V_4 \end{Bmatrix}. \tag{A.3}$$

From Kirchhoff's law, the second gain matrix in Figure A-5, labeled as "Currents(Diode->Junction)", relates the local diode currents to the global junction currents:

$$\begin{Bmatrix} I_1 \\ I_2 \\ I_3 \\ I_4 \end{Bmatrix} = \begin{bmatrix} -1 & 0 & 0 & 1 \\ 1 & 1 & 0 & 0 \\ 0 & -1 & 1 & 0 \\ 0 & 0 & -1 & -1 \end{bmatrix} \begin{Bmatrix} i_1 \\ i_2 \\ i_3 \\ i_4 \end{Bmatrix}. \tag{A.4}$$

Each block, labeled "Diode element" in Figure A-5, defines the constitutive law for each diode (Eq. 2.18) and is implemented in Figure A-6.

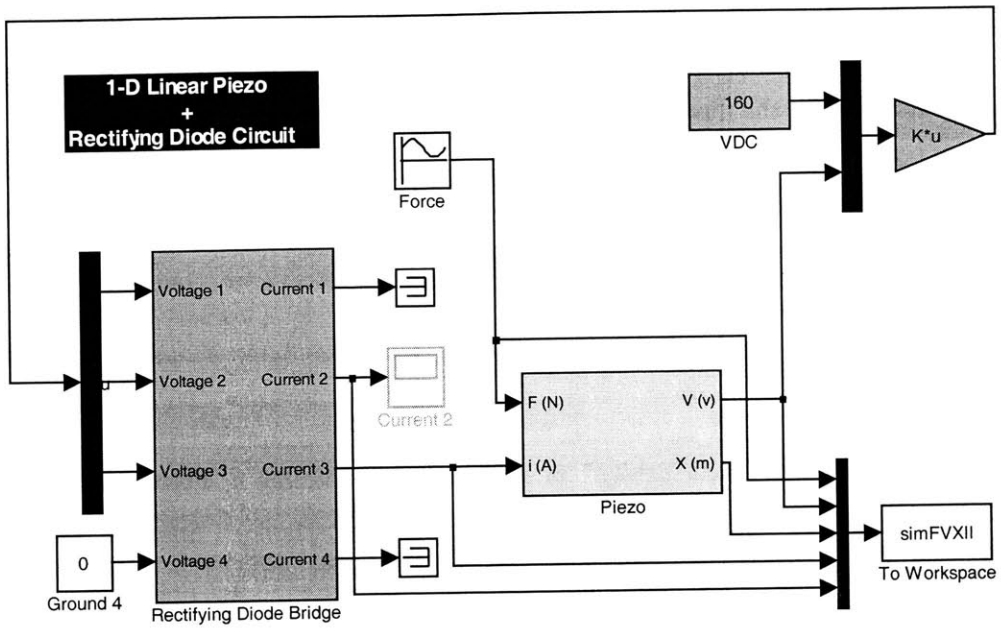

Figure A-3: Linear piezoelectric device with diode bridge.

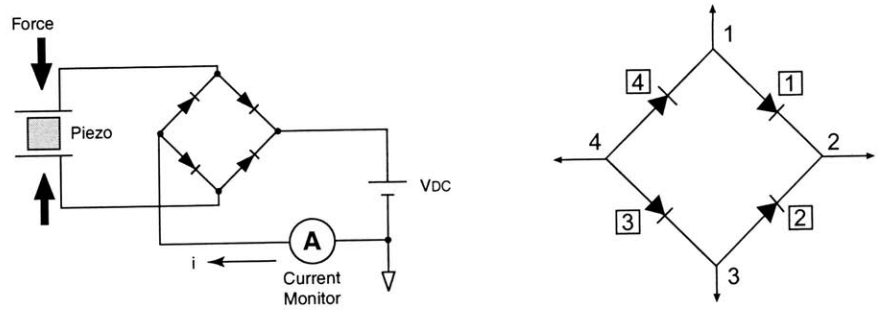

Figure A-4: Labels of voltages and currents in rectifying diode circuit.

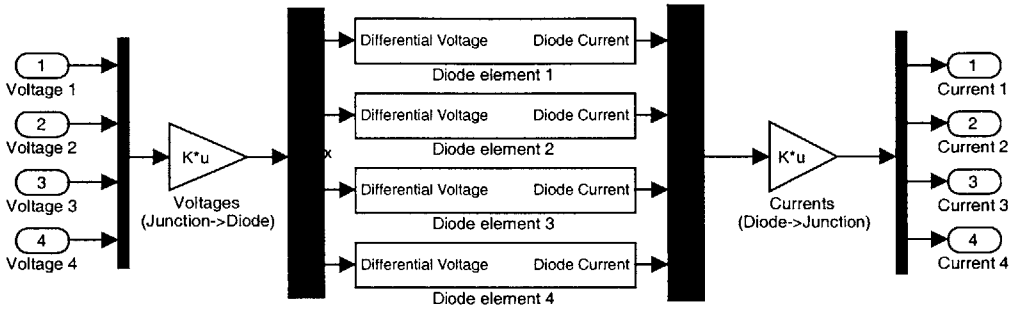

Figure A-5: The details of the block "Rectifying Diode Bridge" in Figure A-3.

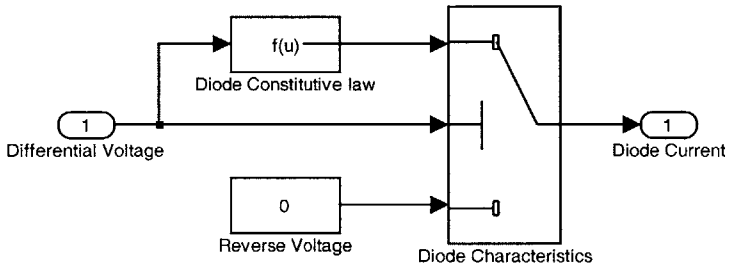

Figure A-6: Implementation of constitutive law of each " Diode element" in Figure A-5 .

A.3 1-D Nonlinear Short Circuit Piezoelectricity

Figure A-7 shows the graphical simulation of the 1-D nonlinear piezoelectric response under short circuit condition using the 1-D model developed in this thesis. The block labeled "Piezo" is detailed in Figure A-8. The s-functions "Dsraterule" and "sfuncES", which code the rate rule (Eq. 3.34) and the constitutive relations

$$E = E(D, D^*, T), \tag{A.5}$$

$$S = S(D, D^*, T) \tag{A.6}$$

are listed in Appendices B.1 and B.2, respectively.

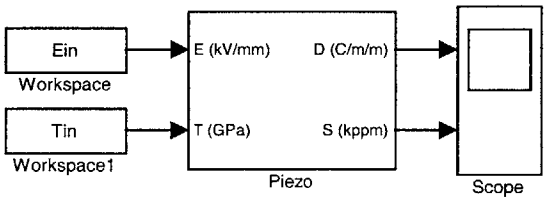

Figure A-7: 1-D nonlinear short circuit simulation.

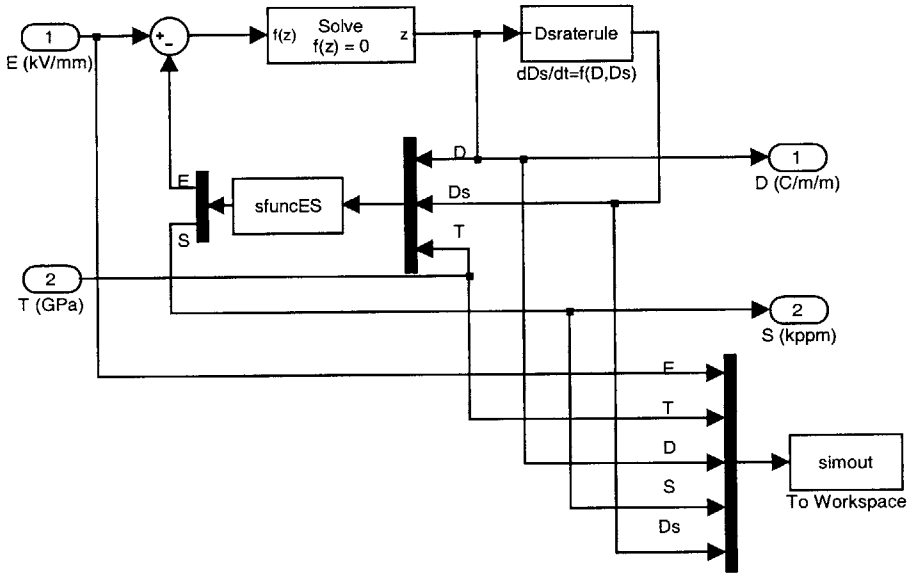

Figure A-8: Details of block "Piezo" in Figure A-7.

A.4 3-D Nonlinear Short Circuit Piezoelectricity

Figure A-9 shows the graphical simulation of the 3-D nonlinear piezoelectric response under short circuit condition using the 3-D model developed in this thesis. The block labeled "Piezo" is detailed in Figure A-10. The s-functions "Dsraterule3D" and "sfuncES3D", which code the rate rule (Eq. 3.65) and the 3-D constitutive relations

$$\mathbf{E} = \mathbf{E}(\mathbf{D}, \mathbf{D}^*, \mathbf{T}), \tag{A.7}$$

$$\mathbf{S} = \mathbf{S}(\mathbf{D}, \mathbf{D}^*, \mathbf{T}) \tag{A.8}$$

are listed in Appendices B.3 and B.4, respectively.

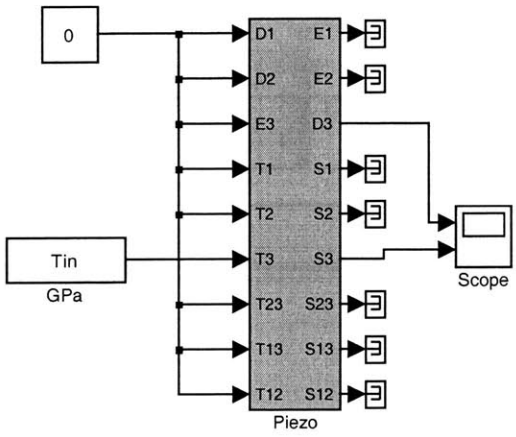

Figure A-9: 3-D nonlinear short circuit simulation.

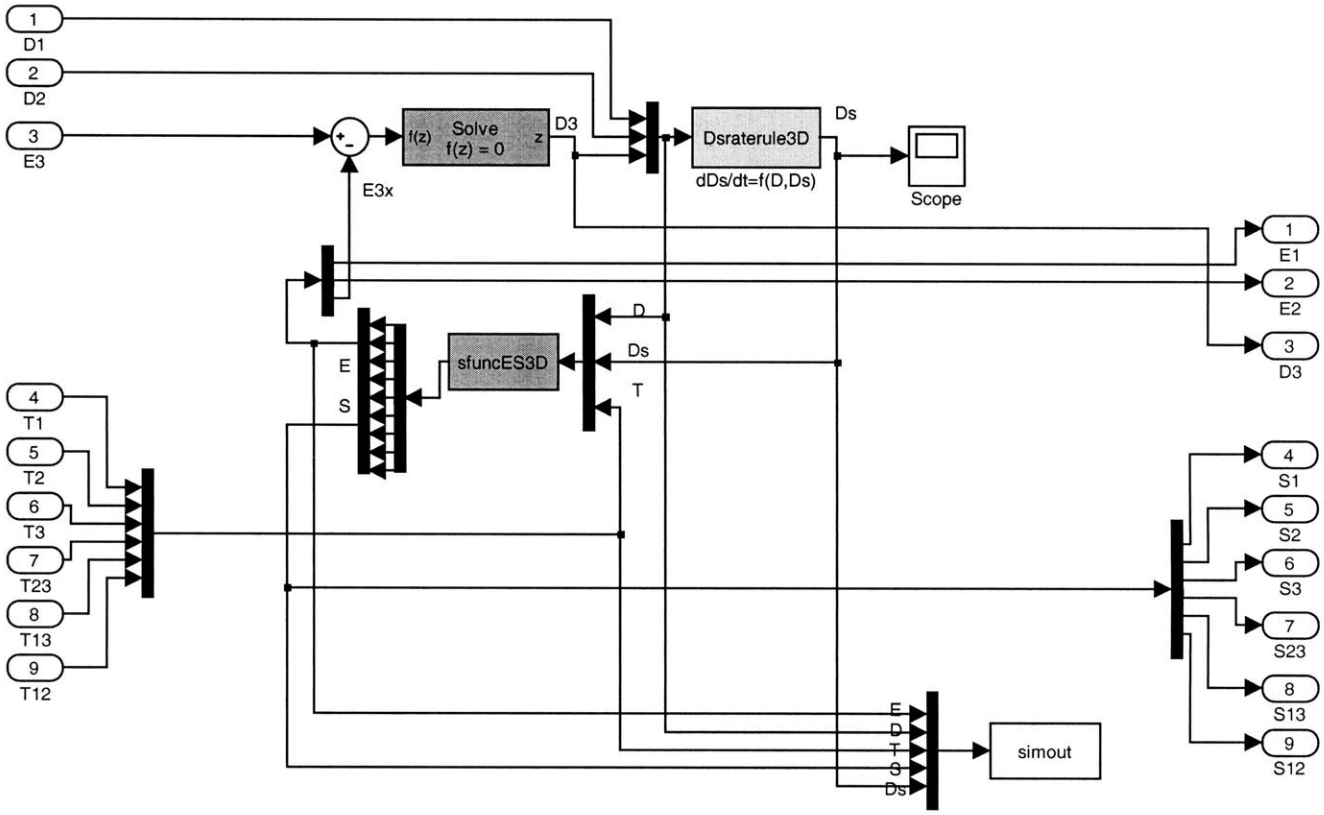

Figure A-10: Details of block "Piezo" in Figure A-9.

A.5 1-D Nonlinear Open Circuit Piezoelectricity

Figure A-11 shows the graphical simulation of the 1-D nonlinear piezoelectric response under open circuit condition using the 1-D model developed in this thesis. The block labeled "Piezo" is detailed in Figure A-12. The s-functions "Dsraterule" and "sfuncES" are listed in Appendices B.1 and B.2, respectively. The initial conditions of D and D^* are specified at the block named "D0" and the s-function "Dsraterule", respectively.

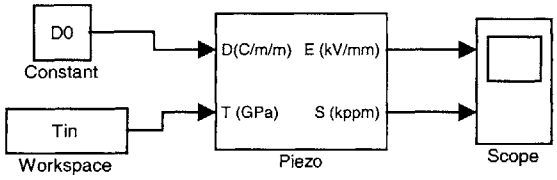

Figure A-11: 1-D nonlinear open circuit simulation.

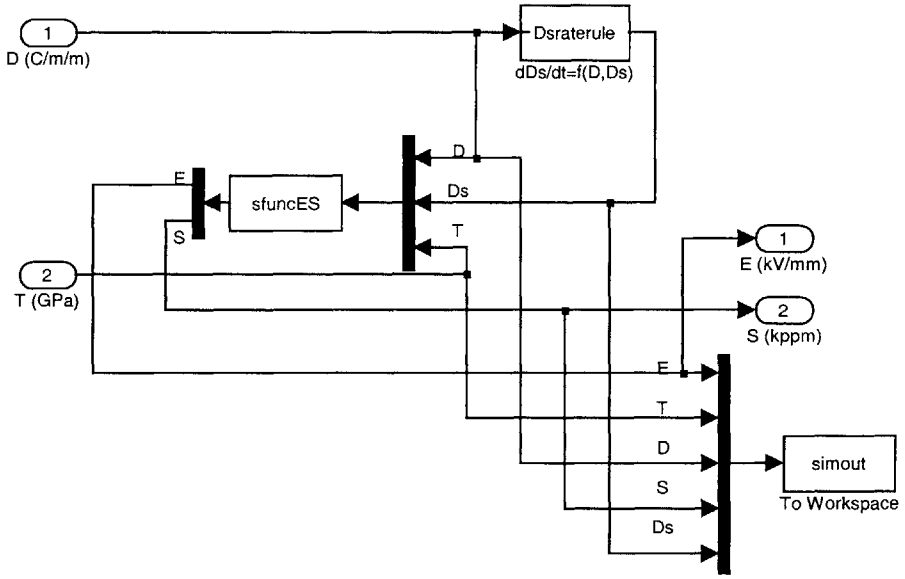

Figure A-12: Details of block "Piezo" in Figure A-11.

A.6 1-D Nonlinear Open Circuit Piezoelectricity with Conduction

To account for the internal conduction of the piezoelectric specimen under open circuit condition, the 1-D model shown in Figure A-11 has been modified by including a linear resistor R as illustrated in Figure A-13. The block labeled "E2V" converts electric field to voltage via the specimen thickness. The block labeled "Q2D" converts charge to electric displacement via the area of the specimen cross section. The block labeled "Piezo" is detailed in Figure A-12. The initial conditions of D and D^* are specified at the block named "D0" and the s-function "Dsraterule", respectively.

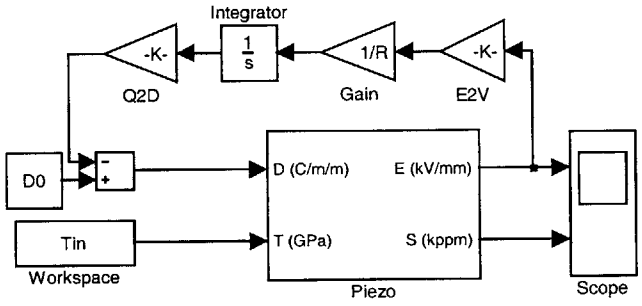

Figure A-13: 1-D nonlinear open circuit simulation with conduction.

A.7 3-D Nonlinear Open Circuit Piezoelectricity

Figure A-14 shows the graphical simulation of the 3-D nonlinear piezoelectric response under open circuit condition using the 3-D model developed in this thesis. The block labeled "Piezo" is detailed in Figure A-15. The s-functions "Dsraterule3D" and "sfuncES3D" are listed in Appendices B.3 and B.3, respectively. The initial conditions of D and D^* are specified at the block named "D0" and the s-function "Dsraterule3D", respectively.

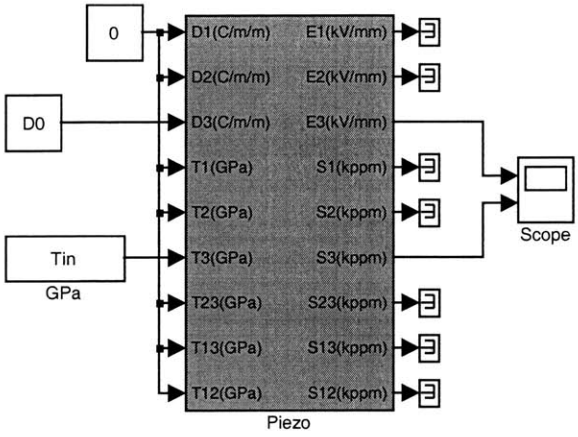

Figure A-14: 3-D nonlinear open circuit simulation.

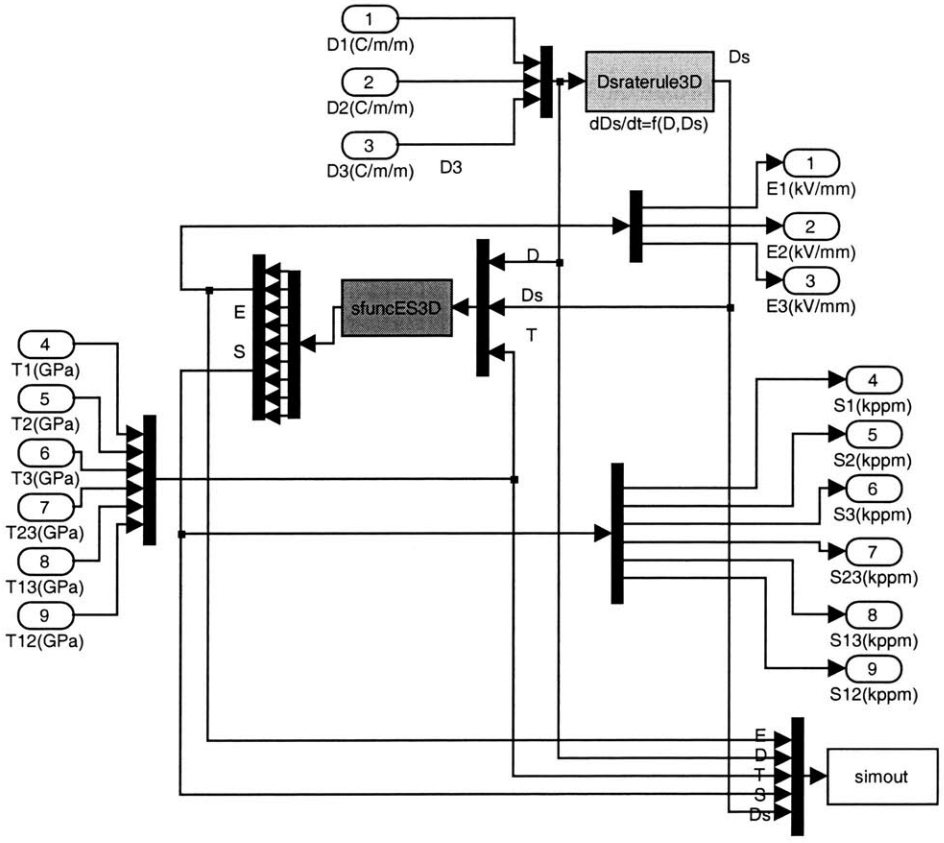

Figure A-15: Details of block "Piezo" in Figure A-14.

A.8 3-D Nonlinear Open Circuit Piezoelectricity with Conduction

To account for the internal conduction of the piezoelectric specimen under open circuit condition, the 3-D model shown in Figure A-14 has been modified by including a linear resistor R as shown in Figure A-16. The block labeled "E2V" converts electric field to voltage via the specimen thickness. The block labeled "Q2D" converts charge to electric displacement via the area of the specimen cross section. The block labeled "Piezo" is detailed in Figure A-15. The initial condition of D and D^* are specified at the block named "D0" and the s-function "Dsraterule3D", respectively.

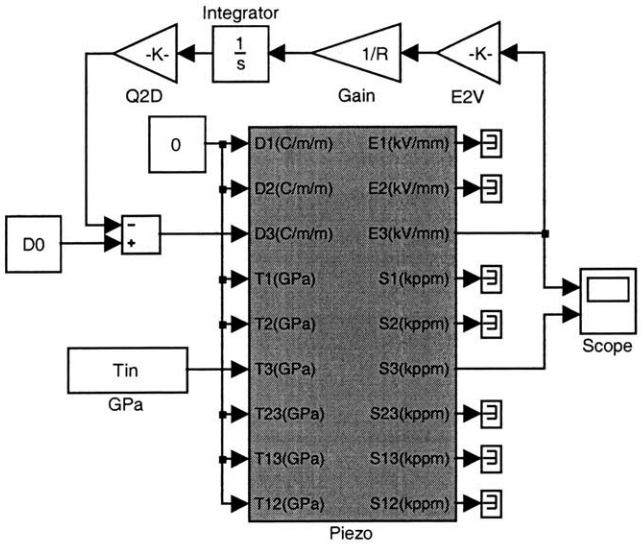

Figure A-16: 3-D nonlinear open circuit simulation with conduction.

A.9 1-D Nonlinear Piezoelectricity with Diode Circuit

To simulate 1-D nonlinear piezoceramics with the diode circuit, the simulation shown in Figure A-3 has been modified by replacing the block labeled "piezo" with the one detailed in Figure A-17. The block labeled "E2V" converts electric field to voltage via the specimen thickness. The block labeled "Q2D" converts charge to electric displacement via the area of the specimen cross section. The block labeled "F2T" converts force to stress via the area of the specimen cross section. The block labeled "S2x" converts strain to displacement via the specimen thickness. The initial conditions of D and D^* are specified at the block named "D0" and the s-function "Dsraterule", respectively.

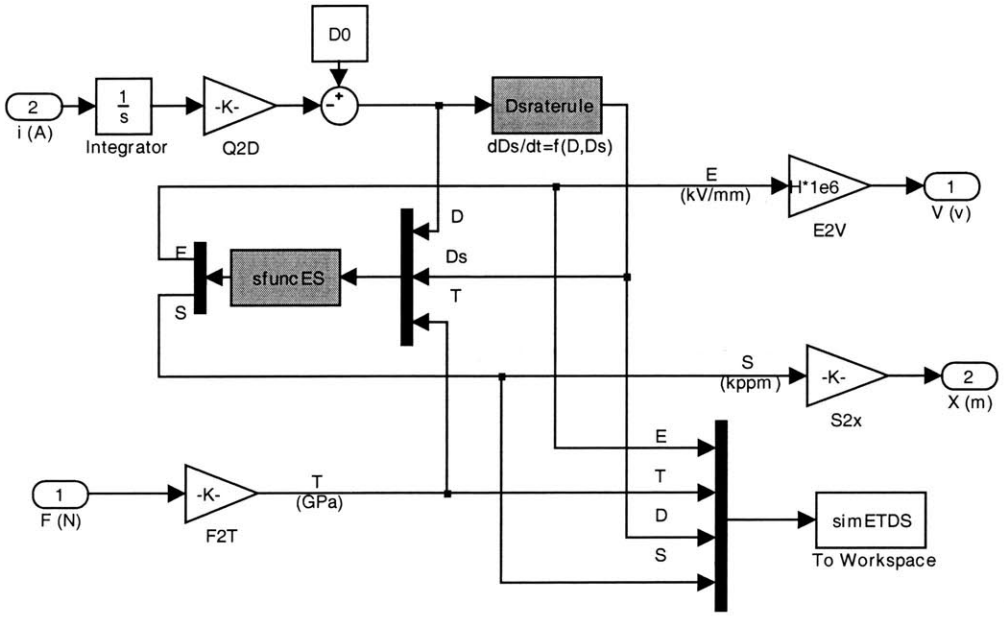

Figure A-17: 1-D nonlinear "Piezo" block for diode circuit simulation used in Figure A-3.

A.10 3-D Nonlinear Piezoelectricity with Diode Circuit

To simulate 3-D nonlinear piezoceramics with the diode circuit, the simulation shown in Figure A-3 has been modified by replacing the block labeled "piezo" with the one detailed in Figure A-18. The block labeled "E2V" converts electric field to voltage via the specimen thickness. The block labeled "Q2D" converts charge to electric displacement via the area of the specimen cross section. The block labeled "F2T" converts force to stress via the area of the specimen cross section. The block labeled "S2x" converts strain to displacement via the specimen thickness. The block labeled "Piezo" in Figure A-18 is detailed in Figure A-15. The initial conditions of D and D^* are specified at the block named "D0" and the s-function "Dsraterule3D", respectively.

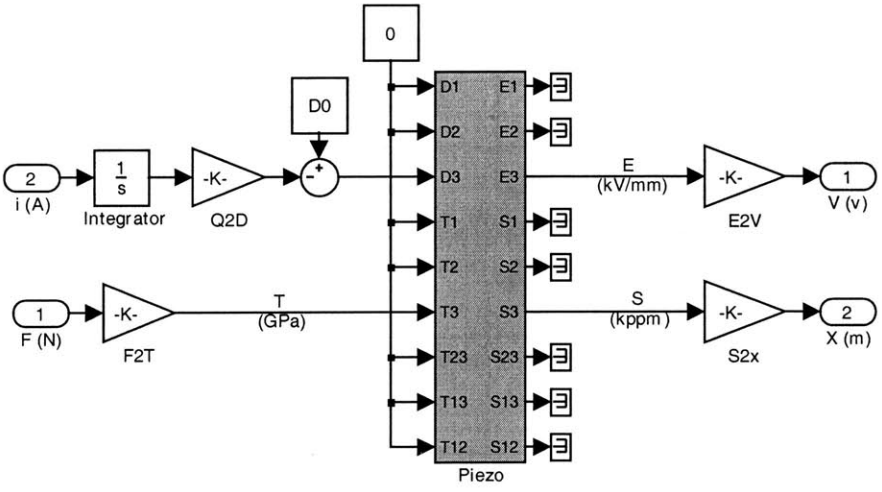

Figure A-18: 3-D nonlinear "Piezo" block for diode circuit simulation used in Figure A-3.

Appendix B

S-Function

B.1 Dsraterule.m

```
function [sys,x0,str,ts] = Dsraterule(t,x,u,flag,tau,dDc,a,Ds0)
switch flag,
%%%%%%%%%%%%%%%%%%
% Initialization %
%%%%%%%%%%%%%%%%%%
case 0,
[sys,x0,str,ts]=mdlInitializeSizes(t,x,u,tau,dDc,a,Ds0);
%%%%%%%%%%%%%%%
% Derivatives %
%%%%%%%%%%%%%%%
case 1,
sys=mdlDerivatives(t,x,u,tau,dDc,a);
%%%%%%%%%%
% Outputs %
%%%%%%%%%%
case 3,
sys=mdlOutputs(t,x,u,tau,dDc,a);
%%%%%%%%%%%%%%%%%%
% Unhandled flags %
%%%%%%%%%%%%%%%%%%
case { 2, 4, 9 },
sys = [ ];
%%%%%%%%%%%%%%%%%%%%
% Unexpected flags %
%%%%%%%%%%%%%%%%%%%%
otherwise
error(['Unhandled flag = ',num2str(flag)]);
```

```
end
% end csfunc
%
%=============================================================
% mdlInitializeSizes
% Return the sizes, initial conditions,
% and sample times for the S-function.
%=============================================================
%
function [sys,x0,str,ts]=mdlInitializeSizes(t,x,u,tau,dDc,a,Ds0)
sizes = simsizes;
sizes.NumContStates  = 1;
sizes.NumDiscStates  = 0;
sizes.NumOutputs     = 1;
sizes.NumInputs      = 1;
sizes.DirFeedthrough = 1;
sizes.NumSampleTimes = 1;
sys = simsizes(sizes);
x0  = Ds0;
str = [ ];
ts  = [0 0];
% end mdlInitializeSizes
%
%=============================================================
% mdlDerivatives
% Return the derivatives for the continuous states.
%=============================================================
%
function sys=mdlDerivatives(t,x,u,tau,dDc,a)
D=u;
Ds=x;
sys=(D-Ds)/tau*(1-exp(-((D-Ds)/dDc)^(2*a)));
% end mdlDerivatives
%
%=============================================================
% mdlOutputs
% Return the block outputs.
%=============================================================
%
function sys=mdlOutputs(t,x,u,tau,dDc,a) D=u; Ds=x;
sys=x;
% end mdlOutputs
```

B.2 sfuncES.m

```
function [sys,x0,str,ts] = sfuncES(t,x,u,flag)
switch flag,
  %%%%%%%%%%%%%%%%%%
  % Initialization %
  %%%%%%%%%%%%%%%%%%
  % Initialize the states, sample times, and state ordering strings.
  case 0
    [sys,x0,str,ts]=mdlInitializeSizes;
  %%%%%%%%%%
  % Outputs %
  %%%%%%%%%%
  % Return the outputs of the S-function block.
  case 3
    sys=mdlOutputs(t,x,u);
  %%%%%%%%%%%%%%%%%%
  % Unhandled flags %
  %%%%%%%%%%%%%%%%%%
  % There are no termination tasks (flag=9) to be handled.
  % Also, there are no continuous or discrete states,
  % so flags 1,2, and 4 are not used, so return an emptyu
  % matrix
  case { 1, 2, 4, 9 }
    sys=[];
  %%%%%%%%%%%%%%%%%%%%%%%%%%%%%%%%
  % Unexpected flags (error handling)%
  %%%%%%%%%%%%%%%%%%%%%%%%%%%%%%%%
  % Return an error message for unhandled flag values.
  otherwise
    error(['Unhandled flag = ',num2str(flag)]);
end
%
%=============================================================================
% mdlInitializeSizes
% Return the sizes, initial conditions, and sample times for the S-function.
%=============================================================================
%
function [sys,x0,str,ts] = mdlInitializeSizes()
sizes = simsizes;
sizes.NumContStates  = 0;
sizes.NumDiscStates  = 0;
sizes.NumOutputs     = 2;
sizes.NumInputs      = 3;
sizes.DirFeedthrough = 1;   % has direct feedthrough
```

```
sizes.NumSampleTimes = 1;
sys = simsizes(sizes);
str = [];
x0  = [];
ts  = [-1 0];   % inherited sample time
% end mdlInitializeSizes
%
%=============================================================================
% mdlOutputs
% Return the output vector for the S-function
%=============================================================================
%
function sys = mdlOutputs(t,x,u)
D=u(1);
Ds=u(2);
T=u(3);
sys(1)= % E(D,Ds,T)
sys(2)= % S(D,Ds,T)
```

B.3 Dsraterule3D.m

```
function [sys,x0,str,ts] = Draterule(t,x,u,flag,tau,dDc,a,Ds0)
switch flag,
  %%%%%%%%%%%%%%%%%%
  % Initialization %
  %%%%%%%%%%%%%%%%%%
  case 0,
    [sys,x0,str,ts]=mdlInitializeSizes(Ds0);
  %%%%%%%%%%%%%%%%
  % Derivatives %
  %%%%%%%%%%%%%%%%
  case 1,
    sys=mdlDerivatives(t,x,u,tau,dDc,a);
  %%%%%%%%%%
  % Outputs %
  %%%%%%%%%%
  case 3,
    sys=mdlOutputs(t,x,u,tau,dDc,a);
  %%%%%%%%%%%%%%%%%%%%
  % Unhandled flags %
  %%%%%%%%%%%%%%%%%%%%
  case { 2, 4, 9 },
    sys = [];
  %%%%%%%%%%%%%%%%%%%%%%
  % Unexpected flags %
  %%%%%%%%%%%%%%%%%%%%%%
  otherwise
    error(['Unhandled flag = ',num2str(flag)]);
end
% end csfunc
%
%=============================================================================
% mdlInitializeSizes
% Return the sizes, initial conditions, and sample times for the S-function.
%=============================================================================
%
function [sys,x0,str,ts]=mdlInitializeSizes(Ds0)
sizes = simsizes;
sizes.NumContStates  = 3;
sizes.NumDiscStates  = 0;
sizes.NumOutputs     = 3;
sizes.NumInputs      = 3;
sizes.DirFeedthrough = 0;
sizes.NumSampleTimes = 1;
```

```
sys = simsizes(sizes);
x0  = [Ds0];  % a vector of 3 element
str = [];
ts  = [0 0];
% end mdlInitializeSizes
%
%=============================================================================
% mdlDerivatives
% Return the derivatives for the continuous states.
%=============================================================================
%
function sys=mdlDerivatives(t,x,u,tau,dDc,a)
D=u;
Ds=x;
% concise form
sys=(D-Ds)/tau*(1-exp(-(norm(D-Ds)/dDc)^(2*a)));
% end mdlDerivatives
%
%=============================================================================
% mdlOutputs
% Return the block outputs.
%=============================================================================
%
function sys=mdlOutputs(t,x,u,tau,dDc,a)
sys=x;
%end mdlOutputs
```

B.4 sfuncES3D.m

```
function [sys,x0,str,ts] = sfuncES(t,x,u,flag) switch flag,
%%%%%%%%%%%%%%%%%%
% Initialization %
%%%%%%%%%%%%%%%%%%
% Initialize the states, sample times, and state ordering strings.
case 0
[sys,x0,str,ts]=mdlInitializeSizes;
%%%%%%%%%%
% Outputs %
%%%%%%%%%%
% Return the outputs of the S-function block.
case 3
sys=mdlOutputs(t,x,u);
%%%%%%%%%%%%%%%%%%
% Unhandled flags %
%%%%%%%%%%%%%%%%%%
% There are no termination tasks (flag=9) to be handled.
% Also, there are no continuous or discrete states,
% so flags 1,2, and 4 are not used, so return an emptyu
% matrix
case { 1, 2, 4, 9 }
sys=[];
%%%%%%%%%%%%%%%%%%%%%%%%%%%%%%%%%%
% Unexpected flags (error handling)%
%%%%%%%%%%%%%%%%%%%%%%%%%%%%%%%%%%
% Return an error message for unhandled flag values.
otherwise
error(['Unhandled flag = ',num2str(flag)]);
end
%
%=============================================================================
% mdlInitializeSizes
% Return the sizes, initial conditions, and sample times for the S-function.
%=============================================================================
%
function [sys,x0,str,ts] = mdlInitializeSizes()
sizes = simsizes;
sizes.NumContStates  = 0;
sizes.NumDiscStates  = 0;
sizes.NumOutputs     = 9;
sizes.NumInputs      = 12;
sizes.DirFeedthrough = 1;   % has direct feedthrough
sizes.NumSampleTimes = 1;
```

```
sys = simsizes(sizes);
str = [];
x0  = [];
ts  = [-1 0];   % inherited sample time
% end mdlInitializeSizes
%
%=============================================================================
% mdlOutputs
% Return the output vector for the S-function
%=============================================================================
%
function sys = mdlOutputs(t,x,u)

D1=u(1);
D2=u(2);
D3=u(3);
Ds1=u(4);
Ds2=u(5);
Ds3=u(6);
T1=u(7);
T2=u(8);
T3=u(9);
T23=u(10);
T13=u(11);
T12=u(12);
sys(1)= % E1(D1,D2,D3,Ds1,Ds2,Ds3,T1,T2,T3,T23,T13,T12)
sys(2)= % E2(D1,D2,D3,Ds1,Ds2,Ds3,T1,T2,T3,T23,T13,T12)
sys(3)= % E3(D1,D2,D3,Ds1,Ds2,Ds3,T1,T2,T3,T23,T13,T12)
sys(4)= % S1(D1,D2,D3,Ds1,Ds2,Ds3,T1,T2,T3,T23,T13,T12)
sys(5)= % S2(D1,D2,D3,Ds1,Ds2,Ds3,T1,T2,T3,T23,T13,T12)
sys(6)= % S3(D1,D2,D3,Ds1,Ds2,Ds3,T1,T2,T3,T23,T13,T12)
sys(7)= % S4(D1,D2,D3,Ds1,Ds2,Ds3,T1,T2,T3,T23,T13,T12)
sys(8)= % S5(D1,D2,D3,Ds1,Ds2,Ds3,T1,T2,T3,T23,T13,T12)
sys(9)= % S6(D1,D2,D3,Ds1,Ds2,Ds3,T1,T2,T3,T23,T13,T12)
```

Bibliography

[1] V. Tikare B. G. Potter, Jr. and B. A. Tuttle. "Monte Carlo Simulation of Ferroelectric Domains Structure and Applied Field Response in Two Dimensions," *Journal of Applied Physics*, Vol. 87, No. 9, pp. 4415-4424, 2000.

[2] Andrey N. Soukhojak and Yet-Ming Chiang. "Generalized Rheology of Active Materials," *Journal of Applied Physics*, Vol. 88, No. 11, pp. 6902-6909, 2000.

[3] Alberto Garcia and David Vanderbilt, "Electromechanical Behavior of BaTiO3 from First Principles," *Applied Physics Letters*, Vol. 72, No. 23, pp. 2981-2983, 1998.

[4] *IEEE Standard on Piezoelectricity*, ANSI/IEEE Std 176-1987.

[5] Sang-Joo Kim and Sunggi Kim, "On the Effects of the Heat Generated during an Electric Field-induced Ferroelectric Domain Switching," *International Journal of Solids and Structure*, Vol. 38, pp. 1311-1325, 2001.

[6] J. Fan, W. A. Stoll, and C. S. Lynch, "Nonlinear Constitutive Behavior of Soft and Hard PZT: Experiments and Modeling," *Acta Materialia*, Vol. 47, No. 17, pp. 4415-4425, 1999.

[7] Ralph C. Smith and Zoubeida Ounaies, "A Domain Wall Model for Hysteresis in Piezoelectric Materials," *ICASE Report*, No. 99-52, 1999.

[8] Henno Allik and Thomas J. R. Hughes "Finite Element Method for Piezoelectric Vibration," *International Journal for Numerical Methods in Engineering*, Vol. 2, pp. 151-157, 1970

[9] E. Bassiouny, A. F. Ghaleb and G. A. Maugin " Thermodynamical Formulation for Coupled Electromechanical Hysteresis Effects - I. Basic Equations," *International Journal of Engineering Science,* Vol. 26, No. 12, pp. 1279-1295, 1988

[10] E. Bassiouny, A. F. Ghaleb and G. A. Maugin " Thermodynamical Formulation for Coupled Electromechanical Hysteresis Effects - II. Poling of Ceramics," *International Journal of Engineering Science,* Vol. 26, No. 12, pp. 1297-1306, 1988

[11] E. Bassiouny and G. A. Maugin " Thermodynamical Formulation for Coupled Electromechanical Hysteresis Effects - III. Basic Equations," *International Journal of Engineering Science,* Vol. 27, No. 8, pp. 975-987, 1989

[12] E. Bassiouny and G. A. Maugin " Thermodynamical Formulation for Coupled Electromechanical Hysteresis Effects - IV. Combined Electromechanical Loading," *International Journal of Engineering Science,* Vol. 27, No. 8, pp. 989-1000, 1989

[13] Peter J. Chen and Stephen T. Montgomery " A Macroscopic Theory for the Existence of the Hysteresis and Butterfly Loops in Ferroelectricity," *Ferroelectrics,* Vol. 23, pp. 199-208, 1980

[14] Peter J. Chen and P. S. Peerey "One Dimensional Dynamic Electromechanical Constitutive Relations of Ferroelectric Materials," *Acta Mechanica,* Vol. 31, pp. 231-241, 1979

[15] Peter J. Chen and T. J. Tucker "Determination of the Polar Equilibrium Properties," *Acta Mechanica,* Vol. 38, pp. 209-218, 1981

[16] Peter J. Chen, C. E. Land, and Marcella M. Madsen "A Theory of the Influences of Space-Charge Field on Domain Switching in PLZT 7/65/35 Ceramic," *Acta Mechanica,* Vol. 43, pp. 61-72, 1982

[17] Peter J. Chen, "Characterization of the Three Dimensional Properties of Poled PZT 65/35 in the Absence of Losses," *Acta Mechanica,* Vol. 47, pp. 95-106, 1983

[18] Peter J. Chen, C. E. Land, and Marcella M. Madsen "Three Dimensional Constitutive Relations for Ferroelectric Materials in the Presence of Quasi-Static Domain Switching," *Acta Mechanica,* Vol. 48, pp. 31-42, 1983

[19] J. S. Cory and J. L. McNichols, Jr., " Nonequilibrium Thermostatics" *Journal of Applied Physics,* Vol. 58. No. 9, pp. 3283-3294, 1985

[20] Craig L. Hom and Natarajan Shankar, " A Fully Coupled Constitutive Model for Electrostrictive Ceramic Materials" *Journal of Intelligent Material Systems and Structures,* Vol. 5, pp. 795-801 , 1994

[21] M. Kamlah, U. Bhle, D. Munz, and Ch. Tsakmakis, "Macroscopic Description of the Nonlinear Electromechanical Coupling in Ferroelectrics" *Smart Structures and Materials 1997: Smart Structures and Integrated Systems, San Diego, CA, USA, Proceedings of SPIE - The International Society for Optical Engineering,* Vol. 3039, pp. 144-155, 1997.

[22] S. C. Hwang, C. S. Lynch and R. M. McMeeking, " Ferroelectric/Ferroelastic Interations and a Polarization Switching Model" *Acta Metallurgica et Materialia,* Vol. 43, No. 5, pp. 2073-2084, 1995

[23] C. S. Lynch "Effect of Uniaxial Stress on the Electro-mechanical Response of 8/65/35 PLZT" *Acta Materialia,* Vol. 44, No. 10, pp. 4137-4148, 1996

[24] W. Chen and C. S. Lynch "A Micro-electro-mechanical Model for Polarization Switching of Ferroelectric Materials" *Acta Materialia,* Vol. 46, No. 15, pp. 5303-5311, 1998

[25] G. A. Maugin and J. Pouget, "Electroacoustic Equations for One-domain Ferroelectric Bodies, *Journal of the Acoustical Society of America,* Vol. 68, No. 2, pp. 575-587, 1980

[26] E. F. Prechtl and S. R. Hall, "Design of a High Efficiency, Large Stroke, Electromechanical Actuator," *Smart Materials and Structures,* Vol. 8, No. 1, pp. 13, Feb. 1999.

[27] N. W. Hagood and A. A. Bent, "Development of Piezoelectric Fiber Composites for Structural Actuation," *34th AIAA/ASME/ASCE/AHS/ASC Structures, Structural Dynamics, and Materials Conference*, LaJolla, CA, pp. 3625-3638, 1993.

[28] H. H. A. Krueger and D. Berlincourt, "Effects of High Static Stress on the Piezoelectric Properties of Transducer Materials," *Journal of the Acoustical Society of America,* Vol. 33, pp. 1339-44, 1961.

[29] Q. M. Zhang, J. Zhao, K. Uchino, and J. Zheng, "Change of the Weak-field Properties of Pb(ZrTi)O3 Piezoceramics with Compressive Uniaxial Stresses and its Links to the Effect of Dopants on the Stability of the Polarizations in the Materials," *Journal of Materials Research,* Vol. 12, pp. 226-234, 1997.

[30] B. Jaffe, W. R. Cook, and H. Jaffe, *Piezoelectric Ceramics.* London, New York,: Academic Press, 1971.

[31] D. J. Warkentin and N. W. Hagood, "Nonlinear Piezoelectric Shunting for Structural Damping," *Smart Structures and Materials 1997: Smart Structures and Integrated Systems, San Diego, CA, USA, pp. 747-757: Proceedings of SPIE - The International Society for Optical Engineering.* v 3041 1997. Society of Photo-Optical Instrumentation Engineers, Bellingham, WA, USA.

[32] M. Umeda, K. Nakamura, and S. Ueha, "Analysis of the Transformation of Mechanical Impact Energy to Electric Energy Using Piezoelectric Vibrator," *Japanese Journal of Applied Physics, Part 1-Regular Papers Short Notes and Review Papers,* Vol. 35, pp. 3267-3273, 1996.

[33] M. Umeda, K. Nakamura, and S. Ueha, "Energy Storage Characteristics of a Piezogenerator Using Impact Induced Vibration," *Japanese Journal of Applied Physics Part 1-Regular Papers Short Notes and Review Papers,* Vol. 36, pp. 3146-3151, 1997.

[34] T. Michelitsch and W. S. Kreher, "Simple Model for the Nonlinear Material Behavior of Ferroelectrics," *Acta Materialia,* Vol. 46, pp. 5085-5094, 1998.

[35] K. Ghandi, "Nonlinear Modeling and Characterization Techniques for Phase Transitions in Electromechanically Coupled Devices," Ph.D. Thesis, Massachusetts Institute of Technology, 1998

[36] J. E. Harper, "Analysis of Nonlinear Electroelastic Continua with Electric Conduction," S.M. Thesis, Massachusetts Institute of Technology, 1999

[37] W. Chen and C. S. Lynch, "Micro-electro-mechanical Model for Polarization Switching of Ferroelectric Materials," *Acta Materialia,* Vol. 46, pp. 5303-5311, 1998.

[38] C. Kim, A. E. Glazounov, F. D. Flippen, A. Pattnaik, Q. M. Zhang, and D. Lewis, III, "Piezoelectric Ceramic Assembly Tubes for Torsional Actuators," *Proceedings of Spie - the International Society for Optical Engineering.* Vol. 3675, 1999, pp. 53-62.

[39] M. Lutz and N. W. Hagood, "Actuation Efficiency in Piezoelectricly Driven Linear and Non-linear Systems," *Proceedings of Spie - the International Society for Optical Engineering.* Vol. 3668, pp. 780-796, 1999

[40] L. P. Huelsman, *Active and Passive Analog Filter Design* McGraw-Hill, Inc., 1993.

[41] D. G. Morris, N. W. Hagood and A. Pizzochero, " Experimental Investigation on the Effect of Environmental Stress on Active Fiber Composite Actuators," *Proceedings of Spie - the International Society for Optical Engineering.* Vol. 3674, pp. 296-305, 1999

[42] T. G. Beckwith, R. D. Marangoni and J. H. Lienhard V, *Mechanical Measurements.* Addison-Wesley Publishing Company, 1993.

[43] A. J. Peyton and V. Walsh, *Analog Electronics with Op Amps, A source Book of Practical Circuits.* Cambridge University Press, 1993.

[44] E. H. Anderson, "Piezoceramic Induced Strain Actuation of One - and Two-dimensional Structures," M.S. Thesis, Massachusetts Institute of Technology, 1989.

[45] M. Gellert and R. Harbord, "Moderate Degree Cubature Formulas for 3-D Tetrahedral Finite-Element Approximations," *Communications in Applied Numerical Methods,* Vol. 7, pp. 487-495, 1991.

[46] K. E. Brenan, S. L. Campbell and L. R. Petzold, *Numerical Solution of Intial-Value Problems in Differential-Algebraic Equations,* Society for Industrial and Applied Mathematics, 1996.

[47] B. Jaffe, W. Cook, and H. Jaffe, *Piezoelectric Ceramics,* Academic Press Limited, 1971.

[48] F. Jona and G. Shirane, *Ferroelectric Crystals,* Dover Publications, Inc. 1993.

[49] N. Hagood, R. Kindel, K. Ghandi, and P. Gaudenzi, "Improving Transverse Actuation of Piezoceramics using Interdigitated Surface Electrodes," Paper No. 1917-25, *Proc. of SPIE's Symposium on Smart Structures and Intelligent Systems,* Albuquerque, NM, 1993.

[50] E. F. Crawley, J. Deluis, "Use of Piezoelectric Actuators as Elements of Intelligent Structures," *AIAA Journal,* Vol. 25. No. 10, 1987, pp. 1373-1385.

[51] J. Rodgers, "Development of An Integral Twist-Actuated Rotor Blade for Individual Blade Control," Ph.D. Thesis, Massachusetts Institute of Technology, 1998

[52] N.W. Hagood, D.C. Roberts, L. Saggere, K.S. Breuer, K.-S. Chen, J.A. Carretero, H.Q. Li, R. Mlcak, S. Pulitzer, M.A. Schmidt, S.M. Spearing, and Y.-H. Su, "Micro Hydraulic Trans- ducer Technology for Actuation and Power Generation," *Proceedings of the SPIE 7th Annual International Symposium on Smart Structures and Materials,* Vol. 3985, pp. 680-688, Newport Beach, CA, March 5-9, 2000.

[53] D. Berlincourt and H. H. A. Krueger, "Important Properties of Morgan Matroc Piezoelectric Ceramics", TP-226, Morgran Matroc, Inc. Bedford, OH 44146.

[54] Seung-Eek Park, Venkata Vedula, Ming-Jen Pan, Wesley S. Hackenberger, Patrick Pertsch and Thomas R. Shrout, "Relaxor Based Ferrorelectric Single Crystals for Electromechanical Actuators", TRS Ceramics, Inc. PA

[55] Crystal Associates, Inc. East Hanover, NJ 07936

[56] D. G. Morris, N. W. Hagood and A. Pizzochero, " Experimental Investigation on the Effect of Environmental Stress on Active Fiber Composite Actuators," *Proceedings of Spie - the International Society for Optical Engineering.* vol. 3674, pp. 296-305, 1999

[57] M. Goldfarb and L. D. Jones, "On the Efficiency of Electric Power Generation with Piezoelectric Ceramic," *Journal of Dynamic System, Measurement, and Control. Transaction of ASME*, vol. 121, September 1999, pp. 566 - 571

[58] O. Yaglioglu, "Modeling and Design Considerations for a Micro-Hydraulic Piezoelectric Power Generator", S.M. Thesis, Massachusetts Institute of Technology, Cambridge, MA, June 2002.

[59] A. F. Devonshire, "Theory of Ferroelectrics", *Philosophical Magazine*, Vol. 3, No. 10, April 1954, pp. 85-130.

[60] K. H. Chan, " Nonlinear Modeling of High Field Ferroelectric Ceramics for Structural Actuation", S.M. Thesis, Massachusetts Institute of Technology, Cambridge, MA, 1994.

[61] A. W. Drake, *Fundamentals of Applied Probability Theory*, McGraw-Hill, Inc.

[62] *Optimization Tool Box*, Mathworks, Natick, MA 01760

[63] M. E. Lines and A. M. Glass, *Principles and Applications of Ferroelectrics and related Materials*, Clarendon Press, Oxford, 1977.

[64] Q. S. Zheng, " On Transversely Isotropic, Orthotropic and Relative Isotropic Functions of Symmetric Tensors, Skew-Symmetric Tensors and Vectors, Part I: Two Dimensional Orthotropic and Relative Isotropic Functions and Three Dimensional Relative Isotropic Functions", International Journal of Engineering and Science, Vol. 31, No. 10, 1993, pp. 1399-1409.

[65] D. Zhou, M. Kamlah and D. Munz, "Rate Dependence of Soft PZT Ceramics under Electric Dield Loading," *SPIE Proceddings, Smart Structures and Materials, 2001*, Vol. 4333, pp. 64-70.

[66] Kenji Uchino, *Ferroelectric devices*, New York, 2000

[67] S. Wan and C.S. Lynch, " Characterization of PZN Single Crystals", 12th IEEE International Symposium on the Application of Ferroelectrics, Honolulu, Hawaii, 2000.

[68] T. Tsurumi, Y. Kumano, N. Ohashi, T. Takenaka and O. Fukunaga, " 90 ° domain reorientation and electric-field-induced strain of tetragonal Lead Zirconate Titanate ceramics", Japan Journal of Applied Physics, Vol. 36, pp. 5970-5975, 1997.

[69] B.K. Mukherjee, W. Ren, S.-F. Liu, A.J. Masys, and G. Yang, "Non-linear properties of piezoelectric ceramics" *Proceedings of the Conference on Smart Structures and Materials 2001, Newport Beach, CA, Mar. 5-8, 2001*, SPIE Proceedings. Vol. 4333, 2001, p. 41-54

[70] M.F. Ashby, "Physical Modelling of Materials Problems", *The Institute of Materials*, 1992

[71] *Using Simulink*, Mathworks, Natick, MA 01760

[72] *Writing S-Functions*, Mathworks, Natick, MA 01760

[73] B. Janos, "Design, Development, and Characterization of Magnetic Particle Active Fiber Composites," Ph.D. Thesis, Massachusetts Institute of Technology, 2001